Bi and Sb Nanowire Assemblies for Thermoelectric Applications

by Michael F. P. Wagner Department of Materials and Earth Sciences

TECHNISCHE
UNIVERSITÄT
DARMSTADT

Zur Erlangung des Grades eines Doktors der Ingenieurwissenschaften
genehmigte Dissertation von Michael Florian Peter Wagner
aus Kelkheim im Taunus
Titel: Bi and Sb Nanowire Assemblies for Thermoelectric Applications

1. Gutachten: Prof. Christina Trautmann
2. Gutachten: Prof. Wolfgang Ensinger

Tag der Einreichung: 30.05.2018
Tag der Prüfung: 24.08.2018

Department of Materials and Earth Sciences
Division of Ion-Beam-Modified Materials
Technische Universität Darmstadt
Alarich-Weiss-Straße 2
64287 Darmstadt

Darmstadt - 2018

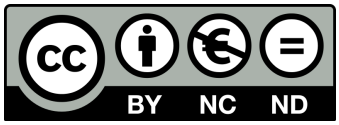

"Somewhere, something incredible is
waiting to be known."
-Carl Sagan

Zusammenfassung

Diese Arbeit präsentiert die Herstellung und Charakterisierung von $Bi_{1-x}Sb_x$ Nanodraht-Gruppen, mit vertikaler oder geneigter geometrischer Anordnung, deren Drahtdurchmesser und Zusammensetzung systematisch und kontrolliert eingestellt wurden. Die Nanodraht-Gruppen wurden mit Hilfe von Ionen-Spur Technology hergestellt, bei der Bi und Sb durch galvanische Abscheidung in die Nanokanäle einer mit Ionen bestrahlten und anschließend chemisch geätzten Polymer Folie abgeschieden wurden. Durch die systematische Variation der Ätz- und Abscheidungsbedingungen, einschließlich gepulster Potentiale und Tensid Konzentrationen im Elektrolyten, wurde der Herstellungsprozess optimiert, sodass homogene und einheitliche gewachsene Nanodraht-Gruppen hergestellt werden konnten. Der Einfluss der Abscheide Parameter auf Morphologie und Kristallstruktur der resultierenden Bi, Sb und $Bi_{1-x}Sb_x$ Nanodraht-Gruppen wurde mittels Röntgenbeugung, sowie hochauflösender Transmission und Rasterelektronen Mikroskopie untersucht. Der Seebeck-Koeffizient und der elektrische Widerstand der Nanodraht-Gruppen wurden detailliert als Funktion der Temperatur und des Nanodraht Durchmessers bestimmt. Die Ergebnisse bestätigen das p- und n-Typ-Verhalten der Sb- und Bi-Nanodrähte und belegen den Einfluss von Größeneffekten auf die thermoelektrischen Transporteigenschaften. Darüber hinaus wurde eine Methode zur Messung aller relevanten thermoelektrischen Eigenschaften entwickelt, um den thermoelektrischen Wirkungsgrad einer gegebenen Nanodraht-Gruppe zu bestimmen. Dazu gehören die Messung der elektrischen und thermischen Leitfähigkeit sowie des Seebeck-Koeffizient der Nanodraht-Gruppe. Zu guter letzt wurden komplexere Nanodraht-Gruppen durch Kombination von Ionenspur-Nanotechnologie und Mikrotechnologie hergestellt, um Thermoelemente die durch Sb- und Bi-Nanodraht-Arrays gebildet werden, herzustellen. Diese dreidimensionalen Nanodrahtanordnungen von parallelen oder miteinander verbundenen Nanodrähten mit einstellbarem Draht-Durchmesser und Dichte, eingebettet in Polymerschablonen, sind von großem Interesse für die zukünftige Implementierung als z.B. flexiblen Infrarotsensoren.

Abstract

This thesis presents the fabrication and characterization of $Bi_{1-x}Sb_x$ nanowire assemblies with well-controlled and systematically adjusted wire diameter, composition, and vertical or tilted geometrical alignment. The nanowire assemblies were fabricated by means of ion-track technology combining chemical etching of ion-irradiated polymer membranes with electrodeposition of Bi and Sb into track-etched nanochannels. By systematic variation of the etching and deposition conditions, including pulsed potential parameters and surfactant concentration in the electrolyte, the fabrication process was optimized yielding homogeneously grown, uniform nanowire assemblies and networks. The influence of the deposition parameters on morphology and crystalline structure of the resulting Bi, Sb and $Bi_{1-x}Sb_x$ nanowires and networks was investigated by means of X-ray diffraction, high resolution transmission and scanning electron microscopy. Seebeck coefficient and electrical resistance of the nanowire assemblies were investigated in detail as a function of nanowire diameter and temperature. The results confirm the p- and n-type behavior of the Sb and Bi nanowires and provide evidence of the influence of size effects on the thermoelectric transport properties. In addition, a method to measure all relevant thermoelectrical cross-plane properties to deduce the thermoelectric efficiency of a given nanowire assembly was developed. This includes the measurement of the electrical and thermal conductivity as well as the Seebeck coefficient of a nanowire assembly. Finally, more complex nanowire systems were fabricated by combining ion-track nanotechnology and microtechnology to prepare thermocouples formed by Sb and Bi nanowire arrays. These three-dimensional nanowire assemblies of parallel or interconnected nanowires with adjustable diameter and density, embedded in polymer templates, are of great interest for future implementation as e.g. flexible infrared sensors.

Contents

List of Abbreviations

Abbreviation	Definition
AAO	Anodic aluminum oxide
BF	Bright field
Bi	Bismuth
BSE	Back scattered electrons
DCM	Dichloromethane
DF	Dark field
DI	Deionised
DOS	Density of states
EDX	Energy dispersive X-ray spectroscopy
HRSEM	High resolution scanning electron microscopy
HRTEM	High resolution transmission electron microscopy
NW	Nanowire(s)
NWA	Nanowire assemblie(s)
NWNW	Nanowirenetwork(s)
PC	Polycarbonate
PET	Polyethylen terephthalat
PVD	Physical vapour deposition
RIE	Reactive ion etching
SAED	Selected area electron diffraction
Sb	Antimony
SCE	Standard calomel electrode
SE	Secundary electrons
SEM	Scanning elecron microscopy
TEM	Transmission electron microscopy
VLS	Vapour-liquid-solid
XRD	X-ray diffraction
At%	Atomic percentage

1 Motivation

> "'**We choose to go to the moon. We choose to go to the moon in this decade and do the other things, not because they are easy, but because they are hard, because that goal will serve to organize and measure the best of our energies and skills, because that challenge is one that we are willing to accept, one we are unwilling to postpone, and one which we intend to win, and the others, too.**"'
> **- J. F. Kennedy -**

In 2015 IBM announced the development of the worlds first functional 7 nm node test chips [1] and in their latest work (2017) they claim to be able to reduce the structure size down to 5 nm [2]. Miniaturization has proven to be a key concept also in other technological fields, as can be seen in the rapid development in micro technologies and the use of the words "'micro"' and "'nano"' in everyday speech. Since the discovery of the first transistor in 1947 up to today, a large number of both simple and sophisticated methods have been developed to fabricate systems in the micrometer and nanometer ranges. These systems can consist of various materials, that are assembled in complex arrangements, which become more sophisticated as the years go by [3, 4, 5]. Much like "Alice in Wonderland", by shrinking in size a new world opens up which sometimes plays by different rules, sometimes contradicting the everyday experience. This happens because other physical processes define the material properties in small structures than in bulk materials [6, 7, 8, 9]. The surface plays an ever increasing role as the volume is decreased, therefore also contributing significantly to the observed material properties. Using these "new" properties allows to improve old concepts as well as to build new devices in various fields, e.g. micro- and nanoelectromechanical systems and lab-on-a-chip applications [10]. This work combines three very important fields of nanotechnology research today: i) the preparation of nanostructures, specifically nanowires ii) the characterization of their properties and iii) the utilization of nanostructures in devices.

(i) Preparation of nanowire assemblies of $Bi_{1-x}Sb_x$:

Nowadays, there exists a large number of methods to prepare nanowires [10]. However, it is still challenging to prepare them with defined properties like the geometrical dimensions, chemical composition and crystal structure, which then leads to specific material properties. In this work two kinds of nanowire assemblies are fabricated, combining ion-track technology and electrochemistry. Nanowire arrays consisting of a large number of randomly distributed, parallel aligned individual nanowires and nanowire networks, with interconnected nanowires forming a three-dimensional net that spans over areas significantly larger than an individual nanowire, allowing it to be handled like a bulk material. Scanning electron microscopy images of both kinds of assemblies are shown in figure 1.1. Both kind of structures are prepared via pulsed potential electrodeposition in ion-track etched polycarbonate templates. The combination of ion-track technology and electrodeposition allows excellent control of the wire diameter, wire density, wire composition and to some degree also crystalline structure [11, 12]. The grown structures were then analyzed by X-ray diffraction (XRD), X-ray spectroscopy (EDX), transmission electron microscopy (TEM) and scanning electron microscopy (SEM) in order to provide informations on their morphological and structural properties. The theoretical background on the processes used to prepare the nanowire assemblies and the techniques used for characterization can be found in chapter 2. In chapter 3 the experimental results are presented.

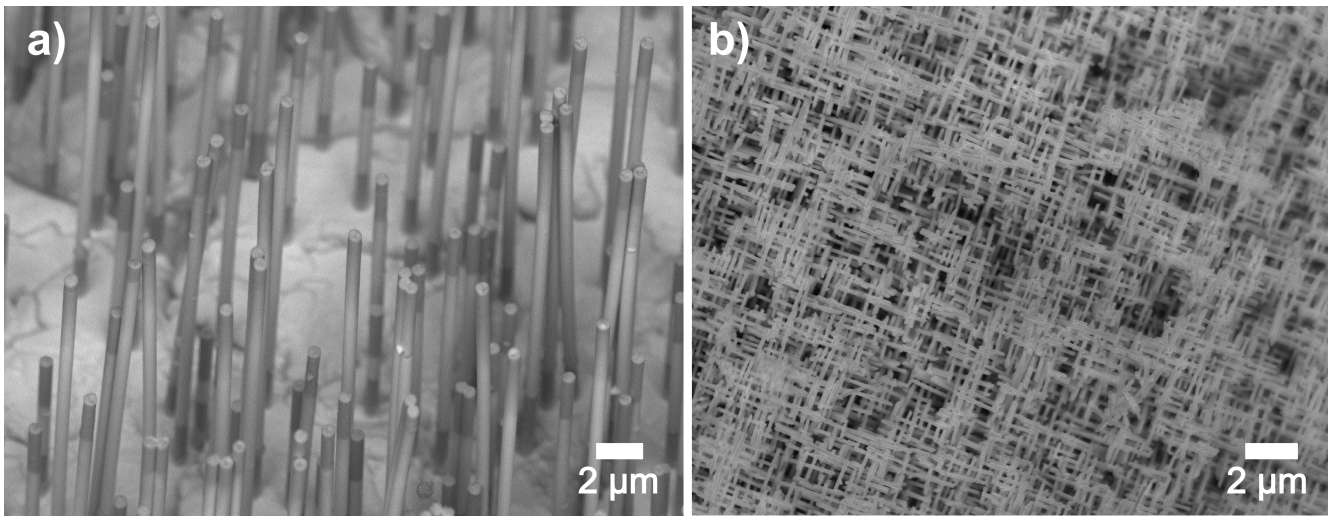

Figure 1.1: Scanning electron microscopy images of a) an array of free standing, parallel oriented nanowires b) a nanowire network.

(ii) Measurement of thermoelectric properties of nanowire assemblies:

The thermoelectric properties of nanowires are especially interesting as theoretical predictions propose high efficiency increases for materials with size confinement [13, 14]. In case of nanowire networks even further increases are predicted due to additional scattering effects of phonons at the wire junctions [15]. These efficiency gains would then allow the use of thermoelectric devices in a much broader spectrum of applications, e.g. waste heat recovery [16, 17], where they are limited now to nice applications due to their poor efficiency. More recent studies also focus on the fact that good thermoelectric materials like $Bi_{1-x}Sb_x$ also belong to the group of topological insulators, where surface states play a significant role in the transport behavior [18]. Due to the high surface to volume ratio in nanowire structures these surface states can significantly influence or even dominate the charge transport, possibly rendering efficiency gains due to confinement invalid [19]. Here, systematic basic research is needed to clarify these matters at hand [20, 21]. With regards to this, $Bi_{1-x}Sb_x$ is an excellent material system as theory predicts an enhancement of the thermoelectric efficiency already at a wire diameters around 60 nm [22]. Additionally the band structure can be fine tuned by the Sb content, allowing the transition from a semimetal to a semiconductor, thus making it an ideal material for transport studies [23]. Additionally $Bi_{1-x}Sb_x$ is one of the best n-type thermoelectric materials at low temperature which also makes it interesting for applications [24]. The characterization of the physical properties of nanowires is extremely difficult as ordinary measurement devices cannot be readily used due to the small geometrical sizes. Over the years various methods and microchips have been developed to make measurements on nanowires feasible [25, 26]. Basic research on the topic of nanostructured thermoelectric materials in Germany has been bundled within the SPP 1386 “Nanostructured Thermoelectric Materials: Theory, Model Systems and Controlled Synthesis” and a summary of the main results of the project can be found in [27], where also some results of this work has already been published. Chapter 4 gives an introduction into the field of thermoelectrics and in chapter 5 the Seebeck coefficient and electrical resistivity of antimony and bismuth nanowire arrays and nanowire networks are presented as well as a newly developed method to fully characterize the cross plane thermoelectric properties (Seebeck coefficient, electrical and thermal conductivity) of nanowire assemblies embedded in polymer.

(iii) Preparation of thermoelectric devices using nanowire assemblies:

Nowadays the focus of scientific interest shifts more and more from the basic materials research to device engineering. Also here nanowire structures are intriguing, as they would allow the preparation of especially thin, e.g. several hundred μm, sensor devices [28]. Due to there small size they could then be easily integrated into devices, becoming the "eyes and ears" of intelligent systems playing a major role in the proclaimed fourth industrial revolution. Nanowire networks are of particular interest here as they provide a mechanically rigid and electrical reliable structure [29, 30]. One possible application of thermoelectric sensors is the contactless measurement of temperatures via the detection of infrared radiation. The construction of such devices using nanowire assemblies however is still challenging although industry already works on their realization. Chapter 6 presents trials on the fabrication of such devises using known processes from micro systems technology in combination with the applied ion-track technology.

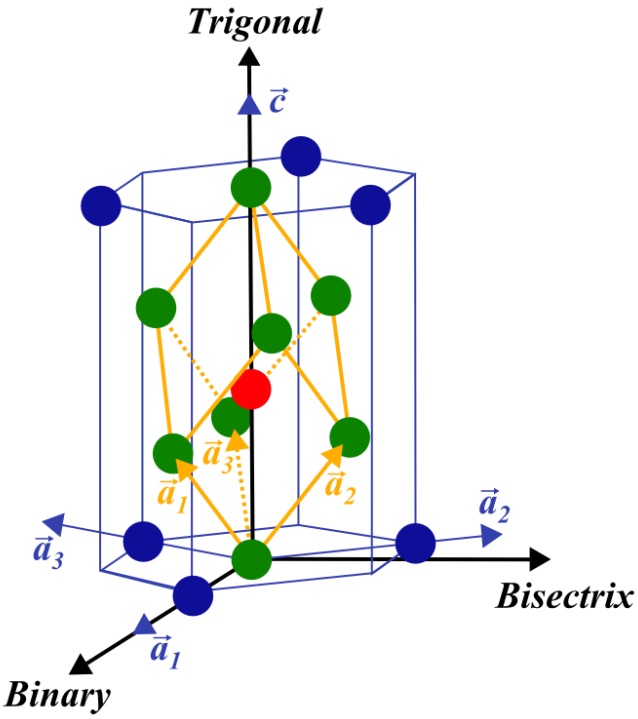

Figure 1.2: Schematic of the crystal structure of Sb or Bi [31]. The rhombohedral unit cell is given by the orange lines, with $\vec{a}_1$, $\vec{a}_2$ and $\vec{a}_3$ being the corresponding rhombohedral lattice vectors. The green and red spheres mark the two atoms in the rhombohedral unit cell. The blue lines represent the hexagonal unit cell with $\vec{a}_1$, $\vec{a}_2$, $\vec{a}_3$ and $\vec{c}$ being the corresponding hexagonal lattice vectors. The hexagonal unit cell contains 6 atoms, but for clarity not all atoms are shown. The trigonal, binary, and bisectrix direction form a Cartesian coordinate system and are parallel to $\vec{c}$ (trigonal), $\vec{a}_1$ (binary) and orthogonal to $\vec{a}_1$ and $\vec{c}$, respectively.

1.1 Antimony, Bismuth and Their Alloy

Antimony, bismuth as well as their alloys possess a rhombohedral crystal structure which belongs to the spacegroup 166 ($R\bar{3}m$), sometimes also referred to as A_7 structure. The structure can also be represented by a hexagonal unit cell, then including six atoms per unit cell, instead of two in the rhombohedral unit cell [32]. A schematic of both structures and how they relate to another is shown in figure 1.2

[31]. The hexagonal system can be described by four lattice vectors $\vec{a}_1$, $\vec{a}_2$, $\vec{a}_3$ and $\vec{c}$. All $\vec{a}$ lie in the same plane with an angle of 120° between them and $\vec{c}$ is oriented orthogonally to them. Due to the fact that $|\vec{a}_1| = |\vec{a}_2| = |\vec{a}_3|$, the lattice parameters a and c suffice to describe the system. For pure antimony $a = 4.3085$ Å and $c = 11.2732$ Å and for pure bismuth $a = 4.5465$ Å and $c = 11.8616$ Å [33, 34]. In this work, lattice planes and directions are always referred to the hexagonal base. In order to emphasize this a four indices description $hkil$ will be used for planes and directions, with $i = -(h + k)$ being replaced by a dot $hk.l$, for simplicity.

Using the hexagonal description, the d-spacing of lattice planes is given by:

$$\frac{1}{d_{hkl}^2} = \frac{4}{3}\frac{h^2 + hk + k^2}{a^2} + \frac{l^2}{c^2}. \tag{1.1}$$

The tables 1.1 a) and b) list the d-spacings, as well as the diffraction angle 2θ and normalized intensity I_0 of the six most prominent planes of Bi and Sb powder samples, when using $Cu_{K\alpha}$ radiation. The intensity in both cases is normalized with regards to the highest reflex. In case Bi and Sb are mixed, the large similarity between their structures allows them to form solid solutions over the whole composition range [35]. The lattice parameters for the solutions almost follow Vegards law, which states that the lattice parameters is equal to the weighted mean of the lattice parameters of the two materials [36, 33]. Since the thermoelectric transport properties will be discussed later in this work, the overview of the thermoelectric transport properties of $Bi_{1-x}Sb_x$ is shifted to a more suitable position and can be found in chapter 4.6.

Table 1.1: d-spacings and diffraction data (normalized intensity I_0, diffraction angle 2θ) of the 6 highest intensity reflections of a) antimony and b) bismuth, based on powder diffraction data JCPDS 35-732 and JCPDS 5-519, respectivly.

a) Antimony

$\{hkl\}$	i_0	d_{hkl} **[Å]**	2θ [°]
012	100	3.11	28.69
104	70	2.25	40.08
122	67	1.37	68.54
116	63	1.42	65.91
110	56	2.15	41.95
214	40	1.26	75.30

b) Bismuth

$\{hkl\}$	i_0	d_{hkl} **[Å]**	2θ [°]
012	100	3.28	27.17
110	41	2.27	39.62
104	40	2.37	37.94
202	23	1.87	48.71
122	16	1.44	64.53
116	13	1.49	62.21

2 Fabrication and Characterization Methods for Nano- and Microstructures

**"Greatness is achieved, not only by doing great things,
but also, by making the small things we do great."
-S. Tarr**

2.0.1 Fabrication Techniques for $Bi_{1-x}Sb_x$ Nanowires

Nanostructures can be classified by the number of dimensions that are restricted to the nanoscale. Layers with a thickness of a few nanometers being two dimensional (2D), wires with restricted diameters being one dimensional (1D) and particles or nanodots, that are restricted in all three dimensions, being zero dimensional (0D) nanostructures. Nanowires in this realm play an interesting role. They connect two distinct points in space, but are limited in the other two dimensions. This makes them an ideal system to study transport phenomena in small structures, and also allows their application as functional elements in future devices. Furthermore, nanowires can be assembled as 3D structures like nanowire networks, which may then form bulk like samples which exhibit the properties of their small building blocks, while still being easily manageable.

Nowadays there exist a respectable number methods that allow the preparation of nanowires of a wide range of materials, crystalline qualities and nanowire arrangements [37, 38, 39, 40, 41, 42], each having their own benefits and limitations. The literature on antimony, bismuth and the alloy of both describes numerous techniques including:

- Sb and Bi nanowires and nanotubes by hydro- and solvothermal synthesis [43, 44, 45]
- Self assembly of Sb nanowires from Sb nanoparticles [46]
- Sb wire growth on graphite by supplying Sb vapour [47]
- Sb nanowire network growth, by a vapor liquid solid (VLS) process using a Ga ion beam [48]
- Bi microwires by the Taylor process [49]
- Bi nanowires by electron beam writing [50]
- Bi whiskers and nanowires by physical vapour deposition (PVD) [51]
- Bi whiskers and nanowires by a non-catalyzed vapour–solid/vapour–liquid–solid method [52]
- Bi whiskers and nanowires by bulk nucleation and growth out of molten gallium [53]
- Stress induced growth of Bi nanowires in composite thin films of Bi and chrome-nitride [54]
- Nanorods of Bi and Sb by impulse plasma in liquid [55]
- $Bi_{1-x}Sb_x$ nanowires in aqueous solution via a template free electrodeposition route [56]
- $Bi_{1-x}Sb_x$ nanowires by template based approaches [57, 58, 59]

In the template based approach several tens of nanometer wide pores of a template get filled with material. There are a lot of varieties of this approach depending on the template material, filling process used and later application. Commonly employed templates include anodic aluminum oxide (AAO) [60], nanochannel glass, lithographically structured photoresist [61] as well as ion track-etched polymers and

mica [11]. For the filling of the pores physical vapor deposition (PVD) [62], pressure injection [38, 63, 64, 65] or electrodeposition [59, 42, 41, 21] is mostly used.

Compared to the previously mentioned methods, the template approach allows for a higher control of the important parameters of the nanowires. By tailoring the template, the diameter, surface morphology, number and arrangement of nanowires can be defined very well. The filling process can then be used to controle the length, wire composition and crystallinity. Additionally the process is low priced, easily up-scalable and facile to integrate into micro- and nanoscale device structures.

In this work, ion track-etched polymer membranes are used to prepare nanowires, by filling the pores in the template via an electrodeposition process. Figure 2.1 sums up the steps involved for the fabrication of nanowires. At first the templates are fabricated by irradiating polycarbonate foils with swift heavy ions and selectively etching the material that was damaged by the ion beam. Afterward a metal contact is prepared on the sample, which is used as a contact during the electrodeposition process. In the following each of these processes will be explained in more detail, while also giving the experimental details used.

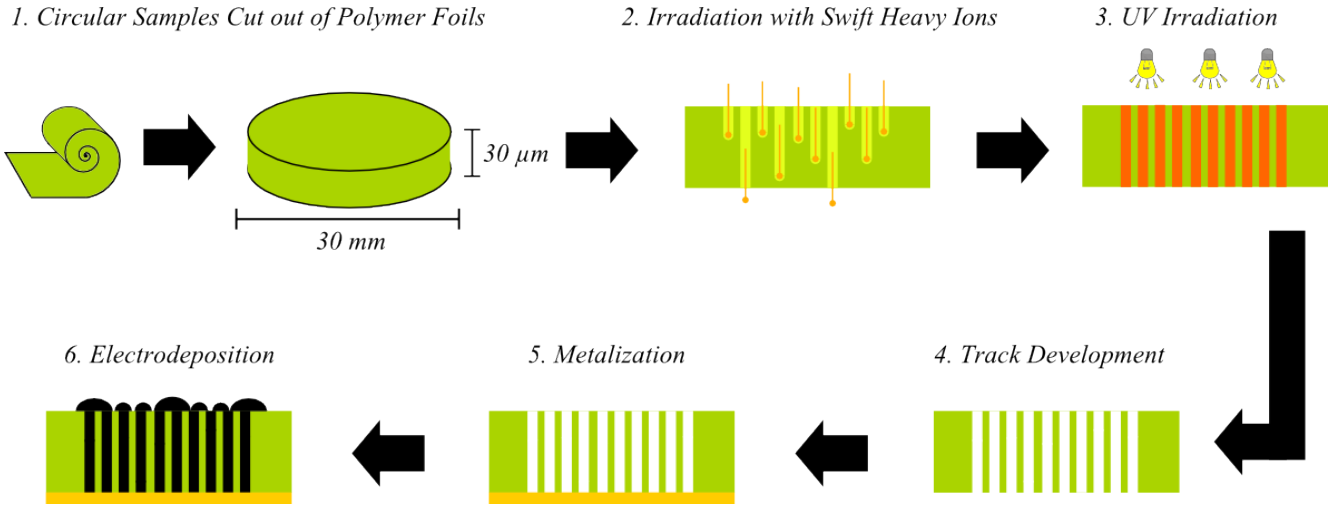

Figure 2.1: Steps followed to fabricate nanowire arrays. First circular disks are punched out of a roll of a commercial polymer such as PC or PET (1) and subsequently irradiated with swift heavy ions (e.g. 2 GeV Au ions) (2) and UV light (3). The damaged ion tracks created in the previous steps are then selectively etched into open pores (4). After an electrical contact has been prepared on one side of the template (5) the pores are filled with material via electrodeposition (6).

2.1 Fabrication of Etched Ion-Track Membranes

2.1.1 Template Materials

The preparation of etched ion-track membranes depends on various parameters before, during and after the irradiation with swift heavy ions [66, 67]. First and foremost a suitable material for the generation of ion tracks needs to be chosen, which in case of this work, was polycarbonate (PC) (Makrofol N from Bayer). Table 2.1 sums up the essential properties of the used material and figure 2.2 shows the repeating chemical unit of polycarbonate. Several aspects speak for the usage of polycarbonate: i) It is easy to generate ion tracks due to the high radiation sensitivity, which goes hand in hand with a high electrical resistivity of the material, which is useful for later processes. ii) It has a homogeneous amorphous structure which

allows the preparation of pores with smooth walls. The development process of the pores can be sensitive to crystalline directions and the use of semi-crystalline polymers can thus lead to rough pore structures due to the different etch rates, as for example seen in polyethylene terephthalate (PET) templates [11]. iii) Templates out of polycarbonate also allow the usage of a broad range of electrolytes, since it is stable in different chemical surroundings ranging from strong acidic to alkaline. iv) Polycarbonate can be easily dissolved in organic solvents like dichloromethane or N;N-dimethylformamide, without damaging the embedded nanowires.

Apart from the requirements for successful ion track generation and electrodeposition, the later application needs to be considered as well. For example in the case of thermoelectric transport measurements on nanowires embedded in a template, it is crucial that the template exhibits a low thermal conductivity additionally to a low electrical conductivity, in order to avoid shortcuts, which would otherwise lead to errors during measurement. Also if one uses nanowires embedded in templates for thermoelectric devices, the efficiency can be greatly decreased by a non suitable template due to parasitic heat loss through the template [68]. Polycarbonate exhibits a low thermal conductivity (∼0.21 W/mK) [69], much lower than AAO (∼1.9 W/mK) [69], which makes it suitable for the measurement of the thermoelectric properties of wires still embedded in the template. Last but not least, polycarbonate also shows good mechanical properties which allows easy sample handling without the danger of damaging the embedded nanowires.

Table 2.1: Selected properties of polycarbonate [70].

Full name	Polycarbonate (PC)
Trade name	Makrofol N (yellow dye)
Fabrication	normal cast film
Company	Bayer
Thickness [μm]	30
κ [W/mK]	∼0.21
Melting temp.[°C]	230
Density [g/cm^3]	1.2
Solvents	Dichloromethane N,N-dimethylformamide
Sum formular	$(C_{16}H_{16}O_3)_n$

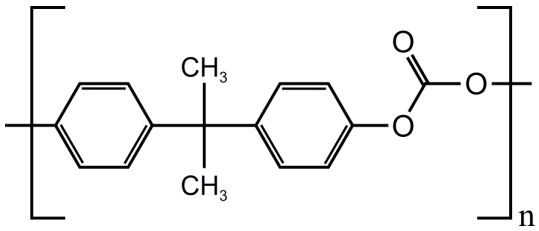

Figure 2.2: Repeating chemical unit of polycarbonate.

2.1.2 Irradiation of Polymers with Swift Heavy Ions

The first step to turn polycarbonate foils into templates is their irradiation with swift heavy ions. Depending on the ion energy, which is usually measured in energy per nucleon [MeV/n], different interactions of ions with matter occur. While at low energy (<∼100 keV/n) elastic collisions dominate and the ions directly displace the atoms in the material, at higher energy ((∼1 MeV/n)) ions interact mainly with the electronic system of the material. Due to these interactions the ions lose energy and slow down until they come to rest. These two regimes are referred to as the nuclear- and electronic stopping regime respectively, as depicted in figure 2.3.

Ion track formation evolves like this [72]: When a swift heavy ion hits a material the ion loses all electrons

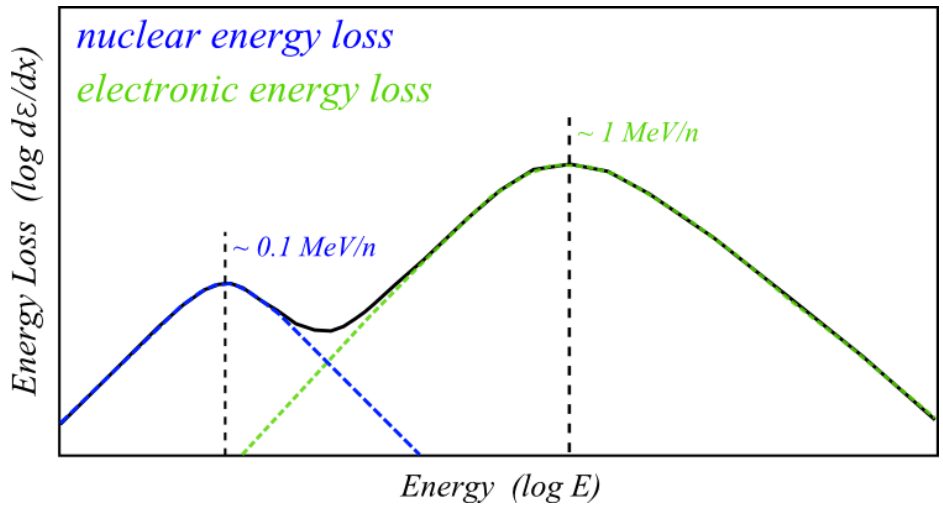

Figure 2.3: Energy loss of projectile ions, while passing through matter, in dependence on their specific energy (energy per nucleon). For "low energy" ions the energy loss is mainly due to nuclear energy loss, while for "high energy" ions the energy loss is mainly due to the interaction of the ions with the electronic system of the target material [71].

whose orbital velocities are smaller than the ion velocity (see Bohrs stripping criterion [73]). These electrons however play no role in the actual track formation process. Due to the high specific energy of the ion (e.g. $\sim$ 11.1 MeV/n for Au used in this work), the interaction with the material is mainly due to electronic stopping. This process either leads to an excitation of the target electrons to higher energy levels or the electrons get ejected from the host atom. The generation of these "hot" electrons happens on a timescale of 10^{-17}-10^{-16} s after the ion impact. If the excited electron relaxes to its initial energy level, the free energy can lead to chain scission or radical production [74]. The ejected electrons, the so-called "delta electrons", form radial cascades that extend outward from the ion path up to several hundred nm, depending on the energy of the initial ion. This can lead to further excitations and ionizations, if the electrons carry enough energy, thereby creating the so called track halo. This process subsides after 10^{-15}-10^{-14} s. The electronic energy loss can be described by the Bethe-Bloch equation 2.1 [75, 76]:

$$\frac{d\epsilon}{dx} = 4\pi \cdot \frac{e^4 \cdot {Z_1}^2 \cdot Z_2 \cdot N}{m_e \cdot v^2} \left[ln\left(\frac{2m_e \cdot c^2 \cdot \beta^2}{I} \right) - \beta^2 - \delta - U \right], \tag{2.1}$$

Z_1: Effective nuclear charge of the projectile ion, Z_2: Nuclear charge of the target atom, e: Elementary electric charge, m_e: Rest mass of the electron, N: Density of target atoms, v: Velocity of the ions, I: Mean ionization energy of the target atom, β: Speed of the ions relatively to the speed of light c, δ: Correction term for the polarization of the target, U: Correction term regarding that electrons from inner shells do not take part at the process.

In order to describe the energy transfer from the electronic system to the lattice system of the material two concurrent models exist, the Coulomb Explosion [77] as well as the Thermal Spike model [78].
The Coulomb Explosion or ion spike model assumes that in the core of the ion path positively charged atomic cores remain. The repelling coulomb forces then lead to bond breaking and the creation of defects like vacancies and interstitials, forming the final ion track.
The thermal spike model on the other hand assumes an energy transfer from the electronic system to the

lattice, thereby generating high temperatures along the ion path which leads to melting of the material. In both cases the processes are quenched after another $\sim 10^{-12}$ s and the disorder is frozen, generating a track, whose core has a diameter of up to ∼10 nm.

The initial ion on the other hand gets slower and slower and captures more and more electrons according to Bohrs stripping criterion. Before the ion reaches its final stopping point nuclear stopping takes over. The ion energy is now distributed in atomic collision cascades in a short distance (∼1 μm). Figure 2.4 shows the energy loss and energy of a gold ion with 11.1 MeV/n, depending on the penetration depth from impact. It is clearly visible that most of the energy is lost due to the electronic stopping. Still after passing the maximum in electronic stopping, also referred to as "'Bragg Peak", the electronic energy loss dominates until only the last few micrometers.

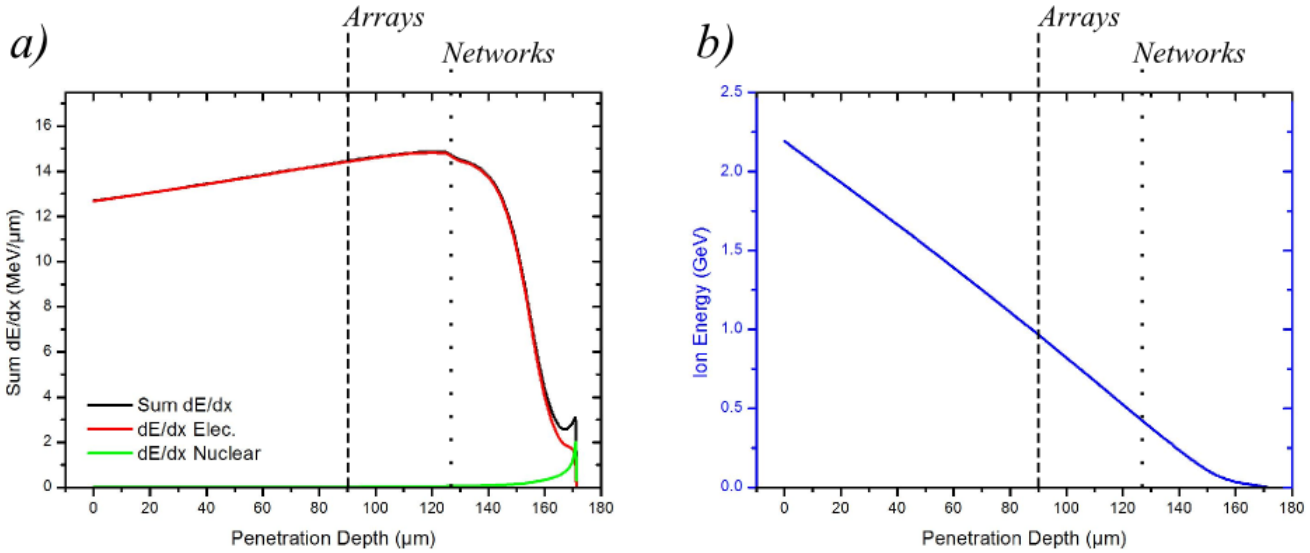

Figure 2.4: a) Energy loss as well as b) ion energy of 11.1 MeV/n Au ions as a function of the penetration length in polycarbonate, calculated using the SRIM 2003 code [79]. The additional lines (at 90 μm and $\sim$ 126 μm) indicate the dE/dx and ion energy after passing a stack of foils for parallel arrays (broken line) and networks (dotted line).

Depending on the material a certain energy loss needs to occur in order to generate an etchable track. Below that level either non continuous tracks are formed or none at all. Polymers have a low radiation hardness which leads to a low threshold for the formation of ion tracks. Knowing the exact energie loss the range of the ions R is given by:

$$R = \int_0^E \left(\frac{d\epsilon}{dx}\right)^{-1} dE. \tag{2.2}$$

Summarizing, in the case of polymers, irradiation with swift heavy ions generates a latent track with a highly disordered core with a diameter of up to ∼10 nm which is surrounded by a circular halo with a diameter of ∼1 μm which was generated by the delta electrons. Due to the energy input of the ion the chemical structure of the material is changed. Mean molecular weights in the track are decreased, small volatile fragments like CO, CO_2 and H_nC_m as well as new molecules and molecules with unsaturated bonds emerged [80], which have an increased tendency to react chemically and are frozen in their metastable states [81].

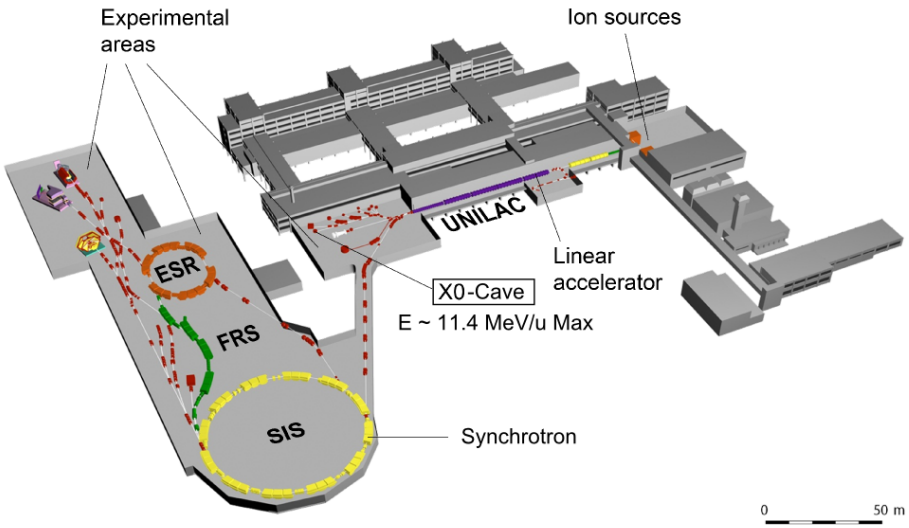

Figure 2.5: Layout of the current GSI heavy-ion accelerator facilities [82].

Experimental

The irradiation of foils was performed a the GSI Helmholtz Centre for Heavy Ion Research in the X0-cave (figure 2.5) using Au or Bi ions, with an energy of ~11.1 MeV/u. The cave is equipped with an automatic sample exchange system, which allows the successive irradiation of samples without breaking the vacuum in the beam line. The samples for irradiation consisted of stacks of three 30 μm thick polycarbonate foils (Makrofol N, Bayer AG), which were punched out of a large polymer roll to generate circular discs with a diameter of 30 mm.

In order to prepare templates with parallel pores the incident beam was kept parallel to the foil normal. In the case of network templates, the foils were irradiated in a sequential process as shown in figure 2.6. Here the incident beam had an angle of 45° towards the foil normal. After an irradiation step the samples were turned by 90° around the foil normal and then irradiated again. This was repeated until the sample was irradiated from four different directions.

Figure 2.4 shows the energy loss as well as the energy of Au ions depending on the penetration depth inside polycarbonate, calculated using the SRIM 2003 code [79]. Starting with an energy of ~2.2 GeV, the ions lose energy with almost constant energy loss during the passage through the material. When they passed through a foil stack for parallel arrays (thickness 90 μm) the ions still have an energy of ~1 GeV when exiting the sample stack. In case of a tilted stack, the ion path is larger (~126 μm) and the ions have an energy of ~0.4 GeV after passing through. In both cases nuclear stopping plays no role and the electronic stopping varies only by 5% within the foils. Therefore the three foils are irradiated under almost the same conditions.

The fluence, number of ions per cm^2 [i/cm^2], during irradiation is monitored and adjusted using a so called "three foil detector" through which the ions have to pass before they pass through the samples. The detector consists of three 1 μm thin Al foils with a high voltage applied between them. When an ion passes through them electrons are ejected from the foils, generating a current which is measured. For calibration of the detector first the flux of the beam is measured using a Faraday cup, by correlating the measured current with the known charge state of the ions. The signal of the three foil detector can then

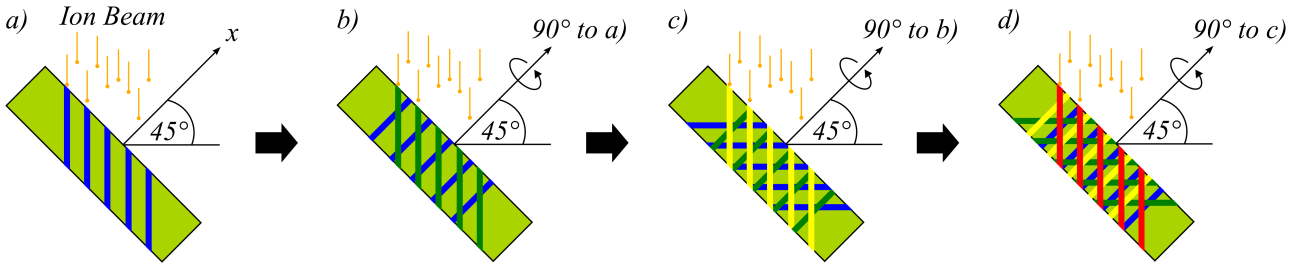

Figure 2.6: Sequential irradiation for the template preparation for nanowire networks. a) The template is tilted by 45° to the incoming ion beam, generating ion tracks (blue). b) The sample is then turned by 90° around the foil normal x, tilted again by 45° to the incoming ion beam, which generates a second set of tracks (green). This is repeated two more times, to generate tilted tracks from additional directions (yellow and red).

be correlated to the current signal from the Faraday cup, allowing an online measurement of the flux. The ions lose their initial charge state and some of their initial energy when passing through the three foil detector, so that the ions generated by the accelerator, having an energy of 11.4 MeV/n, impact the samples with an energy of $\sim$ 11.1 MeV/n. Depending on the exact experiment conditions, errors of up to 30% can be expected for the measurement of the fluence using this method.

The foils for parallel arrays have been irradiated with a fluence of 10^8 i/cm^2. In the case of foils for networks, fluences of $5 \cdot 10^8$ i/cm^2, $1 \cdot 10^9$ i/cm^2 or $2 \cdot 10^9$ i/cm^2 where applied for each of the four directions, leading to total fluences of $4 \times 5 \cdot 10^8$ i/cm^2, $4 \times 1 \cdot 10^9$ i/cm^2 or $4 \times 2 \cdot 10^9$ i/cm^2 for the templates. Due to the angle during irradiation, the track density per cm^2 in networks is lower than the fluence and can be derived by simply multiplying the fluence with the cosine of the irradiation angle. Thus the network templates have total fluences of $1.4 \cdot 10^9$i/cm^2, $2.8 \cdot 10^9$i/cm^2 and $5.7 \cdot 10^9$ i/cm^2, respectively. In this work the different kinds of templates are referred to by the fluence during irradiation and not by their actual pore density. After irradiation the foils are stored for at least half a year in air before usage. Reactions with the surrounding atmosphere, mainly with oxygen, can occur in the tracks in timescales of weeks up to months [83, 66]. This long term process is beneficial for the reproducibility of track etching.

2.1.3 UV Exposure of Irradiated Foils

Shortly before the development of the ion tracks into open pores via wet chemical etching, the irradiated foils are additionally irradiated with UV light (T-30M Vilber Lourmat lamp, 30W, 312 nm) for one hour from each side in order to increase the sensitivity of the ion tracks [66]. As stated above the ion tracks consist of new chemical groups and molecules with unsaturated bonds. These groups absorb UV light better than the pristine polycarbonate, which allows their modification, while leaving the pristine polycarbonate unchanged. Due to the UV light these groups are changed into new compounds possessing a high polarity, also improving the diffusion of the etching solution along the track due to their high affinity to aqueous solutions [80]. Additionally the UV irradiation creates new chain ends and acidic compounds inside the tracks, which are more sensitive to the etching solution [80]. Small angle X-ray scattering experiments confirmed that the pore size distribution (Gaussian distribution) of UV treated foils after the development into pores is indeed smaller and the standard deviation is in the order of 3% [84]. Therefore exposure to UV light prior to the wet chemical etching indeed improves the selectivity of the ion tracks and leads to a more monodispers pore size distribution [85].

2.1.4 Chemical Etching of Ion Tracks

One of the main advantages of ion track-etched polymer templates is the possibility to generate pores of various geometries, e.g. cylindrical pores, conical, bullet-shaped by adjusting the irradiation and etching conditions [86, 81, 11]. In order to generate a pore, the ion track is exposed to an suitable etchant. Figure 2.7 shows the initial stage of the track etching process. In general three etching rates are of interest: V_t describes the fast, highly anisotropic etching rate along the ion track, that is induced by the irradiation damage. V_t can be orders of magnitude higher than the isotropic etching rate V_b of the pristine unirradiated polycarbonate (few nm/min [74]). The geometry of the pores depends on the ratio of the two etching rates (V_b/V_t), the way the etchant is applied (on one side of the template or both), the concentration and composition of the etchant, temperature and etching duration [86]. For the etching procedure used in this thesis, the opening angle of a pore is given by:

$$\sin \alpha = \frac{V_b}{V_t}.$$

In cases where V_t is only slightly higher than V_b, conical pores are generated, while for $V_t \gg V_b$ quasi cylindrical pores can be generated [84].

Using the method of conductometric etching, the track etch rate V_t as well as the radial etch rate of the pores V_r, of single ion-tracks, can be estimated [81]. The etching process depends on the template material (UV stabilizers and plasticizers have a strong influence [67]), the temperature during etching, the concentration of etchant and etch products [81, 67] as well as on the ion fluence (higher fluence leads to smaller etching rates [74]). Due to conductometric etching measurements it is known, that the latent track in polycarbonate consists of different zones [81]. While the track core dissolves fast and depends on the stored energy density along the track [67], the radial etching rate shows a maximum followed by a decrease before it reaches the level of the bulk etching rate V_b at large pore diameters. The decrease in the radial etching rate is attributed to a zone of cross linked polymer in the track halo [87, 88, 89]. In general, due to the many variables influencing the process, the most suitable conditions for a given project need to be found empirically.

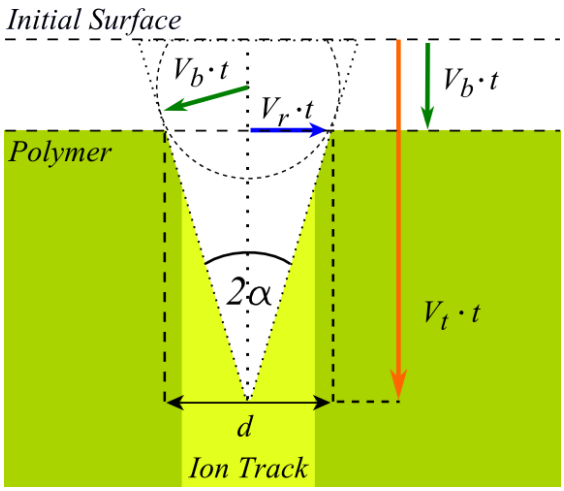

Figure 2.7: Schematic of the initial stage of the development of a pore from one side of the polymer foil. Three etching rates are distinguished: the etching rate along the ion track V_t, the etching rate of the pristine polymer V_b as well as a radial etching rate V_r. The angle α, and thus the shape of the generated pore depends on the ratio of V_b to V_t. For $V_t \gg V_b$ it is possible to achieve quasi cylindrical pores.

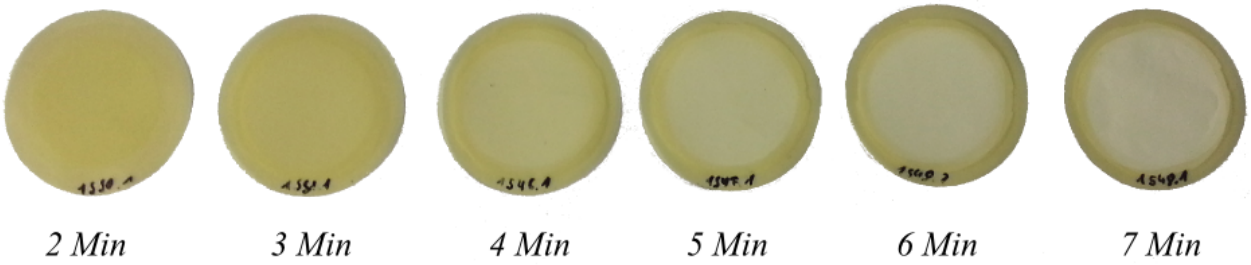

Figure 2.8: Photographs of network templates irradiated with a fluence of 4×10^9 i/cm^2, and etched for times between 2 and 7 minutes. With increasing etching time, the irradiated area of the templates become more whitish.

Experimental

Chemical etching was performed by immersing the irradiated foils in a 6M NaOH solution at 50 °C [80]. The solution was prepared by dissolving sodium hydroxide pellets (Carl Roth, purity ≥ 98%) in DI-water (Millipore Derect-Q5). The solution was heated to 50°C using a water heated thermostat and stirred during the whole process with a magnet stir bar, in order to maintain a constant concentration of the etchant on the template surface and to prevent the buildup of etching products at the liquid-solid interface [67, 81]. Using a customer-made sample holder, three separate foils (one stack) were immersed simultaneously in the etching solution. For the applied etching conditions, the ratio V_t/V_b is in the order of 10^3 [67], allowing the preparation of quasi cylindrical pores. After the etching, the polymer membranes are rinsed several times with DI-water and then stored in DI-water for a day and finaly dried at air. The diameter of the pores increases linearly with the etching time [86]. For the applied etching conditions the radial etching rate is ∼10 nm/min.

There are however limitations for the etching process. For long etching times and/or large fluences, the pores start to overlap severely. In the worst case, this influences the mechanical stability of the templates, making them unusable for further processes. Figure 2.8 shows photographs of network templates, fabricated with different etching times. With increasing etching times the irradiated area turns more whitish. Compared to that, the color of the templates with parallel pores does not change so obviously. Thus the color must be related to the orientation of the channels inside the template. Figure 2.9 shows top views of the pores, using a scanning electron microscope for imaging. In order to avoid charging of the sample a few nm thick gold layer was sputtered on top of the membranes. The pore morphology, as well as their number and size in a given template defines the number of wires, their geometrical sizes as well as the type of their arrangement (parallel or tilted). One should note however, that the template actually only determines the upper limit of these numbers, since also the filling process can influence growth of the material inside the pores, e.g. it has been shown that it is possible to fabricate $Bi_{1-x}Sb_x$ nanowires that have a smaller diameter than the pores of the template [90].

2.1.5 Pore Overlap

To characterize size-dependent properties of nanowire assemblies, the monodispersity of nanowire diameters plays a critical role. As mentioned above, the fabrication parameters of etched ion-track membranes can be tuned to achieve very high monodispersity of the pores.

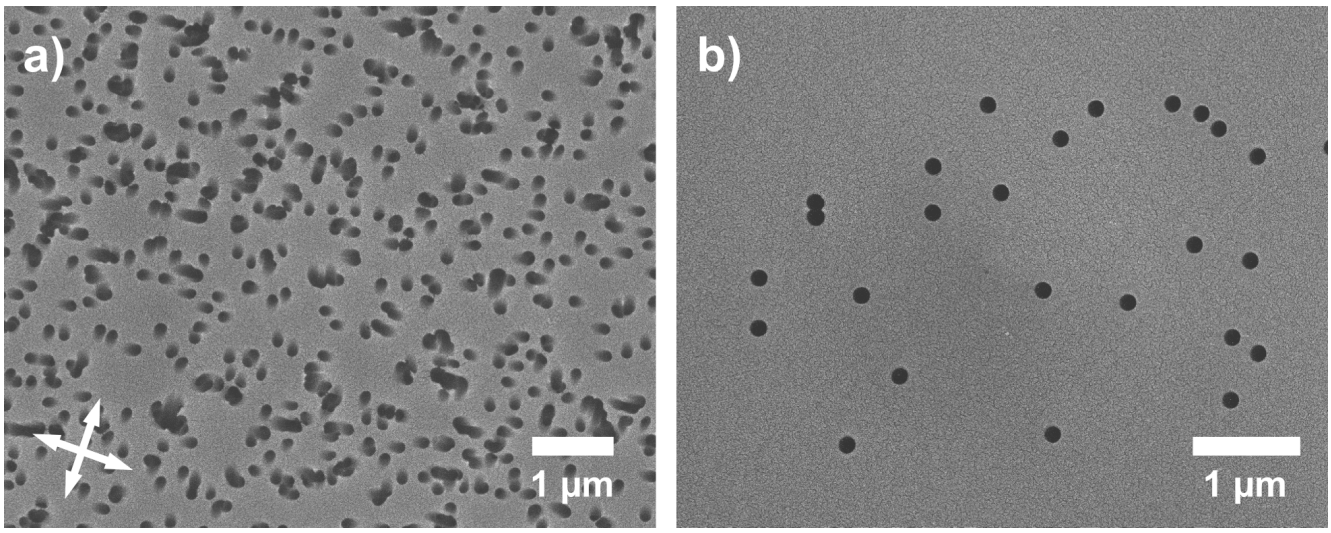

Figure 2.9: SEM images of the top-view of a PC membrane a) with interconnected channels, irradiated with $4 \times 5 \cdot 10^8$ i/cm^2 and etched for 6 minutes (white arrows indicate the 4 directions of irradiation) and b) parallel channels for the preparation of a nanowire array irradiated with 10^8 i/cm^2 and etched for 8 minutes.

Due to the stochastic nature of the spatial distribution of ions during irradiation, the channel diameter should be adjusted such that no pore overlap occurs. In other words, for each given ion fluence, the probability of two or more pores overlapping increases with increasing pore diameter. If pore overlap exists, the nanowires synthesized in the channels would exhibit a broader distribution of diameters, which in turn would cover up possible size effects of the material [68]. Therefore, for the thermoelectrical measurements reported in this thesis, it is important, to prepare the etched ion-track membranes such that the number of overlapping pores is minimum. Below, the number of overlapping parallel pores is calculated as a function of pore diameter and fluence.

In addition, in the particular case of interconnected nanowire networks, the number of intersections of wires from different irradiation directions influences the mechanical rigidity as well as their electrical and thermal transport properties [15]. Therefore, it is important to estimate the number of junctions of a given pore oriented along one direction with pores oriented along the three additional directions in the etched ion-track templates with interconnected nanochannels. In the case of very homogeneous nanowire depositions, as reported in this thesis, this number is equal to the number of junctions of a single nanowire in the given network.

Number of Overlapping Parallel Pores

The probability of a pore to overlap with m other pores can be calculated by equation 2.3 [71]. It should be noted, that this estimate does not take sequential pore chains into account, where e.g. the second pore additionally overlaps with a third one. Table 2.3 and 2.2 show the probability of multipore events for 100 nm and 50 nm diameter pores for the fluences specifically used in this work.

$$w_m = \frac{P^m}{m!} e^{-P} = \frac{(NA_{Overlap})^m}{m!} e^{-NA_{Overlap}}, \qquad (2.3)$$

m: number of pores overlapping ($m = 0$ being a single pore), $P = NA_{Overlap}$: nominal porosity, N: fluence and $A_{Overlap}$: area that needs to be hit by an ion in order to generate an overlapping pore (see figure 2.10). In the case of cylindrical pores with a diameter of d this area is equal to $\pi \cdot d^2$, with d being the pore diameter.

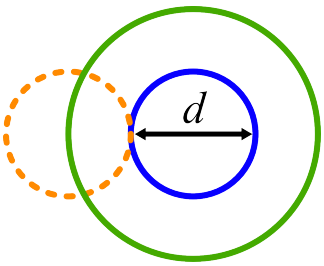

Figure 2.10: Geometrical conditions in order to generate a multipore. In order for a pore (blue) to overlap with another pore (orange), the ion generating the orange pore needs to impact in the green area. The area for overlap is $A_{Overlap}$=$\pi \cdot d^2$, with d being the pore diameter.

Table 2.2: Probability of multipores for 100 nm diameter pores.

Fluence [i/cm^2]	Probability of Singlepores [%]	Probability of Doublepores [%]	Probability of Triplepores [%]	Probability of Quadruplepores [%]
$1 \cdot 10^8$	96.9	3.0	0.1	0.0
$5 \cdot 10^8$	85.5	13.4	1.1	0.1
$1 \cdot 10^9$	73.0	23.0	3.6	0.4
$2 \cdot 10^9$	53.3	33.5	10.5	2.2

Table 2.3: Probability of multipores for 50 nm diameter pores.

Fluence [i/cm^2]	Probability of Singlepores [%]	Probability of Doublepores [%]	Probability of Triplepores [%]	Probability of Quadruplepores [%]
$1 \cdot 10^8$	99.2	0.8	0.0	0.0
$5 \cdot 10^8$	96.2	3.8	0.1	0.0
$1 \cdot 10^9$	92.5	7.3	0.3	0.0
$2 \cdot 10^9$	85.5	13.4	1.1	0.1

Pore Junctions in Network Templates

The etched ion-track templates with interconnected nanochannels employed in this thesis, had been irradiated from four different directions, which are oriented by 90° to one another. Here, the number of junctions of a pore, oriented along a given direction (a), with pores from the additional three directions (b,c,d) (see figure 2.6) is estimated.

Two cases can be distinguished: either a pore along direction (a) overlaps with pores along direction (c), having an angle 180° between them, or the pore overlaps with pores along the (b) and (d) direction, having an angle 90° between them.

Figure 2.11a) and b) display the geometrical arrangements considered in order to calculate the area $A_{Overlap}$, i.e. the area where an ion needs to impact in order to generate a pore junction, when the irradiation is done under 180° to the initial direction (i.e. direction (c)). Due to the tilted irradiation the area of a pore on the template surface (fig. 2.11a) is elliptical instead of circular, with one axis being equal to the diameter d of the pore and the other axis being equal to $= d/cos(\gamma)$, with γ being the irradiation angle. In this case, an ion needs to impact within the green area ($A_{Overlap,180°}$) in order to generate a pore that intersects with the initial pore. The area depends on the pore diameter d, the template thickness D and the irradiation angle γ to the surface normal and is given by:

$$A_{Overlap,180°} = \pi \cdot d \cdot \frac{d}{cos(\gamma)} + 2d \cdot 2Dtan(\gamma). \tag{2.4}$$

Figure 2.11c) shows the geometric arrangement of overlapping pores when the irradiation is done under 90° to the initial direction (i.e. directions c and d). In this case, $A_{Overlap,90°}$ is given by:

$$A_{Overlap,90°} = \pi \cdot \left(d + \frac{d}{cos(\gamma)}\right)^2 + \left(d + \frac{d}{cos(\gamma)}\right) \cdot \sqrt{2(Dtan(\gamma))^2}. \tag{2.5}$$

The total number of junctions of a pore $N_{Junctions}$ is calculated by:

$$N_{Junctions} = f_{corr} \cdot A_{Overlap,180°} + 2f_{corr} \cdot A_{Overlap,90°}, \tag{2.6}$$

with $f_{corr} = f \cdot cos(\gamma)$, being the fluence (ions/area) considering the increase in area caused by the tilt of the sample with respect to the incident ion beam.

Figure 2.12a-c display the number of junctions calculated as a function of pore diameter d, fluence f and irradiation angle γ, respectively. The number of junctions increases linearly with increasing fluence and pore diameter, but non linear with the irradiation angle. For 180° oriented pores, the number of junctions as a function of irradiation angle first increases linearly up to 55° after which a much faster growth is observed. In this case $A_{Overlap}$ increases much faster that the corrected fluence (f_{corr}) decreases. For 90° oriented pores, on the other hand, the number of junctions approaches a maximum at 90°.

Figure 2.12d) shows the number of junctions per pore length as a function of the irradiation angle γ. For irradiation under 180°a maximum is found at 45°. Here, the geometric alignment for irradiation is symmetric to 45° therefore, the maximum fits well with expectations. In case of the irradiation under 90° to the initial direction, a maximum is observed at 60°, afterward the pore length increases faster than the number of hits, due to the fluence getting smaller. Therefore, the maximum number of junctions per pore length, assuming the same irradiation angle for all four directions, is found at an irradiation angle of 52°.

Due to the multipores discussed in the previous section, also the number of junctions in a network is reduced and a precise calculation would need to account for them as well.

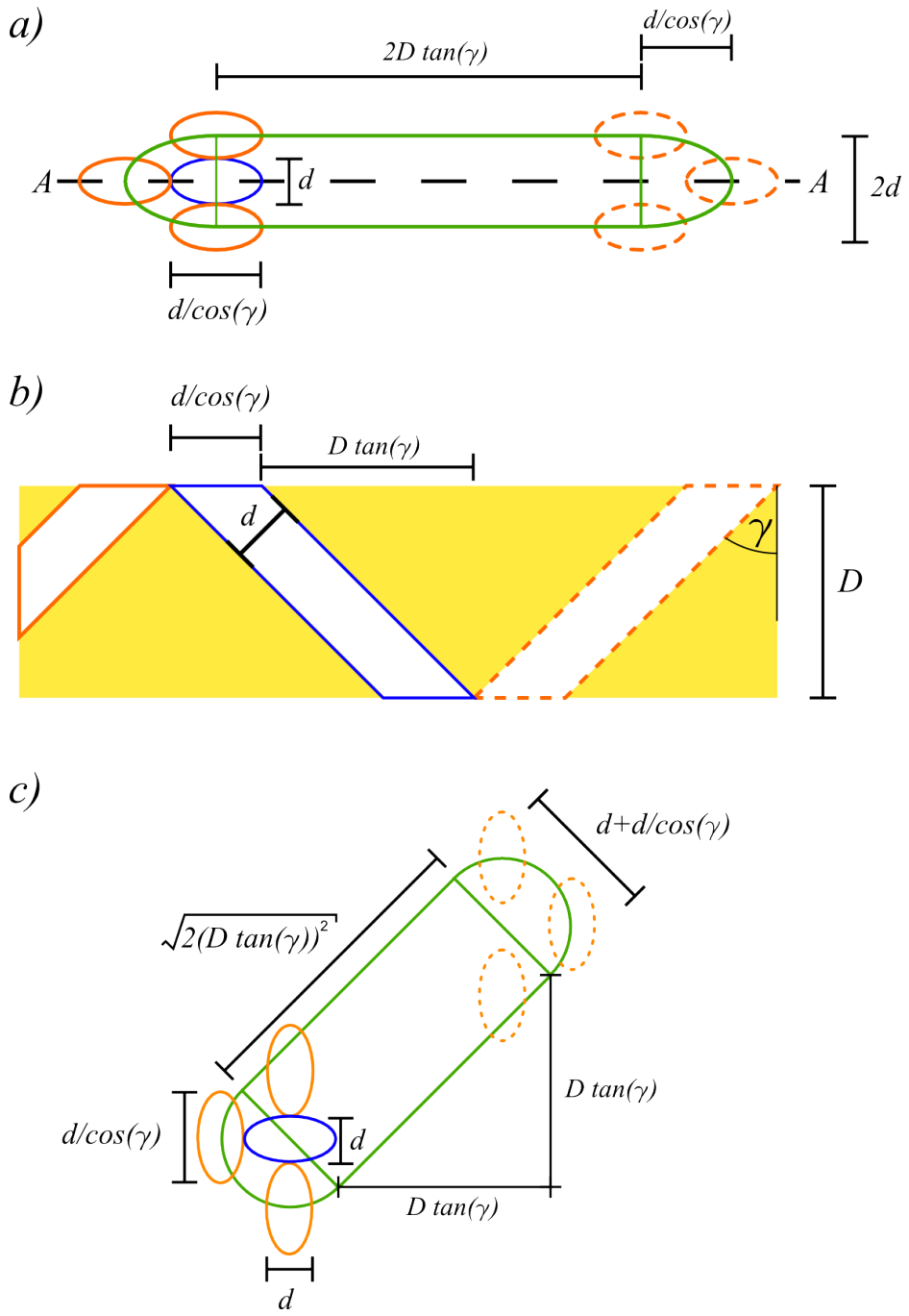

Figure 2.11: Geometric arrangement of overlapping pores a) on the template surface and b) in cross section through the polymer (dashed black line A-A in a), when the irradiation is done under 180° to the initial direction under an angle of γ to the surface normal. c) Geometric arrangement of overlapping pores on the template surface when the irradiation is done under 90° to the initial direction. In order to intersect with an initial pore (blue), with diameter d, an ion needs to impact within the green area, shown in a) and c). The orange pores exemplarily represent the overlapping pores generated after etching, with the solid lined just intersecting at the template surface and the dashed lined just overlapping on the underside of the template, with a thickness D.

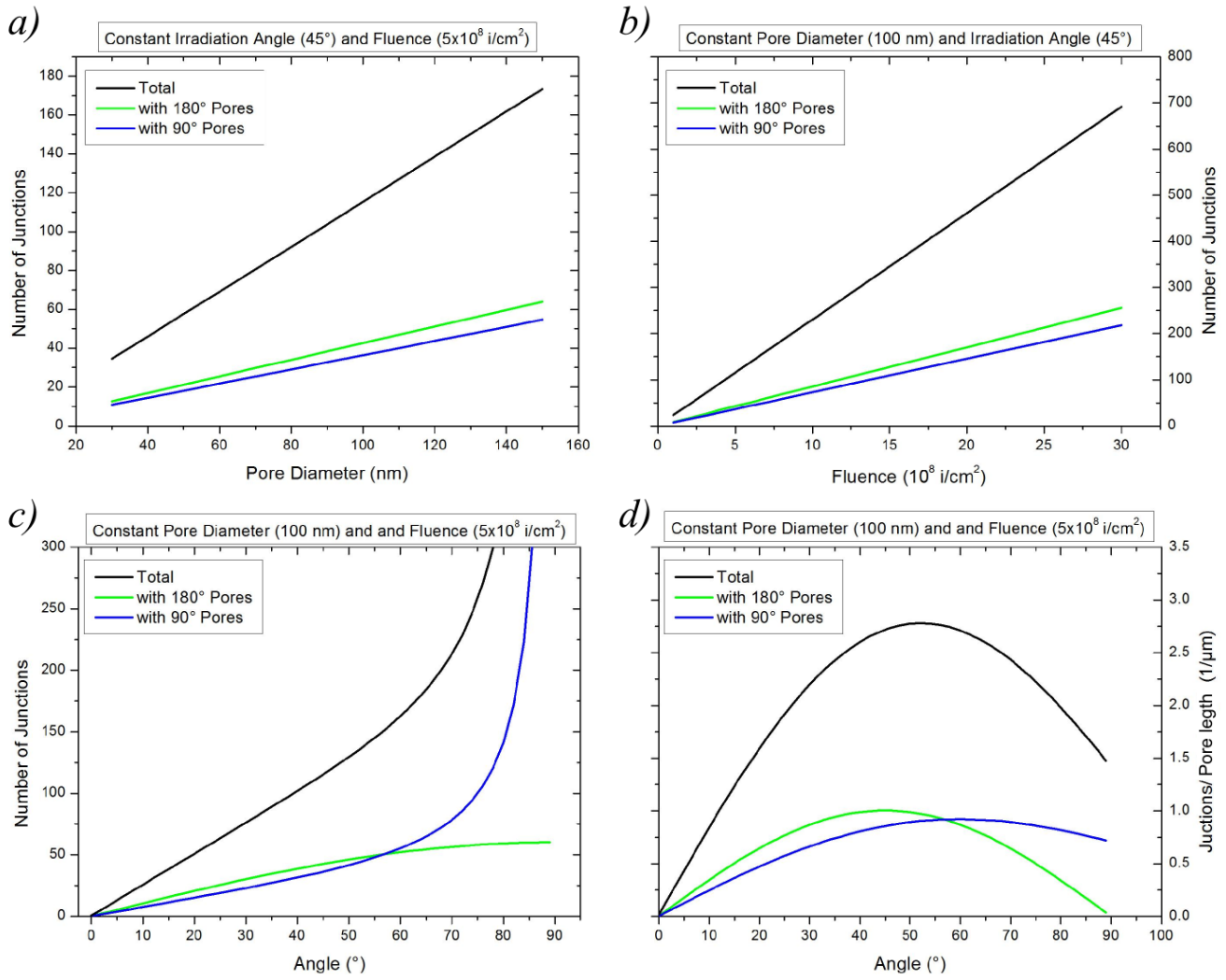

Figure 2.12: Number of pore junctions: a) as a function of pore diameter under constant irradiation angle and fluence, b) as a function of fluence under constant irradiation angle and pore diameter, c) as a function of irradiation angle under constant pore diameter and fluence, d) junctions per pore length as a function of irradiation angle under constant pore diameter and fluence.

2.2 Electrodeposition of Nanowire Assemblies

Nanowires are fabricated by electrodeposition in the pores of the PC templates. The template determines the geometry and arrangement of the wires and the electrodeposition parameters adjust the crystalline structure, composition and morphology of the growing wires. Due to the versatility of the electrolytes that can be used for electrodeposition, nanowires of different materials, ranging from metals to oxides to polymers, can be prepared with controllable morphology, composition and crystallinity [11] using ion track-etched templates. Prior to explaining the experimental details of the growing of nanowire networks and arrays, a short introduction of the most important principals of electrodeposition will be given. The presented topics as well as a more in depth view of the field can be found in textbooks like [91], [92] and [93].

2.2.1 Electrochemical Cells and Electrodeposition

If a metal electrode is immersed in an electrolyte containing its ions, a dynamic equilibrium is established between the oxidation (dissolution) of the metal electrode and the reduction (deposition) of the metal ions in solution. In general, the electrode at which the reduction takes place is referred to as the cathode, or working electrode, while the electrode at which the oxidation occurs is referred to as the anode or counter electrode. The occurring reaction can be described in general as:

$$M^{z+} + z \cdot e^{-} \rightleftharpoons M. \tag{2.7}$$

From left to right the formula describes the reduction of metal ions with a charge of z by using $z \cdot e$ electrons to pure metal. From right to left the formula describes the oxidation of the metal. The electrons for the reaction are either transferred from or to the metal electrode, charging the electrode positive or respectively negative, depending on which reaction is occurring in the system at hand. In this process an electrical double layer, a so called Helmholtz layer, forms between the electrode and the solution, which can simply be described as a capacitor. Under closer inspection, this double layer can be divided in further layers as show in figure 2.13. The inner layer closest to the electrode is called the "Inner Helmholtz Plane" (IHP) and contains solvent molecules or ions that are specifically adsorbed. The so called "Outer Helmholtz Plane" (OHP) is defined by the closest range to which solvated ions can approach the metal electrode. These ions are nonspecifically adsorbed, meaning that they are only attracted due to long-range electrostatic forces.

The potential difference that arises in equilibrium between the metal electrode and the electrolyte, $\phi_M - \phi_S$, can be theoretically described by the Nernst equation 2.8 [92]. It is based on the assumption that at equilibrium the electrochemical potential of the species left and right of the electrode surface are equal.

$$E_{\text{eq}} = \phi_M - \phi_S = E_0 + \frac{RT}{zF} \cdot \ln \frac{a_{M^z}}{a_M}, \tag{2.8}$$

here F denotes the Faraday constant, z is the number of electrons exchanged during the reaction, E_0 is the standard potential, and a_{M^z} and a_M are the activities of the metal ions in solution and the metal ions in the electrode respectively. For pure metals a_M is equal to one. For highly diluted electrolytes the activities

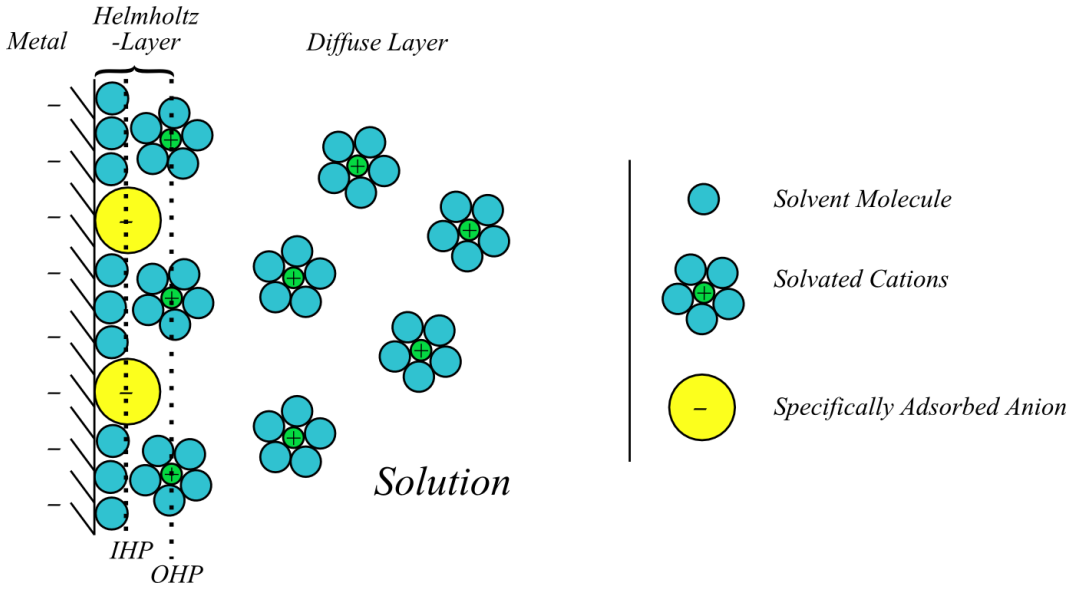

Figure 2.13: Model of the Helmholtz double layer [92].

can be replaced by the respective ion concentrations ($a_{M^z} \rightarrow c_{M^z}$, $a_M \rightarrow c_M$), see equation 2.9, neglecting the ion-ion interaction.

$$E_{\text{eq}} = \phi_M - \phi_S = E_0 + \frac{RT}{zF} \cdot \ln \frac{c_{M^z}}{c_M}, \tag{2.9}$$

However E_{eq} cannot be measured directly, since a second electrode is required, where again a dynamic equilibrium will be established. For this reason it is only possible to measure the relative potential difference between two electrodes, which in open circuit conditions is referred to as the equilibrium cell potentials E_{eq}. In order to compare measured potentials of different systems with one another, a reference electrode has to be introduced into the system, onto which the potential of an electrode is related to. These reference electrodes posses well known potentials, that are established in a fast and reproducible manner. One of them is the standard hydrogen electrode (SHE), whose standard electrode potential is defined as zero at all temperatures. The electrode consists of a platinum electrode that is immersed in an acidic solution and rinsed by pure hydrogen gas. In general all standard electrode potentials are tabulated with respect to the SHE. In practice other reference electrodes are used. Most widely used are saturated calomel electrodes (SCE) and silver chloride electrodes (Ag/AgCl). If not mentioned differently all potentials in this thesis are measured against a saturated calomel electrode (+0.242 V vs. SHE at 25°C [94]).

Electrodeposition

By applying an external voltage E_{ext} between the two electrodes, the system can be pushed out of equilibrium, leading to a response following the principle of Le Châtelier, which can be observed as a current i running through the system. The shift in potential due to E_{ext} is described by the cell overpotential η:

$$\eta = E_{\text{ext}} - E_{\text{eq}} - iR_s, \tag{2.10}$$

where R_s is the resistance of the solution. In case a three electrode setup is used, where a reference electrode is positioned close to the working electrode, the voltage drop iR_s in the solution between the electrodes can be neglected and formula 2.10 can be simplified to:

$$\eta = E_{\text{ext}} - E_{\text{eq}}. \tag{2.11}$$

By definition the cathodic reaction, during which the ions in solution are reduced, takes place if η is smaller than zero and the anodic reaction, at which the oxidation occurs, if η is larger than zero. Note that on the counter electrode an anodic respectively cathodic reaction with the same rate needs to occur. If not, the process will be limited by that reaction. The magnitude of the generated current depends on the rate of the electrode reaction which in turn depends on a multitude of parameters like temperature, electrolyte composition, sample geometry and many more [92]. For a chosen system, after applying a potential, the observed current is depending on the rate of ions being transferred from the bulk electrolyte to the electrode surface (mass transfer), the rate at which electrons are transferred to the ions at the electrode solution interface, the speed of the occurring reaction as well as the rate at which the generated ad-atoms are build into the crystal lattice. Each of these processes can be represented as an additional resistance in the system, leading to an additional potential drop, a so called overpotential. The time needed for each process usually depends on the applied cell overpotential. The slowest of these processes determines the magnitude of the current, being called the rate determining step (RDS).

For large cell overpotentials η, the reaction rate is limited by the mass transfer of ions inside the electrolyte towards the electrode. The mass transfer can in general be carried by diffusion, migration and/or convection. The total flux J_i of a species i, with a charge state of z_i, is then described by the Nernst-Planck-Equation 2.12

$$J_i(x) = J_{i,d}(x) + J_{i,m}(x) + J_{i,c}(x) = -D_i \cdot \nabla c_i - \frac{z_i F}{RT} D_i c_i \nabla \phi + c_i \cdot v(x), \tag{2.12}$$

here $J_{i,d}$ describes the flux due to diffusion, $J_{i,m}$ the flux due to migration and $J_{i,c}$ the flux due to convection. ∇c_i and $\nabla \phi$ are the concentration and potential gradient, respectively and D_i is the diffusion coefficient of species i. If species i is charged, the flux J_i corresponds to a current density j_i:

$$j_i = z_i F J_i \tag{2.13}$$

In case the electrolyte is not stirred and a supporting electrolyte is added to the bath, which generates a high conductivity of the solution, the terms for migration and convection can be neglected. In the case of nanowire growth, electrodeposition occurs at the bottom of the channels, resembling a recessed microdisc electrode array, where each electrode lies at the bottom of a long channel. In such a system the current response in diffusion limitation depends on the geometry (length) of the channel and on the duration of deposition [95]. When a potential is applied at the electrode, the concentration of the active species

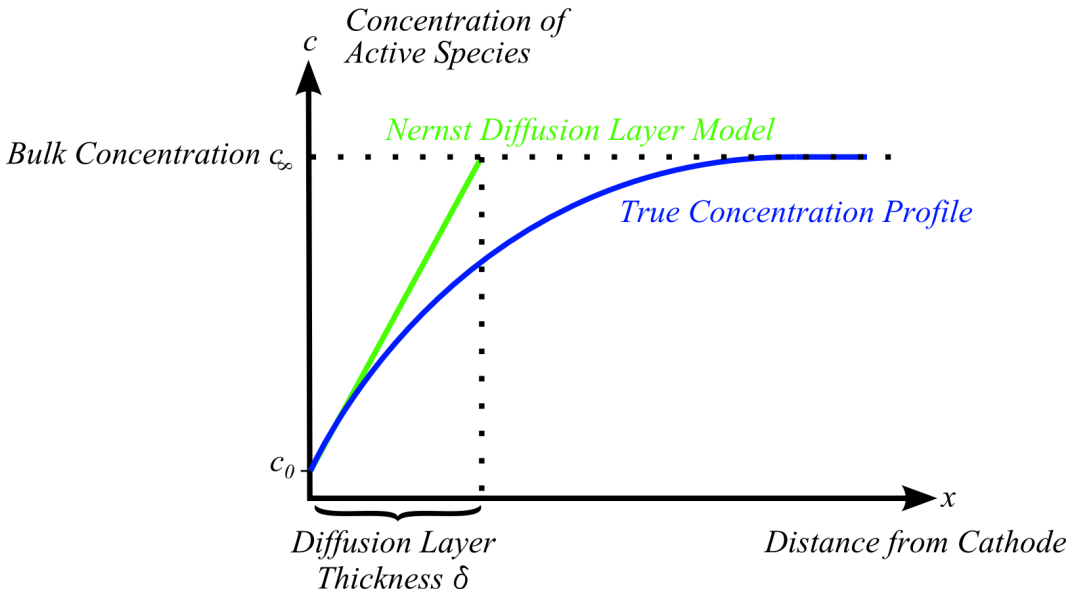

Figure 2.14: Concentration profile of reactant in solution during electrodeposition. The blue curve represents the actual concentration profile, whereas the green curve represents the concentration profile assumed in order to define the Nernst diffusion layer thickness [91].

is quickly depleted to a level given by the Nernst equation 2.8. Due to the slower rate of diffusion, the concentration of ions depletes in a layer close to the electrode, forming a so called diffusion layer. This zone can be approximated by the Nerst diffusion layer model, which describes the diffusion layer as a region with a constant concentration gradient, (figure 2.14). For short deposition times or very long pores (the case when the diffusion zone is limited to the individual pores or if t is small compared to l^2/D, where l is the length of the channel and D is the diffusion coefficient), the current for a single recessed microdisk electrode can be described by the Cottrell equation (2.14) which describes the diffusion for an infinite plane electrode. Here c_∞ is the bulk concentration of the electrolyte, c_0 the concentration of ions at the electrode and $\sqrt{\pi D t}$ is equal to the thickness of the Nernst diffusion layer δ.

$$j = \frac{zFD}{\sqrt{\pi D t}} \cdot (c_\infty - c_0) \tag{2.14}$$

In the case of largest mass transfer ($c_0 = 0$), the limiting current density is given by:

$$j = \frac{zFD}{\sqrt{\pi D t}} \cdot c_\infty \tag{2.15}$$

When the diffusion layer has reached its equilibrium size, and the diffusion zone is still shorter than the pore length, planar diffusion occurs inside the pores, leading to a nearly constant current while the pores get filled with material. For even longer times or respectively when the channel is almost filled up, the thickness of the diffusion layer is greater than the length of the remaining pore. Therefore the diffusion process starts to occur radial to the channel opening and the current behavior is comparable to the sum of all single microdisc electrodes. When the nanowire reaches the poremouth, the growth is not limited to the channels anymore. The material will form so called caps, which lead to an increase in

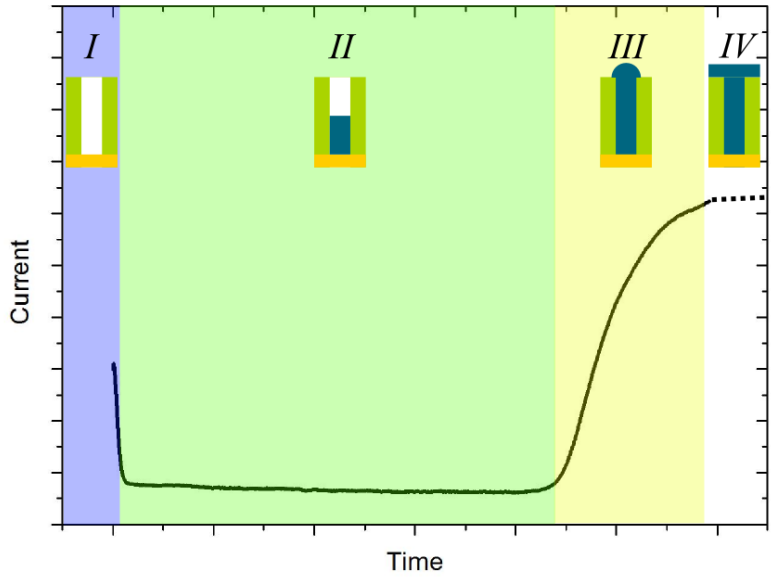

Figure 2.15: Typical current vs. time curve of a potentiostatic deposition process. After an initial drop in current due to the charging of the electric double layer, the current becomes constant while the pores get filled with material. When the growth reaches the top of the pores the process is not geometrically limited anymore and so called caps are formed. If the growth is continued, the material will form a closed layer on the sample surface.

active surface, leading to a strong increase in deposition current. In the final stage, the diffusion zones of the separate microdisks merge, which results in a quasi linear diffusion layer. The current response in this stage resembles that of a macro electrode of the geometrical size of the whole array. Additionally, not related to diffusion, the caps can merge, leading to a thin film on top of the template.

A typical current vs. time curve for potentiostatic electrodeposition inside the pores is depicted in figure 2.15. The high initial current drop is due to the charging of the Helmholtz layer. The charging itself is a non Faradaic process, the charge observed is not transferred through the electrode-electrolyte interface. Bond et al. [96] derived an analytical solution for the diffusion inside a recessed microdisc electrode for stirred and unstirred electrolytes. If no convection occurs their solution approximates the Cottrell equation for short times. But for long times the current density is limited to j_0 given by equation 2.16, where r is the radius of the microdisc (pore) and l the pore length.

$$j_0 = \frac{4zFc_0D}{4l + \pi r} \tag{2.16}$$

This shows that the geometry of the electrodes plays a determinant role on the current density characteristics. Thus to control their geometrical characteristics is important towards gaining a better understanding of the electrochemical deposition process in the channels.

For low cell-overpotentials the reaction rate is limited by the charge transfer through the electric double layer. In these cases the current response can be described by simple rate laws, as shown exemplary with equation 2.17.

$$j = zFJ = zFk(T,\eta)c_{M^z} \tag{2.17}$$

Here c_{M^z} is the concentration of M^z ions and k is a rate constant which depends on the temperature T as well as on the cell overpotential η. The dependency of the current density j on the overpotential can be described by the Butler-Volmer equation (2.18):

$$j = j_a + j_c = j_0 \cdot \left[\exp\left(\frac{\alpha \cdot zF}{RT} \cdot \eta\right) - \exp\left(-\frac{(1-\alpha) \cdot zF}{RT} \cdot \eta\right)\right]. \tag{2.18}$$

The two terms in 2.18 represent the current density of the anodic (j_a) as well as the cathodic reaction (j_c). j_0 is called the exchange current density. It depends on the activation energies as well as on the rate constants of the anodic as well as the cathodic reaction and is thus temperature dependent. α is known as the transfer coefficient, which can adopt values between 0 and 1. If $|\eta|$ is $\gg \frac{RT}{zF}$ the Butler-Volmer equation can be linearly approximated, leading to the so called Tafel equation 2.19.

$$\ln|j| = \ln j_0 - \frac{(\alpha)zF}{RT}|\eta| \tag{2.19}$$

Therefore, if $\ln j$ is displayed as a function of η, a straight line is attained, whose extension to the equilibrium potential E_{eq} intercepts the $\ln j$ axis at $\ln j_0$. The slope can be used to determine α.

2.2.2 Pulse Plating

Pulse plating was developed out of the question how voltage ripples generated by rectifiers influence the properties of electroplated layers. The method was later successfully developed into a key technology for electroplating. In case of pulse plating an alternating potential or current is applied between the electrodes. It has been shown that by carefully adjusting the pulse parameters a precise control of thickness and composition of the deposited layers could be achieved [93, 97, 98, 99, 100]. In contrast to potentiostatic depositions where the reactions at the electrode surface as well as the electrolyte conditions remain essentially unchanged during the process, pulsed potential depositions occur under continuously changing conditions, which allows the preparation of deposits with significantly different properties compared to potentiostatic plating [93]. Pulse waveforms include sinusoidal, saw-tooth, square shaped and many more intricate forms using superimposed pulses. The number of variables however increase, which makes it harder to understand how the waveform influences the process. Therefore usually square or rectangular shaped pulses are employed.

Figure 2.16 shows the variables of an rectangular pulse as well as a current response in case of Sb deposition. The rectangular pulse form is defined by two potentials, V_{on} and V_{off}. In general the potentials may be chosen to allow a bipolar process (cathodic reaction at V_{on}, anodic reaction at V_{off}), or an unipolar process (cathodic reaction at V_{on}, no reaction at V_{off}. Additionally the times t_{on} and t_{off} have to be defined, during which V_{on} and V_{off} are applied respectively. This is done via the duty cycle γ (eq. 2.20) and frequency f (eq. 2.21).

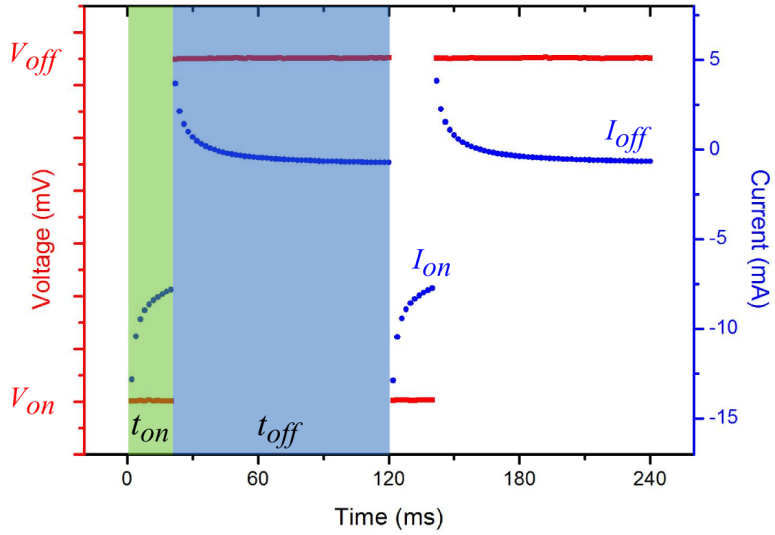

Figure 2.16: Two consecutive voltage pulses (red) as well as the corresponding current response (blue). The voltage is switched to V_{on} for a time t_{on} and afterwards switched to V_{off} for a time t_{off}. The potential for V_{off} is chosen so that the current at the end of V_{off} drops to zero or slightly below.

$$\gamma = \frac{t_{on}}{t_{on} + t_{off}} = t_{on} f \qquad (2.20) \qquad \text{with } f = \frac{1}{t_{on} + t_{off}} \qquad (2.21)$$

t_{on} and t_{off} are limited by the time the electric double layer needs to charge and discharge. The charging and discharging times for typical double layers are in the order of up to 1 ms for charging and up to 7 ms for discharging, depending on the current flow. In theory the charge and discharge times under pulsed potential conditions should be infinitely short since the charging current is proportional to the change in potential dV/dt, which for an ideal potential step is infinite. However, in reality limitations of the instrumentation will result in a charging current transient with a finite magnitude and duration, which cannot be easily calculated as in the case of pulsed current conditions. In case the pulse times are chosen too short, the Faradaic current and thereby the deposition rate will vary with time, making interpretations of the process difficult. Due to the charging of the double layer one therefore might assume that some current is "lost" at the beginning of each pulse. However in an ideal system, the double layer will discharge via the electrolyte during t_{off}, thereby the prior stored charge is used for the reduction of ions during t_{off}. Therefore the current efficiency of the process is not diminished in the ideal case [93]. As mentioned above in pulse plating capacitance effects can influence the final result and need to be take into consideration. Additionally, the process also has effects on the mass transfer, kinetics and electrocrystallization.

Compared to plating under DC conditions where one diffusion layer is formed, in pulse plating two layers can be defined. A layer close to the cathode in which the concentration of species is continuously changing with the frequency of the applied potential and a long range stationary layer. Together these two layers have the same size as the diffusion layer in the DC case as shown in figure 2.17.

During t_{on} ions are reduced and due to the roughness of the surface some areas in the bath may become more depleted of ions than others. During t_{off} however the generated diffusion layer shrinks again, thereby producing a much more homogeneous distribution of ions during the next t_{on} time, leading to a more uniform growth of material. Additionally due to the replenishment of ions and the short time the potential is applied, much higher maximum current densitys can be observed during t_{on} when compared to the expected limiting current density in the case of DC plating. The longer t_{on} the closer the pulse limiting current density j_L is to the limiting current density for DC plating j_G. Depending on the limiting current density different qualities of deposits are achieved. For DC plating powdery deposits are obtained

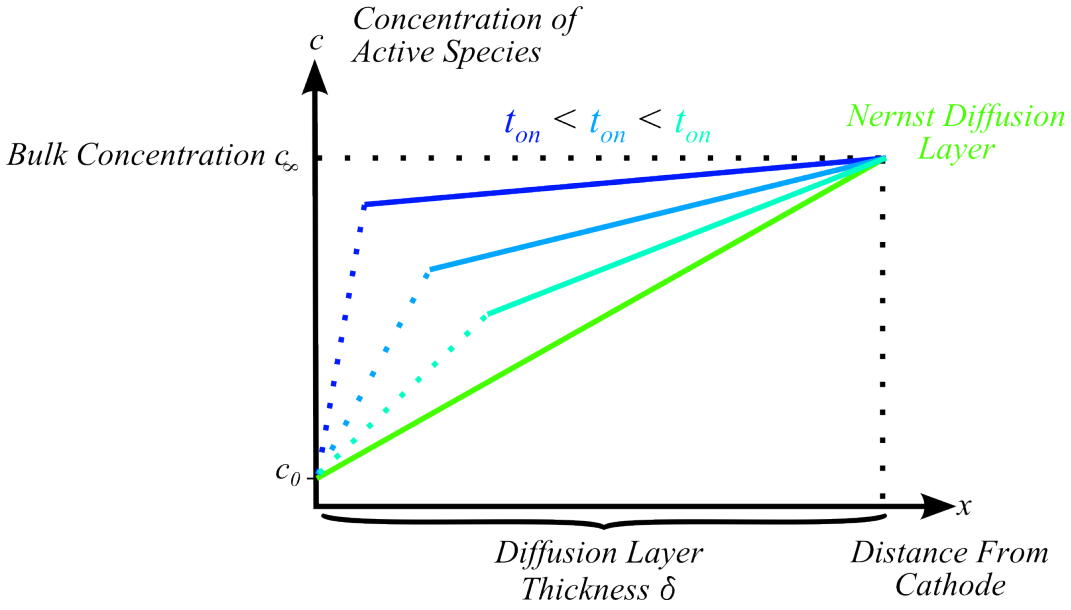

Figure 2.17: The diffusion layer for pulsed deposition can be divided in a stationary (full line) and a dynamic layer (dotted line), where the concentration changes with the applied frequency. The longer the t_{on} time the more the diffusion layer will resemble the Nernst diffusion layer.

when the applied current is close to the limiting current, therefore limiting the used current range to 10-20% of the limiting current in order to achieve dense platings. On the other hand, in the case of pulse plating smooth deposits might even be achieved at the limiting current density, if the generated diffusion layer is small. As a rule of thumb two conditions should be fulfilled to achieve compact non-dendritic deposits, (i) $j_A/j_G < 1$ and (ii) $j_P/j_L < 1$ [101], where j_A is the average current density during a pulse and j_P is the peak current density during a pulse. The applied current or potential also has influence on the crystallization. When an adatom or adion is incorporated into the crystal lattice it can be either used to i) build up an already existing crystal or ii) start the growth of a new one. Case ii) is favored in systems with high adatoms population, low surface diffusion rates and high overpotential. A high current density during the pulse enhances the nucleation rate and enhances the adatom concentration. Thereby pulsed plating can achieve much finer grained deposits compared to DC. During t_{off} re-nucleation due to desorption of impurities can occur. Since the crystal properties influence the physical and mechanical properties of the deposit, one gains a suitable tool to control them.

Faraday Law

In case the average current during pulse plating is equal to the one achieved during DC plating, the same amount of metal can be deposited. Given the total charge Q that flows during the process, the total mass m of the deposited material can be calculated using the Faraday law, equation 2.22.

$$Q = \frac{m \cdot zF}{M} \Leftrightarrow m = \frac{Q \cdot M}{z \cdot F} \tag{2.22}$$

Here z is the valence of the deposited ions, M is the molar mass of the deposited material and F is the Faraday constant. In order to estimate the filling rate of a nanowire network for example, the total charge

Q_{exp}, that flowed during the process is compared to the charge Q_{theo}, that would be required to completely fill the pores of the membrane. The calculations for networks are simplified by assuming that the different pores are not interconnected. Then the total mass m_{total} of all wires in the template is given by equation 2.23, where n is the total number of pores and m_{wire} is the mass of an individual wire. The number of pores n depends on the fluence f, the irradiation angle γ and the surface area A which is exposed to the electrolyte. In case of this work a circular area with radius R is exposed to the electrolyte.

$$m_{\text{total}} = n \cdot m_{\text{wire}} \text{with } n = f_{\text{wires}}(\gamma) \cdot A = f(\gamma) \cdot \pi R^2 \tag{2.23}$$

$m_{\text{wire}}$is given by 2.24, where ρ is the bulk density of the deposited material and V_{wire} the volume of one wire. The volume depends on the radius of a wire r_{wire} and the length of the wire l_{wire}. Since the channels are tilted by an angle of γ referred to the template normal, the length of a wire is calculated by $h \sin\alpha$ where h is the thickness of the template.

$$m_{\text{wire}} = \rho \cdot V_{\text{wire}} = \rho \cdot \pi {r^2}_{\text{wire}} \cdot l_{\text{wire}} = \rho \cdot \pi {r^2}_{\text{wire}} \cdot h \sin\alpha \tag{2.24}$$

Thus the theoretically required charge is calculated by:

$$Q_{\text{theo}} = \frac{m_{\text{total}} \cdot zF}{M} = \frac{n \cdot m_{\text{wire}} \cdot zF}{M} = \frac{f(\gamma) \cdot \pi R^2 \cdot \rho \cdot \pi {r^2}_{\text{wire}} \cdot h \sin\alpha \cdot zF}{M} \tag{2.25}$$

2.2.3 Experimental Details or "How to Cook Nanowires"

The following sections will explain step by step how the nanowire networks and arrays were prepared as well as what equipment was used.

Preparation of Initial Electrical Contacts

Since polycarbonate is an electrical insulator and the electrodeposition is carried out by applying a potential to the sample, a conducting layer is needed on one side of the template, which serves as an electrical contact. This initial layer is prepared by sputtering a thin layer of gold (∼100 - 200 nm) on one side of the template, using an Edwards S150B sputter coater at a chamber pressure of approximately 10^{-1} torr with 1.5 kV and a current of ∼18 mA. The polycarbonate foil has a smooth and a rough side. The rough side has the advantage that the prepared layer can stick more easily to the surface. In some cases however the gold layer was prepared on the smooth side of the template, to achieve an especially flat surface.

In principle the sputtered layer would be enough to allow the electrodeposition of nanowire arrays and nanowire networks. However for pore diameters larger than ∼40 nm the sputtered layer does not close the pores completely [102]. This allows leakage of the electrolyte to the backside of the template obscuring the data gained during the electrodeposition process. Also it has been observed, that in rare cases the

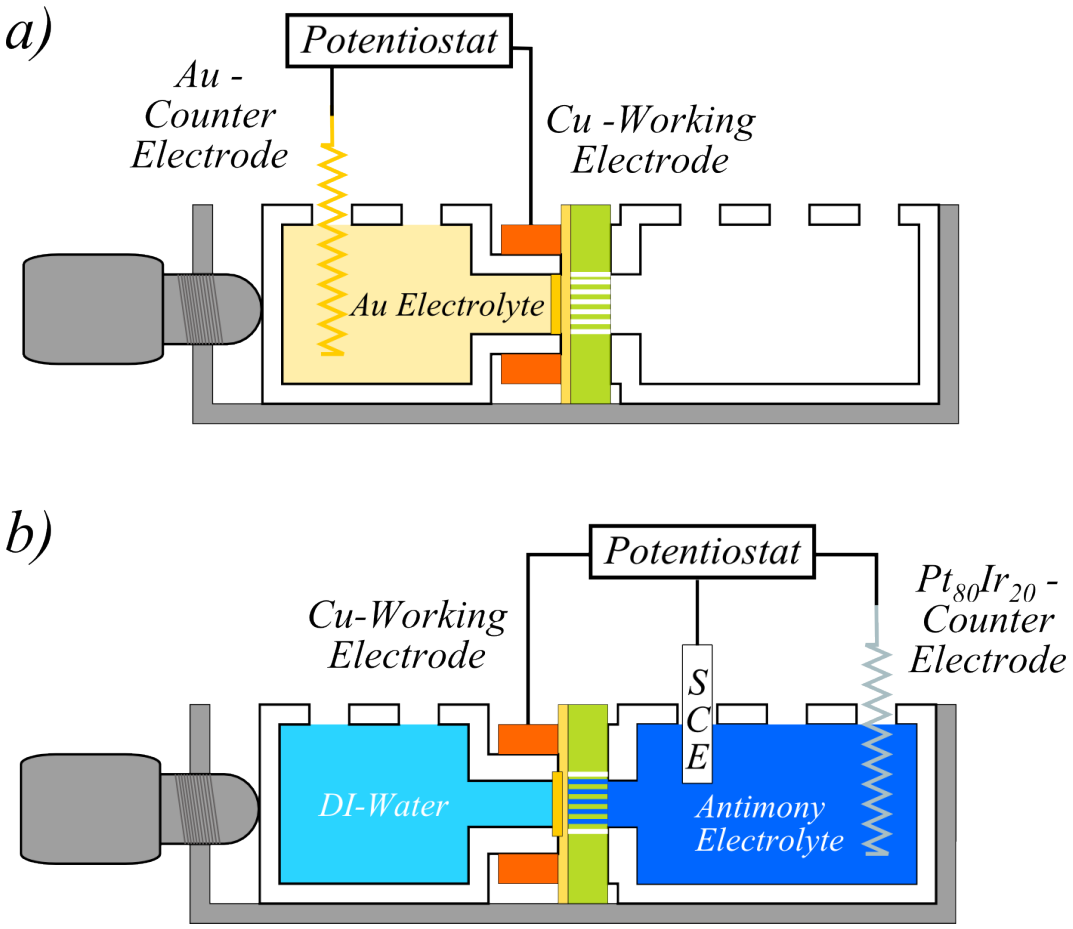

Figure 2.18: a) Electrode setup used for the electrodeposition of gold on top of a sputtered gold layer. The Teflon compartment facing the sputtered layer is filled with Au electrolyte, while the other compartment facing the pores is empty. The potential in this case is applied between a Au-counter electrode and the sputtered Au layer on top off the template. b) Three electrode setup used to fill the pores with material (in this case antimony). The Sb electrolyte is filled into the compartment facing the pores, while the other compartment is filled with DI-water, in order to compensate the pressure of the Sb electrolyte and to keep the temperature on both sides of the template stable. Here the potential is applied between the reinforced Au layer on top off the template and a saturated calomel reference electrode.

grown material can form tubes rather than wires when the backelectrode is not completely closed and the pore diameter is large. In order to close the pores completely and also to achieve an improved mechanical stability of the gold layer after eventual dissolution of the polymer, the sputtered gold layer is reinforced by an electrodeposited gold layer (∼1 μm) using a commercial Au sulfide electrolyte (Gold-SF by Metakem). A schematic of the two electrode setup used is shown in figure 2.18 a. The compartments are made from Teflon and have an opening diameter of $2R = 12$ mm. In this case the sputtered gold layer works as the working electrode and a gold spiral is used as a counter electrode. The cell on the opposite side of the template is left empty.

Depending on the batch of Au electrolyte used, the parameters for deposition had to be adjusted to achieve the same Au layer quality. The chosen potential at room temperature therefore varied between -0.7 V and -1 V, depending on the electrolyte batch. The electrode reaction in the case of the gold deposition reads:

$$Au^+ + e^- \rightleftharpoons Au \tag{2.26}$$

Figure 2.19 a) displays a photo of a PC template with sputtered and galvanically reinforced gold electrode and b) a SEM image taken after the removal of polycarbonate. One can clearly see that the gold layer grows a bit into the template, forming short gold rods with a typical length of a few 100 nm.

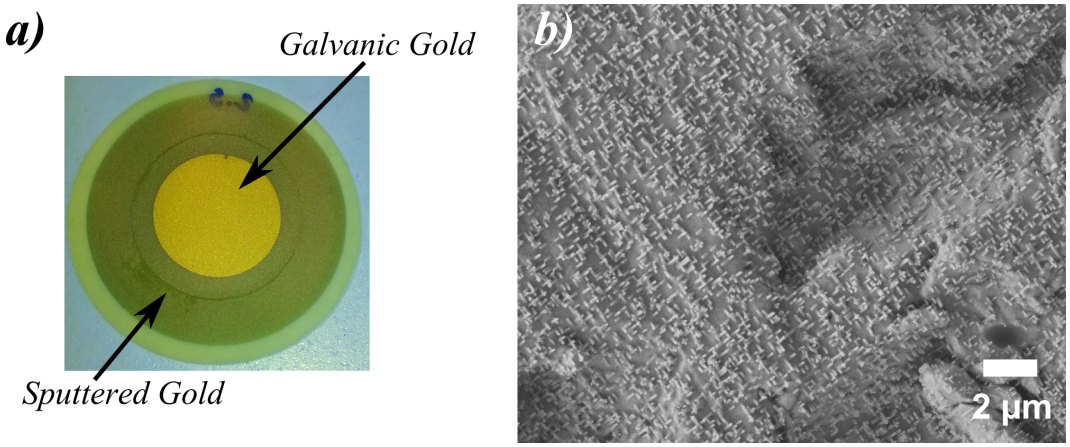

Figure 2.19: a) Photo of a PC template with sputtered and galvanically reinforced gold electrode. The outer area shows the sputtered gold layer, while in the center the galvanic gold layer is visible. b) SEM image of the side of the reinforced backelectrode that is facing the template, after dissolution of polycarbonate. The image is representative for the area where later wire growth would take place. Due to the electrodeposition the gold grows a bit inside the pores, forming short gold rods of a few 100 nm length.

After the gold deposition the template is removed from the setup and dried with nitrogen. When the foil is completely dry it is placed in between two Teflon compartments with an inner diameter of $2R = 8$ mm. Thereby the galvanic gold layer completely closes the sample towards the other compartment and thus prevents the leakage of electrolyte to the other side.

Antimony/Bismuth Electrolytes

The electrolytes used for the electrodeposition of bismuth and antimony were based on aqueous solutions as reported in [103, 58, 59]. For reasons that are still under discussion it was not possible to grow nanowire networks with these electrolytes as previously reported by [104]. Therefore an additional surfactant was introduced into the solution in order to improve the wetting of the electrolyte. The electrolytes consisted of Sb(III)-chloride (Merk, analytical purity) and/or Bi(III)-chloride (Merk, analytical purity) which supplies the active ions for deposition. The compositions where adjusted to always contain 0.1 mol/l as the sum of the two salts. In order to adjust the pH value and the content of chlorides the solution contains 1.95 mol/l HCl (Carl Roth). 0.3 mol/l tartaric acid (Carl Roth, purity 99.5%) was added in order to prevent the oxidation of the metal ions. As a conducting salt 0.2 mol/l NaCl (Carl Roth, analytical purity) was added and finally 1.09 mol/l glycerol (Carl Roth, purity 99.5%), as well as 1 ‰ of Dowfax 2a1 surfactant was added in order to improve the wetting of the electrolytes.

Vereecken et al. investigated the electrolyte without additional surfactant and found that the standard potentials for Sb and Bi lie very close to each other, allowing the codeposition of both materials in order to fabricate alloy nanowires. Figures 8.1 to 8.3 in the supplementary information (chapter 8.2) shows the cyclic voltammograms of the used electrolytes at 40°C, confirming that both materials have similar reduction potentials.

Wetting of Pores with Electrolyte

In order to further improve the penetration of the electrolyte into the pores, the electrolyte was degased at 140 mbar using a KNF Neuberger Vacuumcontroller and ultrasound, before filling it into the Teflon compartment. Then the whole setup was placed inside a vacuum chamber, which subsequently was evacuated to a pressure of 140 mbar and kept there for 45-60 minutes. This way part of the air inside the pores expanded and any bubbles that might have formed during the filling process vanished. Afterwards the second cell compartment was filled with distilled water, in order to compensate the pressure of the electrolyte, as well as to keep the temperature on both sides of the template stable. The setup was then placed on top of a heating stage and heated to 40 °C. After about 30 minutes the temperature of the electrolyte was stable. However, earlier experiments showed, that when the template was left to soak in the electrolyte on the heating stage for longer times, an increase in the deposition current was observed, probably due to a better wetting of the pores [104]. Therefore, network templates were left for 2 hours and array templates for 1 hour on the heating stage, in order to improve the wetting of the pores before the depositions were started. Figure 2.18 b) shows exemplary the setup for the electrodeposition inside the pores. In this case a standard calomel reference electrode (SCE) was introduced in order to better control the applied voltage.

Electrodeposition

In order to fill the pores of the templates with material, a pulsed potential is applied between the working and reference electrode by using a Gamry Reference 600 potentiostat. In opposition to traditional galvano plating, where the process is controlled by applying a current density between the working and counter electrode, a potential is usually applied for electrodeposition in ion track-etched templates. This is done because the exact electrode area is usually not known, and in order to prevent additional reactions, which might occur due to a potential change when the metal ions close to the cathode get depleted. In order to

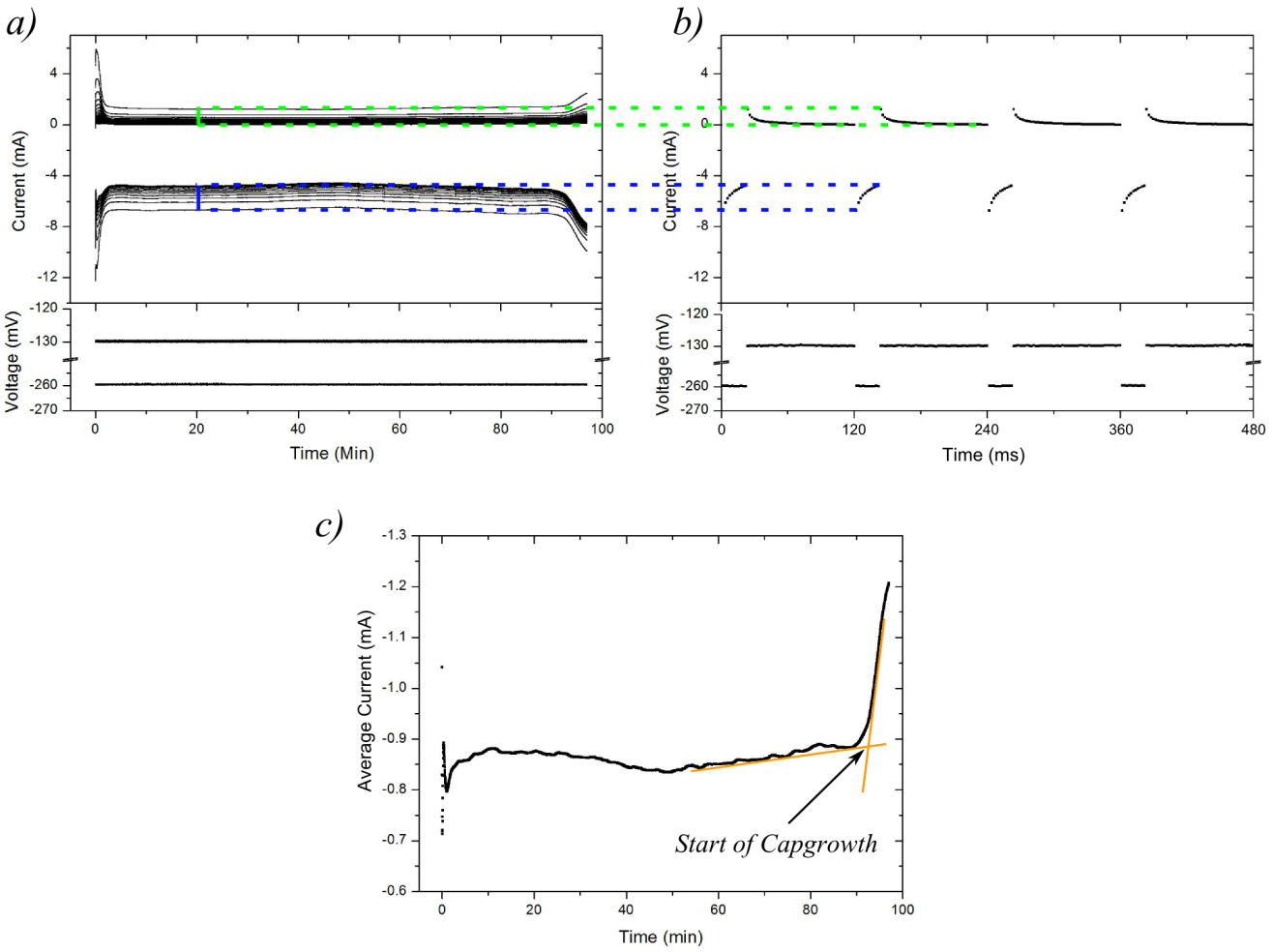

Figure 2.20: a) Acquired current and applied voltage during a Sb deposition in a network template irradiated with $4 \times 1 \cdot 10^9$ ions/cm^2 and pore diameters of $\sim$ 80 nm. Due to the high measurement frequency the individual points during a pulse merge together appearing as coherent lines. b) Voltage pulses as well as corresponding current response after 20 min of deposition. Although cap growth is also visible as a current increase in these plots, it is easier to look at a curve of the average current. c) Dependence of the averaged current of 10 consecutive pulses during the whole process time.

prevent oxidation of the deposited metal, a unipolar pulse profile was chosen. V_{off} was therefore selected so that at the end of the pulse the current would drop to zero or stay slightly below zero, as shown in figure 2.16. V_{on} was selected dependent on the material that should be deposited. For the deposition of Sb a potential of $-260\ mV$ and $-130\ mV$ was chosen for V_{on} and V_{off}, respectively, based on previous experiences [104]. For bismuth and the alloy $Bi_{1-x}Sb_x$ different potentials were tested, as will be shown later. In all cases a duty cycle of $16.6\bar{6}\%$ and a frequency of $8.3\bar{3}$ was chosen. This relates to t_{on} and t_{off} times of 20 ms and 100 ms, respectively [104]. For Sb and Bi, or their alloy deposition, the occurring reaction reads:

$$(1-x)Bi^{3+} + xSb^{3+} + 3e^- \rightleftharpoons Bi_{1-x}Sb_x. \tag{2.27}$$

During the deposition, the applied voltage as well as the current response is monitored. Figure 2.20 a) shows the data acquired during the deposition of a pure antimony nanowire network using a template which was irradiated with $4 \times 1 \cdot 10^9$ ions/cm^2 and etched for 4 minutes. Due to the high measurement frequency of 500 Hz, the individual measuring points, seen in fig. 2.20 b), merge into lines. Negative currents are related to the reduction of ions while positive currents relate to the oxidation of material. During experiments the used software only shows the last 10 minutes of the deposition, which sometimes makes it difficult to distinguish the onset of cap growth, as will be shown in the case of bismuth and $Bi_{1-x}Sb_x$ alloy depositions. In order to better compare different depositions with each other, the current is averaged over ten successive pulses and plotted against the time. For the deposition shown in 2.20 a) this leads to the relation between the current and time shown in figure 2.20 c). Comparing this figure with the current response during a potentiostatic deposition (figure 2.15) bears some resemblances. The current response seen in the first phase however is not related to the charging of the electrical double layer, since this occurs at the beginning of each separate pulse. The initial behavior is more likely due to the establishment of the long range diffusion zone, the initial phases of crystallization on top of the back electrode and eventual special geometric conditions of the starting layer at the bottom of the pores. In the second phase the current shows a more or less stable regime, comparable to the phase of nanowire growth during potentiostatic depositions. As in the potentiostatic case, the pores slowly get filled until the wires reach the template surface. At that stage the current increases due to the formation of caps and the resulting increased active surface area.

Determination of the Charge used for Electrodeposition

In order to get an idea how well the templates are filled, the charge Q_{exp}, that was accumulated during deposition, is compared to the charge Q_{theo} that is theoretically required, see equation 2.25. In order to calculate the charge Q_{exp}, first the time for initial cap growth is determined. For this, two tangents are applied to the average current-time curve, as seen in figure 2.20 c). The intersection point of both lines marks the start of cap growth. Q_{exp} is then the integrated charge from the beginning of the deposition to this point in time.

2.3 Experimental Methods for Sample Characterization

The following sections give a brief introduction to the morphological, structural and chemical characterization methods used in this work and how the samples were prepared for them. For in depth descriptions of the methods the reader is referred to literature [105, 106, 107, 108].

High resolution scanning electron microscopy (HRSEM)

The surface morphology, geometry and composition of the nanowires and nanowire networks was investigated using a Jeol JSM-7401F HRSEM. The method makes use of a finely focused electron beam that is scanned across the sample surface. The signals generated at several points on the sample are then assembled into a complete image. When the electrons hit the material several interactions can occur, as shown in figure 2.21. The signals are not all generated in the same sample volume and the generation depth l_m varies with incident beam energy E_0 and investigated material. As an estimate for the generation depth l_m the Castaings equation can be used [107]:

$$l_m = 0.033 \cdot (E_0^{5/3} - E_C^{5/3}) \frac{A}{\rho Z}, \tag{2.28}$$

with E_C being the characteristic X-ray energy and A, ρ and Z being the atomic mass, density and atomic number of the material, respectively.

Most important for imaging in SEM are the secondary electrons (SE) and back scattered electrons (BSE) that are generated in a depth up to ∼50 nm and ∼200 nm, respectively. As SE electrons are generated closer to the surface they are used to image the surface morphology. The BSE can be used to generate images with mass contrast, as the scattering depends on the atomic number of the material and thus allows to study the elemental distribution. In this work mainly the SE electrons images were obtained to analyze the morphology of the nanowires and networks. For this the microscope was operated at an acceleration voltage of 10 kV and a working distance of 8 mm.

Prior to SEM measurements, the template was removed completely in order to avoid charging effects of the polymer due to the electron beam. This was done by immersing usually a quarter of a sample in dichloromethane (DCM, Merck, for analysis), with the solvent being exchanged at least three times over the course of 2 - 3 days. In case the growth uniformity along the template was studied, only the top layer of polymer was removed by reactive ion etching (RIE). This dry etching process uses a plasma which can contain a variety of etching gases depending on the material that should be etched. The etching process is carried out chemically by the reactive ions generated by the plasma, but material can also be removed by the ions due to sputter effects. In order to remove the polymer an oxygen plasma with 250 W was used. The reaction chamber was kept at a pressure of 60 mTorr with an oxygen flow of 30 sccm. Depending on the time inside the process chamber, more and more polymer is removed. The measured etching rate under the stated process conditions is ∼0.5 μm per minute. In order to avoid charging of the polymer in the SEM, the surface was subsequently coated with a ∼ 8 nm thick layer of Au, using an Edwards Sputter Coater S150B.

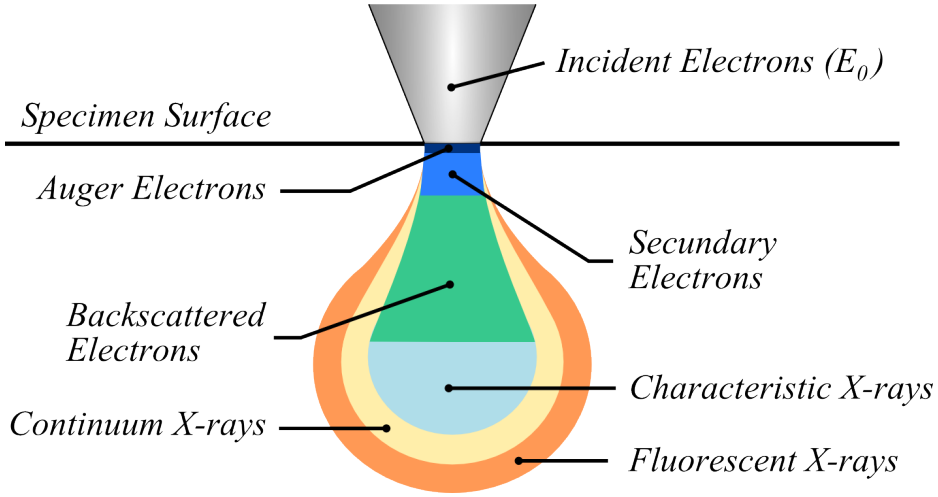

Figure 2.21: Excitation bulb of the incident electron beam with matter [107].

Energy dispersive X-ray spectroscopy (EDX)

As shown in figure 2.21, also X-rays are generated due to the interaction with the electron beam. Among them are characteristic X-rays that are emitted when an electron from an inner shell is expelled by the electron beam and an electron from a higher energy shell retakes its place, emitting the surplus energy as X-rays. These signals can then be used to qualitatively and quantitatively analyze the chemical composition of the sample. Depending on the used beam energy and material, these characteristic X-rays are emitted from a depth of up to ∼350 nm. Comparing the measured intensity of signals from different elements, conclusions can be drawn on the composition of the sample.

The X-ray spectra were measured using an CDU LEAP DETECTOR by EDAX. For quantitative analysis of the EDX spectrum the EDAX Genesis software was employed using the Sb-L (∼3.6 to 4.3 keV) and the Bi-L (∼9.4 to 15.2 keV) lines for quantification. The electron beam for X-ray excitation was operated at an acceleration voltage of 20 kV and a working distance of ∼8 mm.

X-ray Diffraction (XRD)

In order to obtain information about the crystal orientation of a large number of nanowires X-ray diffractograms were recorded at the Technische Universität Darmstadt by Dr. J. Brötz using a Seifert, XRD 3003 PTS-3 with Bragg-Brentano geometry. The method uses a collimated beam of Cu-K_α X-rays to irradiate the sample. Due to the wavelength in the order of the crystal lattice dimension (Cu-$K_{\alpha 1}$ = 0.15405 nm, Cu-$K_{\alpha 2}$ =0.15444 nm [106] the beam is diffracted on the crystal lattice plains. Figure 2.29a) shows the schematic of X-ray diffraction on crystal lattice planes with a plane distance of d_{hkl}. The diffraction angle θ for constructive interference depends on the used radiation wavelength λ and the plane distance d_{hkl}. The relation between the two is given by Braggs law:

$$n\lambda = 2d_{hkl} \cdot sin\theta, \tag{2.29}$$

where n is the diffraction order. Since Sb, Bi and $Bi_{1-x}Sb_x$ belong to the space group R3m additional requirements for constructive interference apply. Due to symmetry rules only reflexes with an hkl that fulfill $-h + k + l = 3n$, with n being a positive integer lead to constructive interference. The plot of the measured intensity in dependence on the scattering angle provides information about crystal phase, crystallographic orientation, lattice parameters of the crystal as well as defects and stresses.

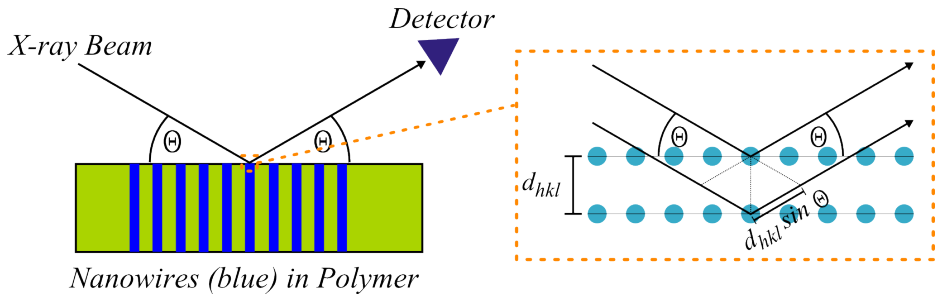

Figure 2.22: Schematic of X-ray diffraction on crystal lattice planes with a plane distance of d_{hkl} [106].

By comparing the peak intensity $I(hkl)$ for different planes with the intensities of a standard powder sample $I_0(hkl)$, it is possible to calculate the texture coefficient (TC). The TC is used to indicate a preferred orientation of the crystallites in the sample and is defined as [109]

$$TC(hkl_j) = n \cdot \frac{I(hkl_j)/I_0(hkl_j)}{\sum_{i=1}^{n} I(hkl_i)/I_0(hkl_i)}, \tag{2.30}$$

with n being the number of reflections that are considered. A texture coefficient larger than unity indicates a preferential orientation of the crystals in the investigated direction of the nanowire. In case the TC is unity for all reflexes, then no preferred orientation is present.

In order to prepare the nanowire samples for the XRD measurement the gold backelectrode was removed by Lugols iodine, if possible without damaging the wires, in order to avoid additional reflexes in the diffraction patterns. Especially in case of the Bi nanowire networks the Au layer could not be dissolved without damaging the sample.

It should be emphasized once again, that that all planes in the diffractograms are indexed using the hexagonal lattice description for Bi and Sb given by the JCPDS file 35-732 and 5-519. In order to remark this, the Miller-Bravais indices $(hkil)$ are used. However, as the index $i = -(h + k)$ and the emphasis on symmetry related planes is not wanted, the index i is replaced by a dot.

Transmission electron microscopy (TEM)

Transmission electron microscopy was done at the Max Planck Institute for Solid State Research in Stuttgart using an Jeol JEM-ARM200F high resolution transmission electron microscope (HRTEM) by Dr. W. Sigle. The TEM makes use of a parallel electron beam that is accelerated by 100 - 500 kV. Due to the high energy of the electrons they can completely pass through a thin material ($\leq$100 nm thickness). Additionally to the signals generated similar to the SEM, the direct transmitted beam, as well as elastically and inelastically scattered electrons can be used for imaging.

For TEM imaging, usually either the primary beam (bright field, BF) or the elastically scattered electrons (dark field, DF), that passed through the sample, are used. Contrast in BF images can be generated by differences of the thickness or density of the sample as well as defects and strain fields. DF images can be used to image parts of the sample with a similar crystal structure.

Due to the high energy of the electrons, they posses a short wavelength which allows them to be diffracted on the crystal lattice plains of the sample. This way so called selected area electron diffraction patterns (SAED) can be obtained by adjusting the magnetic lense system in the TEM. The SAED patterns include information on the crystal orientation of the single wires.

In order to prepare the wires for TEM measurements the polycarbonate matrix was completely dissolved using dichloromethane (DCM). This was done by immersing a quarter of the sample in dichloromethane (DCM, Merck, for analysis). The wires were subsequently detached from the backelectrode by exposing the sample immersed in DCM to ultrasound (Elma, TranssonicT460/H). Afterward, the solution containing the nanowires was centrifuged three times at 4000 rpm for 45 min using a Heraeus Biofuge primo R Centrifuge. In between the centrifugation steps 2/3 of the DCM were replaced with fresh solution and the

solution mixed in order to disperse the wires in the solution. The method for cleaning was developed by L. Burr for gold nanowires and the exact procedure can be found in [110]. Afterward, the solution was drop cast on Cu TEM grids (Plano GmbH) and dried in air.

TEM bright field images as well as high resolution TEM images were subsequently taken operating the microscope at an acceleration voltage of 200 kV.

3 Fabrication and Characterization of $Bi_{1-x}Sb_x$ Nanowire Assemblies

"**An expert is a person who has made all the mistakes that can be made in a very narrow field.**"
-Niels Bohr

The following sections present the experimental results obtained on the electrodeposition of pure antimony, pure bismuth and $Bi_{1-x}Sb_x$ alloy nanowire assemblies. The results are separated by material, showing the data acquired during electrodeposition as well as the morphological and structural features of the prepared nanowire arrays and -networks, using high resolution scanning electron microscopy (HRSEM), energy dispersive x-ray spectroscopy (EDX), x-ray diffraction (XRD) and high resolution transmission electron microscopy (HRTEM). Parts of these results, concerning the Sb nanowire networks, have already been published in [111].

As already mentioned in section 2.2.3, when showing the measured current vs. time diagrams of a complete deposition process, multiple lines appear due to the high measurement frequency (500 Hz), as the individual measurement points during a pulse merge together. Negative currents are related to the reduction of ions while positive currents relate to the oxidation processes. In order to better compare different depositions with each other, the average current is used, which is given by the average current in ten successive pulses.

3.1 Antimony Nanowire Arrays

As discussed in chapter 2.2.3, the nanowire arrays are prepared by electrodepositing material in etched ion track membranes. The process during deposition is monitored by current vs. time curves. Previously optimum conditions were found for potentiostatic [58] and pulsed potential depositions [59] of Sb nanowires in parallel channels. Applying the same conditions for the growth of nanowire networks resulted in depositions with varying results, ranging from no deposition to growth of material in limited areas of the membrane. Complete nanowire networks could however be fabricated when the deposition temperature was increased to 40°C [104]. Later experiments again resulted in no deposition of material, most likely due to a bad wetting of the interconnected channels in polycarbonate with electrolyte. Thus, the electrolyte was modified by adding a surfactant (DOWFAX 2a1) to improve the wetting. Since the composition of the electrolyte is known to affect the crystallinity of the deposited material, the influence of the surfactant on the growth was studied by preparing nanowire arrays using electrolytes with and without surfactant.

All electrochemical depositions of Sb presented here, unless mentioned otherwise, have been carried out under pulsed deposition at an on/off-potential of -260 mV/-130 mV vs. SCE, using on/off-times of 20 ms/100 ms. Deposition with surfactant were performed at 40°C, while depositions without were performed at room temperature. Figure 3.1 shows the current vs. time curve for an Sb deposition at 40°C in a network template having ~80 nm diameter large pores that was irradiated with $4 \times 5 \cdot 10^8$ i/cm^2. It also stands representative for the general behavior during Sb depositions, be it parallel arrays or networks of nanowires. As previously explained in chapter 2.2.2, the first minutes of the depositions usually show a complex behavior of the current. Growth begins on the gold substrate and the long range diffusion layer is established. As the pores get filled up, the current response in each pulse becomes similar, since the

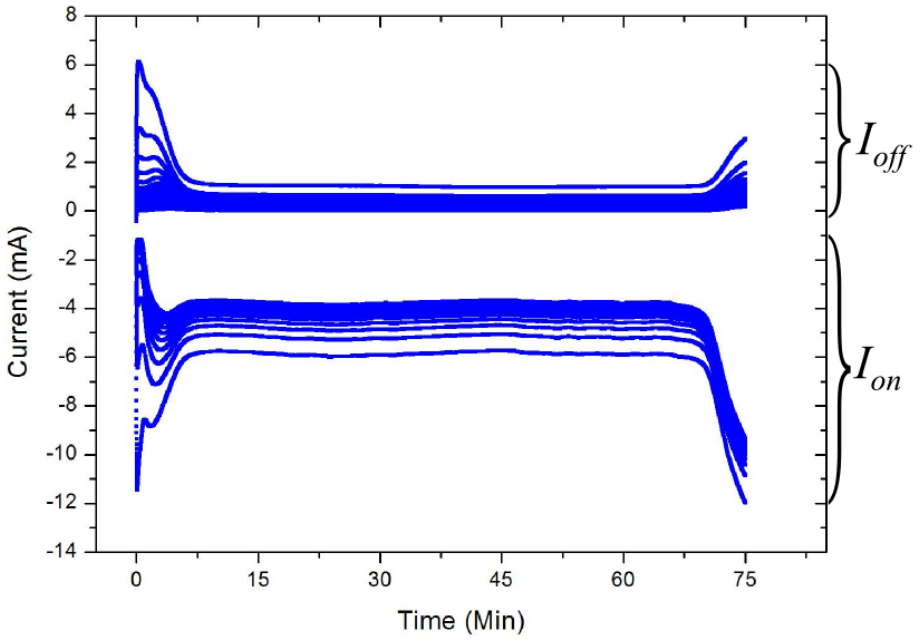

Figure 3.1: Current vs. time behavior for a Sb deposition in a template (fluence $4 \times 5 \cdot 10^8$ i/cm^2, pore diameter ~80 nm), using an on/off-potential of -260 mV/-130 mV vs. SCE with on/off-times of 20 ms/100 ms, at 40°C.

active area for deposition stays constant. At the end of the deposition the anodic- and cathodic-current increase. This happens because caps form on the surface as the growth is no longer limited by the pores, which significantly increase the active area for deposition. The preparation of Sb nanowire arrays was already previously researched in the materials research group at GSI by S. Müller [58] and M. Cassinelli [59] and the main focus of this work is on the preparation of nanowire networks.

3.1.1 Influence of Surfactant on Growth

For the electrodeposition of nanowire networks it was necessary to add a surfactant (Dowfax 2a1) to the electrolyte in order to achieve growth inside the templates. Therefore, to study how the surfactant influences the nanowire growth, templates with parallel channels were used. All the templates used for the study were irradiated with 10^8 i/cm^2. Since also the pore diameter can influence the growth, series of templates were etched, to generate membranes with channel diameters ranging between ~30 nm to 160 nm. In the following the improved deposition conditions for Sb (surfactant, 40°C), will be compared with the initial conditions (no surfactant, room temperature) [58, 59].

Figure 3.3a) shows representative average current - time curves recorded during the electrodeposition of Sb at room temperature, using an electrolyte without surfactant, as used in [58, 59]. Figure 3.3b) shows the corresponding average current - time curves recorded during an electrodeposition of Sb at 40°C using an electrolyte with a 1 ‰ surfactant. The depositions without surfactant in general seem to finish faster than the depositions with surfactant. This is even more surprising considering that the depositions with surfactant were done at 40°C, which should increase diffusion processes. Therefore it seems that the surfactant in fact decreases the reaction rate, leading to slower growth.

Figure 3.2c) shows the deposited charge till cap growth of all Sb array depositions in this work. The dashed

green line represent the calculated charge that is required for 100% filling of the pores. The blue lines represent the calculated maximum and minimum required charge to fill 100% of the pores, considering an error of 30% for the pore density and an error of 10% for the etching rate. The calculated charges were determined by using the Faraday law (eq. 2.2.2). The deposited charge till cap growth scatters strongly for the depositions with and without surfactant, so that no systematic increase of the charge with pore diameter can be observed. It should be noted that the used templates were not all irradiated and/or etched at the same date, so that variations in the preparation process may be the cause for the large scattering of values. At this point there seems to be no obvious difference between the filling of the templates in the cases with and without surfactant. By bare eye, both processes seem to homogeneous fill the pores all over the active template area. Therefore both procedures seem to work equally well, although the depositions without surfactant are faster.

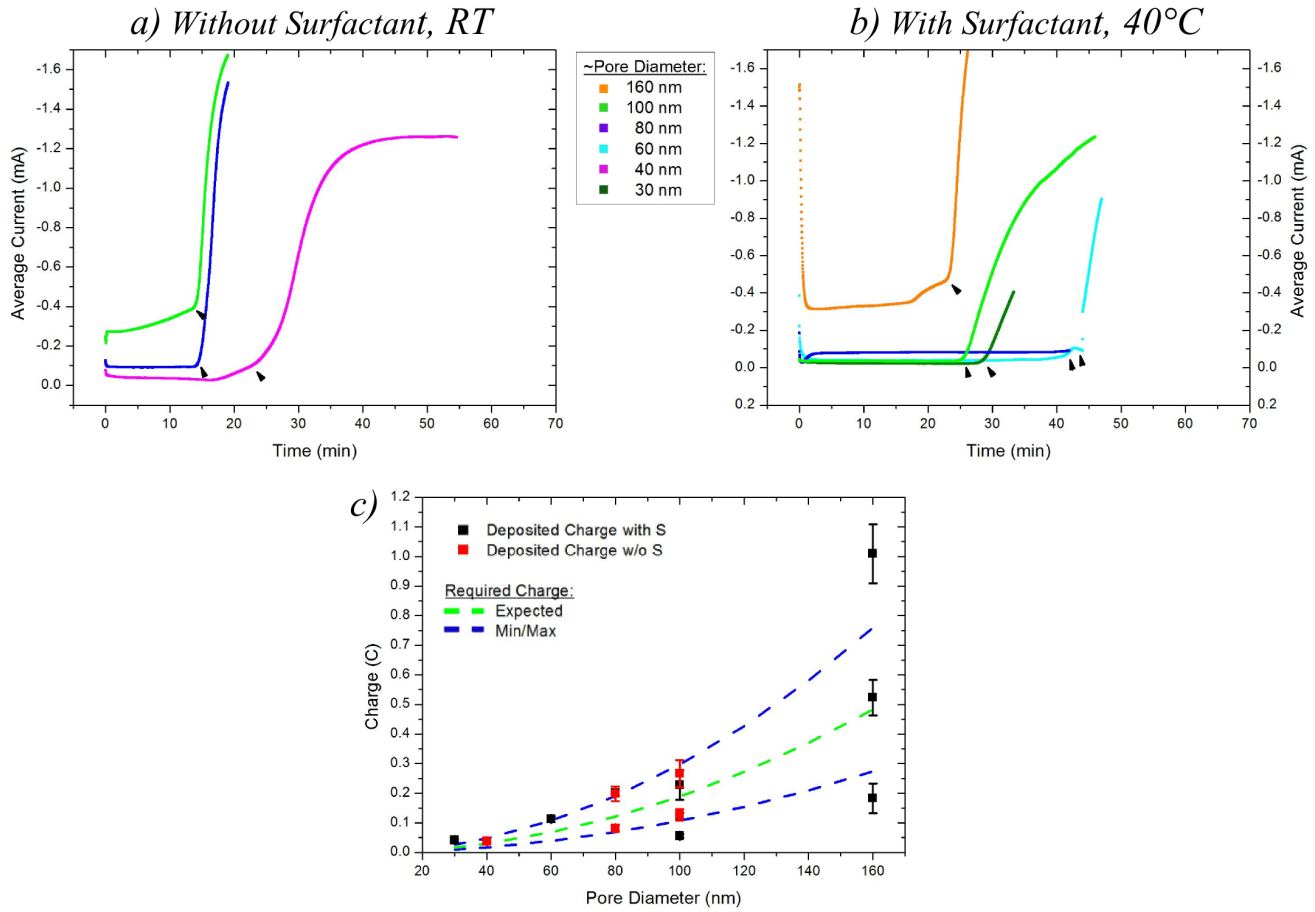

Figure 3.2: Representative average current vs. time curves for Sb nanowire array depositions at an on/off-potential of -260 mV/-130 mV vs. SCE, using on/off-times of 20 ms/100 ms, a) without surfactant at room temperature and b) with surfactant at 40°C. The used templates were irradiated with 10^8 i/cm^2 and had pore diameters ranging from ∼ 30 to 160 nm. The black arrows indicate the onset of cap growth. c) Deposited charge till the onset of cap growth, for Sb array depositions with and without surfactant. The dashed green line represents the calculated charge that is needed to fill 100% of the pores. The blue lines represent the calculated maximum and minimum required charge to fill 100% of the pores, considering an error of 30% for the pore density and an error of 10% for the etching rate. The calculated charges were determined by using the Faraday law (eq. 2.2.2).

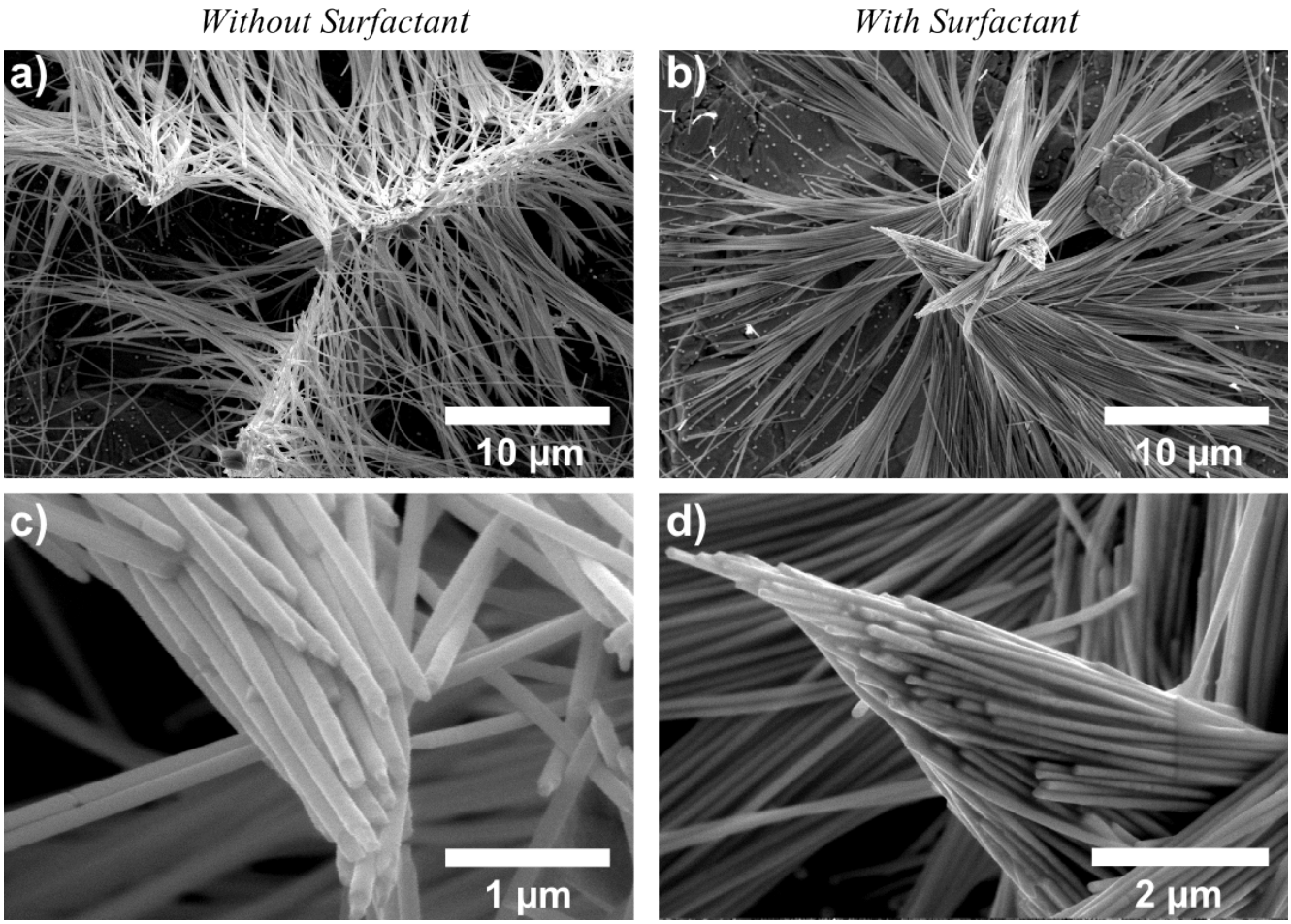

Figure 3.3: SEM images of Sb wires (diameter ∼100 nm) prepared without (a,c) and with surfactant (b,d).

Figure 3.3 shows SEM images of Sb nanowires with a diameter of ∼100 nm prepared without (a, c) and with (b, d) surfactant. The wires start to bend without the support of the polymer membrane due to their high aspect ratio. In some cases this leads to a breaking of the wire from the backelectrode. If a wire breaks, it usually seems to happen at, or close to the interface to the backelectrode. Shorter wire parts may however have been removed during the sample preparation, so that only the long wires remained. The wires prepared with and without surfactant exhibit a smooth surface and a homogeneous wire diameter along the length of the wires. The studies conducted showed no influence of the surfactant on the nanowire diameter, even if the amount of surfactant in the electrolyte was doubled.

Transmission electron microscopy (TEM) measurements on 40 nm diameter Sb nanowires were performed in a JEM-ARM200F HRTEM. A selection of representative pictures and selected area electron diffraction (SAED) patterns are shown in figure 3.4. The images confirm that wires prepared with and without surfactant both show a smooth surface.

Surprisingly all observed wires were covered by a thin layer of carbon (5 - 10 nm thickness). Probably, the layer is formed from polycarbonate rests that had not been dissolved completely, even though the wires had been cleaned several times. The observed crystal structure of Sb nanowires prepared with and without surfactant is quite similar. The images of the wires show contrast lines attributed to bending effects. HRTEM images revealed no grain boundaries along these imaged sections. For all 5 wires investigated, single-crystalline sections of several μm length were observed. In one case of wires prepared without

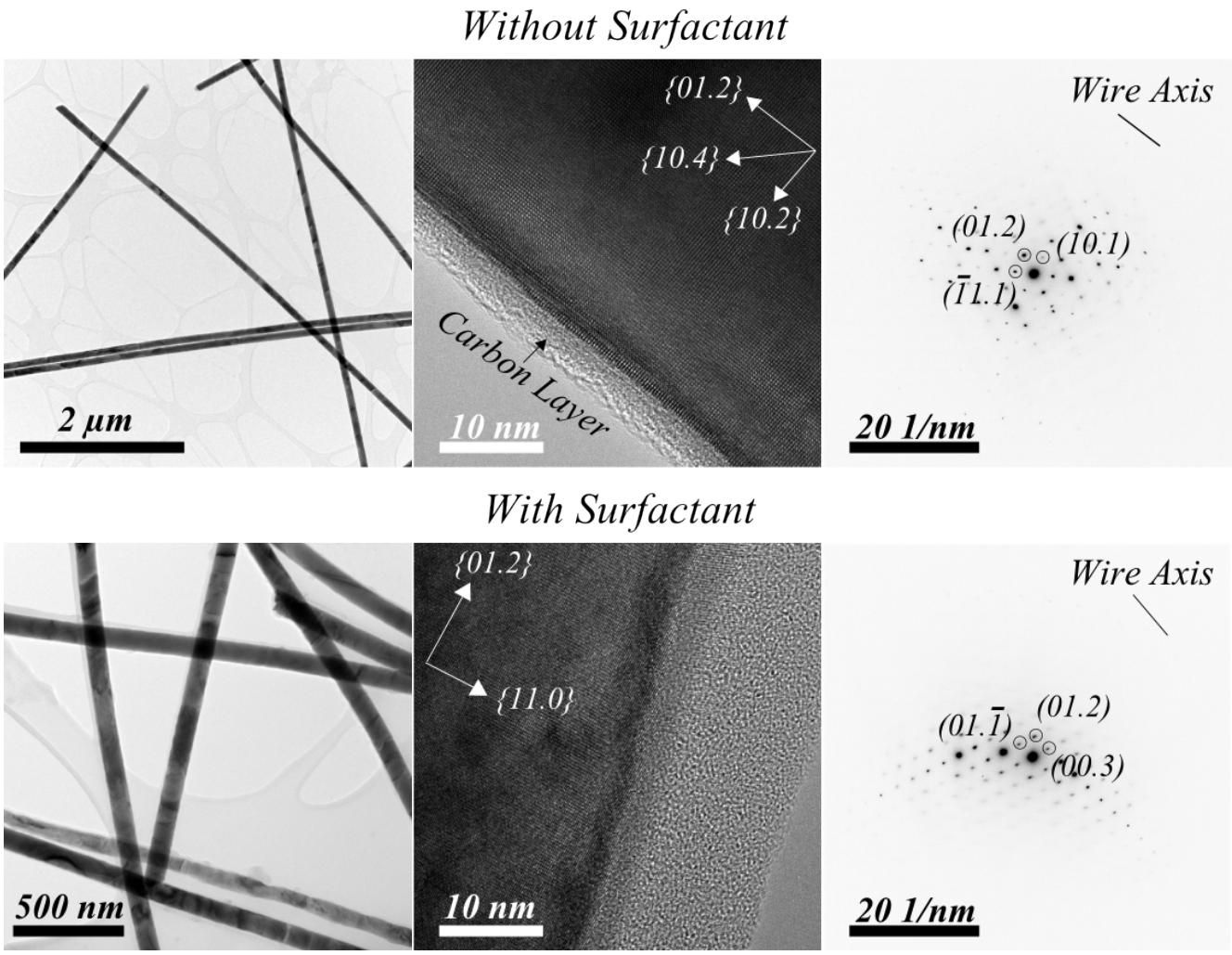

Figure 3.4: Representative TEM images and SAED patterns of Sb wires prepared with and without surfactant. The shown images belong to different Sb wires and show exemplary the high quality of the crystal structures of the wires.

surfactant even a 10 μm large grain was found. This also means that the pulsing of the potential does not generate additional grain boundaries, since the largest growth rate per pulse for nanowire arrays is in the order of 260 nm/pulse, being much smaller than the observed grain sizes.

The plane distances were indexed using the standard powder diffraction data JCPDS 35-732. Wires prepared without surfactant exhibit {01.2} and {10.1} planes perpendicular to the wire axis. Wires prepared with surfactant exhibited also {11.0} planes perpendicular to the wire axis. Due to the small number of wires measured (5 per sample) this is only an indication for the growth directions and additional XRD measurements were carried out to complete the structural characterization.

XRD of nanowire arrays embedded in the polymer template allows to investigate the crystal structure of a large amount of wires. To avoid additional reflexes in the diffraction patterns, the gold backelectrode was removed prior to the measurements, using Lugols iodine. Figure 3.5 shows the XRD patterns of samples prepared with electrolytes containing different amounts of surfactant. The measured series additionally includes samples prepared with electrolytes containing 0.5 ‰ and 2 ‰ of surfactant, in order to see if the amount of surfactant can influence the direction of crystal growth in the wires. The vertical lines at

the bottom of figure 3.5 correspond to the reflex positions and normalized intensities of a Sb powder sample, according to JCPDS 35-732. The data acquired were normalized to the {01.2} reflex. All samples have been prepared at 40°C, except for one sample containing no surfactant, which was prepared at room temperature.

Both samples prepared without surfactant show the same strong {01.2} texture and only a small reflex of the {20.2} planes is visible. Their diffractograms are similar to the ones reported for Sb nanowire arrays prepared with pulsed electrodeposition at room temperature, using similar growth parameters [59]. The temperature therefore seems to have no influence on the crystalline growth of the Sb wires. For the samples prepared with surfactant, as in the case without, a strong {01.2} texture is visible. However, with surfactant also the {20.2} reflexes become more prominent. Therefore it can clearly be stated that the surfactant does influence the crystal growth direction in the Sb wires.

Although the TEM measurements showed crystals with {11.0} planes perpendicular to the wire axis, in the case of wires prepared with surfactant, there is no reflection visible for these planes in the XRD patterns. Therefore either the amount of these crystallites is low, or the wire growth in both cases was different although the same procedures were applied. It should also be mentioned that the small reflection at ~ 27.5° is an artifact generated by the setup.

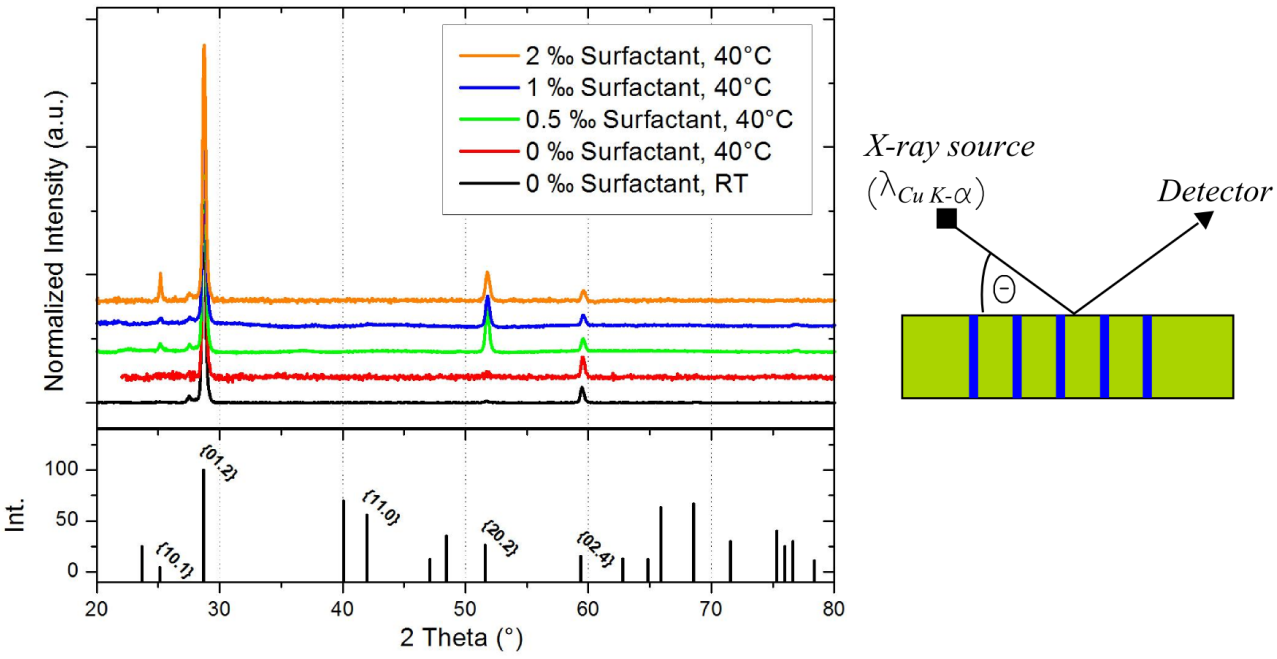

Figure 3.5: X-ray diffraction patterns of parallel arrays of Sb nanowires (10^8 i/cm^2, ~100 nm wire diameter), embedded in the polycarbonate. The samples were prepared with electrolytes containing different amounts of surfactant (0 to 2 ‰). Except for one sample without surfactant, which was prepared at room temperature, the samples were deposited at 40°C. The data acquired was normalized to the {01.2} reflex of Sb. The diffractograms for the different samples are vertically shifted for better visibility. In the bottom row the powder diffraction data according to JCPDS 35-732 is shown, including the planes indexes for the visible planes in the diffractograms. On the right hand side the alignment of the nanowires with respect to the θ-2θ measurement geometry is shown.

In conclusion it can be said that the Sb wires prepared with and without surfactant exhibit similar grain sizes and crystallinity. The addition of surfactant however, leads to an increasing growth of {20.2} planes in relation to the {01.2} planes.

3.1.2 Uniformity of Growth

The uniformity of the nanowire growth is a crucial factor for the implementation of nanowires in future devices. In order to test if the deposition process fills all pores at an equal rate, SEM images were taken of an Sb array embedded in a template, after different thicknesses of polymer had been removed from top of the sample, using a reactive ion etching process (see chapter 2.3)[112, 113].

The Sb array was deposited in a template that had been irradiated with 10^8 i/cm^2 and had a pore diameter of ∼160 nm. For electrodeposition an Sb electrolyte containing 1 ‰ of surfactant was used, applying the standard conditions mentioned above. Since the deposition was continued beyond the onset of cap growth, the sample was ultrasonicated in water previous to the measurement in order to remove the caps on the template surface. In order to avoid charge up of the polymer during the SEM measurements, a thin layer of gold (∼10 nm) was sputtered onto the sample.

Figure 3.6a) shows an SEM image of the surface of the template before a RIE process was applied. The bright spots indicate where a wire tip has reached the surface, whereas the black spots indicate empty pores at the surface. Figure 3.6b) to d) shows the surface of the template after 1 min to 3 min of reactive ion etching. For the used process, the polymer is etched with a rate of 0.5 μm per minute. This was estimated by measuring the step height between etched and unetched areas which were covered by a glass substrate, using a DEKTAK profilometer.

Three things became obvious when comparing these pictures: i) more and more wires appear in the pores, ii) the pores increase in size and iii) the surface of the polymer becomes rougher.

In order to quantify the filling ratio, the number of observable filled and unfilled pores was counted at several positions on the sample and plotted against the etch depth (figure 3.7). The error bars here indicate the standard deviations between different locations on the sample. Whereas on the initial surface 58 % of the pores appear to be filled on average, the ratio increases to 98 % only 2 μm below the surface. Using Faradays Law (eq. 2.22) and considering the charge deposited till cap growth a filling rate of 88 % ±6 % was calculated for the sample, which fits well with the observed value.

The difference in wire height can be explained either by wires breaking at different lengths during ultrasonnication or due to differences in the pore lengths due to the rough surface of the polymer onto which the initial electrical contact for electrodeposition is prepared (see inlet in figure 3.6a) and d)). Measurements of the rough side of the polycarbonate foil, using a DEKTAK profilometer, showed a surface roughness in the order of 2 μm. Therefore the initial starting height of the wires can also be up to 2 μm, so that if all the pores were filled at the same speed, the first wires reaching the top would be 2 μm shorter than the last. Based on this analysis the pulsed electrodeposition process seems to allow uniform growth of wires inside the pores.

The RIE-induced increase in pore size depends linearly on the etching time, with an etching rate of ∼130 nm/min. No overall shrinkage of the polymer was observed after the plasma process in contrast to statements in other works [112]. The increase in surface roughness is due to polymer residues forming wisp like structures, as seen in figure 6.16 c). The influence of the plasma process can also be used to

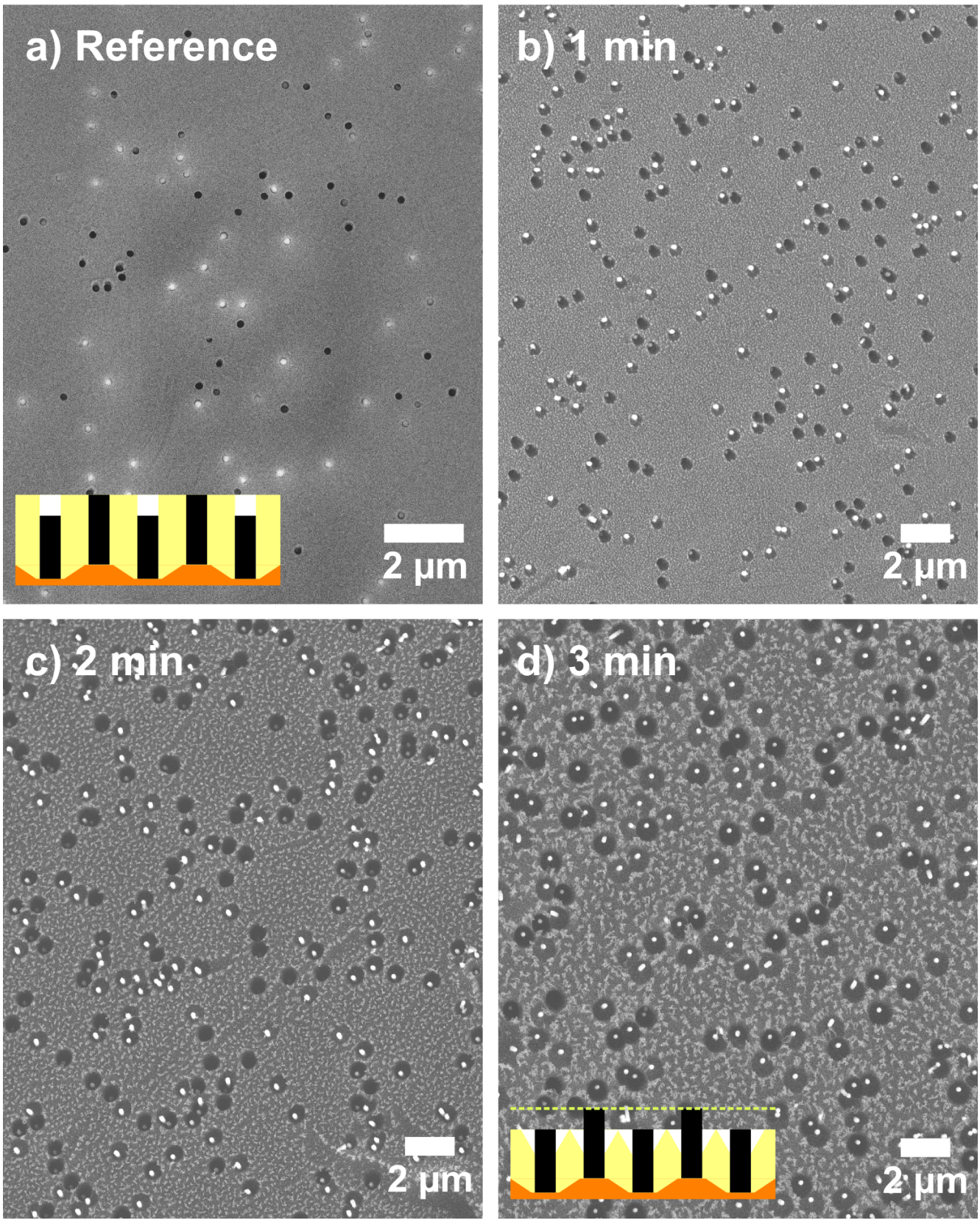

Figure 3.6: SEM images of the smooth surface of a template, a) after initial nanowire growth and b) - d) after polymer has been removed from the top, using a reactive ion etching process for 1 to 3 minutes. With increasing time more and more polymer is removed, revealing the wire tips below the surface, indicating the high filling ratio of the template. Additionally an increase in pore diameter and surface roughness of the polymer is visible.

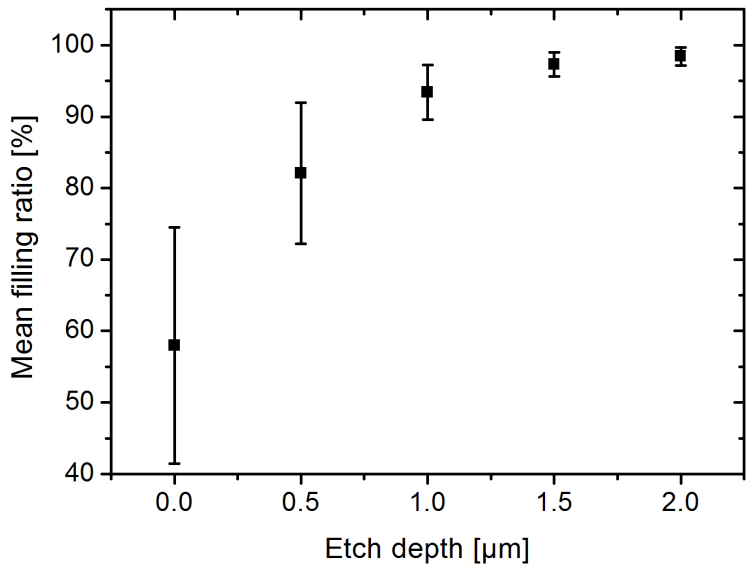

Figure 3.7: Filling ratio, analysed from SEM images, depending on the etch depth below the initial surface. The error bars represent the standard deviations of the filling ratio between different locations on the sample.

change the surface wetting of polycarbonate from superhydrophobic to superhydrophilic, depending on the plasma process and additional treatments afterwards [114].

3.2 Antimony Nanowire Networks

3.2.1 Electrodeposition

The depositions of Sb nanowire networks were performed under the same conditions as nanowire arrays discussed above (40°C, on/off-potential of -260 mV/-130 mV vs. SCE, on/off-times of 20 ms/100 ms), using the electrolyte containing 1 ‰ of surfactant. The nanowire network depositions performed without surfactant yielded very inhomogeneous filling, i.e. only in small areas in the template, or no deposition at all. Currently this is attributed to the fact that the interconnections of pores hinder the wetting of the template, since for parallel arrays this problem did not occur. Why this was not observed in the previous study [104], is yet not understood.

Figure 3.8a) to c) show exemplary deposition curves for Sb networks with various pore densities and pore diameters. The general trend that larger pores and higher pore density lead to a higher current during deposition, due to a larger active area, can be seen. However, for larger pores this trend is not always confirmed, maybe due to changes in the growth process in bigger pores. The average current vs. time curves of templates with small pore sizes show a current decrease midways or closer to the end of a deposition. Due to the short etching process the pores are probably not perfect cylindrical, but rather biconical. Since the area of the pore would therefore decrease towards the center of the template, also the current would decrease towards the constriction and increase again afterward, explaining the observed behavior.

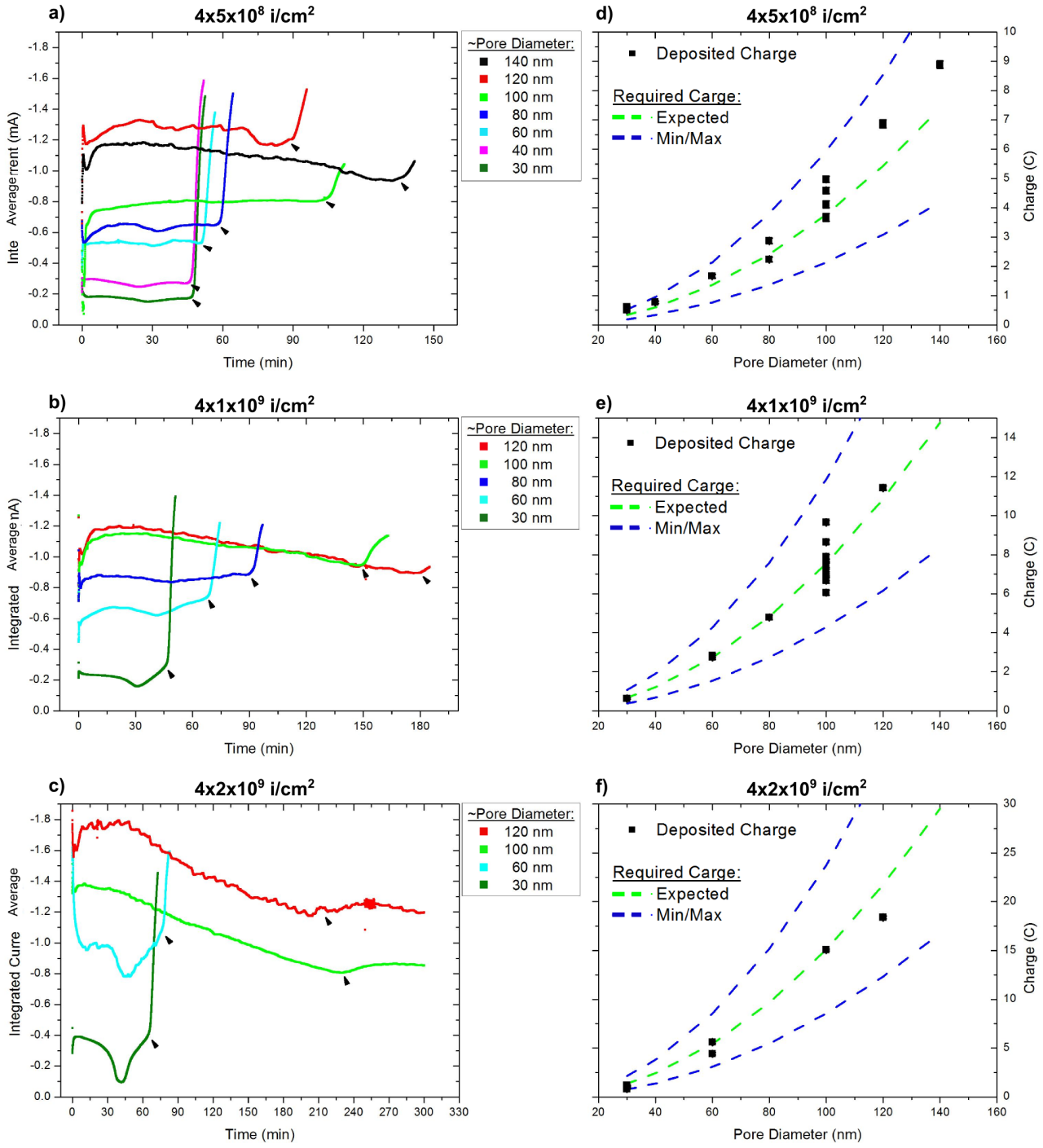

Figure 3.8: a) to c) Exemplary deposition curves for Sb nanowire networks. The used templates had a pore density of a) $4 \times 5 \cdot 10^8$ i/cm^2, b) $4 \times 1 \cdot 10^9$ i/cm^2 and c) $4 \times 2 \cdot 10^9$ i/cm^2 and various pore diameters. Deposition was done at 40°C, using on/off-potential of -260 mV/-130 mV vs. SCE and on/off-times of 20 ms/100 ms. The black arrows indicate the onset of cap growth. d) - e) Deposited charge till the onset of cap growth for Sb nanowire networks. The dashed green line represents the calculated charge that is needed to fill 100% of the pores. The blue lines represent the calculated maximum and minimum required charge to fill 100% of the pores, considering an error of 30% for the pore density and an error of 10% for the etching rate. The calculated charges were determined by using the Faraday law (eq. 2.2.2).

Figure 3.8d) to f) show the deposited charge until cap growth (black arrows in deposition curves) of Sb nanowire network depositions done during this work. The dashed green line represents the calculated charge that is needed to fill 100% of the pores. The blue lines represent the calculated maximum and minimum required charge to fill 100% of the pores, considering an error of 30% for the pore density and an error of 10% for the etching rate. The calculated charges were determined by using the Faraday law (eq. 2.2.2).

Most of the points align along the green line, which corresponds to the expected values from the samples, therefore we assume a good filling of the different network templates. In fact when comparing these values with previous works [104], the filling ratio has been improved significantly by the introduction of the surfactant.

3.2.2 Morphological Characterization of Sb Nanowire Networks

The morphology of nanowire networks was studied, in order to see how the wire density and wire diameter influences the structural integrity of the networks, and if the surfactant in the electrolyte has any visible influence on the growth.

Figure 3.9a) to e) shows SEM images of Sb nanowire networks with a wire diameter of ∼100 nm and wire density of a) $4 \times 5 \cdot 10^8$ i/cm^2, b) $4 \times 1 \cdot 10^9$ i/cm^2 and c) $4 \times 2 \cdot 10^9$ i/cm^2. Figure 3.9a) shows a closeup of the Sb network with the smallest wire density. Although the network appears to be intact on a small scale, a view of the larger scale shows that the network is not mechanically stable and breaks into smaller pieces, figure 3.9b). When the wire density is increased the networks are stable, i.e. no cracks are observed in the surface and no broken pieces of network are found. This fits well with previous observations for Sb nanowire networks prepared without surfactant [104]. Altogether the Sb networks seem to grow in a homogeneous fashion and samples with good quality can be produced with the mentioned parameters. No visible influence of the surfactant on the morphology was observed.

Testing the uniformity of growth using RIE like with parallel arrays, shown in section 3.1.2, was not carried out since the overlap of wires would make the counting of the pores very challenging.

As indication for the growth uniformity for networks the cap formation on top of the template was examined instead. For these tests Sb networks were grown from the smooth side of the template toward the rough side. This procedure was chosen so that the growth would start on a similar height in the template, thereby preventing the height difference of 2 μm observed in the case of parallel arrays, due to the surface roughness of the rough side.

Figure 3.10 shows the rough side of a template with ∼100 nm diameter pores that had been irradiated with $4 \times 1 \cdot 10^9$ i/cm^2, after 7 min of cap growth. The caps grow homogeneously distributed over the surface and show crystal facets. As the caps grow, the individual caps seem to merge to bigger structures which at least partially align along the irradiation directions. They fill the valleys on top of the surface at first and wire tips just reaching the surface can be seen on the same height level as the caps, wherever the roughness allows it. Therefore, like with the parallel arrays of Sb wires, the network pores get filled in a very homogeneous way from the bottom to the top.

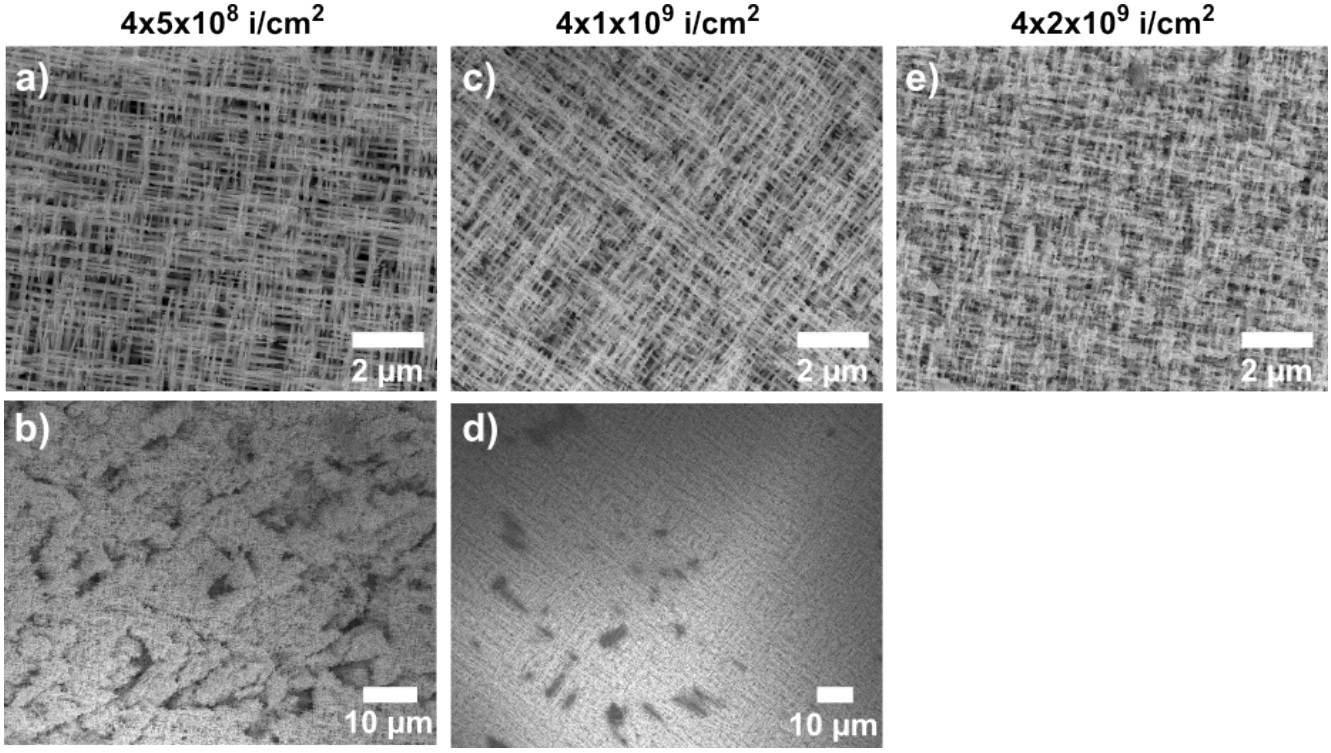

Figure 3.9: SEM images of Sb nanowire networks with wire densities of a-b) $4 \times 5 \cdot 10^8$ i/cm^2, c-d) $4 \times 1 \cdot 10^9$ i/cm^2 and e) $4 \times 2 \cdot 10^9$ i/cm^2) and same wire diameter $\sim$ 100 nm. b) After the template was dissolved the network broke apart into smaller pieces, which are still stable on a smaller scale, as seen in a. d) When the wire density is increased the network is stable and shows a uniform surface without breaks. The darker spots in figure d) are Sb caps that formed on the surface of the template.

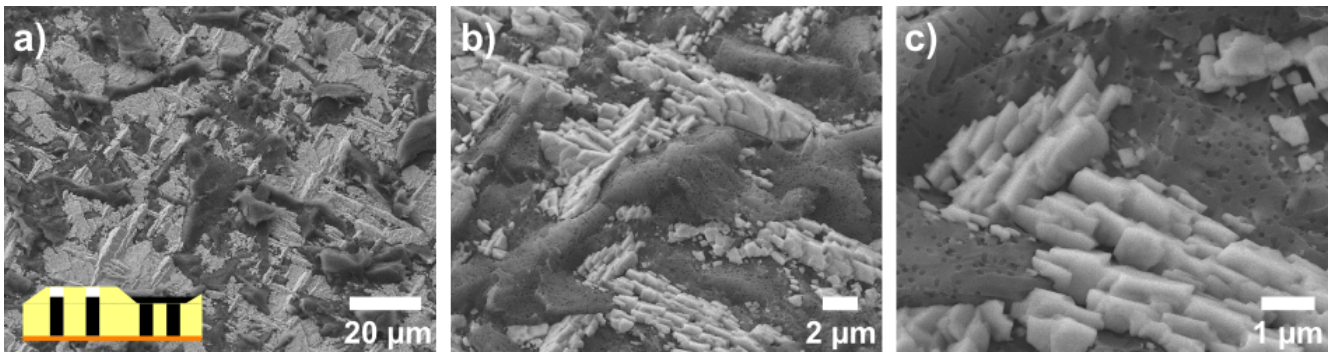

Figure 3.10: SEM images of the rough side of a template with $\sim$100 nm diameter pores that had been irradiated with $4 \times 1 \cdot 10^9$ i/cm^2. The pores were filled with Sb via a pulsed potential deposition at 40°C, using on/off-potential of -260 mV/-130 mV vs. SCE and on/off-times of 20 ms/100 ms. The deposition was stoped after 7 minutes of cap growth. In this case the growth has been carried out from the smooth to the rough side of the template. Cap growth starts in the valleys where crystalline caps form on the tips of the wires that grow and merge together with neighboring ones. Also an alignment of at least some of the caps along the irradiation directions is visible.

3.2.3 Crystallographic Characterization of Sb Nanowire Networks

Influence of Pore Tilt on Growth Process

Whereas for a nanowire array the pores in the template are individual and oriented parallel to the foil normal, the pores of a template for a nanowire network are interconnected and tilted by 45° to the foil normal.

In order to investigate the influence of the pore tilt on the crystal growth of nanowires and to exclude any influence due to the crossing of pores, diffractograms were taken from parallel arrays of nanowires. One nanowire array was prepared in a template that was irradiated with 10^8 i/cm^2 parallel to the foil normal (referred to as parallel wires) and another one in a template that was irradiated with 10^8 i/cm^2 under an angle of 45° towards the foil normal (referred to as tilted wires). Both templates were etched to generate ~100 nm diameter pores and filled with Sb using the process given above using electrolyte with surfactant. The deposition was stopped as soon as the first indications of cap growth were observed. Additionally the gold backelectrode was removed after wire growth using Lugols iodine to avoid additional reflexes in the diffraction patterns.

Figure 3.11 a) shows the diffractograms of the tilted wires (black) and the parallel wires (orange line), measured at $\chi = 0°$. The parallel wires exhibit the {01.2} and {20.2} reflex, whereas the tilted wires additionally show the {10.4} and {11.0} reflex. When the tilted wires are turned by $\chi = 45°$, they align in a similar fashion in the diffractometer as the parallel wires at $\chi = 0°$. Figure 3.11 b) shows the diffractograms of the tilted wires at $\chi = 45°$ (black) and the parallel wires at $\chi = 0°$ (orange line). In this case the diffractogram of the tilted pores does not show the {10.4} and {11.0} reflex anymore and is almost similar to the diffractogram of the parallel pores. This indicates that the growth direction aligns to the pore axis, with a possible explanation being the reduction of surface energy of the wire [115].

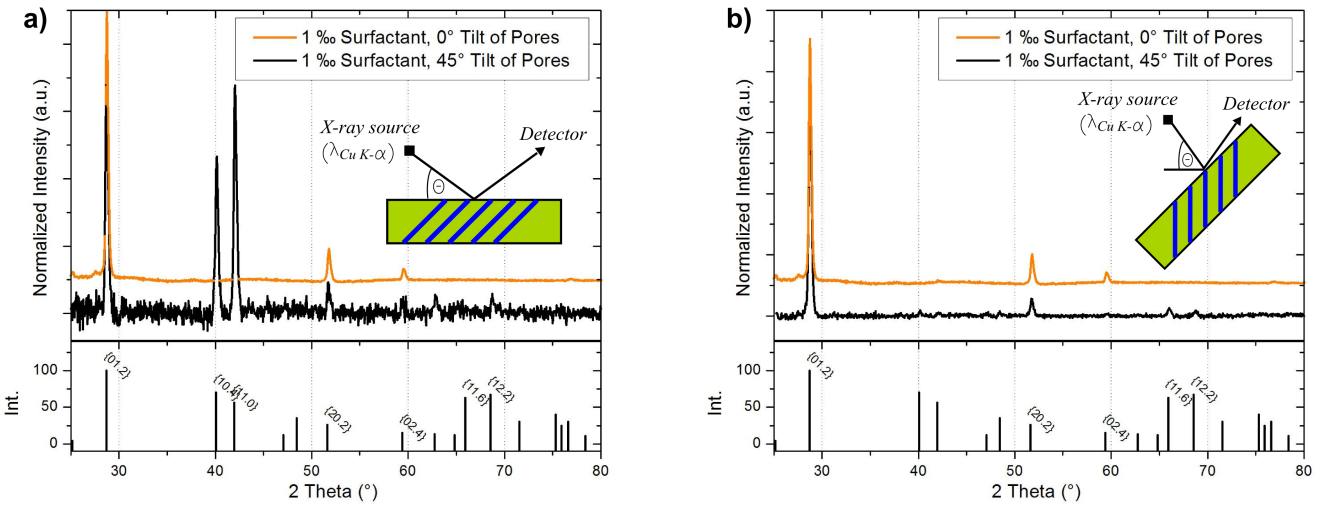

Figure 3.11: a) Diffractograms of the tilted wires (black) and the parallel wires (orange line), both measured at $\chi = 0°$, normalized to the {01.2} reflex. b) Diffractograms of the tilted wires at $\chi = 45°$ (black) and the parallel wires at $\chi = 0°$ (orange line), normalized to the {01.2} reflex. The small insets show the orientation of the sample with tilted pores during measurement.

Crystallographic Characterization of Sb Nanowire Networks by XRD and TEM

For XRD measurements a series of Sb nanowire networks, grown in templates irradiated with a fluence of $4 \times 5 \cdot 10^8\ i/cm^2$ and pore diameters of ~40 nm, ~80 nm and ~120 nm were investigated. Figure 3.12 shows the measured diffractograms normalized to the {01.2} reflex. The Sb network with a diameter of 40 nm only shows reflexes that can be assigned to {01.2}, indicating a strong texture of the sample. This texture decreases as the pore diameter increases and additional crystal orientations like {11.0} and {10.4} become more prominent. It is likely that the larger pore diameter allows the growth of multiple grains with various orientations that compete with one another, leading to the decrease in texture.

It is a bit surprising that the {11.0} and {10.4} reflexes are not more prominent, as these reflexes showed high intensities in the case of the parallel wires in the tilted array, discussed above. Whereas for the tilted parallel nanowire arrays a strong {01.2} reflex was observed along the wire axis, the networks show it under 45° to the wire axis. A χ scan kept at $\theta = 42°$ also revealed that the {11.0} planes are perpendicular to the wire axis in the Sb nanowire network. For reasons yet not understood, the crystal orientation differs from what would be expected based on the measurements on tilted Sb nanowire arrays. Whether or not the pore overlap has an influence on the crystal orientation is still under discussion.

It should be mentioned that previous measurements on a Sb network (fluence of $4 \times 1 \cdot 10^9\ i/cm^2$, wire diameter of ~100 nm), prepared under similar conditions, showed a similar behavior to the parallel arrays [111]. However, this is just an indicator that small changes in the preparation process might lead to major changes in the growth process.

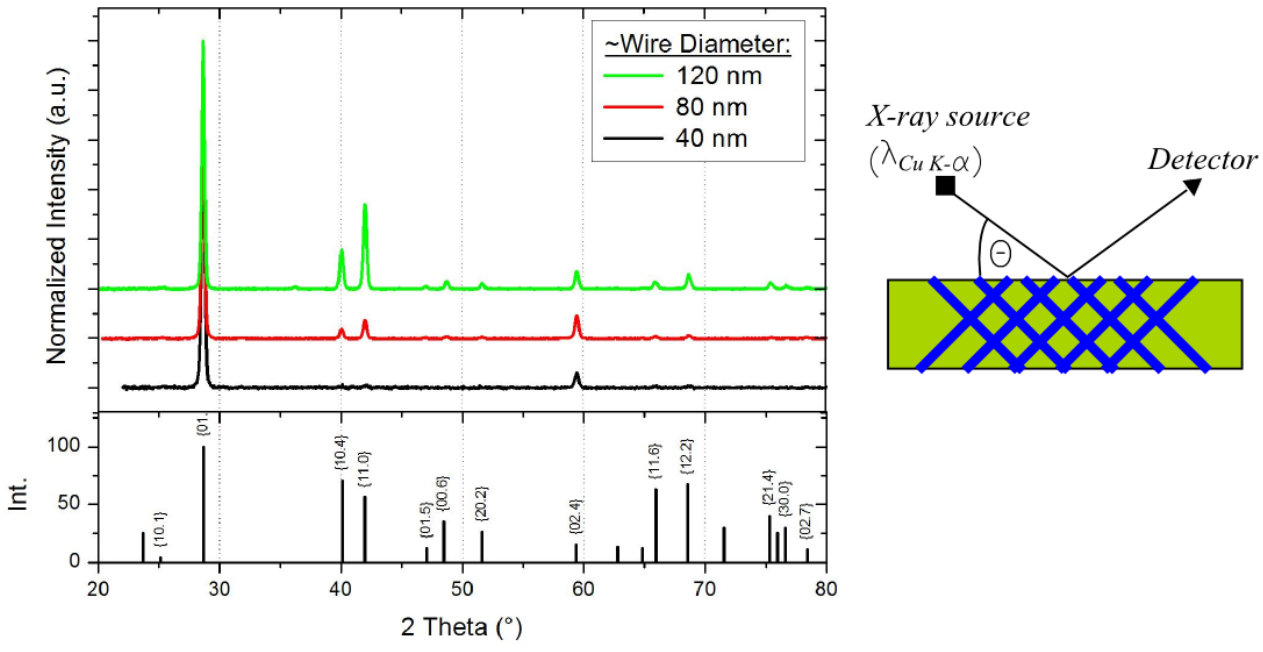

Figure 3.12: XRD pattern of Sb nanowire networks normalized to the {01.2} reflex. The networks were grown in templates irradiated with $4 \times 5 \cdot 10^8\ i/cm^2$ and pore diameters of ~40 nmn 80 nm and 120 nm. The pores were filled with Sb via a pulsed potential deposition at 40°C, using on/off-potential of -260 mV/-130 mV vs. SCE and on/off-times of 20 ms/100 ms. The sketch on the right side shows the orientation of the sample during XRD measurement.

TEM measurements were performed on fragments of a Sb nanowire network using a JEM-ARM200F HRTEM. The initial network was prepared in a template, that was irradiated with $4 \times 5 \cdot 10^8\ i/cm^2$ and had a pore diameter of ∼80 nm, by applying the standard procedure given above. After the polycarbonate template had been dissolved, the sample was ultrasonicated in dichloromethane, which broke the network apart. Subsequently the solution with network fragments was pipetted on a Cu TEM grid and dried in air. Due to this process however the information about the initial position of the fragment within the network is lost.

Figure 3.13a) shows a TEM image of broken Sb network piece with an intersection of two nanowires. The SAED patterns and HRTEM images for the three indicated positions are shown below, figure 3.13b) to g). The center of the intersection of both wires itself was too thick to be measured in transmission, so that information was only gained at the edges of the nanowires.

On all three positions a similar SAED pattern could be obtained, indicating that the crystal orientation is the same before and after the intersection. This leads to a rotation of the crystal orientation in relation to the wire axis by 90° between the two conjoined wires, schematically depicted in figure 3.13h). Otherwise the intersection does not seem to influence the crystal growth in the wire parts. In position 1 and 3 the {10.1} planes are oriented perpendicular to the wire axis, which fits well to the results of the XRD measurement of a Sb nanowire network. When measuring the plane distance in the HRTEM images, an interplanar distance of 0.175 nm was found, which can be related to the {20.2} planes. Why the {10.1} planes were not visible in the HRTEM is still under discussion. Also using the SAED patterns to identify the growth in other directions gave no clear results. In those cases a planar distance of 0.137 - 0.139 nm was calculated. Taking the error into account the {11.6} and/or {20.5} planes could be attributed to these planes, with planar distances of 0.141 nm and 0.143 nm, respectively.

The observed length of single crystal segments within the Sb network is at least in the order of several 100 nm. Longer grains could not be observed due to the size of the broken network pieces.

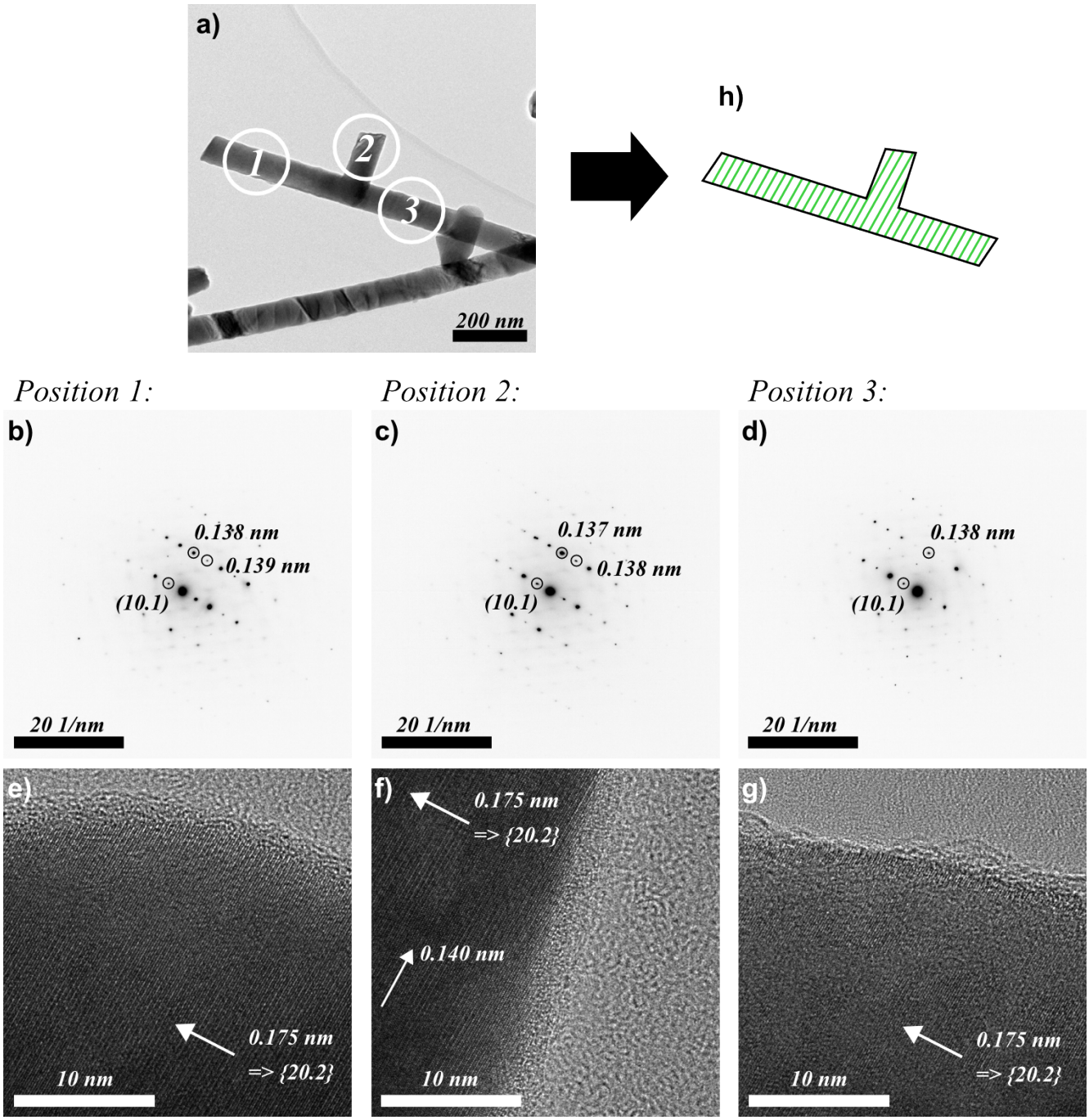

Figure 3.13: a) TEM image of a broken network piece with an intersection of two ~80 nm diameter Sb nanowires. b-d) SAED patterns and e-g) HRTEM images of the three indicated positions. The HRTEM and SAED patterns show the same crystal orientation of the wires before and after the intersection. Therefore it is assumed that the intersection of pores do not influence the crystal growth. This does however lead to a change in crystal orientation by 90° between the two conjoined wires at the intersect. h) Schematic of the {10.1} planes (green) in the network piece.

3.3 Bismuth Nanowire Networks

3.3.1 Influence of Applied Potentials on Growth Process

First a series of Bi nanowire networks was prepared with various on and off-potentials, using on/off-times of 20 ms/100 ms, in order to study the influence of the deposition potential on the growth. The used templates were irradiated with $4\times5\cdot10^8$ i/cm^2 and had pore diameters of ∼100 nm. The used Bi electrolyte contained 1 ‰ of surfactant and the depositions were done at 40°C. As in the case of Sb networks, the surfactant (DOWFAX 2a1) needed to be introduced in the electrolyte to allow the electrodeposition of material inside the pores.

Figure 3.14a) shows the average current vs. time curves for Bi depositions using an on-potential between -260 mV and -200 mV and an off-potential of -170 mV vs. SCE. The off-potential of -170 mV vs. SCE was chosen based on previous tests, showing an off-current that is close to zero or slightly negative at the end of the off-time. Depositions with on-potentials lower than -200 mV vs. SCE were not carried out, since the off-potential was lying at -170 mV vs. SCE.

As a general trend one can see that a higher on-potential leads to a higher average current during wire growth, which is in agreement with the measured cyclic voltammograms of the electrolyte, shown in figure 8.2. Additionally, for higher on-potentials the current during wire growth increases during deposition, the larger the on-potential the larger the slope. Due to the higher current also the onset of cap growth occurs sooner, as indicated by black arrows. The depositions in the case of on-potentials of -260 mV and -240 mV were continued for times far beyond the initiation of cap growth.

Figure 3.14b) shows exemplary the current vs. time plot of the Bi network deposited with -200 mV/-170 mV vs. SCE. For this sample, as for all other samples deposited with an off-potential of -170 mV vs. SCE, the off-current decreased further during cap growth, in contrast to the Sb depositions where it increased. Probably because the off-potential is more negative than the equilibrium potential of Bi.

Figure 3.14c) shows the average current vs. time curves for Bi depositions using various off-potentials vs. SCE. In the case of the sample with an off-potential of -140 mV a higher on-potential was chosen, in order to allow a deposition in a reasonable process time. Figure 3.14d) and e) shows the corresponding current vs. time plots for the depositions at off-potentials of -160 mV and -140 mV, respectively.

Comparing figure 3.14b), c) and d) it becomes obvious that the more positive the off-potential, the more positive the off-current, which could be expected. However, comparing figure 3.14b) and d), it seems that also the the on-current is influenced, becoming more negative in the beginning of a pulse, the more positive the off-potential. A possible explanation can be, that while applying the off-potential Bi gets redissolved into the electrolyte. The more positive the off-potential the more Bi is dissolved, increasing the Bi concentration in the electrolyte, close to the working electrode. During the following application of the on-potential then more ions are available to be reduced, which increases the observed current. Another possible explanation is that due to the higher off-potential more charge is needed to polarize the electric double layer when applying the on-potential, leading to higher non-faradaic currents that contribute to the current signal at the beginning of the on-time. Looking at the behavior at the onset of cap growth there is no fundamental difference between the samples, however the sample with an off potential of -140 mV differs. In this case a decrease in on- and off-current, as well as an increase in off-current during the start of cap growth is visible.

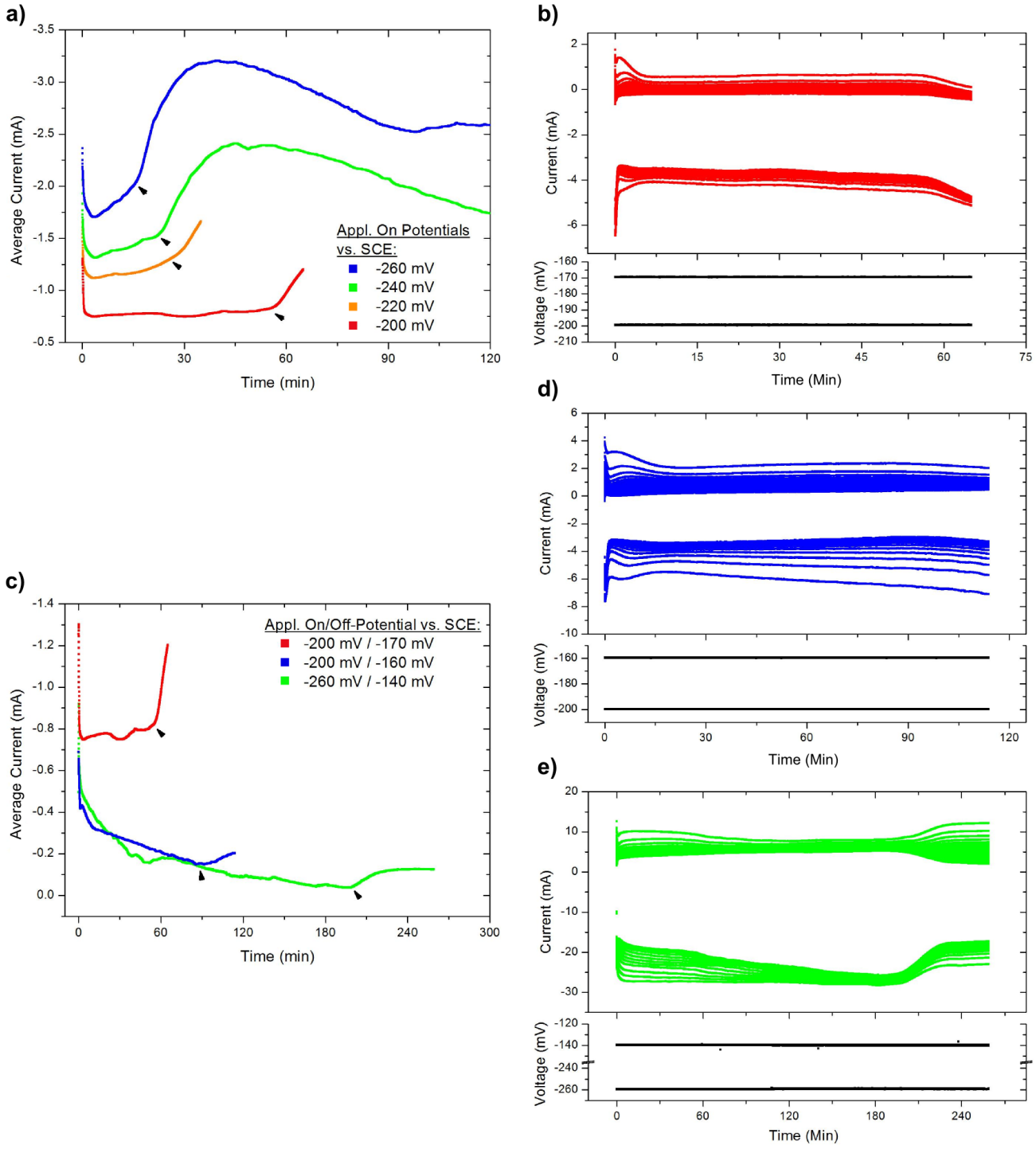

Figure 3.14: Deposition curves for Bi depositions in network templates irradiated with $4 \times 5 \cdot 10^8$ i/cm^2, having pore diameters of ~100 nm. The used electrolyte contained 1 ‰ of surfactant and electroplating was done at 40°C. a) Average current vs. time curves for Bi depositions using a pulsed potential with various on-potentials and an off-potential of -170 mV vs. SCE . The black arrows indicate the onset of cap growth. b) Current vs. time plot for the deposition of Bi corresponding to the red average current vs. time. in a) and c). c) Average current vs. time curves for Bi depositions using various on-/off-potentials vs. SCE. The black arrows indicate the onset of cap growth. d) Current vs. time plot for the deposition of Bi corresponding to the blue average current vs. time. in c). e) Current vs. time plot for the deposition of Bi corresponding to the green average current vs. time. in c).

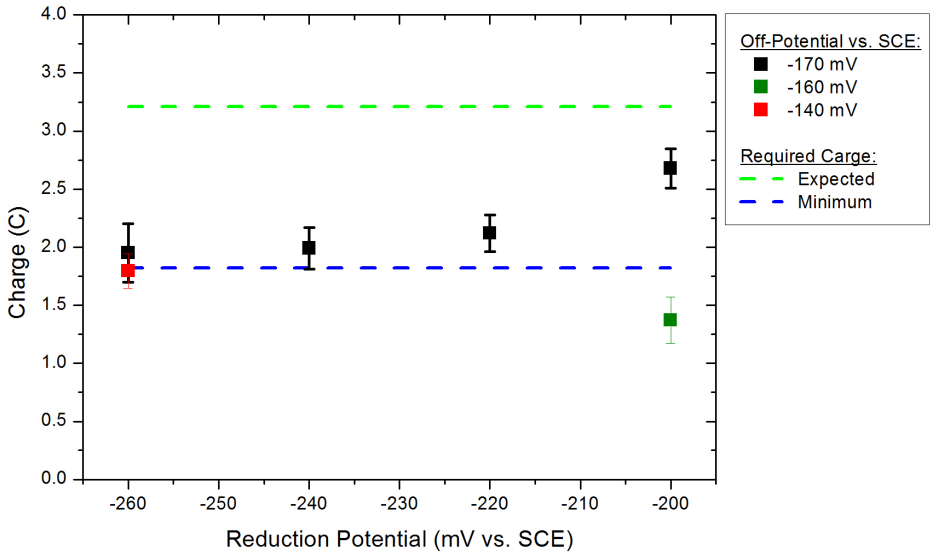

Figure 3.15: Deposited charge till the onset of cap growth for Bi nanowire network depositions at various on-/off-potentials. The used templates were irradiated with $4 \times 5 \cdot 10^8$ i/cm^2 and had pore diameters of ∼100 nm. For the samples shown the used electrolyte contained 1 ‰ of surfactant and electroplating was done at 40°C. The dashed green line represents the calculated charge that is needed to fill 100% of the pores. The blue lines represent the calculated minimum required charge to fill 100% of the pores, considering an error of 30% for the pore density and an error of 10% for the etching rate. The calculated charges were determined by using the Faraday law (eq. 2.2.2).

In general, the shift in on-current is smaller than the shift in off-current, leading to a net reduction of the average current during deposition when the off-potential is shifted to more positive values. It should also be mentioned that for the depositions done at off potentials of -160 mV and -140 mV, the current during wire deposition shows a negative slope.

Figure 3.15 shows the deposited charge till the onset of cap growth, black arrows in deposition curves of figure 3.14a) and c), of the above discussed Bi network depositions. The dashed green line represents the calculated charge that is needed to fill 100% of the pores. The blue lines represent the calculated minimum required charge to fill 100% of the pores, considering an error of 30% for the pore density and an error of 10% for the etching rate. The calculated charges were determined by using the Faraday law (eq. 2.2.2).

Within the tested parameters the highest filling ratio of the templates was achieved at an on-/off potential of -200 mV/-170 mV vs. SCE. The fast growth at high on-potentials seems to come at the cost of filling ratio, since the fast growth also means the inclusion of more defects into the structure and in general a more inhomogeneous growth in the pores. But also the much slower growth at more positive off-potentials does not lead to improvements of the filling, showing that both on- and off-potentials need to be chosen carefully to guarantee good growth.

After deposition of the Bi networks the polymer was removed and the morphology studied by SEM, shown in figure 3.16. The Bi networks do not show the same level of uniform growth, when compared to the Sb networks. The surface shows a lot of cavities and in the case of the networks grown at an off-potential

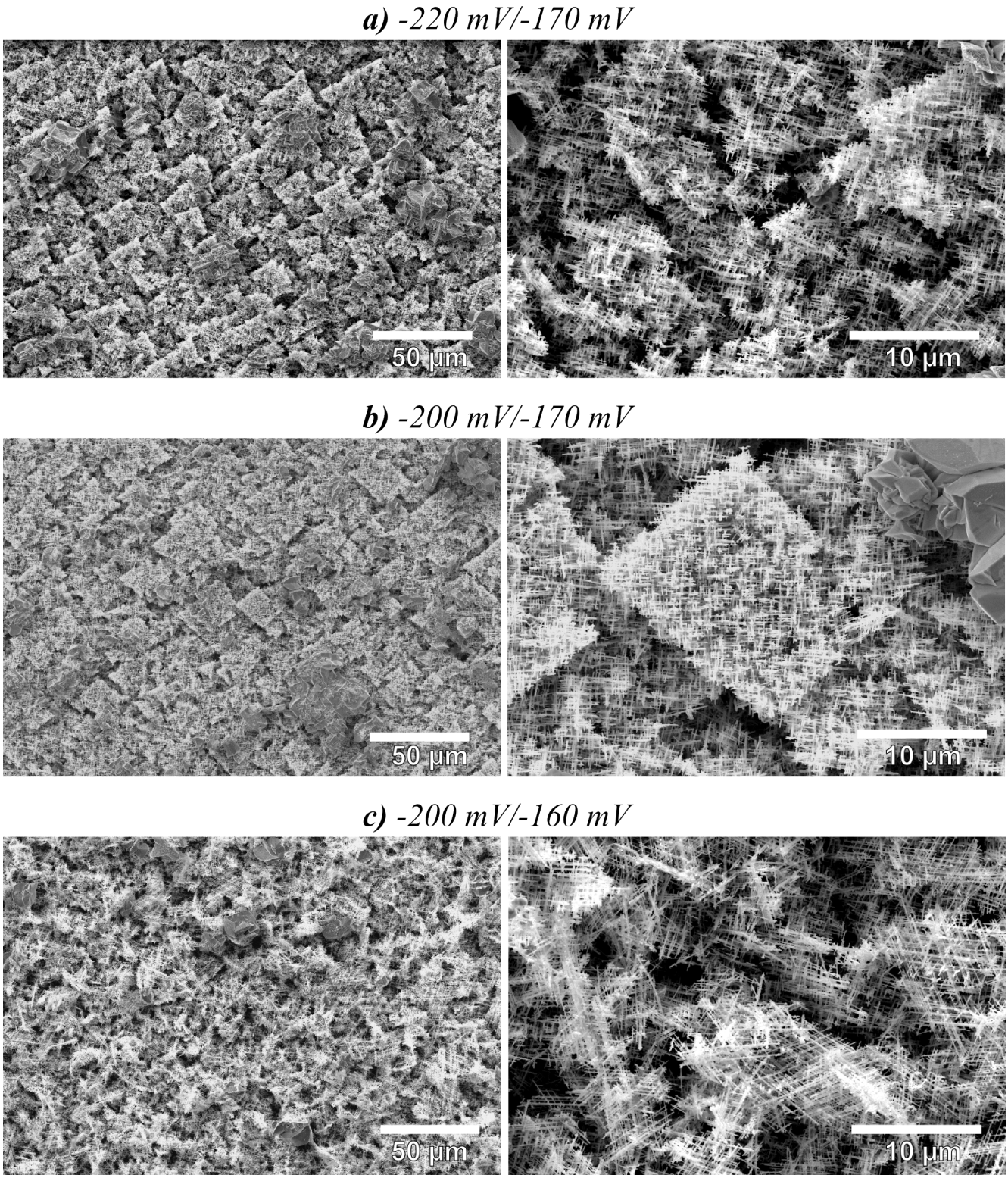

Figure 3.16: SEM images of a bismuth networks, prepared in templates irradiated with $4 \times 5 \cdot 10^8\ i/cm^2$ and having a pore diameter of ∼100 nm, deposited at 40°C, using various on-/off-potential and on/off-times of 20 ms/100 ms. The used Bi electrolyte contained 1 ‰ of surfactant.

of -170 mV shows rhombus shaped structures that are nested inside each other. The Bi network grown at an on-/off potential of -200 mV/-160 mV does not show these structures, however as it was not stable without the template and fell apart during the sample preparation process, the structure might have been lost.

The rhombus shaped structures were never observed for the Sb networks, however the caps formed on top of the Sb networks sometimes also appeared rhombus shaped. The morphology of Bi networks grown in templates irradiated from three directions, shown in figure 8.4 in the supplementary informations, show triangles instead of rhombuses. It is interesting to notice that the tips of the rhombuses, or triangles in case of three directions, point in the irradiation directions. Clearly the observed morphology arises due to the pore arrangement in the template. A possible explanation could be that each rhombus (triangle) is single crystalline and grew from a single point of origin. For the sample with the higher on-potential, the rhombus shaped structures seem to appear more clearly. Also these structures seem to be less stable, which might also be due to the fact that less material was deposited and the cavities are bigger. Also, the wire surface itself was much rougher than compared to the Sb nanowire networks. The grown caps on top of the Bi networks, shown in figure 3.17, have a crystalline appearance, showing several crystal facets.

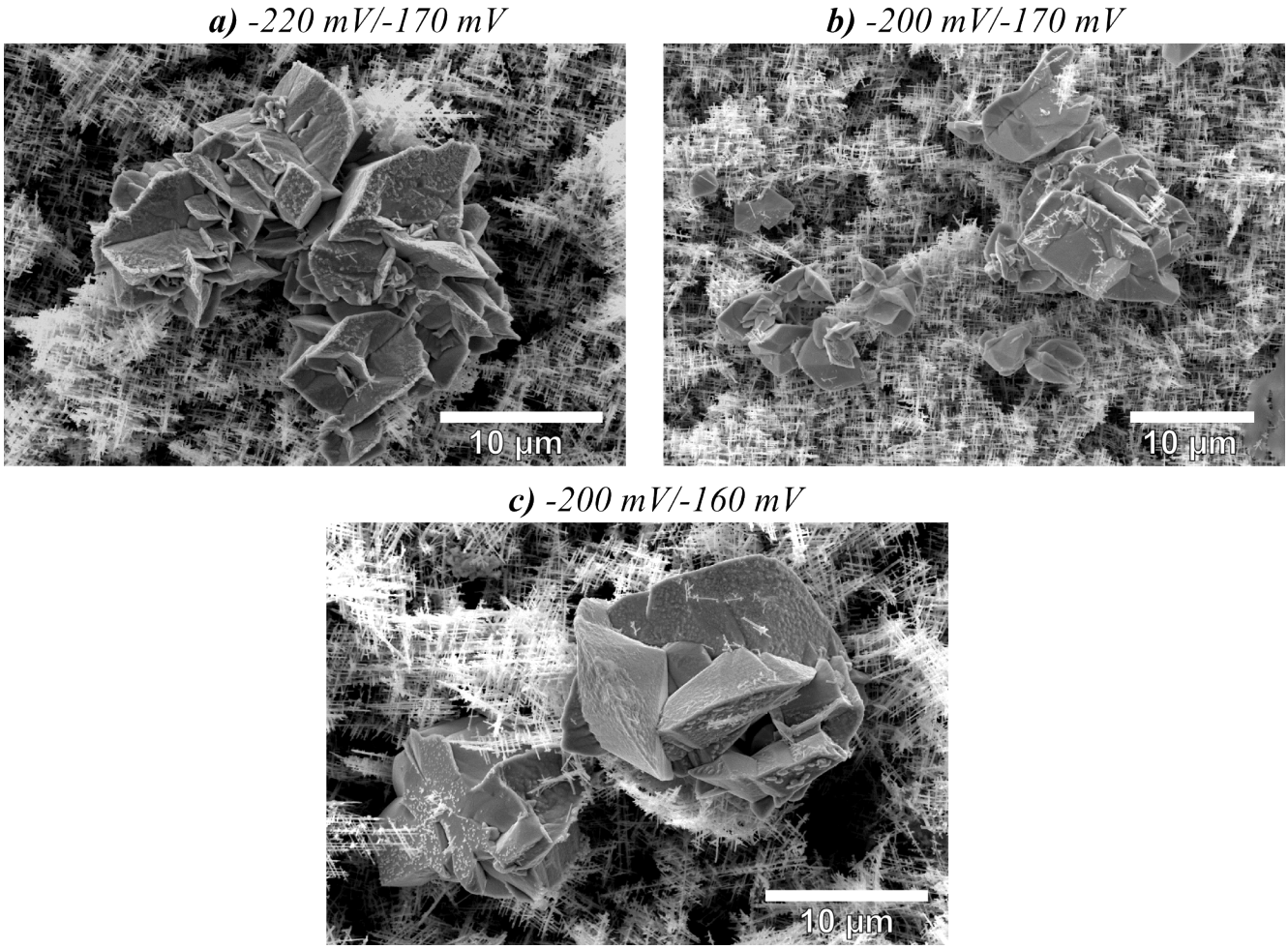

Figure 3.17: SEM images of a bismuth caps grown on top of networks, prepared in templates irradiated with $4 \times 5 \cdot 10^8\ i/cm^2$ and having a pore diameter of ∼100 nm, deposited at 40°C, using various on-/off-potential and on/off-times of 20 ms/100 ms. The used Bi electrolyte contained 1 ‰ of surfactant.

The network grown with an on-/off-potential of -260 mV/-140 mV vs. SCE could not be examined with the SEM. For this sample only the backelectrode remained as the network seemed to have completely fallen apart during the dissolution of the polymer membrane.

The non uniform growth of Bi also means that the lower deposited charge is not necessarily related to fluctuations in the template irradiation and etching rates. In fact as the used templates were irradiated at almost the same time as the ones used for the Sb networks, it is very likely to assume that the charge required is in fact close to the expected value (dashed green line in fig. 3.15). Considering this the highest filling ratio amounts to 83 %, using an on-/off potential of -200 mV/-170 mV vs. SCE.

3.3.2 Influence of Temperature on Growth Process

Sb depositions at elevated temperature provided higher filling ratios of the pores [104]. In order to investigate the influence of temperature on the Bi network deposition, networks were prepared at room temperature and at 40°C, using the same pulsed potentials, pulse times and electrolyte composition for both samples. The used templates were irradiated with $4 \times 5 \cdot 10^8$ i/cm^2 and had pore diameters of ∼100 nm.

The average current vs. time curves at room temperature and 40°C are shown in figure 3.18, for on-/off-potentials of -220 mV/-170 mV and -200 mV/-170 mV, using on-/off-times of 20 ms/100 ms. In both cases the depositions at room temperature exhibit a lower average current when compared to the deposition at 40°C. This is attributed to the higher diffusion and reaction rates of Bi ions at elevated temperatures.

When comparing the deposited charge at the onset of cap growth, the depositions done at room temperatures yield higher filling ratios. The deposited charge was ∼2.1 C and ∼2.7 C at 40°C and -220 mV and -200 mV, respectively, whereas the deposited charge was ∼2.5 C and ∼3.4 C at 40°C and -220 mV and

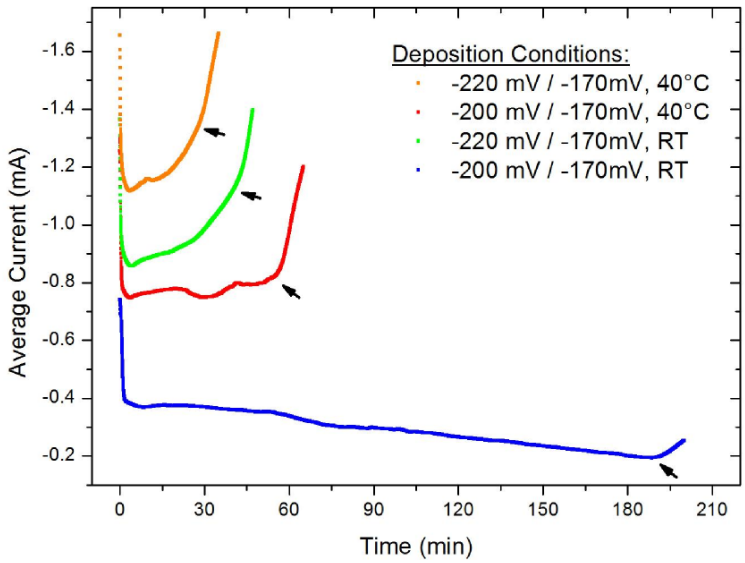

Figure 3.18: Average current vs. time plots for Bi depositions at 40°C and room temperature. The used templates were irradiated with $4 \times 5 \cdot 10^8$ i/cm^2 and had pore diameters of ∼100 nm. The electrolyte contained 1 ‰ of surfactant and pulse on-/off-times of 20 ms/100 ms were used.

-200 mV, respectively. Considering the estimated values for pore density and pore diameters the deposition at room temperature and -200 mV therefore has a estimated filling rate of 105%. Figure 3.19 shows SEM images of the nanowire network grown at room temperature using an on-potential of -220 mV vs. SCE. Again the same rhombus shaped structures as in the sample prepared at 40°C are visible. However the growth seems to be more homogeneous, which is also reflected by the higher deposited charge till cap growth. Opposite to the previous samples, the formed caps on top have a more polycrystalline appearance. During the preparation of the sample grown at -200 mV vs. SCE, the complete top part of the network broke away as a stable layer of material, crumbling of when trying to handle it. The network left on the backelectrode did not show the rhombus like structures, so that it may be assumed that the open gaps in the network between the structures may close during further growth.

For all further depositions of Bi an on-/off potential of -200 mV/-170 mV vs. SCE was chosen, since the deposited charge was always the highest using these potentials. Although the filling rates at room temperature was higher it was decided to continue the depositions at 40°C, in order to keep the process closer to the Sb one. Additionally it was shown that Bi wires prepared at elevated temperatures possess larger grain sizes, which should be favorable for electric transport [116].

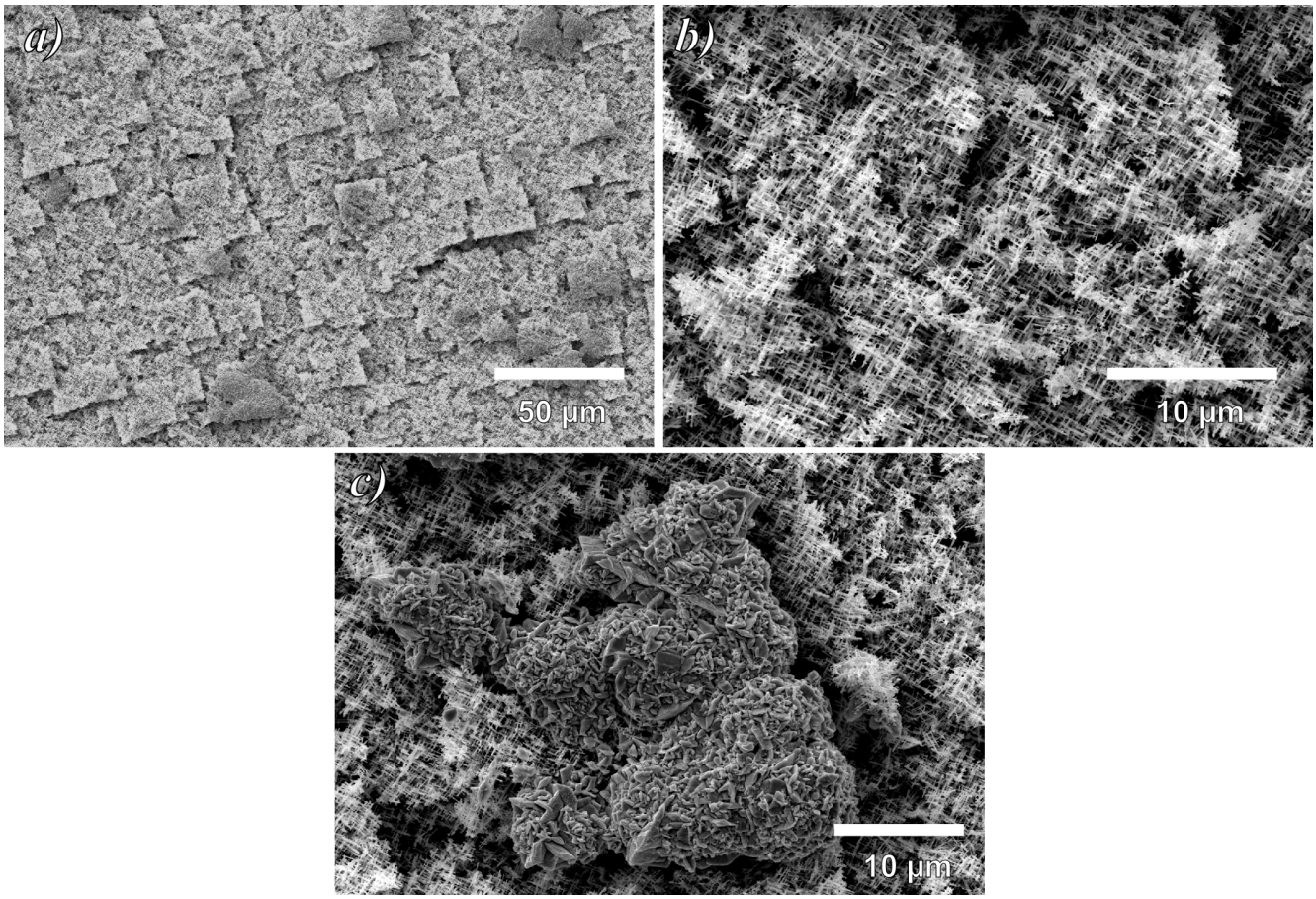

Figure 3.19: SEM images of a bismuth network, grown in a template irradiated with $4 \times 5 \cdot 10^8\ i/cm^2$, having a pore diameter of ∼100 nm, deposited with an on-/off-potential of -220/-170 mV vs. SCE, at room temperature using the bismuth electrolyte containing surfactant.

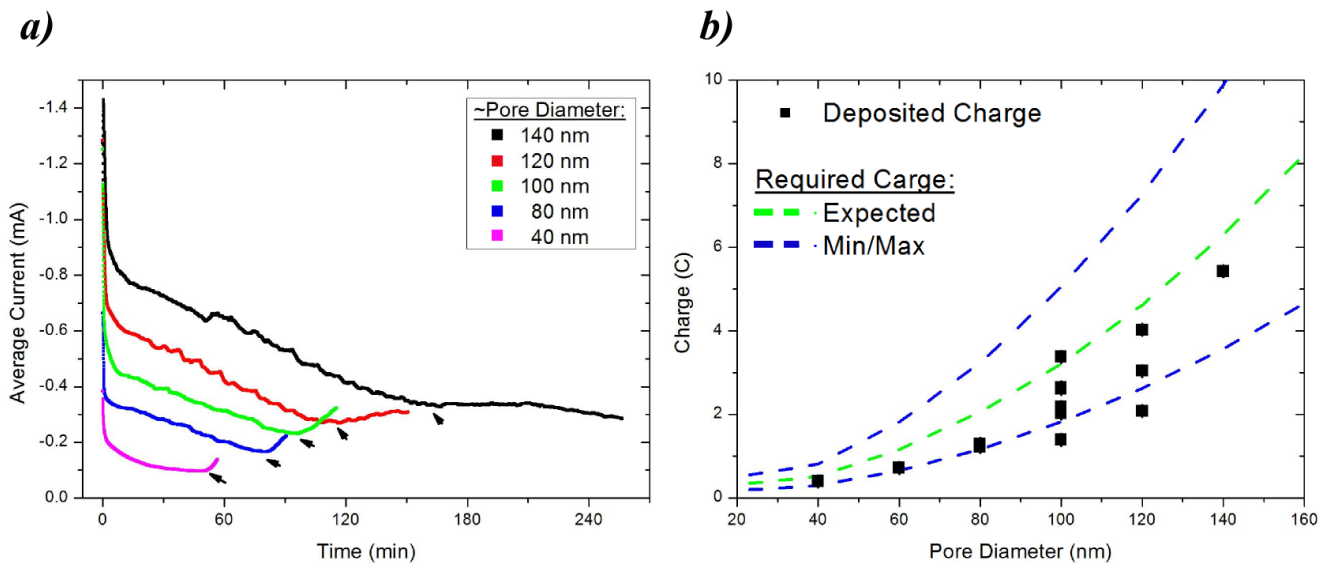

Figure 3.20: a) Bismuth depositions in network templates ($4 \times 5 \cdot 10^8\ i/cm^2$) with different pore diameters and b) deposited charge till cap growth. The dashed green line represents the calculated charge that is needed to fill 100% of the pores. The blue lines represent the calculated maximum and minimum required charge to fill 100% of the pores, considering an error of 30% for the pore density and an error of 10% for the etching rate. The calculated charges were determined by using the Faraday law (eq. 2.2.2).

3.3.3 Influence of Diameter on Growth Process

Figure 3.20a) shows the average current for Bi depositions in network templates irradiated with a fluence of $4 \times 5 \cdot 10^8\ i/cm^2$ with various pore diameters. The depositions were done at an on-/off-potential of -200 mV/-170 mV vs. SCE, at 40°C using a Bi electrolyte containing 1 ‰ of surfactant.

There is a clear trend visible, that the larger the pore diameter, the larger the average current during plating. The current itself shows a steady decline during wire deposition and the time till cap growth increases with increasing pore diameter. The increase in current can be readily understood as the active area increases with increasing pore diameter. The decline in current during wire deposition, is not always observed and samples with constant average current during wire growth have been observed as well when using the same electrodeposition conditions. Whether or not the template preparation can influence the current behavior is still under discussion.

Figure 3.20b) shows the deposited charge till cap growth for all the Bi networks prepared in this work. The dashed green line represents the calculated charge that is needed to fill 100% of the pores. The blue lines represent the calculated maximum and minimum required charge to fill 100% of the pores, considering an error of 30% for the pore density and an error of 10% for the etching rate. The calculated charges were determined by using the Faraday law (eq. 2.2.2).

In general the deposited charge follows the behavior expected for increasing pore diameters. From the previous tests with different deposition potentials it is already known that the Bi networks do not grow as homogeneous as the Sb networks, therefore it is reasonable that the deposited charge is lower than the assumption (green).

3.3.4 Crystallographic Characterization

Figure 3.21 shows the XRD patterns of Bi networks with several diameters embedded in polycarbonate. Below the diffractograms, reference data of Bi (black) and Au (orange) powder samples (JCPDS 5-519 and JCPDS 4-784) is shown, respectively. The diffractograms were normalized to the {01.2} reflexes.

The highest intensities are measured for Au reflections, which become smaller with increasing wire diameter. It was not possible to remove the Au backelectrode in the cases of the Bi networks, as the used Lugols iodine would also severely damage and dissolve the Bi wires. Therefore the Bi reflexes for the {10.4}(∼37.9°), {01.5}(∼44.6°) and {12.2}(∼64.5°) planes might be hidden beneath the Au reflexes. The reflexes that can be attributed to Bi are indicated by a star icon. The reflex at ∼28°, seen in the diffractogram of the network with wire diameters of 80 nm, might indicate additional bismuth-oxide in the sample, but was not observed in the other samples. Overall the measured diffractograms resemble more that of a polycrystalline sample. However, one needs to keep in mind that these only accounts for the structure under 45° to the wire axis. Further measurements to conclude the growth direction parallel to the wire axis need to be carried out in the future.

TEM measurements on pieces of a Bi nanowire network with a wire diameter of ∼ 80 nm are shown in figure 3.22 and 3.23. As in the case of Sb nanowire networks, crystal growth is not necessarily disturbed in an intersection, as can be seen in figure 3.22, where the diffraction pattern does not change before and after an intersection. That this is not always the case is shown in figure 3.23. Here the crystal structure in the different branches differs significantly from another. In this case the planes were not indexed since within the error margins of the plane distance measurements several possible planes can be found. Therefore only the calculated plane distances for the indicated reflexes are given.

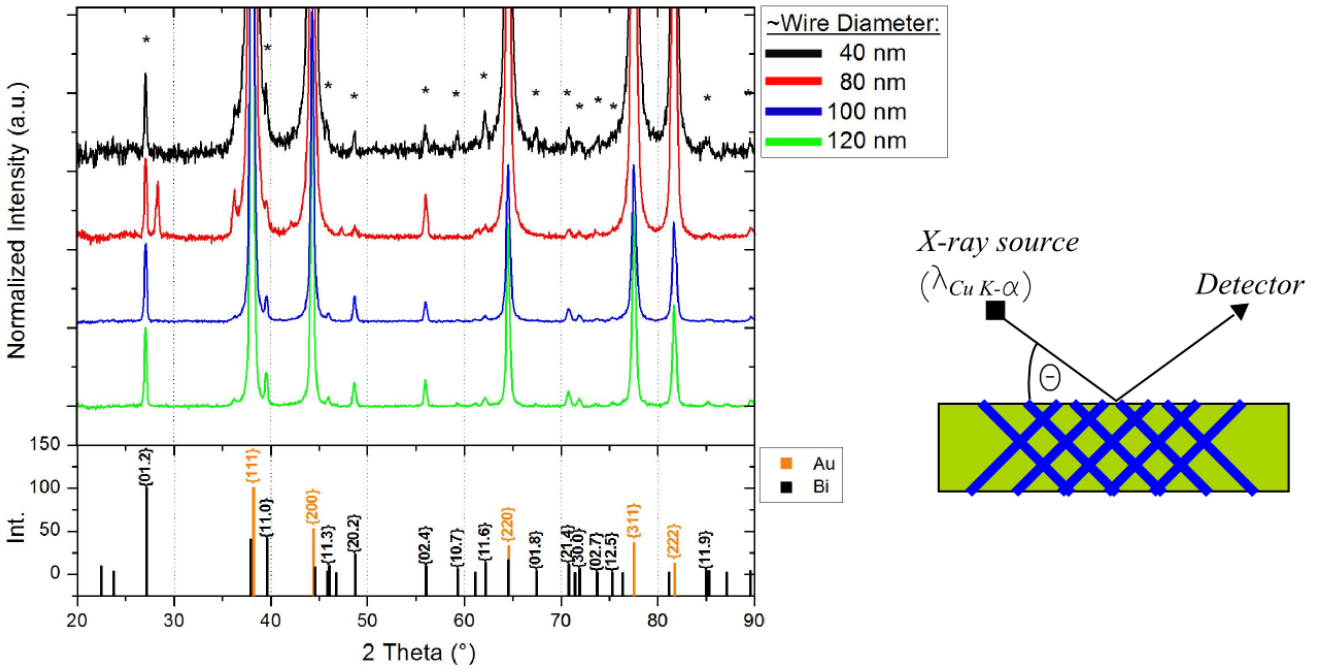

Figure 3.21: XRD diffractograms of Bi networks with different wire diameters, irradiated with $4 \times 5 \cdot 10^8$ i/cm^2, deposited with an on-/off-potential of -200/-170 mV vs SCE, at 40°C, using the bismuth electrolyte containing surfactant. The reflexes that can be attributed to Bi are indicated by a star icon. The bottom row shows the powder reference data taken form JCPDS 5-519.

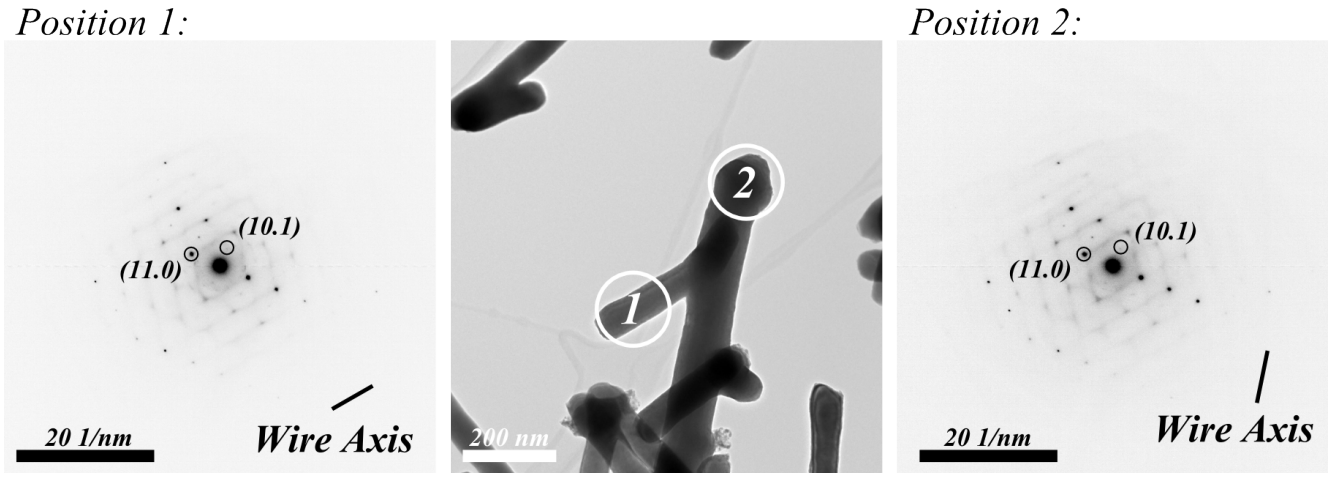

Figure 3.22: TEM image and SAED patterns of a Bi nanowire network showing the same crystal structure before and behind an intersection.

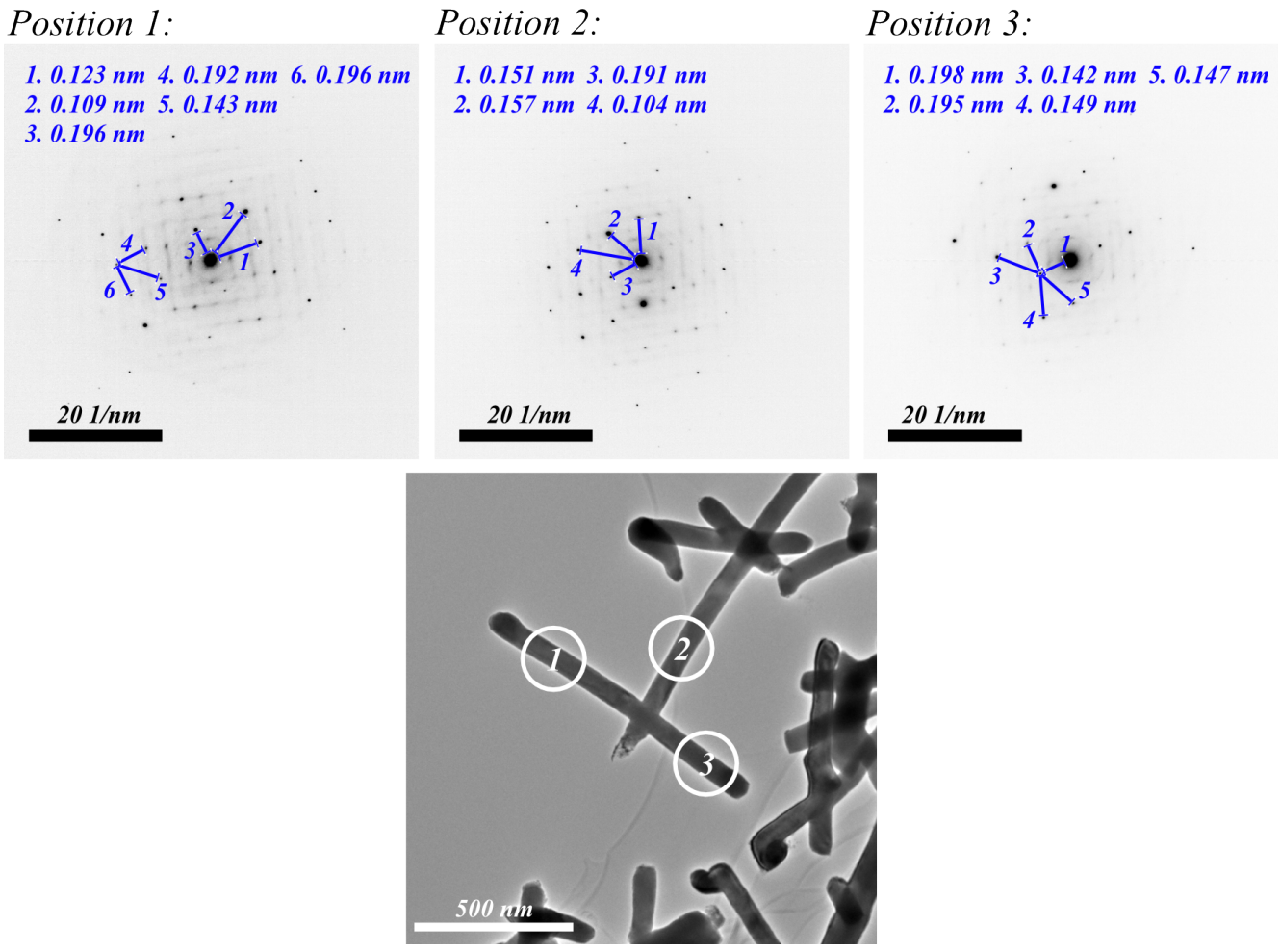

Figure 3.23: TEM image and SAED patterns of a Bi nanowire network showing a different crystal structure before and behind a wire intersection. The calculated interplanar distances are given for various directions, indicated in blue.

3.4 Bismuth Nanowire Arrays

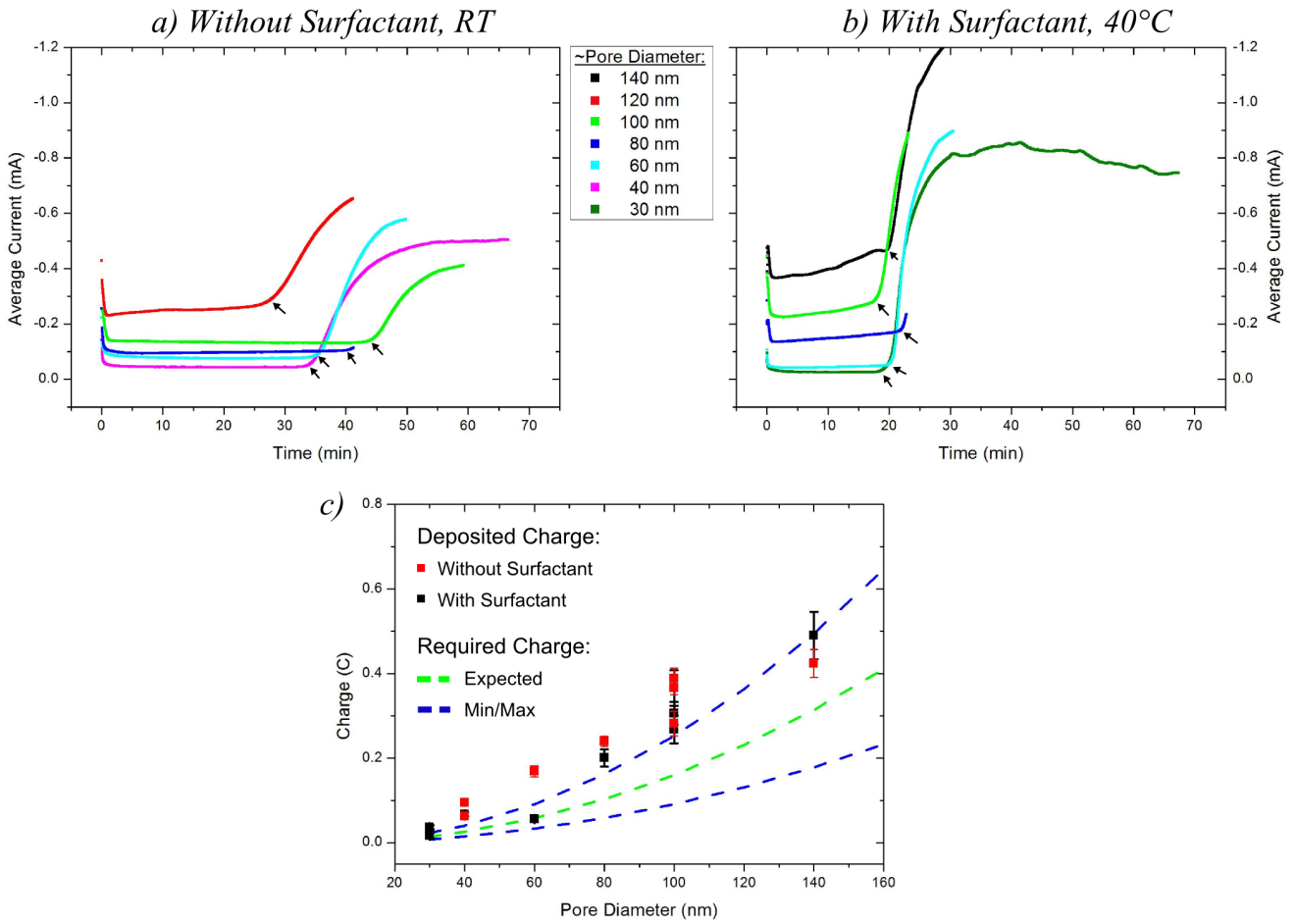

Figure 3.24: Representative average current vs. time curves for Bi nanowire array depositions at an on/off-potential of -200 mV/-170 mV vs. SCE, using on/off-times of 20 ms/100 ms, a) without surfactant at room temperature and b) with surfactant at 40°C. The used templates were irradiated with 10^8 i/cm^2 and had pore diameters ranging between ∼30 nm to 140 nm. The black arrows indicate the onset of cap growth. c) Deposited charge till the onset of cap growth, for Bi array depositions with and without surfactant. The dashed green line represents the calculated charge that is needed to fill 100% of the pores. The blue lines represent the calculated maximum and minimum required charge to fill 100% of the pores, considering an error of 30% for the pore density and an error of 10% for the etching rate. The calculated charges were determined by using the Faraday law (eq. 2.2.2).

3.4.1 Influence of Surfactant on Growth

In order to see how the surfactant influences the growth, Bi nanowire arrays were electrodeposited in templates with 10^8 i/cm^2, using electrolytes with and without surfactant. In both cases Bi was deposited by pulsed potential using an on-/off-potential of -200 mV/-170 mV vs. SCE, and on-/off times of 20 ms/100ms. To allow a better comparison with previous works in the materials research group, the depositions without surfactant were carried out at room temperature.

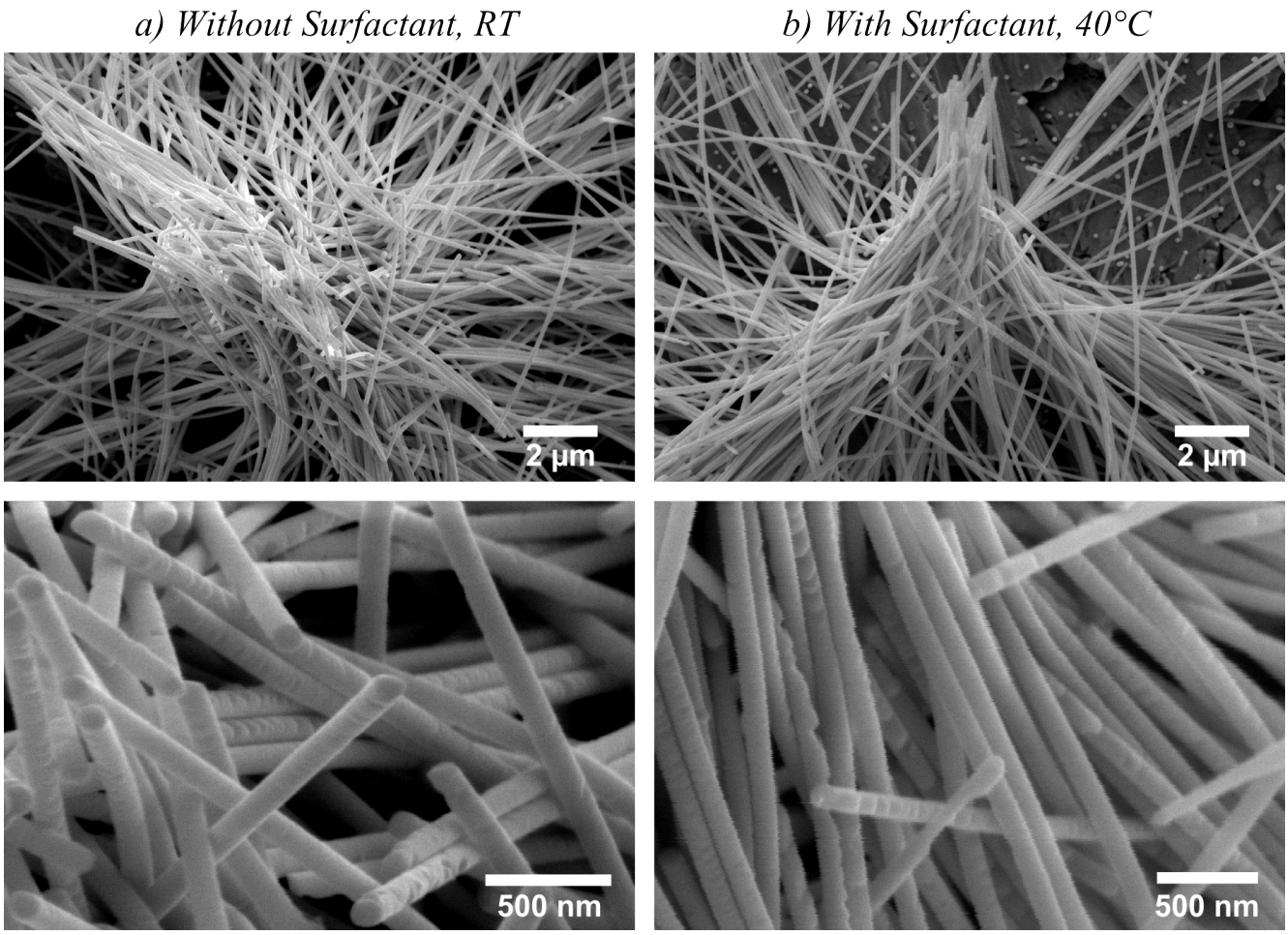

Figure 3.25: SEM images of Bi nanowires, with a wire diameter of 100 nm, grown without and with 1 ‰ surfactant in the electrolyte.

Figure 3.24 shows selected average current vs. time curves for the deposition in templates with 10^8 i/cm^2 and various pore diameters, using a) electrolytes without and b) with surfactant. The depositions without surfactant require longer times till cap growth. It seems that in the case of Bi the temperature has a higher influence on the growth than in the case of Sb, as can also be seen in the higher current during deposition. However, when comparing the charge till cap growth, fig. 3.24c), both procedures lead to the equal amount of deposited charges at the time of cap growth. Surprising here is the fact that the deposited charge surpasses even the highest expected value required for filling, even though similar templates as in the case of Sb depositions have been used. One possibility explanation would be that additional side reactions occur during electroplating, which decrease the plating efficiency.

The morphology of Bi nanowires was investigated by SEM. Figure 3.25 shows Bi nanowires with a wire diameter of ~100 nm, prepared using an electrolyte a) without and b) with 1 ‰ of surfactant. The wires homogeneously fill the pores all around the active area of the template, as expected from the deposited charge. On closer inspection, most of the wires prepared with and without surfactant exhibit a rough surface. Previously, in the case of Bi_2Te_3 nanowires, it was reported that the surface roughness depended on the applied voltage during potentiostatic deposition [12]. Smooth Bi_2Te_3 wires were obtained at small overpotentials, whereas higher overpotentials lead to rough surfaces. The images of the nanowires do not reveal differences in the wire growth with and without surfactant.

Figure 3.26 shows the diffractograms of Bi nanowire arrays still embedded in the polycarbonate template. One sample was grown at room temperature with an electrolyte without surfactant, the other one was grown at 40°C with an electrolyte containing 1 ‰ surfactant. In this case the Au backelectrode was removed successfully without damaging the deposited Bi wires.

The diffractograms reveal a {11.0} texture of the grown Bi nanowires. As in the case of Sb, the surfactant inside the electrolyte seems to decrease the texture of the wires, while still leaving a preferred orientation. Cassinelli et. al. [59] also prepared Bi nanowires via pulsed electroplating and observed a {11.0} texture in 18 nm and 79 nm diameter Bi nanowires. However not as strong as in the here presented cases.

The crystallinity of 80 nm diameter Bi wires, prepared without and with surfactant, was studied by TEM. Selected images and SAED patterns of the samples are shown in figure 3.27. In both cases, single crystalline sections of several μm length were found in the Bi wires. This means that also in the case of the Bi nanowires the pulsed potential does not lead to small crystals. The images of the wires also show contrast lines attributed to bending effects. HRTEM images usually revealed no grain boundaries along these imaged sections, as was also observed on the Sb nanowires. Compared to the Sb nanowires more defects were found in the wires, which is in agreement with the higher growth rates. However, there was no obvious difference between the two kinds of Bi wires.

The HRTEM images of the Bi wires showed a $\sim$ 5 nm thick amorphous layer of carbon at their surface, indicating that polycarbonate rests were still attached to the wire surface. Also wires with different amounts of surface roughness were found. Not all wires showed these roughness and even smooth wires

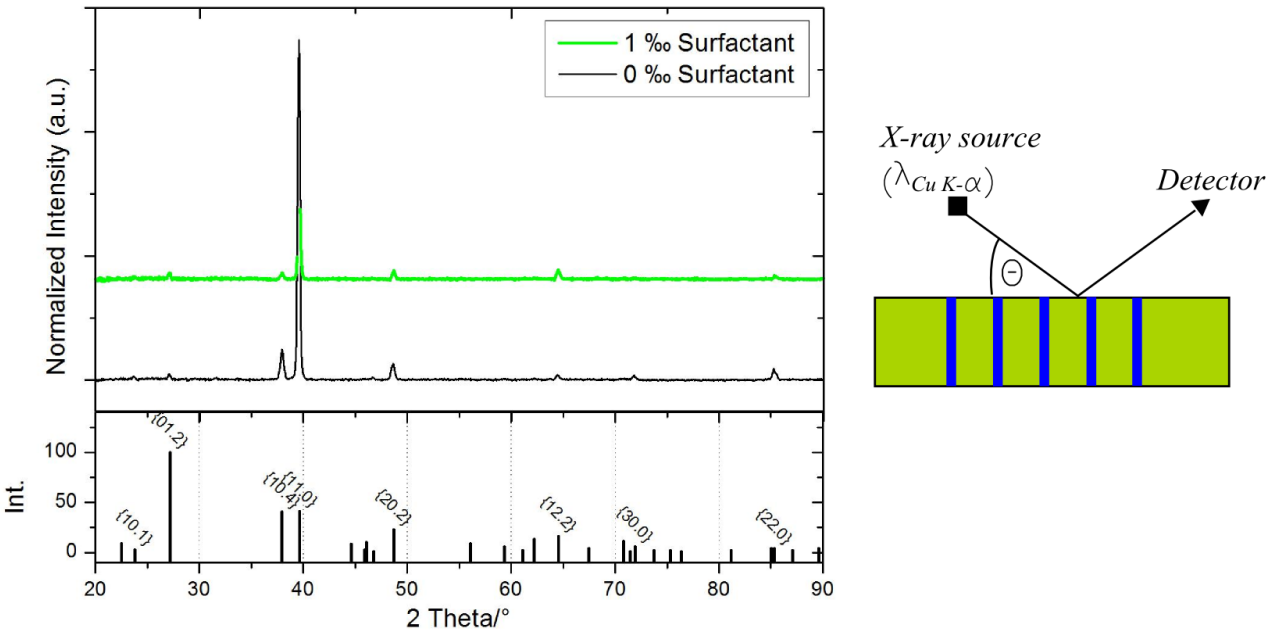

Figure 3.26: XRD data of Bi wires (diameter ~100 nm, 10^8 i/cm^2), grown with 1 ‰ surfactant at 40°C and without surfactant at room temperature. Electrodeposition of both samples was carried out at an on/off-potential of -200 mV/-170 mV vs. SCE, using on/off-times of 20 ms/100 ms. The data is normalized to the {01.2} reflex. The bottom row shows the powder reference data taken form JCPDS 5-519. The sketch on the right side shows the orientation of the sample during XRD measurement.

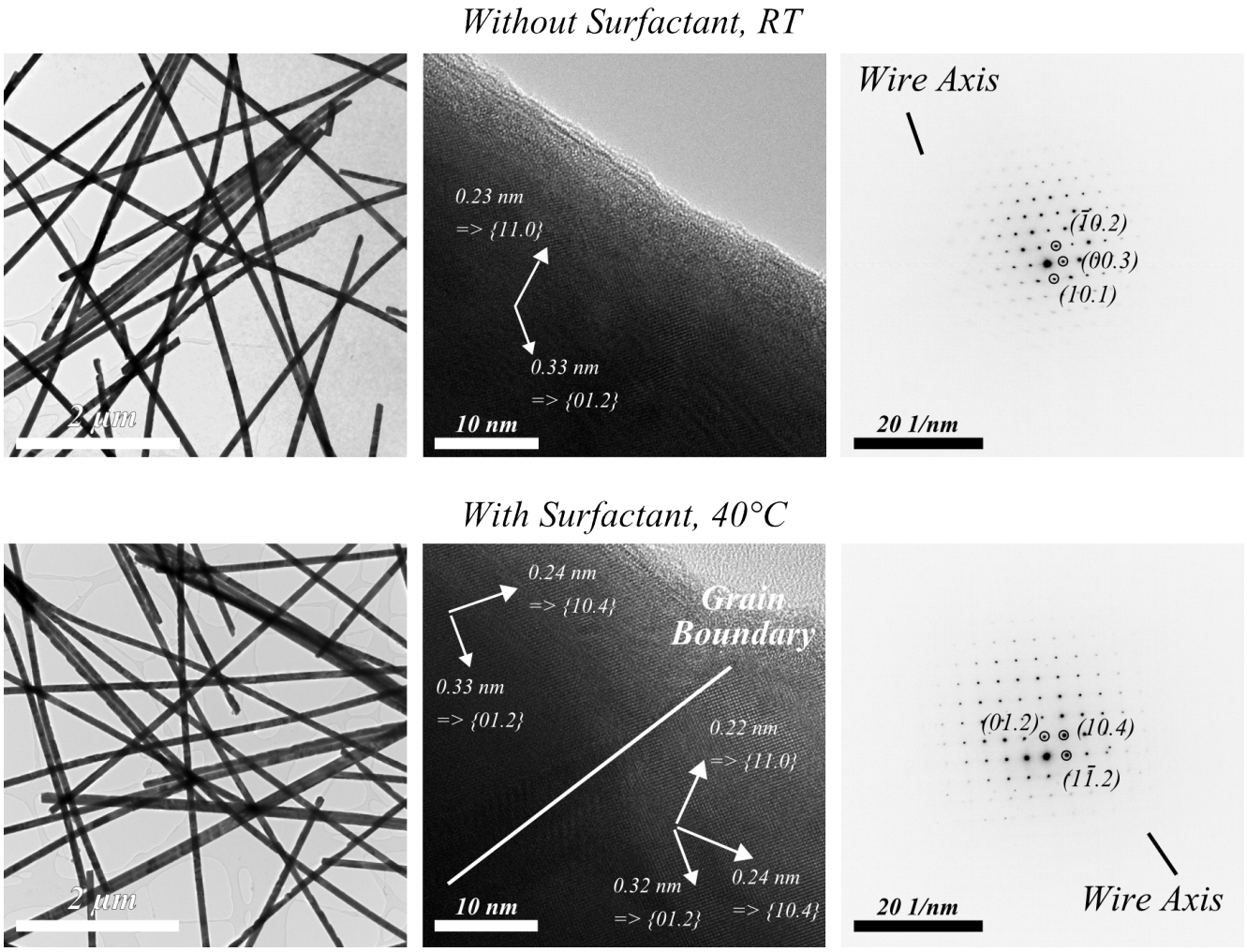

Figure 3.27: Selected TEM images of Bi wires, with a diameter of 80 nm, grown without surfactant at room temperature (top) and with 1 ‰ surfactant at 40°C (bottom). Electrodeposition of both samples was carried out at an on/off-potential of -200 mV/-170 mV vs. SCE, using on/off-times of 20 ms/100 ms.

were found. The growth direction along the wire axis, determined from the SAED patterns, matches well with the directions observed using the XRD data. The found planes perpendicular to the wire axis were {10.1}, {01.2}, {10.4} and {11.0}.

To conclude in the case of the bismuth wires the surfactant causes a decrease in texture of the grown wires. Otherwise no obvious differences between the grown Bi wires were found.

3.5 Bismuth & Antimony Alloys

3.5.1 $Bi_{1-x}Sb_x$ Nanowire Networks

The electrolyte for the electrodeposition of $Bi_{1-x}Sb_x$ was prepared with the same basic components as the electrolytes for pure Bi and pure Sb. In order to vary the compositions, different amounts of Bi-chloride and Sb-chloride were used, adding up to a total amount of 0.1 mol/l. As was shown by Vereecken [103],

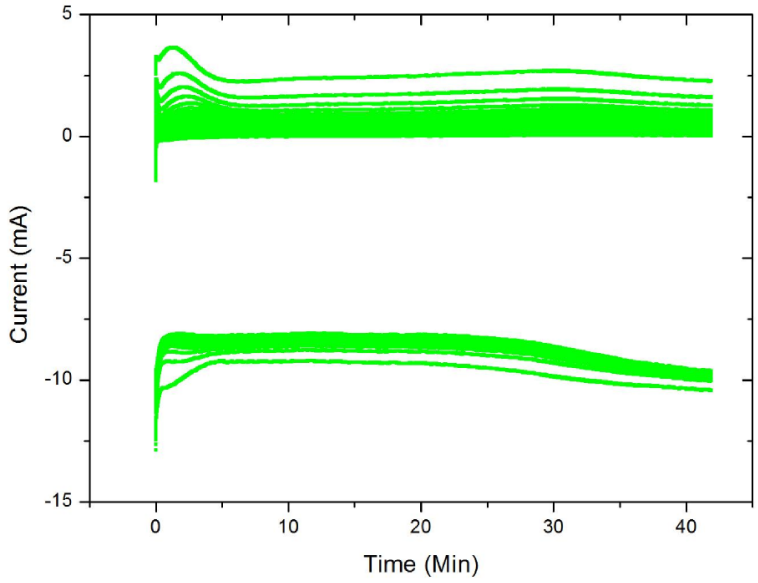

Figure 3.28: Current vs. time plot of a $Bi_{1-x}Sb_x$ electrodeposition, using an on-/off-potential of -240 mV/-160 mV vs. SCE with an electrolyte containing 0.085 mol/l Bi(III)Cl and 1 ‰ of surfactant, at 40°C. The used template had been irradiated with $4 \times 5 \cdot 10^8\ i/cm^2$ and had a pore diameter of $\sim$ 100 nm.

the reduction potentials for Sb and Bi are very close in this electrolyte, allowing the co-deposition of both materials during electrodeposition. According to Rabin et al. [22], p-type $Bi_{1-x}Sb_x$ wires with x= 0.13 and a diameter of 60-20 nm should show the highest figure of merit (zT ∼1). Therefore, a similar composition was sought for the nanowire networks.

3.5.2 Influence of Deposition Voltage

Series of $Bi_{1-x}Sb_x$ nanowire networks were electrodeposited applying a pulsed potential with various on/off-potentials and on/off-times of 20 ms and 100 ms, respectively. The used templates were irradiated with $4 \times 5 \cdot 10^8$ i/cm^2 and had a pore diameter of $\sim$ 100 nm. The used electrolyte contained 0.085 mol/l Bi(III)Cl, in order to fabricate networks close to the optimum composition [58, 59], as well as 1 ‰ of Dowfax 2a1 surfactant.

Figure 3.28 exemplary shows the current vs. time plot of a $Bi_{1-x}Sb_x$ deposition. The deposition was done using an on-/off-potential of -240 mV/-160 mV vs. SCE at 40°C. The observed behavior closely resembles the pure bismuth depositions. The onset of cap growth is again indicated by a change to more negative values in both on- and off-current. Since this is barely visible, it is difficult to stop the depositions at a certain time after cap growth.

Figure fig. 3.29 shows the average current vs. time plots for various on-potentials at off-potentials of a) -160 mV and b) -170 mV. As expected, a higher on-potential leads to an increase in the average current during deposition, while a higher off-potential leads to a decrease in the average current

Figure 3.30 shows SEM images of the $Bi_{1-x}Sb_x$ networks prepared within the series. As was already observed in the case of pure Bi, the network seems to consist of rhombus shaped structures that are nested inside each other. The tips of the rhombuses are aligned along the irradiation directions.

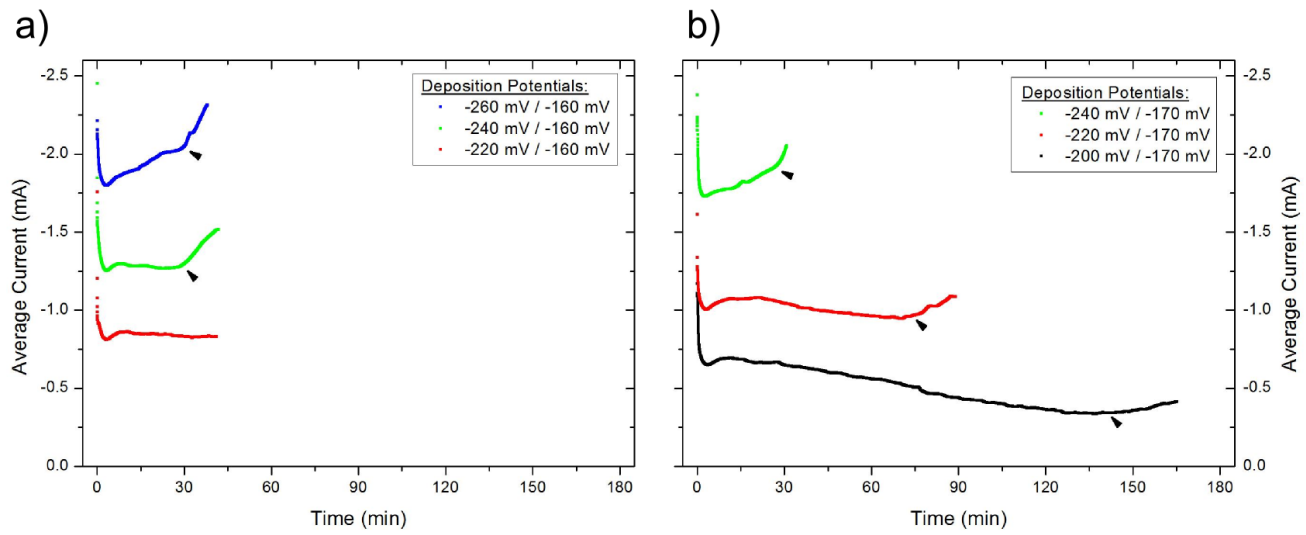

Figure 3.29: Average current vs. time curves for the deposition of $Bi_{1-x}Sb_x$ nanowire networks, using different on-potentials, for an off-potential of a) -160 mV and b) -170 mV vs. SCE. The used templates were irradiated with $4 \times 5 \cdot 10^8$ i/cm^2 and had a pore diameter of $\sim$ 100 nm.

Figure 3.30a)-c) show the influence of an increasing on-potential on the morphology at a fixed off-potential of -160 mV vs. SCE. At an on-potential of -220 mV the visible structures seem more roundish and the overall network is slightly unstable without the supporting polycarbonate. With increasing on-potential the rhombuses develop more defined edges and grow in size, which has a positive effect on the stability of the overall structure.

An increase in the wire density also leads to a stable network at low on-potentials. For networks prepared in templates that were irradiated with $4 \times 1 \cdot 10^9$ i/cm^2, the growth appears homogeneous and the rhombus shaped structures almost vanish. Otherwise the observed changes with increasing on-potential are similar to the previous case.

An improved stability of the overall network can also be achieved by increasing the off-potential to -170 mV. Figure 3.30d) shows a network grown at an on/off-potential of -220 mV/-170 mV. Here the network is stable, whereas for the network grown at the same on-potential and at an off-potential of -160 mV broken pieces were found. The increased off-potential seems to lead to a more homogeneous growth in height of the network, as not so many trenches are visible, which results in the increased stability.

The composition of the grown networks was investigated using EDX. The atomic percentage (At%) of Bi in the wire as a function of the used deposition potentials is shown in figure 3.31. No obvious correlation between the two parameters is observed, fitting well to previous observations on $Bi_{1-x}Sb_x$ nanowire arrays, that the potential only has a small influence on the wire composition [58, 59]. For the same deposition conditions differences of up to 10 At% were measured for the Bi content, which is partially due to error of the EDX measurements. As the composition can have a large influence on the thermoelectric properties of $Bi_{1-x}Sb_x$ alloys, more precise measurements would be required.

One additional method to determine the Sb content would be to measure the shift of reflexes in XRD in relation to the position in pure Bi. Since the lattice constant in the case of $Bi_{1-x}Sb_x$ depends almost linearly on the Sb content, an increase in Sb composition leads to a shift of the reflexes to larger angles [34].

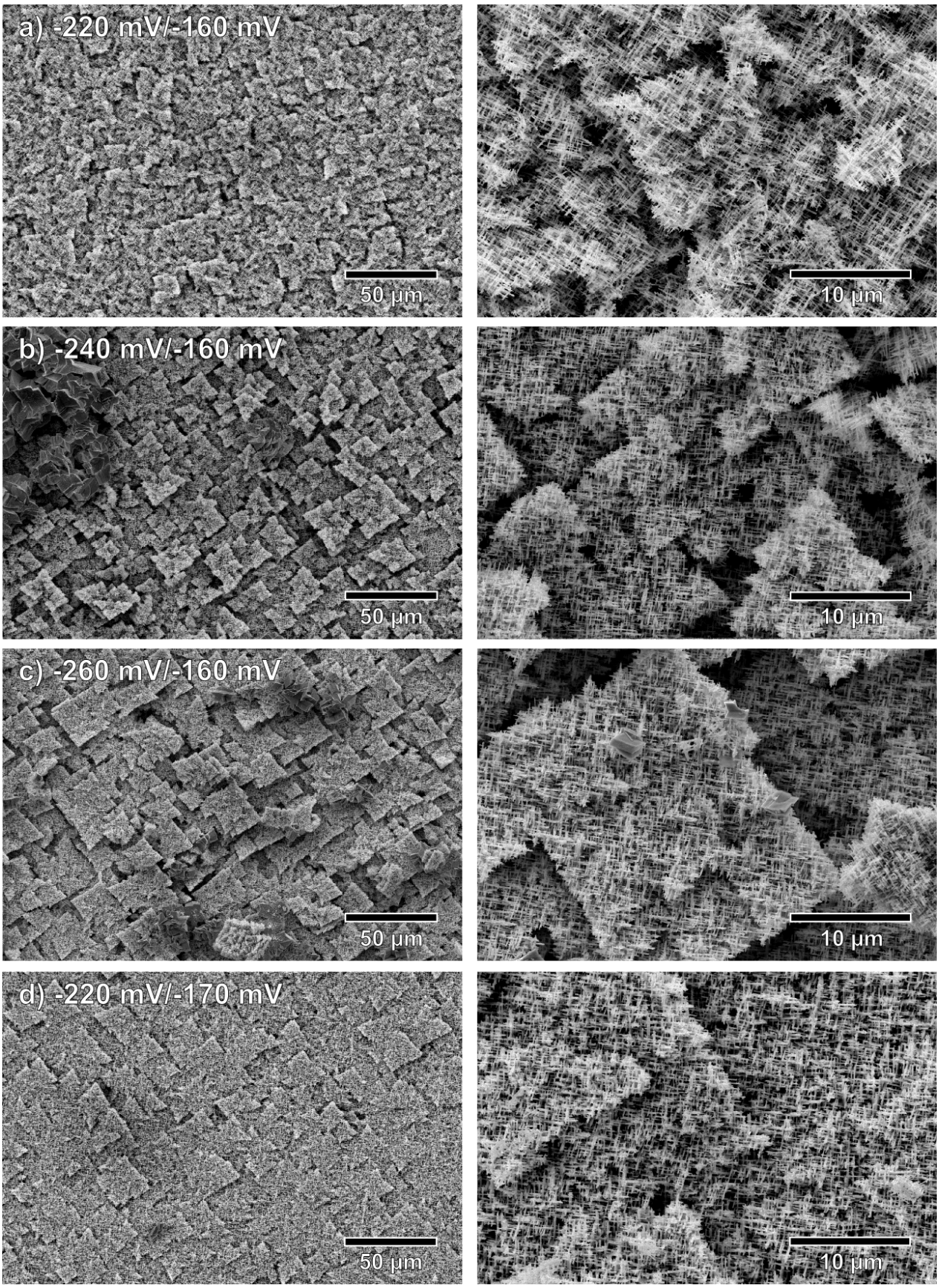

Figure 3.30: SEM images of $Bi_{1-x}Sb_x$ networks, grown in templates irradiated with $4 \times 5 \cdot 10^8$ i/cm^2 and having a pore diameter of ∼100 nm. Electrodeposition was done at the given on/off-potentials at 40°C, using an electrolyte containing 0.085 mol/l Bi(III)Cl and 1 ‰ of surfactant.

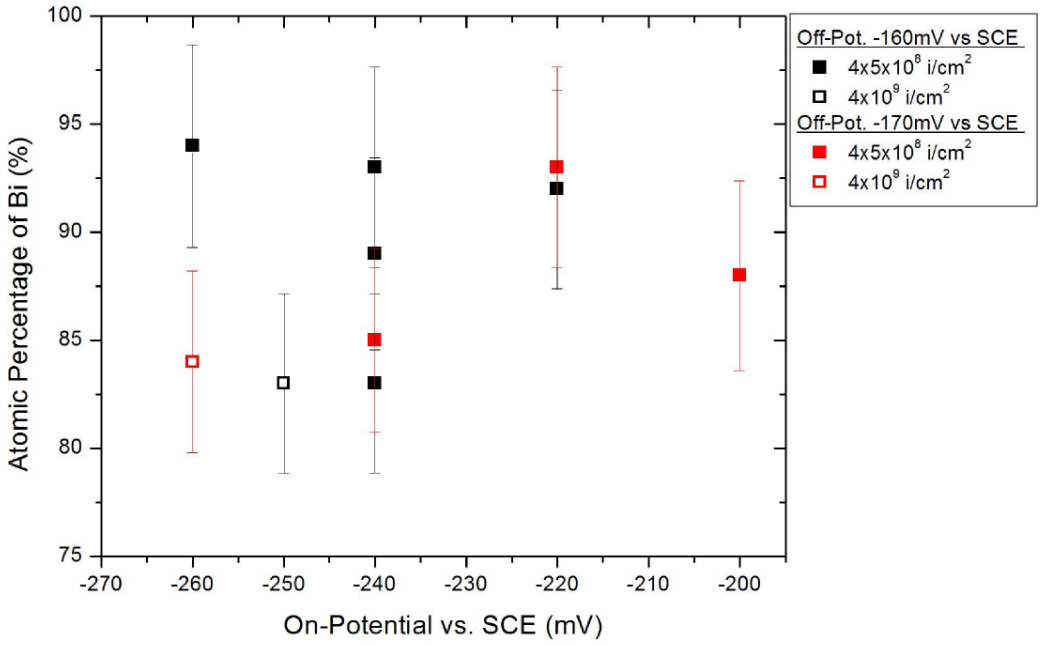

Figure 3.31: Atomic percentage of Bi in $Bi_{1-x}Sb_x$ nanowire networks as a function of the chosen potentials for electrodeposition. The networks were grown in templates that had a pore diameter of ∼100 nm and were irradiated with $4 \times 5 \cdot 10^8$ i/cm^2. The data was deduced from EDX measurements and an error of 5% was assumed.

Also the composition of the electrolyte seems to affect the shapes of the structure. Figure 3.32 shows the morphology of networks grown with an electrolyte containing 0.080 mol/l Bi and one with 0.075 mol/l Bi, using an on-/off-potential of -230 mV/-150 mV. In the case of the network grown with 0.025 mol/l Sb content (figure 3.32a) the growth seems dendritic, whereas with an Sb content content of 0.020 mol/l (figure 3.32b) the globular structures emerge.

Figure 3.33 shows the dependence of the Bi content in the nanowire network in dependence of the Bi content in the used electrolyte. On the right side of each data point the used on-/off-potentials for the electrodeposition are given. In previous studies on parallel nanowire arrays, it was observed that the electrolyte composition has a much higher influence on the wire composition [58, 59]. Therefore in order to achieve a certain composition of the nanowires one would chose an electrolyte with a corresponding ion concentration and fine tune the composition via the used potential. For nanowire networks a similar trend is visible, but can not finally be confirmed yet.

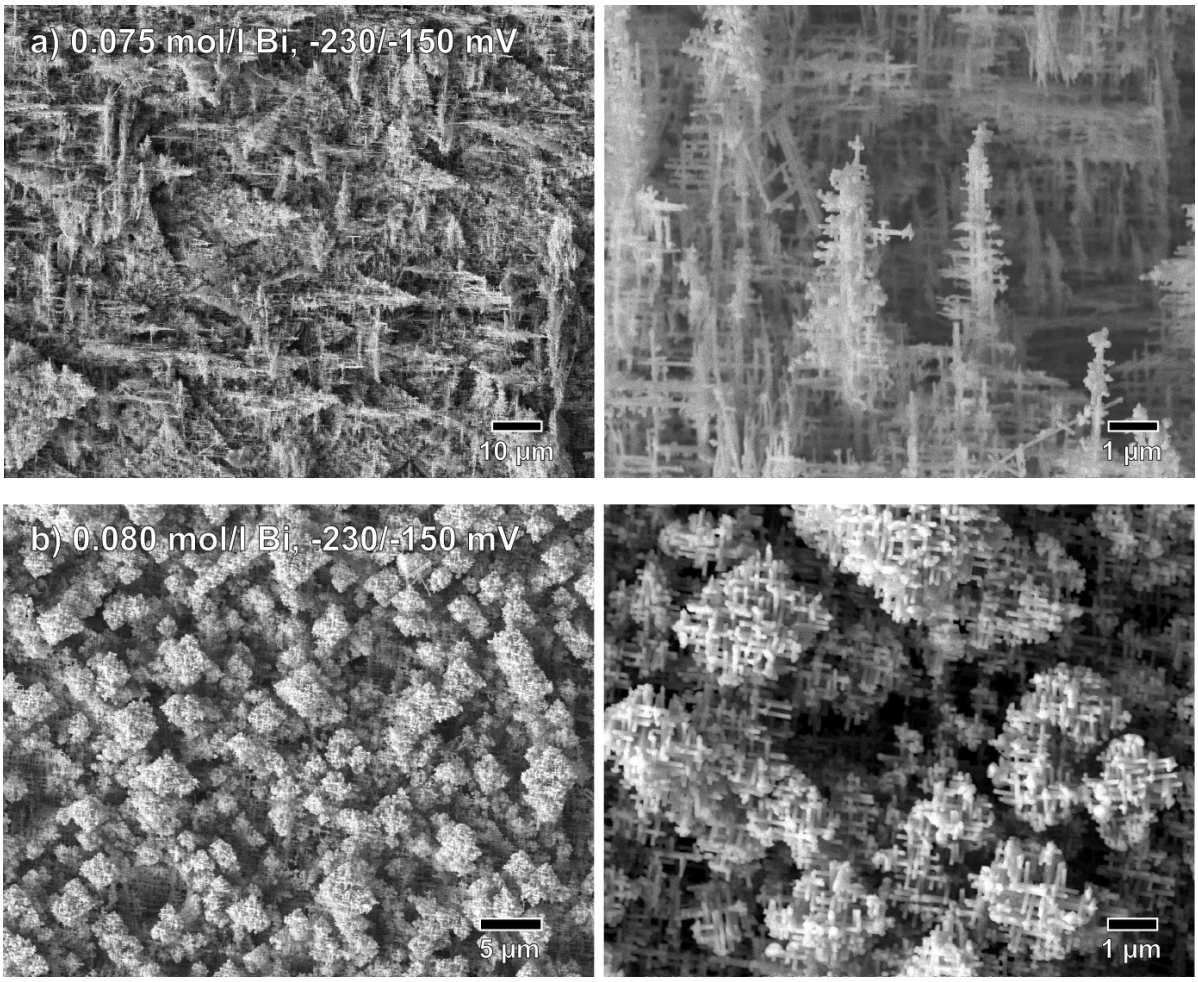

Figure 3.32: Morphology of $Bi_{1-x}Sb_x$ networks $4 \times 1 \cdot 10^9$ i/cm^2 with different electrolyte composition.

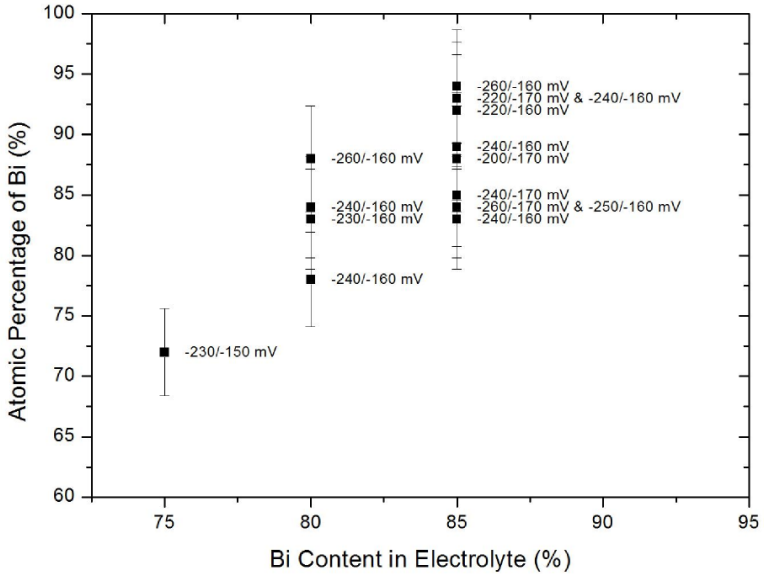

Figure 3.33: Atomic percentage of Bi in $Bi_{1-x}Sb_x$ nanowire networks as a function of the composition of the used electrolyte. On the right side of each data point the used on-/off-potentials for the electrodeposition are given.

3.6 Summary

Nanowire arrays and nanowire networks of Sb, Bi and $Bi_{1-x}Sb_x$ were grown via pulsed electrodeposition in the pores of polycarbonate ion track-etched membranes. The addition of Dowfax 2a1 surfactant to the used electrolytes enabled the reproducible and homogeneous electrodeposition of nanowire networks of the various materials. Whereas the surfactant is required for the electrodeposition of nanowire networks, no improvement of the deposition process was found for nanowire arrays. The best pulsed electrodeposition conditions for growth of the networks, are summarized in table 3.1.

Table 3.1: Best electrodeposition conditions for growth at 40°C for Sb, Bi and $Bi_{1-x}Sb_x$ nanowire networks, when using a pulse potential with on-/off-times of 20 ms and 100 ms, respectively.

Material	On-potential [mV vs. SCE]	Off-potential [mV vs. SCE]	Temperature [°C]
Sb	-260	-130	40
Bi	-200	-170	20
$Bi_{1-x}Sb_x$	-220	-170	40

The Sb nanowires prepared with and without surfactant exhibited a smooth surface. They were made up of single crystalline sections of at least several μm length and showed a strong {01.2} texture, that decreased when surfactant was used.

Opposite to that, Bi nanowires prepared without and with surfactant both had a rough surface, but also showed single crystalline sections of at least several μm length. Diffractograms on the Bi arrays showed a strong {11.0} texture of both kinds of wires, that also decreased when surfactant was added to the electrolyte.

The wires sections of Sb networks showed a smooth surface, like Sb nanowires grown in arrays. Experiments on Sb nanowire arrays, grown in pores that were tilted towards the foil normal, indicate that the crystal growth orientation along the wire axis is equal in both cases. TEM measurements on pieces of Sb nanowire networks showed that the intersections do not necessarily interfere with the crystal growth. Therefore, by keeping the crystal orientation after a junction, the crystal orientation in relation to the wire axis of the two wires is tilted by the angle between them.

The surface of the wire sections of Bi and $Bi_{1-x}Sb_x$ (5 At% $\leq x \leq$ 20 At%) networks appeared rough, similar to what was observed on the Bi nanowire arrays. The growth at the applied conditions usually lead to an irregular growth front of the networks, that was made up of rhombus shaped structures, whose corners were aligned along the irradiation directions.

4 Thermoelectricity

"We do not know a truth without knowing its cause."
-Aristotle

The following chapter gives a short introduction into the theory of thermoelectrics. Further introduction on the topics can be found in references like [117, 118, 119], where also most of the information presented was taken from. At first the basic thermoelectric effects as well as their application in devices will be explained. The description of the efficiency of these devices will then lead to the thermoelectric transport properties in order to understand the interplay of transport properties and the limitations in material design. Following this, ways to improve the thermoelectric figure of merit will be discussed with special emphasis on possible advantages and drawbacks of size reduction of materials. The chapter finishes with a summary of the thermoelectric properties of $Bi_{1-x}Sb_x$ materials.

4.1 Thermoelectric Effects

The first thermoelectric effect, the so called Seebeck effect, was first observed by T.J. Seebeck in 1821 [120]. The effect describes the appearance of a voltage, also called thermo voltage, in a material along which a temperature gradient is applied. For small temperature gradients, the relation between the generated voltage V_{th} and temperature difference ΔT can be described by:

$$V_{th} = S_{ab} \cdot \Delta T, \tag{4.1}$$

where $S_{ab} = S_b - S_a$ is the differential Seebeck coefficient and $\Delta T = T_H - T_C$, with T_H and T_C being the temperature of the hot and cold side, respectively. The differential Seebeck coefficient needs to be used because when the voltage is measured a second material needs to be introduced into the system. This material then also "sees" the temperature difference and generates a thermo voltage ($S_b \Delta T$), so that the voltage measured is generated in fact by both materials. Figure 4.1 illustrates this behavior. By using a superconducting material as second material it is however possible to define an absolute scale for the thermoelectric properties of materials [121]. In the cases where the absolute properties of a material are referred to, the index $_{ab}$ will be replaced by the symbol of the material.

In order to understand the effect on a more microscopic level, the difference between the energy distribution (fermi distribution) of the charge carriers at the hot and cold end is considered. At the hot side the charge carriers have a much higher energy, leading to higher mean velocities. The higher velocity then leads to a net flow of charge from the hot to the cold side, yielding a potential difference. The sign of the generated voltage depends on the majority charge carriers. The Seebeck coefficient is positive for *p*- and negative for *n*-type materials, allowing the quick classification of semiconductors by measuring the Seebeck coefficient. In cases where both electrons and holes contribute to conduction, the total Seebeck coefficient can be expressed using the partial Seebeck coefficients of electrons S_n and holes S_p as well as their respective conductivities σ_n and σ_p [118, 31].

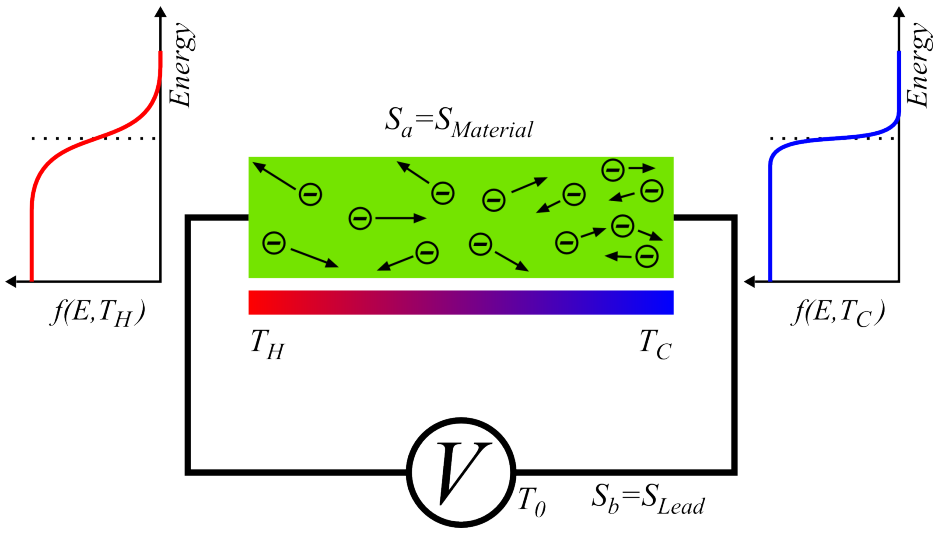

Figure 4.1: Due to the different temperatures at both ends of the material the Fermi distribution of the charge carriers, f(E,T), at both ends differs from one another. The charge carriers at the hot end have higher mean velocities, which leads to a net flow of charge from the hot to the cold side, which leads to a potential difference between the ends.

$$S_{total} = \frac{\sigma_n S_n + \sigma_p S_p}{\sigma_n + \sigma_p} \tag{4.2}$$

In 1834 Peltier discovered, that if an electrical current is driven through the junction of two different conductors heat may be transferred to, or removed from the junction, essentially building up a temperature gradient along the materials [122]. The direction of the gradient depends on the direction of the electrical current applied in the material. The relation between the applied current I and the transported thermal energy Q is given by eq. 4.3, where Π_{ab} is the differential Peltier coefficient, which like the Seebeck coefficient depends on the materials combined.

$$Q = \Pi_{ab} \cdot I \tag{4.3}$$

The origin of the Peltier effect lies in the different energy levels of charge carriers inside the connected materials. As example, figure 4.2 shows the situation for an electron that is driven from a metal contact A trough a n-type material into a metal contact B. However, in order to allow conduction the electrons need to be lifted from the lower energy states, that they occupy in the metal contact, into the conduction band of the n-type material, which lies at a higher energy level. The energy for the transfer is taken from the thermal energy in contact A, which therefore cools down. When the electrons pass from the n-type material to a metal contact B they shed the surplus energy, which is transferred to the atomic lattice and thereby heats up contact B. This way it also becomes obvious why the gradient depends on the direction of the electrical current. It should also be mentioned that the same process occurs in a p-type material, but in this case holes would need to be considered instead of electrons.

By using thermodynamics W. Thomson (later Lord Kelvin) could prove that the Seebeck and Peltier effect have the same physical basis [123]. The correlation between the Seebeck and Peltier effect is called the

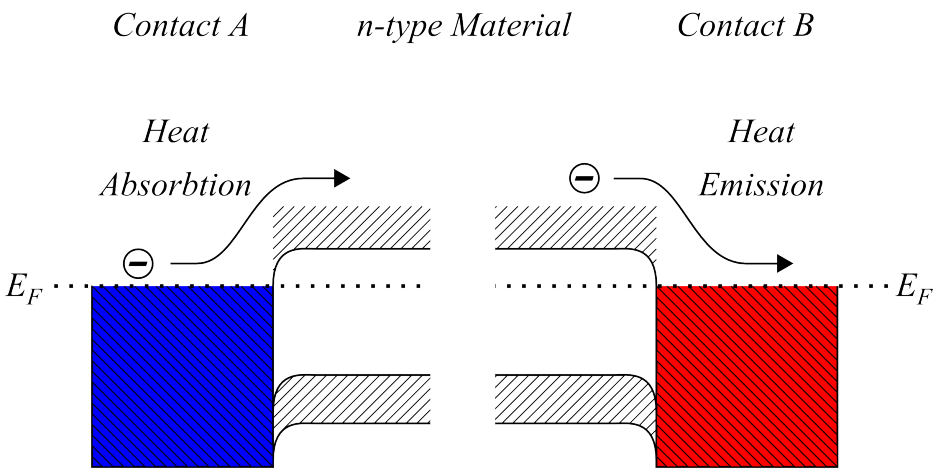

Figure 4.2: When electrons pass from metal contact A to the n-type material they need to acquire a higher energy state in order to pass. This energy is taken from the thermal energy of contact A, leading to cooling. When the electrons pass from the n-type leg to contact B, this energy is no longer needed and emitted as thermal energy, which heats up contact B. The same occurs in a p-type leg, but in this case holes would need to be considered instead of electrons.

first Kelvin relation, which reads:

$$\Pi_{ab} = S_{ab} \cdot T \text{ or } \Pi_a = S_a \cdot T. \tag{4.4}$$

This relationship then also allows to give absolute values for the Peltier coefficient of individual materials. Furthermore W. Thomson showed that there is a third thermoelectric effect, which occurs when a current is driven through a material, along the direction of a temperature gradient [123]. The so called Thomson effect describes the generation or absorption of heat, while the charge carriers travel through the temperature gradient. This so called second Kelvin relation is described by:

$$T\frac{dS_{ab}}{dT} = \chi_a - \chi_b, \tag{4.5}$$

where χ_a and χ_b are the so called Thomson coefficients.

4.2 Thermoelectric Devices

To harness the thermoelectric effects for application, usually a n- and a p-type material are connected electrically in series and thermally in parallel, so that their thermoelectric effects add up constructive. This arrangement is called a thermocouple and is shown in figure 4.3 in its different modes of operation. Since the output of a single thermocouple is still rather small, usually several thermocouples are connected to one another in order to make up the final devices. The electrical and thermal transport in the n- and p-type leg, when the temperature gradient lies in x direction, can be described by:

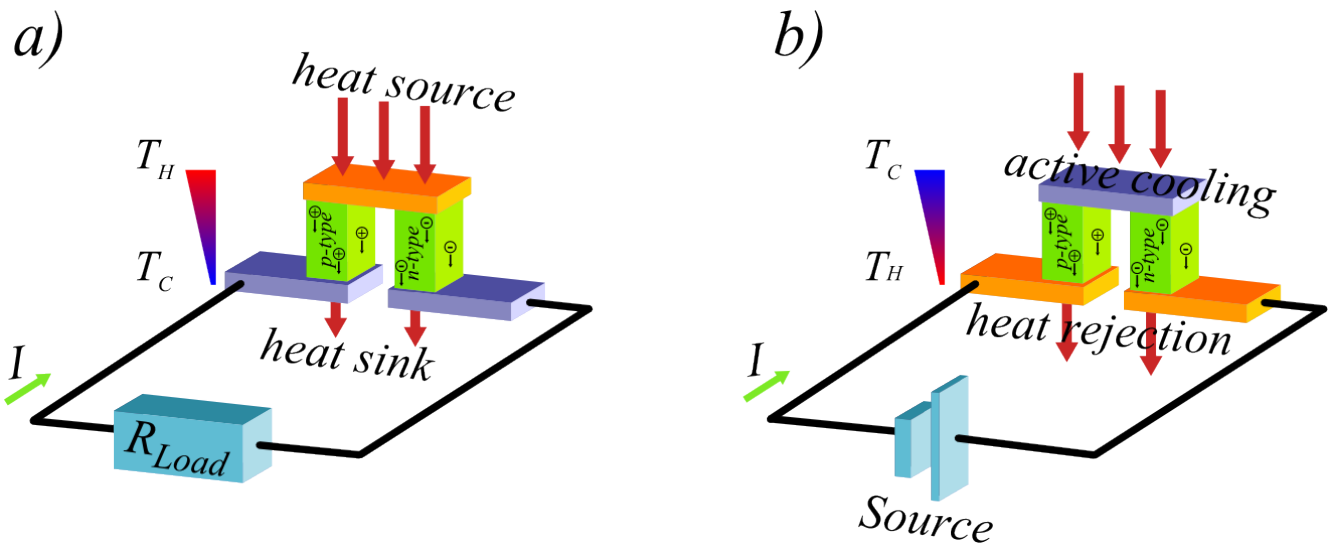

Figure 4.3: Individual thermocouple in operation. a) When a temperature gradient is applied a voltage is generated by the Seebeck effect. b) When a current is driven through the device, one side heats up, while the other one is cooled down due to the Peltier effect.

$$j_{n,p} = \sigma_{n,p}\left(\frac{\Delta V}{\Delta x} - S_{n,p}\frac{\Delta T}{\Delta x}\right) \text{ and } \Phi_{n,p} = S_{n,p}\,T\,j_{n,p} - \lambda_{n,p}\frac{\Delta T}{\Delta x}. \tag{4.6}$$

j is the current density $\left[\frac{A}{m^2}\right]$ that is generated by an external electrical field $\frac{\Delta V}{\Delta x}$ and the field generated by the Seebeck effect in the material with an electrical conductivity σ. Φ is the heat flux density $\left[\frac{W}{m^2}\right]$ due to the Peltier effect ($= STj$) and the thermal conductivity of the material λ.

Due to their versatility, thermoelectric devices are attractive for a large variety of applications [124, 17, 125, 117]. The Peltier effect enables them to be used in portable cooling devices, microcoolers for electronics [126, 127] and even personal climate systems in cars [128]. The Seebeck effect enables their use as sensors [129, 28, 130] and power generators, for example as alternative to photovoltaic cells or in combination with them [131, 132]. Power generation particularly plays an important role in space applications, where thermoelectric devices are used in "radioisotope thermoelectric generators" [133], which are used to power deep space probes that can not be powered by solar panels due to the large distance to the sun [134]. Furthermore the use of thermoelectric devices for waste heat recovery sees an increased interest in the recent years [135]. Basically this technology allows to generate electrical power from heat which is lost e.g. in conventional combustion processes, for example in steam turbines or car exhausts and thereby allows to improve their efficiency. Additionally, systems using body heat are tested or already available [136]. Furthermore thermoelectrics are interesting for the industry 4.0 since they could allow the autonomous operation of sensors spread throughout a factory [137].

Since thermoelectric devices are solid state construction, they have several advantages when compared to other technologies in similar applications [138]. They do not have any moving parts which makes them highly reliable, almost maintenance free and produce no acoustic and electrical noise. Additionally they can be easily scaled and therefore be much smaller and lighter than comparable devices. Last but not least, they can be considered more environmentally friendly since they do not produce or require environmental harmful substances, like for example chlorofluorocarbons as refrigerant, to operate.

4.3 Efficiency of Devices and Materials

In order to understand the current challenges of thermoelectric devices the efficiency of said devices needs to be considered, which was first derived by Altenkirch [139, 140]. As an example the efficiency of a thermoelectric generator should now be shortly derived [118]. As shown by W. Thomson (Lord Kelvin) a thermocouple is a type of heat engine which uses electrons instead of physical gasses or liquids as working fluids and therefore follows the laws of thermodynamics. Its efficiency η_D will depend on the thermocouple properties, as well as the resistance of the external load R_L and can be expressed as,

$$\eta_D = \frac{\text{energy supplied to the load}}{\text{heat absorbed at the hot junction}} = \frac{w}{q} \tag{4.7}$$

Due to the temperature difference the device will drive a current through the load which can be expressed as:

$$I = \frac{(S_p - S_n)(T_H - T_C)}{R_D + R_L}, \tag{4.8}$$

where S_p and S_n is the Seebeck coefficient of the p- and n-type thermocouple leg, respectively and $R_D = R_p + R_n$ is the electrical resistance of the device (thermocouple legs). With this the power to the load can be described as:

$$w = I^2 R_L = \left[\frac{(S_p - S_n)(T_H - T_C)}{R_p + R_n + R_L}\right]^2 \cdot R_L. \tag{4.9}$$

The heat that is drawn from the source is made up of three parts, eq. 4.10. The first part is due to the Peltier effect. The heat drawn from the hot junction is equivalent to $q_{Pel} = \Pi_{np} \cdot I$, which can be written as $q_{Pel} = (S_p - S_n)T_H \cdot I$ by considering the first Kelvin relation. The second part is due to the thermal conduction from the hot to the cold side which is equal to $q_{therm.cond.} = (K_p + K_n)(T_H - T_C)$, where K_p and K_n are the thermal conductances of the p- and n-type thermocouple leg, respectively. The third part is due to the joule heating of the legs which amounts to $q_{Joule} = \frac{1}{2} R_D I^2$. Only 1/2 of the joule heat needs to be considered since the generated heat is equally divided between the hot and cold junction.

$$q = (S_p - S_n)T_H I + (K_p + K_n)(T_H - T_C) - \frac{1}{2} R_D I^2 \tag{4.10}$$

The efficiency of the device η_D can therefore be expresses as:

$$\eta_D = \frac{\left[\frac{(S_p - S_n)(T_H - T_C)}{R_p + R_n + R_L}\right]^2 \cdot R_L}{(S_p - S_n)T_H \cdot I + (K_p + K_n)(T_H - T_C) - \frac{1}{2} R_D I^2}. \tag{4.11}$$

The maximum efficiency of the device, derived from equation 4.11, reads [117]:

$$\eta_{D,Max} = \frac{T_H - T_C}{T_H} \frac{\sqrt{1+ZT_M}-1}{\sqrt{1+ZT_M}+T_C/T_H}, \tag{4.12}$$

with

$$T_M = \frac{1}{2}(T_H + T_C) \text{ and } Z = \frac{(S_p - S_n)^2}{(K_p + K_n)(R_p + R_n)}. \tag{4.13}$$

Here Z is the so called figure of merit of the device. In order to obtain a dimensionless figure of merit, Z is usually multiplied by the absolute temperature T. The first part of eq. 4.12 is the known Carnot limit for all heat engines, which can be achieved for the limit of $ZT_M \Rightarrow \infty$. Since $K_{p,n}$ and $R_{p,n}$ depend on the geometry of the thermocouple legs, Z can be maximized if the relation:

$$\frac{L_n \cdot A_p}{L_p \cdot A_n} = \left[\frac{\lambda_n \cdot \sigma_n}{\lambda_p \cdot \sigma_p}\right]^{1/2}, \tag{4.14}$$

is satisfied. Here $L_{p,n}$ and $A_{p,n}$ are the lengths and cross sections of the p- and n-type leg, respectively. With this, the dimensionless figure of merit can be written as:

$$ZT = \frac{(S_p - S_n)^2}{\left[(\lambda_p/\sigma_p)^{1/2} + (\lambda_n/\sigma_n)^{1/2}\right]^2} \cdot T, \tag{4.15}$$

which then only dependent on the material properties of the two legs. As Z is in unit of $[1/K]$ it is usual to make it dimensionless by multiplying it by the absolute temperature T.

For Peltier devices the coefficient of performance also depends on the figure of merit and the maximum cooling temperature can be described by $\Delta T_{Max} = \frac{1}{2} Z T_H^2$ [118]. Furthermore the detectivity of thermoelectric sensors is proportional to $\sqrt{ZT}$ [141] and the figure of merit influences the signal-to-noise ratio. Since the figure of merit determines most of the important performance characteristics of thermoelectric devices, its improvement is the driving force behind material design for thermoelectrics for the last years. ZT however defines the figure of merit for a device and general efforts try to optimize the thermoelectric performance of a material. Therefore the figure of merit zT for a single material is defined on the basis of 4.15 by:

$$zT = \frac{S_i^2 \cdot \sigma_i}{\lambda_i} \cdot T = \frac{S_i^2 \cdot \sigma_i}{\lambda_{i;El.} + \lambda_{i;Ph.}} \cdot T, \text{ with i standing for p or n.} \tag{4.16}$$

Here λ_i can be expressed by the electrical contribution to the thermal conductivity $\lambda_{i;El.}$ and the phonon thermal conductivity $\lambda_{i;Ph.}$. The factor $S_i^2 \cdot \sigma_i$ is known as the "power factor" and is used to describe the power output of thermoelectric generators. This means that a good thermoelectric material needs to have a low thermal conductivity, to be able to maintain a large temperature gradient, a high electrical conductivity, in order to produce low amounts of Joule heating and electrical noise, and a high Seebeck coefficient, in order to generate a high voltage output.

Table 4.1 and figure 4.4 provides informations on of the state of the art of high zT materials in devices applied at different operating temperatures as well as how the figure of merit depends on the temperature for selected materials.

Table 4.1: High zT materials for different operation temperatures [142].

Temperature (K)	Type	Material	~ max zT
<200	n	$Bi_{1-x}Sb_x$	0.8
200-450	n,p	Bi_2Te_3	0.8
	n,p	$Bi_xSb_{2-x}Te_3$	0.9
400-800	p	Zn_4Sb_3	1.3
	n,p	PbTe	0.7 - 0.8
	p	TeAgGeSb (TAGS)	1.2
750-1000	p	$CeFe_4Sb_{12}$	1.1
	n	$CoSb_3$	0.8
1000-1200	p,n	SiGe	0.6 - 1.0

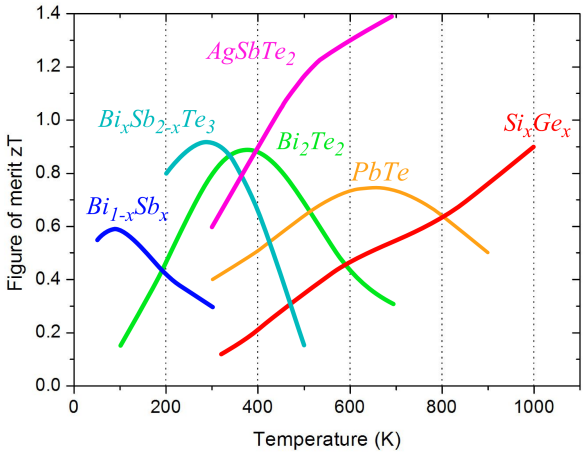

Figure 4.4: Dependence of the figure of merit zT on temperature for a number of selected materials, according to [143].

In the low temperature region, up to around 150°C alloys of bismuth, antimony and tellurium show the highest zT values. $Bi_{0.92}Sb_{0.08}$ for example has a maximum zT of ~0.5 at ~70 K and is usually applied for thermoelectric cooling, providing the best n-type material currently available [144, 117]. For applications around room temperature bismuth-telluride and antimony-telluride alloys are applied as n- and p-type material respectively, having a zT value in the range of unity. For higher temperatures between 300 - 800 °C lead-telluride and up to ~1200 °C silicon-germanium alloys are used, both having zT values close to unity.

As shown above, the figure of merit for state of the art thermoelectric materials is currently in the order of one. Therefore the efficiency of thermoelectric devices falls behind other technologies and limits their use to niche applications where other technological aspects, like reliability, play a more important role. In order to compete with other technologies, ZT values should be in the range of 2-3 for power generation and in the range of $2-4$ for cooling applications [145, 17, 146]. Nowadays, several materials with zT higher than unity exist, but industrial application is still pending. The improvement of the figure of merit beyond unity is difficult due to the fact that except for the phonon thermal conductivity all material properties in question are all closely related to one another. For example the thermal and electrical conductivity of electrons are correlated by the Wiedemann-Franz law and the Seebeck coefficient is related to the electrical conductivity via the Mott equation. These correlations are discussed in the following.

4.4 Interplay of Thermoelectric Transport Properties

Figure 4.5 shows how the figure of merit, as well as S, σ and λ depend on the charge carrier density n. The dependence of the Seebeck coefficient on the charge carrier density can be described by the Mott relation [147]:

$$S = \frac{\pi^2 k_B^2 T}{3e}\left\{\frac{d\left[ln(\sigma(E))\right]}{dE}\right\}_{E=E_F} = \frac{\pi^2 k_B^2 T}{3e}\left\{\frac{1}{n}\frac{dn(E)}{dE} + \frac{1}{\mu}\frac{d\mu(E)}{dE}\right\}_{E=E_F}, \tag{4.17}$$

where k_B is the Boltzmann constant, e is the elementary electrical charge, μ is the mobility of the charge carriers and E_F is the Fermi energy. For metals or highly degenerate semiconductors S can also be described by [148]:

$$S = \frac{8\pi^2 k_B^2}{3eh^2} m^* T\left[\frac{\pi}{3n}\right]^{\frac{2}{3}}, \tag{4.18}$$

with h being the Planck constant and m^* being the density of states effective mass of the charge carriers, which is calculated by $m^* = N_v^{2/3}(m_1 m_2 m_3)^{1/3}$. Here N_v is the number of equivalent valleys in a band and m_1,m_2 and m_3, are the effective masses along the axes of symmetry. On the other hand the dependence of the electrical conductivity on n is described by:

$$\sigma = ne\mu. \tag{4.19}$$

Therefore a lower charge carrier density will result in a larger Seebeck coefficient, but also in a lower electrical conductivity. For this reason an improvement of zT by purely doping is limited [149]. The other way around, by increasing the electric conductivity also has its limitations, as especially in metals the thermal conductivity is dominated by the charge carrier contribution. The dependency of the thermal conductivity on the electrical conductivity, can be described by the Wiedemann-Franz law:

$$\lambda_{El.} = L\sigma T = Lne\mu T, \tag{4.20}$$

where L is the Lorenz number. The law was derived for metals, but it can also be applied to highly degenerate semiconductors. In principle L is a constant, however it was shown that it can vary with carrier concentration and can differ from the bulk value for nanowires [150, 151]. Balancing all effects leads to a maximum in zT that can be found for carrier concentrations in the range between 10^{19} and 10^{21} carriers per cm^3, which falls in between semi-conductors and semi-metals.

The common approach to derive an expression for the transport coefficients is based on the stationary Boltzmann equation in relaxation time approximation, which relates the effects of external applied fields and the scattering of charge carriers. For an exact derivation of the formalisms, the reader is referred to literature [118]. Here, the results should only be briefly reproduced. Based on this approach, the electric

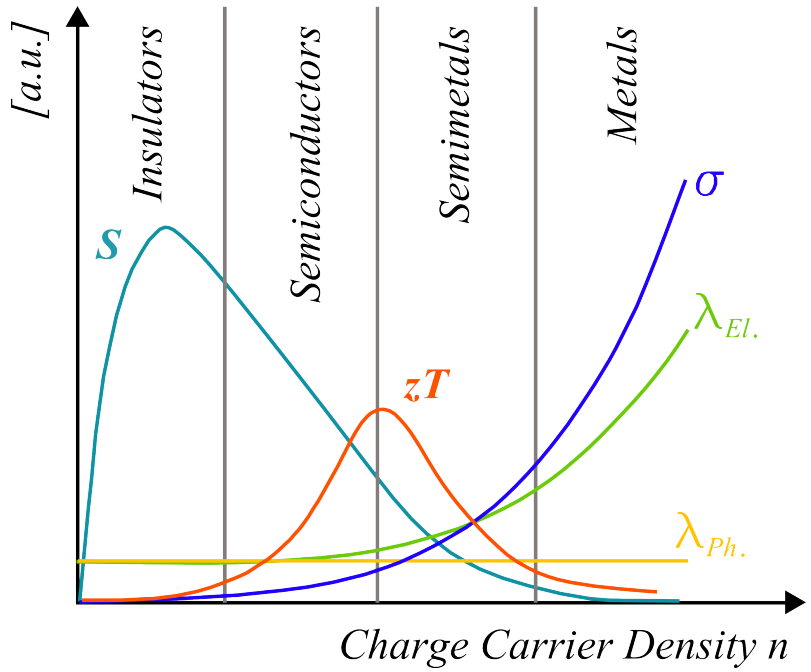

Figure 4.5: Transport properties as a function of charge carrier density [117, 152]

current density, j, and the heat flux density Φ in a material can be calculated by:

$$j = \mp\frac{2e}{3m^*}\int_0^\infty g(E)\tau(E)E\frac{df_0(E)}{dE}\left\{\frac{dE_F}{dx}+\frac{(E-E_F)}{T}\frac{dT}{dx}\right\}dE, \tag{4.21}$$

$$\Phi = \pm\frac{E_F}{e}j+\frac{2}{3m^*}\int_0^\infty g(E)\tau(E)E^2\frac{df_0(E)}{dE}\left\{\frac{dE_F}{dx}+\frac{(E-E_F)}{T}\frac{dT}{dx}\right\}dE. \tag{4.22}$$

Here g(E) is the density of electron states, $\tau(E) = \tau_0 E^r$ is the relaxation time, with τ_0 and r being constants depending on a given scatter process, f_0 is the Fermi-Dirac distribution function of the charge carriers in equilibrium. Using the appropriate boundary conditions, the transport parameters can then be derived. To express the obtained formulas more easily the so called transport coefficients K_s are defined:

$$K_s = \frac{8\pi}{3}\left(\frac{2}{h^2}\right)^{3/2}(m^*)^{1/2}T\tau_0(s+r+3/2)(k_BT)^{s+r+3/2}F_{s+r+\frac{1}{2}}. \tag{4.23}$$

with the function F_n $(n = s+r+1/2)$ being a Fermi-Dirac integral:

$$F_n(\xi) = \int_0^\infty x^n f_0(x,\xi)dx, \text{ with } f_0 = \frac{1}{e^{x-\xi}+1} \text{ and } x = \frac{E}{k_BT}, \xi = \frac{E_F}{k_BT} \tag{4.24}$$

The ratio of j (Eq. 4.21) to the electric field dE_F/dx when the temperature gradient dT/dx is zero leads to the electrical conductivity (4.25). The ration of Φ to the temperature gradient when the electric current is zero leads to the contribution of charge carriers to the thermal conductivity (4.26 and the Seebeck coefficient is equal to the ratio of the electric field to the temperature gradient, also when the current is set to zero (4.27).

$$\sigma = \frac{e^2}{T} K_0, \tag{4.25}$$

$$\lambda_{El.} = \frac{1}{T^2}\left(K_2 - \frac{K_1^2}{K_0}\right), \tag{4.26}$$

$$S = \pm\frac{1}{eT}\left(E_F - \frac{K_1}{K_0}\right). \tag{4.27}$$

Equations 4.25-4.27 relate the transport properties to the scattering parameters, the effective mass and the Fermi energy. It also becomes obvious that these properties are closely connected to one another. In case one considers a metallic material were $E_F >> k_B T$ some approximations can be employed to simplify the equations, leading to:

$$\sigma = \frac{8\pi}{3}\left(\frac{2}{h^2}\right)^{3/2} e^2 (m^*)^{1/2} \tau_0 E_F^{r+3/2} \tag{4.28}$$

$$\lambda_{El.} = L\sigma T \text{ with } L = \frac{\pi^2}{3}\left(\frac{k_B}{e}\right)^2. \tag{4.29}$$

$$S = \mp\frac{\pi^2 k_B}{3e}\frac{r+3/2}{(E_F/k_B T)}, \tag{4.30}$$

4.5 How to Improve Thermoelectric Materials

In order to enhance the figure of merit of bulk materials, the strategy is to reduce the lattice thermal conductivity and/or increase the power factor.

In order to decrease the thermal conductivity several approaches are found in literature: i) The use of heavy element compound semiconductors which naturally have low lattice thermal conductivities due to the low sound velocities in the material (e.g Bi_2Te_3, PbTe and BiSb) [149]. ii) Alloy point defect scattering, where the heat conducting phonons are scattered by the mass fluctuations in the crystal lattice, thereby decreasing the thermal conductivity (e.g. $Si_{1-x}Ge_x$)[153, 154]. It should be noted that

the used guest elements should not have an electronegativity too different from the host material, as this can otherwise also negatively affect the charge carrier mobility. iii) The use of multilayer systems in order to increase interface scattering of phonons [155, 156]. iv) The "phonon-glass electron-crystal" approach, where materials with complex unit cells are investigated [150]. These materials have a high electrical conductivity due to their highly periodic crystal structure but low thermal conductivity resulting from complex structural features (e.g. clathrates, skutterudites and zintl compounds) [117, 157, 158]. In general, since the contribution to the lattice thermal conductivity of phonons is approximately equal for each wavelength, it is advantageous to have structural complexity on different length scales in order to decrease the thermal conductivity. Since the mean free path of phonons is usually in a larger range than those of the charge carriers it would also be possible to keep the charge transport largely unchanged by carefully choosing the length scale of the scattering objects [149].

In order to increase the power factor, methods like resonant energy level doping or the energy filtering of electrons via a potential barrier are mentioned [159, 160, 148, 161]. In the first case dopands are used that have energy levels near the Fermi level of the host material. This way the local density of states is increased, which leads to a higher Seebeck coefficient without significantly changing the carrier concentration. In the second case low energy charge carriers are filtered out, either by scattering or a potential barrier, which leads to an increase of the Seebeck coefficient [159, 148].

In this work, nanowires and nanowire networks are used, where so called "size effects" may lead to an increase of the figure of merit. The idea that the reduction of dimensionality to 2D or 1D structures can lead to an increase of zT was first proposed by L. D. Hicks and M. S. Dresselhaus in 1993 and sparked great interest in the research community [13, 14]. Later these predictions were refined for the power factor by J. E. Cornett and O. Rabin, who showed that a decrease in nanowire diameter would first lead to a decrease in the power factor before positive effects take over [162].

In principle two effects can lead to an improvement of zT in nanowires [147]. When the wire diameter is close to the phonon mean free path, the increase in phonon boundary scattering at the nanowire surface leads to a decrease in the lattice thermal conductivity [163, 164]. For example, in individual silicon nanowires a reduction of the thermal conductivity by two orders of magnitude was reported for 22 nm diameter wires [165, 166] and a 70% decrease was reported for Bi_2Te_3 nanowires when decreasing the diameter from 300 nm to 25 nm [167]. In the case of nanowire networks, the junctions of nanowires are predicted to lead to additional scattering effects for phonons and simulations based on Bi_2Te_3 show an increase of the figure of merit by about an order of magnitude [15].

When the wire diameter is decreased further and is getting close to the Fermi wavelength of the charge carriers, the carriers "feel" the spatially confinement and the density of states (DOS) changes. Figure 4.6 shows the DOS for charge carriers in a given materials with different degrees of confinement [168]. The large gradient of the DOS with energy in low dimensional systems should lead to an increased Seebeck coefficient (see Mott relation 4.17) in case the Fermi level is well aligned to it, e.g. close to a maximum in 1D materials [147, 169].

Potential Drawbacks of Size Reduction

Although size reduction appears to be a promising route to enhance zT, the approach has some drawbacks. As the size of the material is decreases also the charge carrier conductivity can be affected negatively due to scattering at the surface [170]. Two models are interesting to describe the electrical conductivity of nanowires: The model of Mayadas and Shatzkes [171] which describes the scattering at grain boundaries

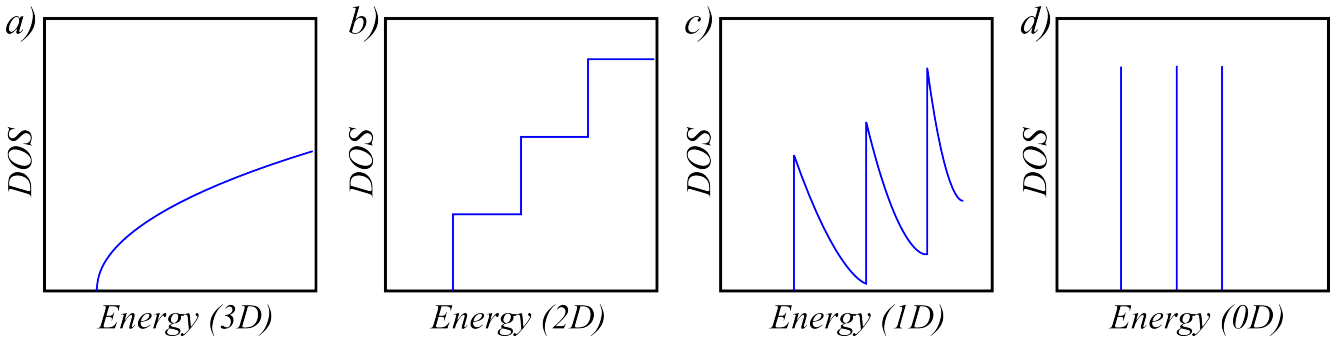

Figure 4.6: Schematic of the density of states (DOS) as a function of energy for: a) bulk material (3D), b) thin films (2D), c) nanowires (1D) and quantum dots (0D) [149].

and the model of Fuchs-Sondheimer and Dingle which describes the scattering on surfaces. The latter was applied on thin wires with circular cross section [172, 173, 174].

A rather new development is the fact that many of the high zT bulk materials, that are of interest for nanowire thermoelectrics, belong to the material class of topological insulators. One of the special property of this kind of materials (e.g. Bi_2Te_3, Sb_2Te_3 and Bi_2Se_3 [175, 21]) is that they possess symmetry protected surface states [176]. When the surface to volume ratio increases, i.e. the nanowire diameter decreases, the surface states become more important and can influence or even dominate the observed transport properties [177, 19, 178, 18, 179]. Calculations showed that due to the influence of these surface states zT of nanowires will most likely not exceed the bulk values unless diameters below 10 nm are achieved or the topological states are otherwise suppressed, e.g. by magnetic impurities [19].

Another challenge is the thermal stability of nanowires, since nanowires tend to fragment due to Rayleigh instability already below their bulk melting point and can easily be oxidized [180, 181], thus limiting the temperature range of potential devices. Finally also environmental risks should be considered as nanoparticles can easily be incorporated, with potential harmful effects [182, 183].

4.6 Transport Properties of Bismuth and Antimony

In order to understand the transport properties of $Bi_{1-x}Sb_x$, the behavior of the band structure at the T-, H- and L-points of the Brillouin zone are of special interest. Figure 4.7 shows a schematic of the band structure of bulk $Bi_{1-x}Sb_x$ as a function of the Sb content (x). In the pure form both Sb and Bi are semimetals, due to an indirect band overlap between the valence band and the conduction band. For Bi this occurs between the valence bands at the T-point and conduction band at the L-points and for Sb between the valence bands at the H-point and conduction band at the L-points [184]. Additionally there is also a direct band gap found at the L-point of both materials. The thermoelectric transport properties of both materials depend strongly on the crystal orientation, which is due to the large anisotropic Fermi surface [185]. Figure 4.8 gives an overview of the Seebeck coefficient S, thermal conductivity λ and electrical resistivity ρ of both materials along the binary (a-axis) and trigonal (c-axis) directions [185, 117].

When antimony is added to bismuth, the bands start to shift and at $x = 0.04$ the direct band gap vanishes. The bonding and anti-bonding bands at the L-points are inverted and by further increasing the Sb content the material becomes semiconducting, with an indirect band gap between $x = 0.07 - 0.09$ and a direct

band gap between $x = 0.09 - 0.22$. For even higher Sb contents the material becomes again semimetallic as the valence band at the H-point shifts above the conduction band at the L-point. Due to the changes in the band structure, the alloying of Bi with Sb can also improve the Seebeck coefficient of the alloy compared to the pure materials. In case of pure Bi, the small band overlap leads to a contribution of both holes and electrons to the Seebeck coefficient, which cancel each other out due to their opposite contribution to the Seebeck coefficient [186]. In the semiconductor phase however, due to the band gap,

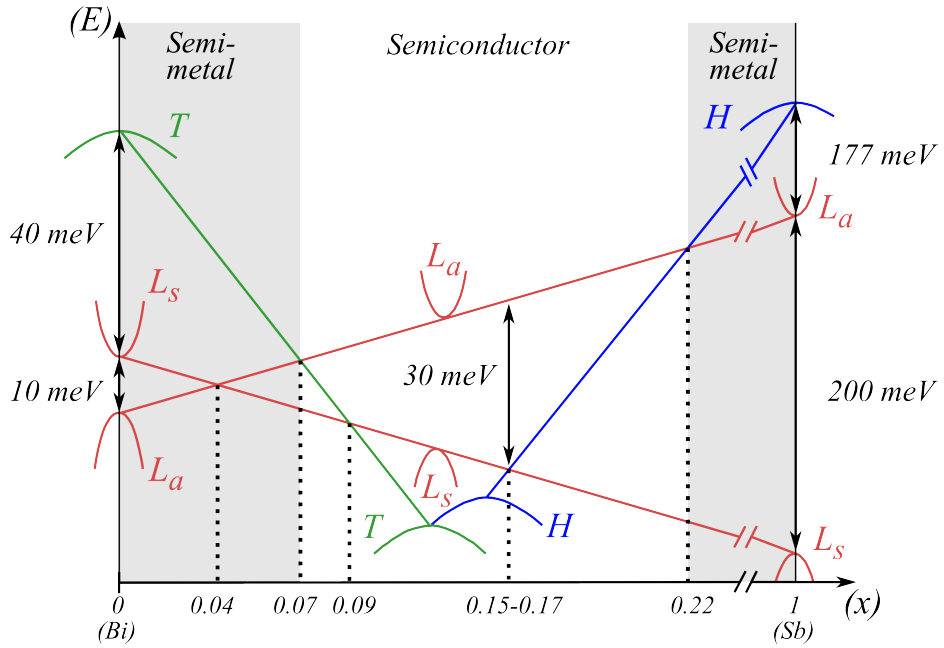

Figure 4.7: Band structure of bulk $Bi_{1-x}Sb_x$ alloy at 0 K as a function of the Sb content (energy not to scale), according to [35].

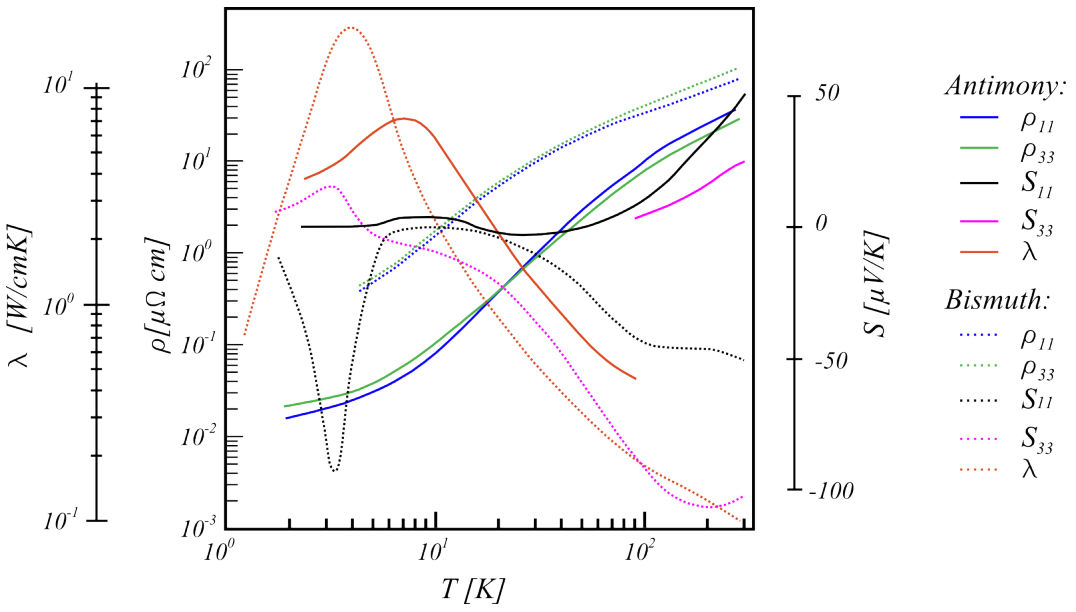

Figure 4.8: Overview of the thermoelectric transport properties of Bi (dotted lines) and Sb (full lines) as function of temperature for the binary (a-axis) and trigonal (c-axis) direction denoted by the indexes 11 and 33, respectively, according to [185, 117]. $\rho = 1/\sigma$: specific electrical resistivity.

single carrier transport can be achieved, leading to an improvement of the Seebeck coefficient [187]. The maximum figure of merit for bulk $Bi_{1-x}Sb_x$ is observed at ∼70 K (fig. 4.4) with zT∼0.4 and ∼0.5 for $x = 0.08$ and 0.16, respectively [117].

4.6.1 Effects of Size Reduction

The Fermi wavelength of the charge carriers in bismuth and antimony at room temperature is quite large, namely in the order of 40-70 nm for Bi and ∼ 40 nm for Sb [188, 189]. Therefore quantum size effects should already be seen for relatively large nanowire diameters. An additionally effect in Sb and Bi is that the valence and conduction bands shift depending on the material dimensions, which is a consequence of the energy bands splitting into sub-bands. Like in the case of alloying, this can lead to the transition of the material from a semimetal to a semiconductor, possibly increasing the Seebeck coefficient. For Bi and Sb this transition occurs for diameters smaller that 65 nm and 10 nm, respectively [190, 191, 188, 192].

As mentioned above, nanowires should also exhibit a decrease in phonon thermal conductivity due to diffuse scattering of phonons at the surface. Experimental studies on Bi nanowires with diameters between 330 nm and 60 nm confirm this, showing a decrease of a factor of up to ten at 300 K when comparing with the bulk value. The large decrease however is also attributed to additional grain boundary scattering and not only related to scattering at the surface [193, 194]. Initial calculations for $Bi_{1-x}Sb_x$ based on semi-classical Boltzmann transport equations predicted a zT value of 1.2 for p-type $Bi_{1-x}Sb_x$ with a wire diameter of ∼40 nm and an Sb content of ∼13% and even a zT value of 2.5 for n-type $Bi_{1-x}Sb_x$ nanowires for diameters below ∼25 nm [22, 192]. More recent studies, which also consider topological states however, conclude that size reduction will probably not yield a higher figure of merit than the bulk material, due to the dominance of the surface states on the transport properties [19, 195].

All in all systematic studies on the thermoelectric properties of $Bi_{1-x}Sb_x$ nanowires are still scarce. This is partially due to the challenges to prepare nanowires with controlled geometrical, compositional and structural characteristics and partly due to the challenge to characterize the thermoelectrical properties of nanowire samples.

5 Thermoelectric Characterization of Bi and Sb Nanowire Assemblies

"A very great deal more truth can become known than can be proven"
-Richard Feynman

5.1 Seebeck Coefficient and Electrical Resistance of Nanowire Assemblies

The experimental setup used in order to measure the cross plane Seebeck coefficient as well as the electrical resistance of nanowire assemblies embedded in polymer is shown in figure 5.1. The setup was previously designed by S. Müller [58] and later M. Cassinelli added a layer of thermal conducting paste between the sample and the copper blocks to improve thermal contact between the sample and the heat sinks [20].

The sample, nanowire ensemble embedded in polymer template, is placed between two copper blocks (orange) that serve as electrical contacts and heat sinks. In order to have a good electrical contact to the wires, a ~200-300 nm thick gold layer was sputtered on top of the grown caps additionally to the gold layer on the bottom of the samples, that was used as the working electrode during electrodeposition. For the measurement of the Seebeck coefficient a thin layer of thermal paste (PK-1 Thermal Compound by Prolimatech, $\lambda = 10.2$ W/mK) was applied between the copper blocks and the sample, in order to improve the thermal contact, which is vital in order to achieve a good measurement [20, 179].

To firmly attach the copper blocks to the sample, the stainless steel frames around the Cu blocks are tightened together by nylon screws, which have a low thermal conductivity. For the generation of a

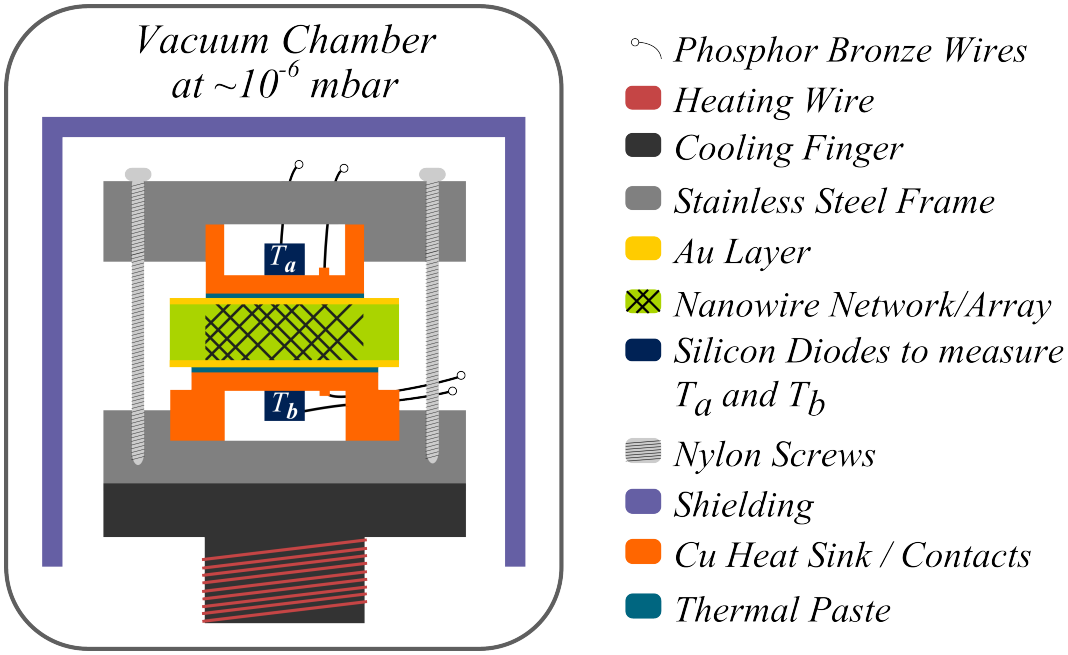

Figure 5.1: Setup for cross plane characterization of the Seebeck coefficient as well as the electrical resistance of nanowire assemblies embedded in polymer template.

temperature gradient, the setup uses a cooling finger with a heating wire coiled around. The cooling finger is constantly cooled using a COOLPAK 6000 cryostat with a helium evaporation cooler, which allows to cool the system down to ∼20 K. To control the temperature of the stage a Lakeshore 336 temperature controller activates the heating wire whenever the temperature measured by the silicon diode T_b is below the set temperature. The silicon diode T_b also serves as a measurement for the temperature at the bottom of the sample. The silicon diode T_a measures the temperature on top of the sample. To improve the thermal contact of the diodes to the copper blocks, a thin layer of indium was introduced between them. In order to prevent heat exchange due to convection, the whole system was placed in a vacuum chamber that operates at a pressure of $\sim 10^{-6}$ mbar, which was generated by a rotary pump and a turbomolecular pump. In addition a heat shield consisting of an aluminum cup, surrounded by several layers of thin thermal insulation material, was placed above the sample. All leads to the contacts were made from a non-magnetic phosphor bronze by Lakeshore, due to its low thermal conductivity and low Seebeck coefficient over the tested temperature range (smaller 1 $\mu V/K$ [196]).

Measurement Procedure

Two measurement runs per sample are performed, one without the thermal paste between the Cu-blocks and sample, in order to avoid an additional electrical resistance in the system and one with thermal paste between the Cu-blocks and the sample in order to more accurately measure the Seebeck coefficient. In both cases, the temperature program is set to hold at certain temperature steps, which can be seen in figure 5.2a). The temperature steps start at 300 K and are reduced down to 40 K in steps of 20 K every 40 minutes. A last step at 30 K was performed but usually not considered for data evaluation, due to inaccurate measurements of the temperature difference in that temperature range. Since the system is dynamically heated and cooled from below, a temperature gradient is generated between the top and the bottom of the sample holder, which is shown in the inlet of figure 5.2a). This leads to the generation of a thermal voltage in dependence of the time due to the Seebeck effect which is shown in figure 5.2b). The measurement routine is set to acquire data every 10 seconds. During the routine first the temperatures T_a and T_b are measured followed by the thermo voltage. The thermal voltage was measured at zero current, in order to prevent effects due to Peltier cooling, using a Keithley 2182A Nanovoltmeter. At the end of the measurement routine, an I-V curve was recorded, in order to determine the resistance of the sample using a Keithley 2400 Sourcemeter. The maximum amperage was individually selected for a given sample and was set at the start of the measurement run. The chosen value was set to be as small as possible in order to avoid damage of the wires, but large enough to enable a reliable measurement. Depending on the wire diameter, usually the current was in the order of 0.5 A to 0.05 mA, for large diameter (∼140 nm) and small diameter wires (∼40 nm), respectively.

Data Processing and Evaluation

For the determination of the electrical resistance of the samples at a certain temperature step, the mean slope of the measured I-V curves during that step is analyzed. The data during the change of temperature steps is not taken into consideration, since the fast change might lead to situations where the temperatures measured are not in equilibrium with the sample. In order to determine the Seebeck coefficient the generated thermal voltage was plotted against the temperature difference ΔT at a given temperature. For measurements without thermal paste, the observed temperature difference during a temperature step were between 1.0 and 1.3 K, whereas with paste the differences were between 0.6 and 1.0 K. The measured data between the temperature steps was again not considered.

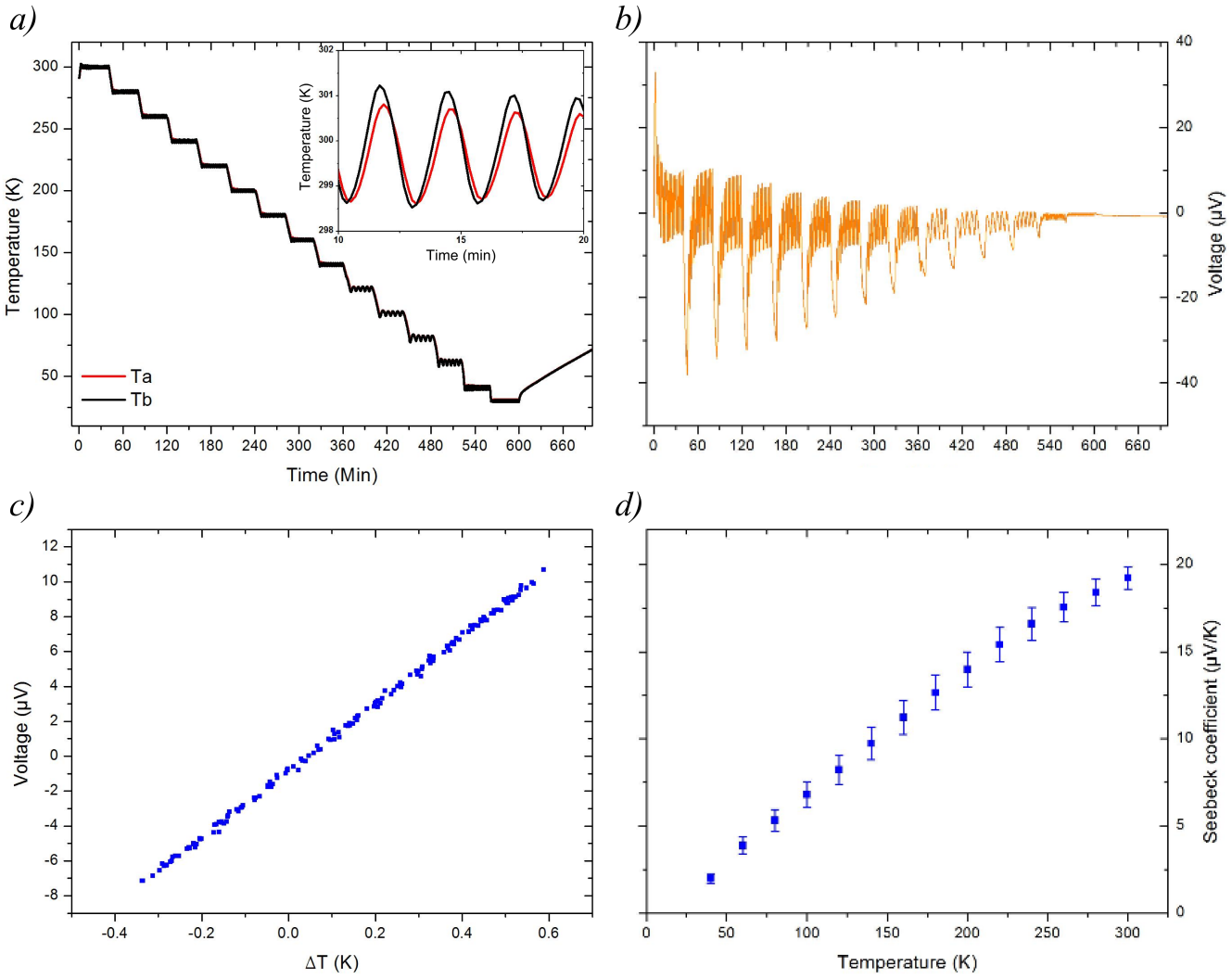

Figure 5.2: Example of data evaluation for a Sb nanowire array with 10^8 i/cm^2 and a wire diameter of ~60 nm. a) Measured temperatures on the top and bottom copper block (T_b and T_a respectively) during a measurement run. The temperature at the top and the bottom of the sample differ (inset of a), leading to the generation of a thermo voltage, shown in b). c) Generated thermovoltage in dependence of the temperature gradient along the sample at 300 K. The slope of the linear fit leads to the Seebeck coefficient of the sample at this temperature. The evaluated Seebeck coefficients for the different temperature steps is shown in d).

For the sample at 300 K, the thermo voltage as a function of the temperature difference between top and bottom is shown in figure 5.2c). The measured data points all lie on a line, as expected from eq. 4.1.

Since the silicon diodes were not perfectly calibrated to one another, see figure 8.5 in the appendix, a small shift of the measured voltage to the zero point is observed. The misalignment does not change severely at a certain temperature, so that the effect on the slope and therefore on the measured Seebeck coefficient can be neglected. Figure 5.2d) shows the dependence of the Seebeck coefficient ($S = V/\Delta T$) on temperature. The generated thermo voltage is given by the contribution of the cables, copper heat sinks, thermal paste layer and the nanowire assembly, including the gold layers on top and bottom. The generated thermo voltage is then given by:

$$U_{th} = \int_{T_0}^{T_1} S_{Cable} + \int_{T_1}^{T_2} S_{Cu} + \int_{T_2}^{T_3} S_{Th.Paste} + \int_{T_3}^{T_4} S_{NWA} + \int_{T_4}^{T_5} S_{Th.Paste} + \int_{T_5}^{T_6} S_{Cu} + \int_{T_0}^{T_6} S_{Cable} \qquad (5.1)$$

Assuming that the thermal conductivities of copper and thermal conducting paste in relation to their thickness is high, the temperatures $T_1 = T_2 = T_3$ and $T_4 = T_5 = T_6$. Equation 5.1 then becomes:

$$U_{th} = S_{Cable}\Delta T - S_{Sample}\Delta T \text{ with } \Delta T = T_4 - T_3 = T_6 - T_1. \qquad (5.2)$$

Since the Seebeck coefficient S_{Cable} is $< 1\ \mu V/K$, as can be seen in chapter 8.3 and in [196], the influence of the leads to the measured signal will be neglected. The error of the electrical measurements is very small (<1%) and the error of the Seebeck calculation is mainly due to the uncertainty of the measured temperature gradient, which is due to the non perfect alignment of the two diodes to one another. The measured temperature difference between the diodes changes with ambient temperature even if no temperature difference is applied between them. Considering the measured temperature differences the errors amount to 2-8% for measurements without paste and 3-13% for measurements with paste for the temperature range of 300 K to 40 K, respectively.

Although the errors for measurements without paste appear to be smaller, these measurements seem to suffer from a larger systematic error of the temperature measurement. Figure 5.3 shows the measured Seebeck coefficients, measured with and without a thermal conducting paste between the sample and the copper blocks, for a) an antimony and b) a bismuth nanowire array, with a wire density of 10^8 i/cm^2 and a wire diameter of ~100 nm. Both samples were prepared with electrolytes without surfactant. In both cases the Seebeck coefficient is larger for the measurements with paste than without paste. This was evident in almost all measurements, indicating that the measured temperature gradient in the case without paste is larger than the actual temperature gradient present across the sample, probably due to the heat transfer resistance across the interfaces. An additional effect might be that different areas on the sample see a different temperature gradient when no paste is applied. Since the measured voltage is a combination of the values of all wires, this might also explain the scatter of the measured values.

Therefore there is an additional systematic error of the temperature gradient, especially in the case of the measurements without paste. Sometimes it was observed that measurements with paste showed lower values than without paste. The amount of paste was kept constant for all the samples, by spreading the paste in a 7 mm diameter circular opening in a Tesafilm 4124 and removing the surplus paste, before removing the tape. Also the time for cap growth was kept constant. However, due to the different porosities

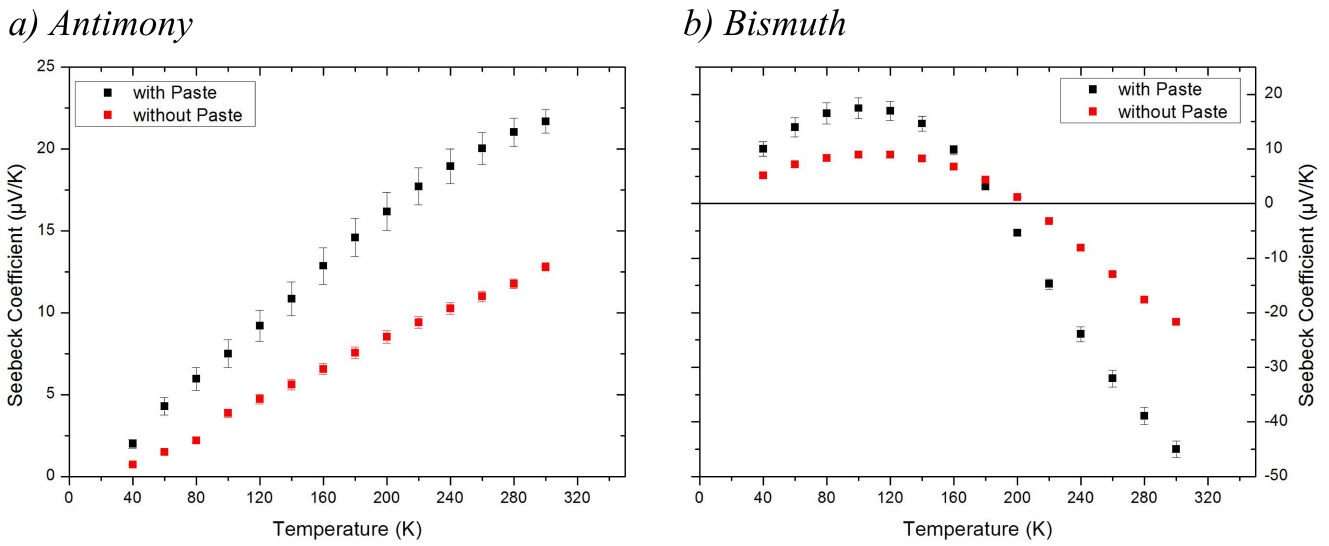

Figure 5.3: Measured Seebeck coefficients, with and without applying a thermal conducting paste, for a) an antimony nanowire array and b) a bismuth nanowire array, both with a wire density of 10^8 wires/cm^2 and a wire diameter of ∼100 nm. Both were prepared with electrolytes without surfactant. In both cases the absolute Seebeck values measured with paste are higher, indicating that the measured temperature gradient in measurements without paste is to large.

of the templates the surface generated by the caps for each sample is slightly different, as the cap layer on top of the sample becomes denser the higher the porosity. The effect, that the size of the caps can influence the measurement, was previously shown by M. Cassinelli [20]. It is possible that there is an optimum amount of paste for each cap density. Therefore the measurement has an systematic error even with the paste and further measurements are required to get a better understanding of it. Thin film standards for thermoelectrics are scarce, due to the requirements on reproducibility of the samples [197], making calibration challenging. All results for the Seebeck measurements are taken from measurements with paste, as the error should be the smallest in this case. The Seebeck measurements of the samples without paste are shown in the appendix 8.4.

5.2 Results

Measurements of the Seebeck coefficient and electrical resistance alone do not allow precise conclusions on the physical processes governing the transport properties of a material [19, 198], because especially in semimetals like Bi and Sb transport is determined by contributions of electrons as well as holes [186] and depending on the wire diameter eventually also surface states [19]. The partial Seebeck coefficients of electrons and holes are sensitive to small changes in the intrinsic properties of the materials like carrier concentration, carrier effective mass, scatter times or mean free path lengths [198]. Additionally, for Sb and Bi, these properties will differ for different crystal orientations, depend on composition, defect density and size of the sample [185, 31]. This especially makes it difficult to compare results obtained by different groups, as usually not all properties are well characterized.

In the case of the studied nanowire assembles, it should be mentioned that the measured values always show an average of the sample since a large number of wires are contacted simultaneously, and nanowires grown in multipores can influence the results [68, 152]. For this reason, we restrain from giving exact

interpretations of the results and keep the explanations on a descriptive level, while mentioning the theories that could explain the behavior. In order to better understand the underlying processes and get closer to the truth, it is imminent to characterize the crystal structure better and measure the band structure, carrier density and mobilities of the charge carriers as well [199].

5.2.1 Seebeck Coefficient of Antimony Nanowire Assemblies

The Seebeck coefficient of Sb nanowire arrays prepared without surfactant at room temperature and with surfactant at 40°C is presented in figure 5.4 a) and b). As expected for a p-type material the Seebeck coefficient is in both cases positive. For Sb arrays prepared without surfactant the Seebeck coefficient at 300 K is between 21-25 μV/K, whereas for Sb arrays prepared with surfactant the value is between 18-20 μV/K. At 60 K both kinds of wires show similar values between 3-4 μV/K. The lower Seebeck coefficient

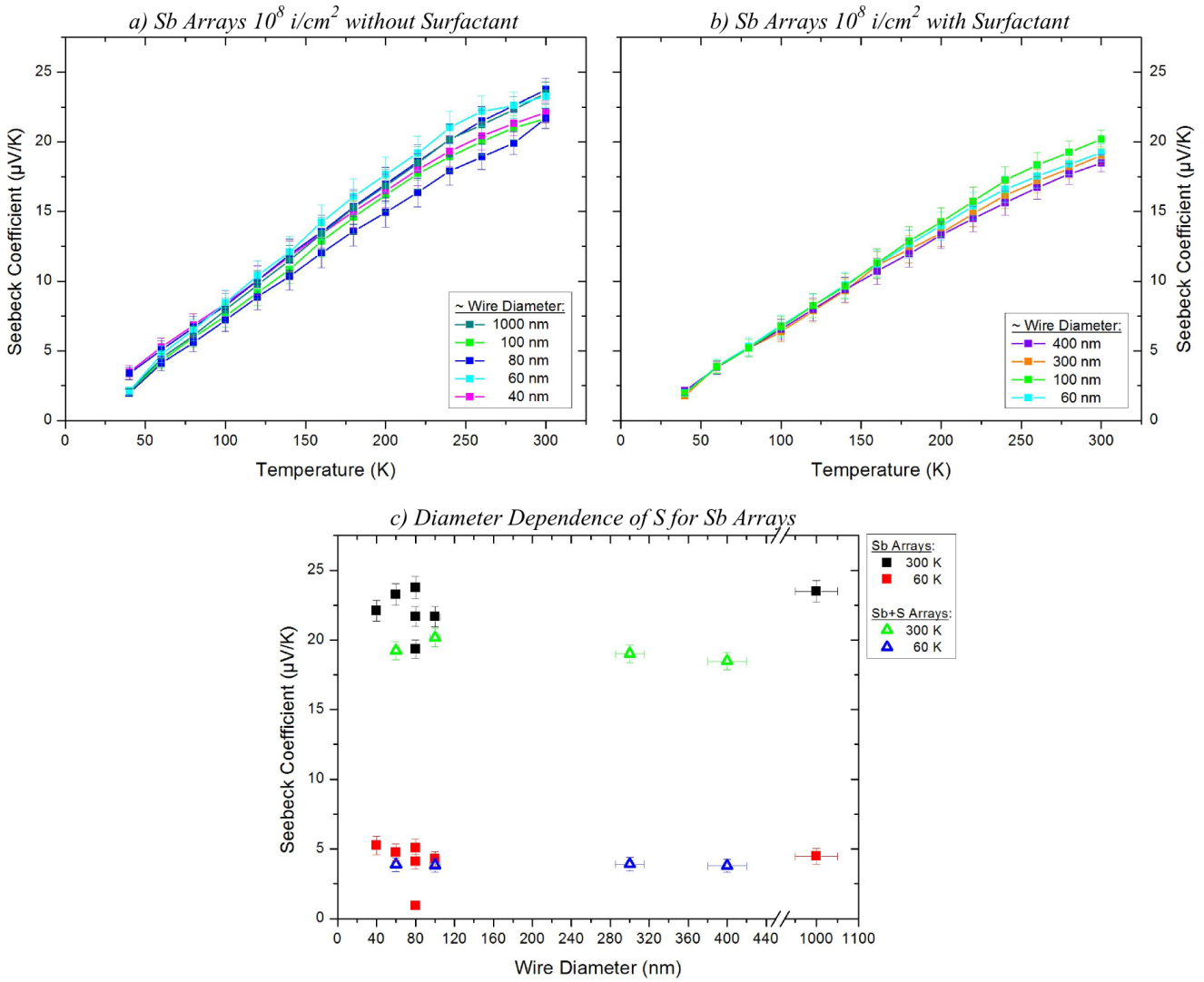

Figure 5.4: Measured Seebeck coefficients in dependence of temperature of Sb nanowire arrays with 10^8 i/cm^2 and various diameters, prepared a) without surfactent at room temperature and b) with surfactant at 40°C. c) Diameter dependence of the measured Seebeck coefficient at 300 K and 60 K for Sb arrays prepared without and with surfactant.

at 300 K might be explained by the lower texture of the crystals in the samples prepared with surfactant. However, in the case of the arrays prepared without surfactant differences up to ∼5 μV/K have been observed between samples that were prepared identically. Therefore, the observed differences between samples prepared without and with surfactant might be caused by additional effects other than the crystallinity of the samples. In both cases the observed Seebeck coefficients are lower than the maximum bulk value reported in literature even for large diameters (∼45 μV/K in trigonal direction [117]). However, considering the fact that the wires are not oriented in trigonal direction but textured in the {01.2} direction the values are reasonable and comparable to the bulk value. With decreasing temperature, a monotonic decrease in S is measured, analogue to the behavior observed in Sb bulk material [185]. In contrast to previous measurements [20, 179], which showed a non monotonic dependence of S on the diameter for Sb nanowires with a {012} texture, no clear dependence on the wire diameter is observed. In fact, as shown in figure 5.4 c), there seems to be no dependence on the wire diameter at all.

As explained in chapter 2.3, by varying the fluence, the interconnectivity of the nanowire networks is controlled, i.e. an increase in fluence leads to an increase in the number of interconnections and a decrease in the spacing between them. The possible diameter range of the nanowires in a network that can be prepared decreases with increasing irradiation fluence, as the pore overlap decreases the mechanical stability of the polymer templates. Figure 5.5 shows the measured Seebeck coefficients in dependence of temperature of Sb nanowire networks with different wire densitys and wire diameters. In general the observed behavior of the Sb nanowire networks is quite similar to the behavior of the measured Sb nanowire arrays. The Seebeck coefficient at 300 K is in the order of 20 - 25 μV/K and decreases monotonic with decreasing temperature, to a value of 3 - 4 μV/K at 60 K. In case a sample showed a lower value at 300 K, either the sample was remeasured after renewal of the thermal paste or a new sample, that was prepared under the same conditions, was measured. These measurements usually showed a Seebeck coefficient in the previous mentioned range, so that smaller recorded values can be assigned to bad thermal contact of the sample to the Cu blocks. Again no clear dependence of the Seebeck coefficient on the wire diameter is observed. Also the wire density does not seem to affect the observed behavior.

5.2.2 Electrical Resistance of Antimony Nanowire Assemblies

The measured electrical resistances of the measured Sb nanowire assemblies at room temperature vary in a range of 1.88-0.08 Ω for arrays and 0.07-0.007 Ω for networks, when no thermal conducting paste is applied. Usually samples with larger diameter wires show smaller resistances, but no systematic dependence on the wire density is observed. However, the measured values are much larger that theoretically expected, so that it is probable that the measured resistances are dominated by contact resistances between the Cu blocks and the samples. Therefore, discussion is limited to the relative resistance values.

Figure 5.6 shows the relative resistance as a function of T for various samples. In most cases the thermal paste has no significant influence on the measured relative resistance of the samples.

The resistance of Sb nanowire assemblies show linear decrease of the resistance with decreasing temperature (metal-like), which is similar to bulk behavior. However, the resistance change between room temperature and 40 K is smaller when compared to bulk. For Sb arrays prepared without and with surfactant, shown in figure 5.6 a) and b), it is usually in the order of 20-30% for wire diameters smaller than 100 nm, but can also decrease by about 40% in larger diameter wires. The trend that the decrease in resistance with decreasing temperature is stronger in larger diameter wires is also visible in Sb nanowire networks. Here a decrease of up to 60% between room temperature and 40 K is observed. Similar behavior for Sb nanowires and thin films has already been reported in literature [200, 190, 188, 152, 20]. The mean free

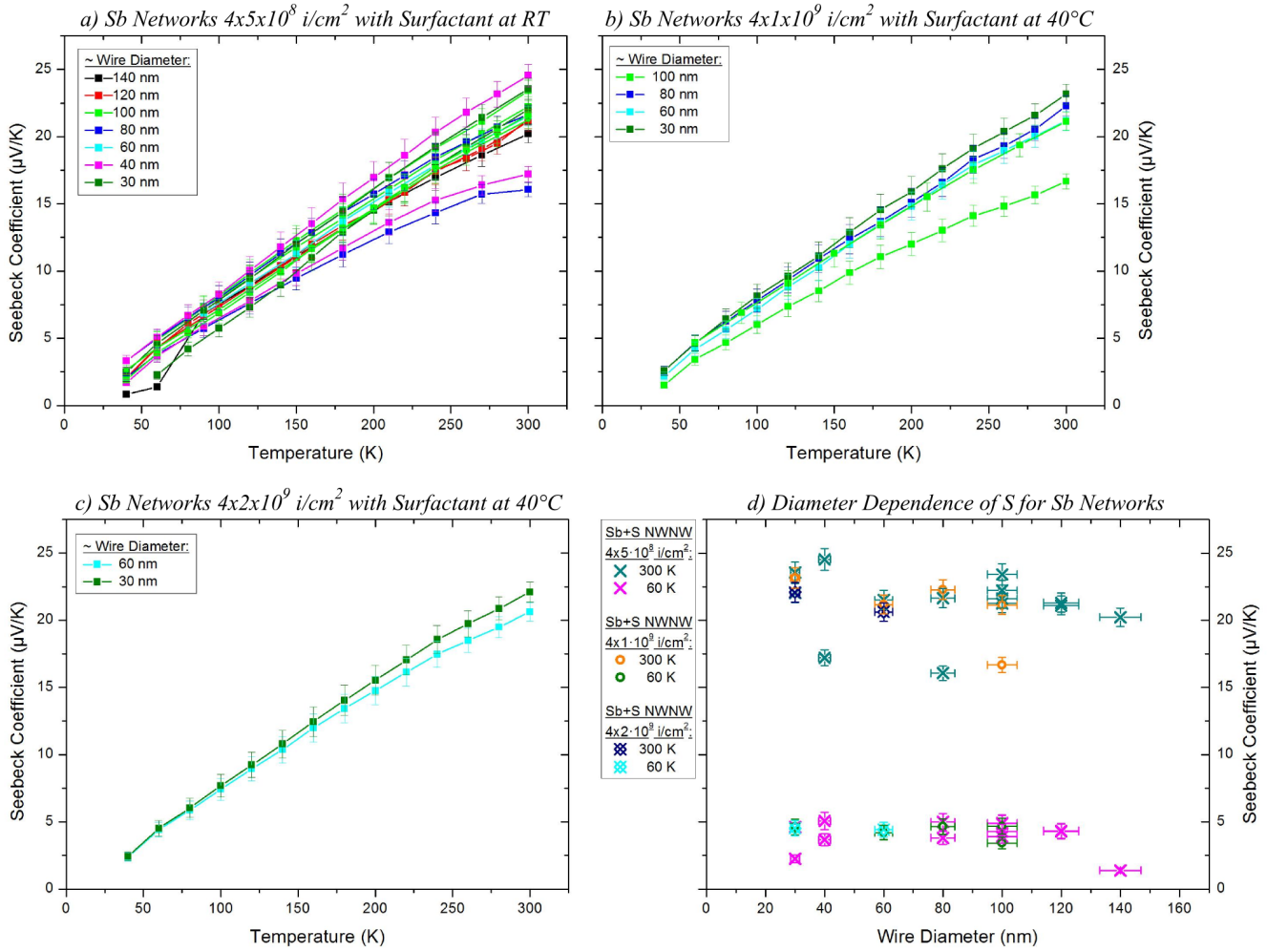

Figure 5.5: Measured Seebeck coefficients in dependence of temperature of Sb nanowire networks with various diameters, deposited in templates irradiated with a) $4 \times 5 \cdot 10^8$ i/cm^2 b) $4 \times 1 \cdot 10^9$ i/cm^2 and c) $4 \times 2 \cdot 10^9$ i/cm^2. All samples were electrodeposited using an electrolyte with surfactant at 40°C. d) Diameter dependence of the measured Seebeck coefficient at 300 K and 60 K for Sb networks.

path length of charge carriers in Sb is between 100-200 nm [201], therefore finite-size effects like the additional scattering of charge carriers on the wire boundaries could explain the observed behavior.

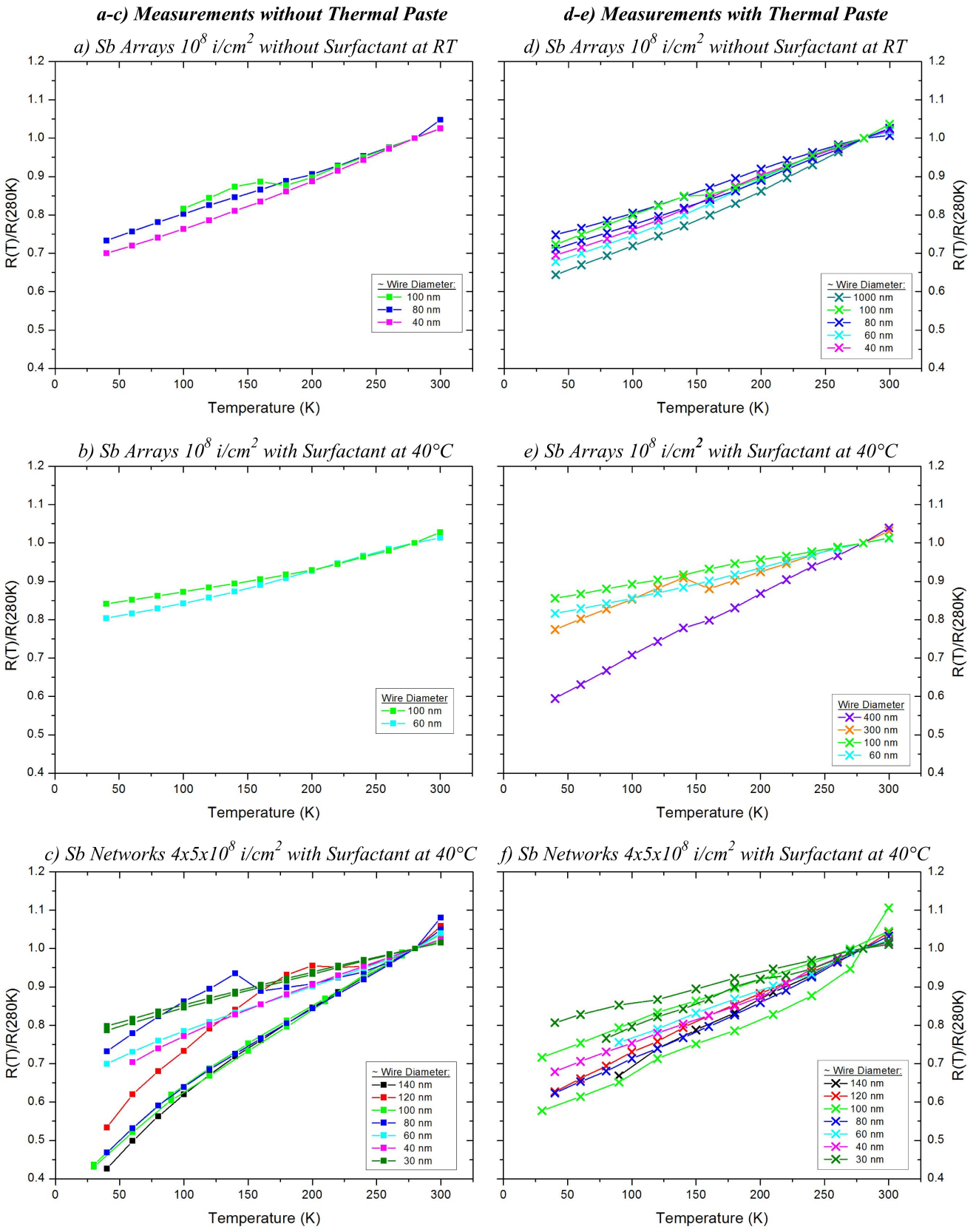

Figure 5.6: Relative electrical resistance as a function of temperature, of Sb nanowire arrays with 10^8 i/cm^2 prepared a) without and b) with surfactant, as well as of c) nanowire networks with $4 \times 5 \cdot 10^8$ i/cm^2, prepared with surfactant. Figures a)-c) show the relative electrical resistance of the samples when no thermal paste is applied between the samples and the Cu blocks, while d)-f) show the relative electrical resistance when thermal paste was applied.

5.2.3 Seebeck Coefficient of Bismuth Nanowire Assemblies

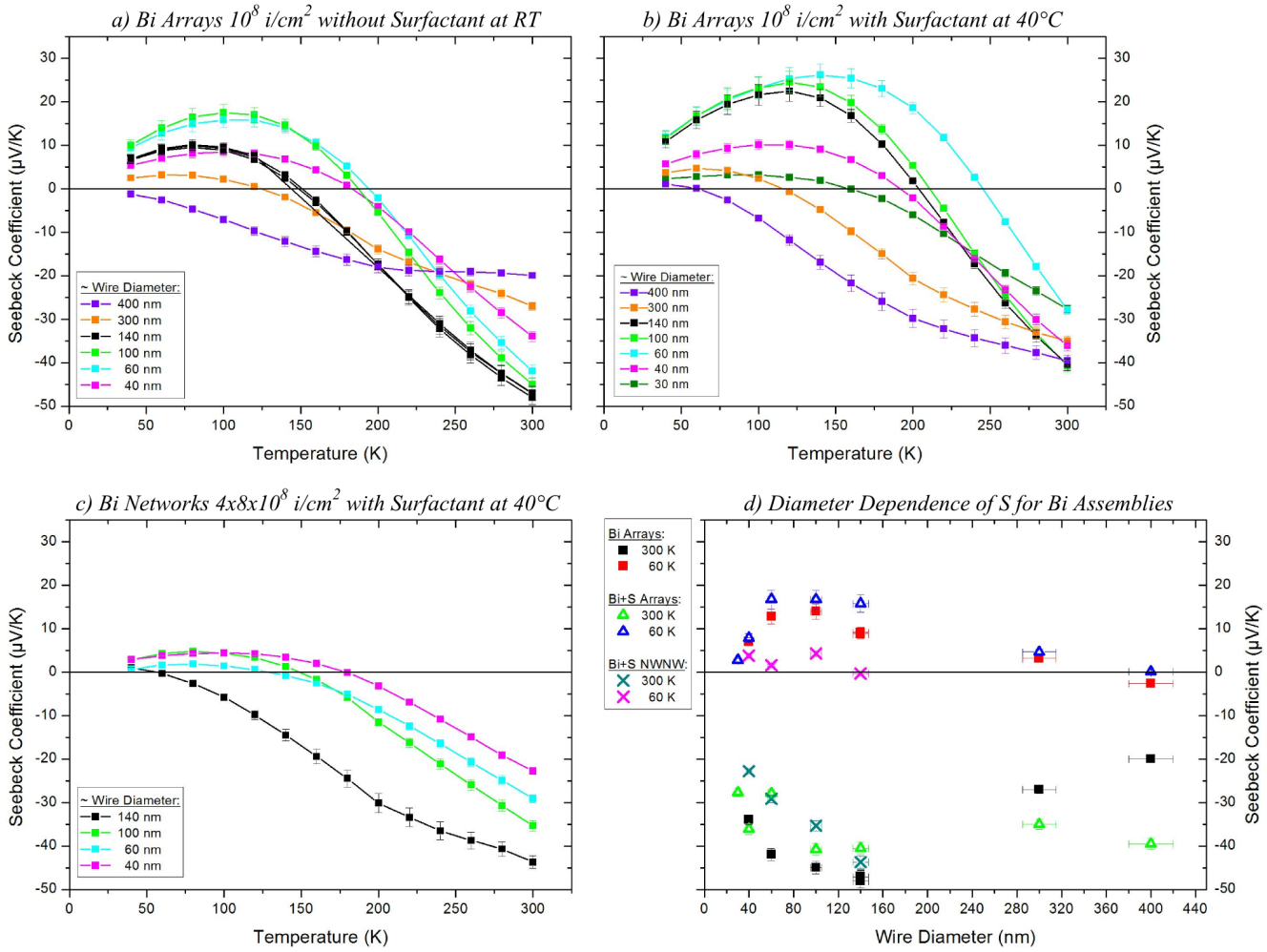

Figure 5.7: Measured Seebeck coefficients, in dependence of temperature, of Bi nanowire arrays with 10^8 i/cm^2 prepared a) without surfactant at room temperature and b) with surfactant at 40°, as well as of c) nanowire networks with a fluence of $4 \times 5 \cdot 10^8$ i/cm^2, prepared with surfactant at 40°. d) Dependence of the Seebeck coefficient on the wire diameter at 300 K and 60 K of the mentioned samples.

The Seebeck coefficient of Bi nanowire arrays prepared without surfactant at room temperature and Bi arrays and Bi nanowire networks prepared with surfactant at 40°, is presented in figure 5.7 a)-c). All samples show a negative Seebeck coefficient at 300 K which ranges between -45 μV/K to -20 μV/K for nanowire arrays and nanowire networks with diameters between 400-40 nm. Although these values are far away from the highest bulk value even for large diameters (∼120 μV/K in trigonal direction [198]), the values become reasonable when the orientation of the wires are considered. Taking mean free path limitations of the charge carriers into consideration a Seebeck coefficient of ∼-40 μV/K to -50 μV/K for binary and bisectrix direction are predicted for 200 nm to 100 nm wires [198]. In general there is a trend visible, that for wires with a diameter smaller than ∼ 140nm the absolute value of the Seebeck coefficient decreases with decreasing wire diameter, as shown in figure 5.7d). For wire diameters larger than 140 nm the Seebeck coefficient stays approximately the same when considering the same ∼5 μV/K spread of measured values as has been observed for Sb. In the case of the lower values of S for large diameter Bi arrays, it is reasonable to assume a measurement error, as the measurements without an additional thermal paste (see chapter 8.4) show equal or larger values when compared with the Seebeck coefficient

of 140 nm wires. In case of the 40 and 30 nm Bi nanowires prepared with surfactant the higher values might be either due to a different crystal structure, the semimetal to semiconductor transition or due to the influence of quantum size effects and surface states [202, 31, 179]. In literature the loss of S with decreasing wire diameter is attributed to the influence of surface states on the transport properties [19, 31, 179]. However, especially for the "larger" diameter wires presented the effects of mean free path limitation of the charge carriers should be considered, in order to explain the observed behavior [203, 198].

Another striking feature is the sign change of the Seebeck coefficient. Figure 5.8a) shows the transition temperature as a function of the wire diameter. For the measured samples the transition starts at ~200 K and ~250 K for nanowire arrays without and with surfactant, respectively and ~170 K for networks.Murata et al. predicted such a behavior in wires with diameters between 100 - 5000 nm in the bisectrix direction due to mean free path limitations of the charge carriers in Bi [203, 198] and similar observations were found experimentally [204, 31, 198].

Considering the theoretical predictions, the sign change should occur at lower temperatures for larger diameters and vanish for bulk Bi [203, 198]. A similar trend can be observed in the shown data, with the exception of some smaller diameter wires where effects like the semimetal to semiconductor transition, the influence of quantum size effects and surface states also need to be considered. For networks, the shift to positive is smaller and occurs at lower temperature when compared to the arrays. This is probably due to additional scattering effects in networks, because of a eventually more polycrystalline crystal structure, but also due to the intersections of nanowires.

In general, the higher the transition temperature for the sign change, the higher the maximum positive Seebeck coefficient, as shown in figure 5.8b). The most extreme is observed for Bi arrays with a diameter of 60 nm, where the positive Seebeck coefficient at 150 K is almost as high as the negative at 300 K.

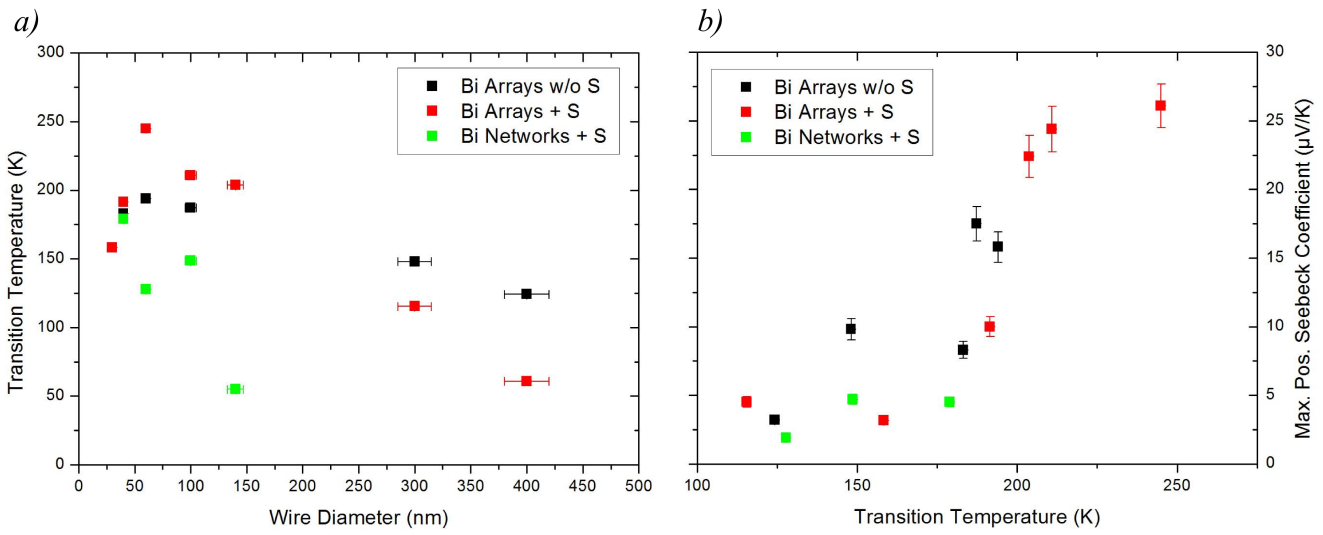

Figure 5.8: a) Transition temperature of the Seebeck coefficient of Bi nanowire arrays with 10^8 i/cm^2 prepared without surfactant at room temperature and prepared with surfactent at 40°, as well as of Bi nanowire networks prepared with surfactent at 40°. b) Maximum positive Seebeck coefficient as a function of the transition temperature.

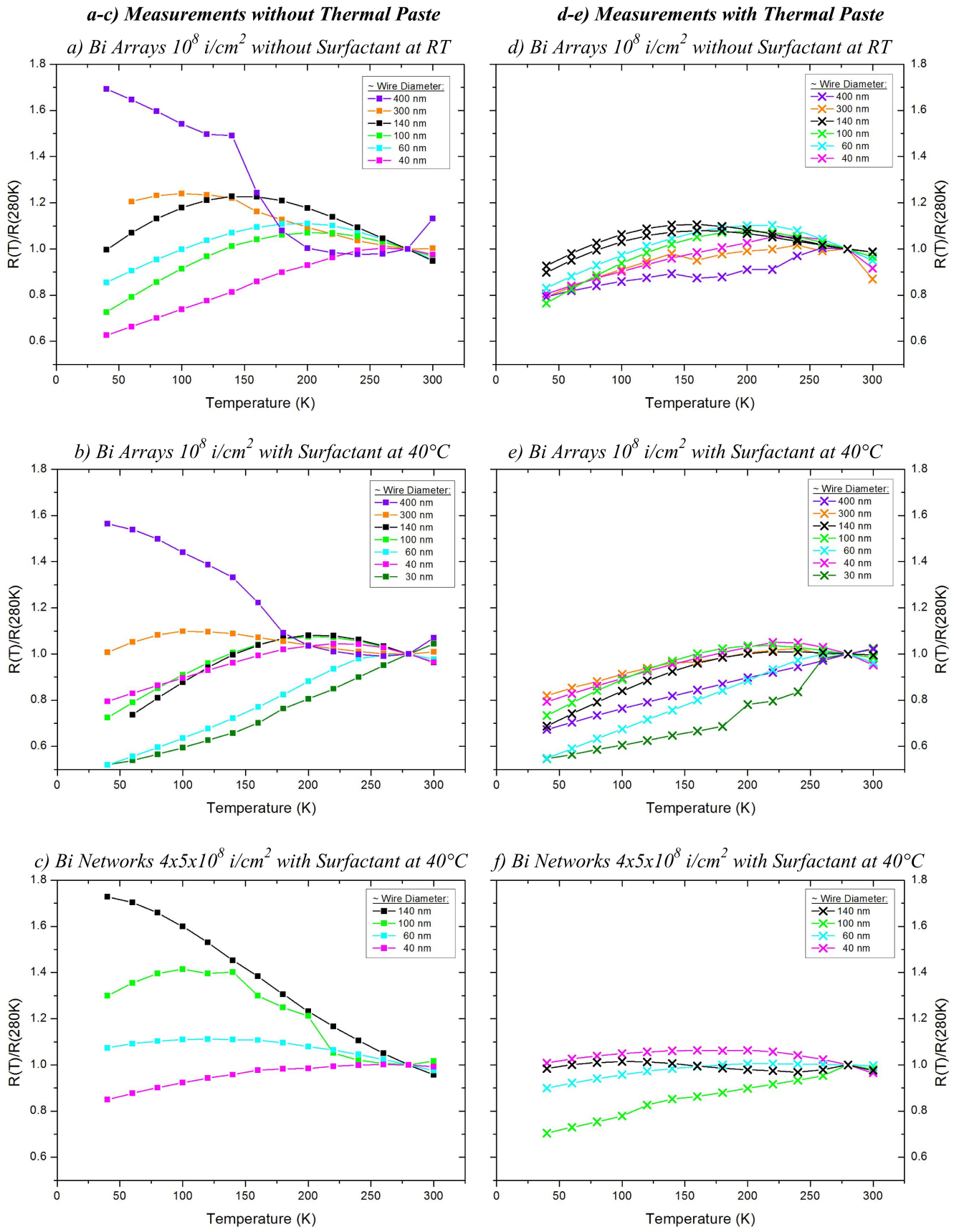

Figure 5.9: Relative electrical resistance, R(T)/R(280 K), as a function of temperature of Bi nanowire arrays with 10^8 i/cm^2 prepared a) without surfactant at room temperature and b) with surfactant at 40°, as well as of c) nanowire networks with $4 \times 5 \cdot 10^8$ i/cm^2, prepared with surfactant at 40°. Figures d)-f) show the relative electrical resistance of the samples when the thermal paste was applied.

5.2.4 Electrical Resistance of Bismuth Nanowire Assemblies

The measured absolute electrical resistances of the Bi nanowire assemblies varies in a range of 3.4 - 0.02 Ω for arrays with wire diameters down to 60 nm. No clear systematic dependence on the diameter was observed. Smaller diameters showed much larger values (∼100 - 1000 Ω for 40 nm and ∼30 $K\Omega$ for 30 nm). The exact reason for the high increase in resistance is yet under discussion. Reasons can be lower filling rates of the samples with smaller pore diameters or that the nanowires with smaller diameters might have a bi-conical shape instead of cylinders, limiting the current transport at the bottleneck, also the contact resistance should be considered. For Bi nanowire networks the absolute electrical resistances varied between 23 - 0.002 Ω, at room temperature. As in the case of Sb nanowires, the discussion will be limited to the relative resistance values measured without thermal conducting paste, as depicted in figure 5.9a)-c).

In contrast to Bi bulk, the relative resistance of nanowire assemblies shows a non-monotonic dependency on the temperature. The measurements with thermal paste for larger diameter wires (> 100 nm) can deviate significantly from the measurements without paste. The reasons for this are still under discussion. There is a tendency that the maximum of the resistance shifts to higher temperatures as the wire diameter decreases. For smaller wires in the range of 60 - 30 nm this can even lead to an almost linear dependence on the temperature. Similar behavior of Bi nanowires with diameters in the range of 1 μm to 40 nm can be found in literature [186, 205, 204, 189, 179]. Since the mean free path of charge carriers in Bi is ∼100 nm at room temperature [206], the observed behavior is usually attributed to finite- and quantum size effects. For wires with diameters smaller than 60 nm also the semimetal to semiconductor transition could influence the observed behavior [202].

5.3 Complete Characterization of Crossplane Thermoelectric Transport Properties

The setup used in the previous sections allows the measurement of the Seebeck coefficient as well as the resistance of a sample. In order to additionally measure the thermal conductivity of one and the same sample, a previously designed steady state method by H. Reith was further developed [207]. The revised setup allows to completely characterize the cross plane thermoelectric properties (Seebeck coefficient, electrical resistance, thermal conductivity) of an embedded nanowire assembly and can in principle also be applied for other thin film samples. The work presented in the following section was published in [111].

5.3.1 Experimental

Sample Preparation

In order to completely characterize the thermoelectric properties of embedded nanowire assemblies, a simultaneous measurement of the cross-plane thermal resistance R_T, electrical resistance R and Seebeck coefficient S is needed. Figure 5.10 shows a schematic of the experimental setup employed. A ∼4 mm × 1.5 mm piece, cut out of a nanowire assemble in polymer, is glued to a 300 μm thick silicon wafer that is covered with a 300 nm thin Si_3N_4 insulating film, using a silver-filled epoxy (Elecolit 323 by Panacol), with the cap side facing the epoxy. In order to harden the epoxy faster, the sample is put into an oven at

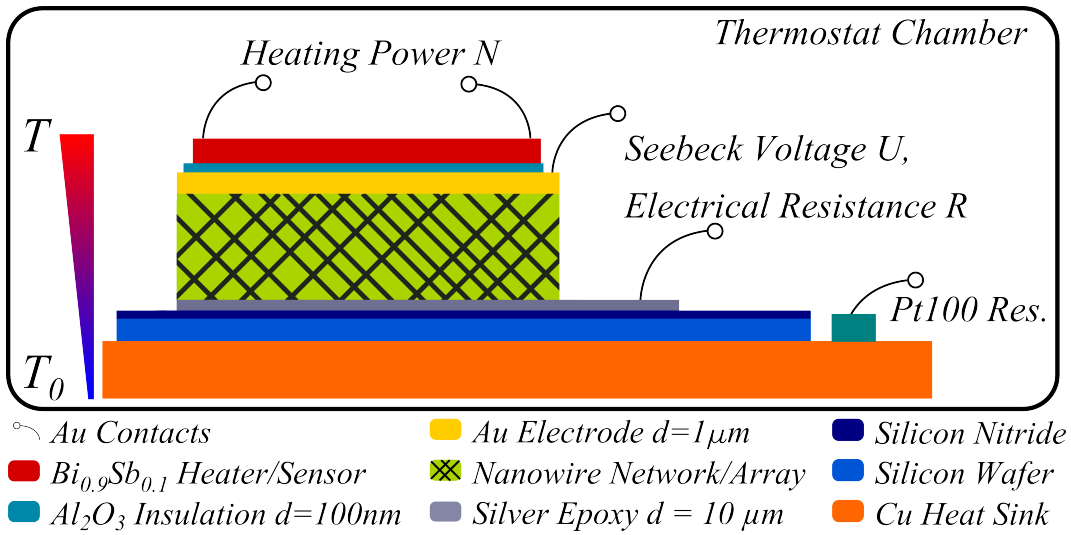

Figure 5.10: Sample setup for a steady state method for the complete characterization of thermoelectric transport properties in cross plane direction.

110 °C for one hour. Measurements on glued samples revealed a layer thickness of ∼10 μm for the silver epoxy after the heat treatment. The length of the silver epoxy layer is ∼3 mm larger than the sample, in order to allow the electrical contact to the bottom side. In order to electrically contact the sample to the measurement platform, two thin gold wires (diameter ∼ 50 μm) are attached to the silver epoxy and the gold layer on top (working electrode from electrodeposition) of the samples respectively, again using the same silver epoxy and an additional heat treatment.

In the next step the sample is covered by a ∼100 nm thick Al_2O_3 layer, using atomic layer deposition (ALD), to insulate the sample electrically from the heater, that is applied afterward. Due to the excellent conformal coverage of the ALD process it is possible to reliably insulate the samples.

Using an aluminum mask, the heater was then deposited on top of the sample. For this 0.1 g of Sb and 1.0 g Bi were placed together in a small tungsten pan and then evaporated onto the sample at a chamber pressure of $2{\cdot}10^{-5}$ mbar. The deposited layer thickness was monitored during the process by an oscillating quartz crystal. The generated film had a thickness of ∼100 nm and a composition of $\sim Bi_{0.9}Sb_{0.1}$. This material was chosen as it has a negative temperature coefficient. Due to this, if the heater gets damaged during the measurements, an increase in resistance would be seen instead of a decrease, as the temperature rises.

For electrical contacting, four gold wires were attached with silver-epoxy to the heater, using the same process as for the other contacts before. Due to the masking the prepared thin film almost had the same width and length as the sample underneath. The large lateral dimensions l and b of a few millimeters (similar to the sample size), when compared to the thickness of the sample d (∼ 30 μm), allows to generate an almost perfect heat flux from the heater to the substrate. The silicon chip with the nanowire sample on top was then placed on top of a copper heat sink. In order to guarantee a good thermal contact between silicon and copper, thermal conducting paste (MX-4 by ARCTIC) was applied in between. The whole setup was then placed inside a Dewar vessel, whose temperature was controlled by a Lauda RM6 thermostat, using water for heating and cooling of the Dewar. Previous test using an oven as well as a heating plate for temperature control of the stage proved to have an insufficient level of temperature stability during measurements. Lastly the connections from the sample were connected to their respective measurement devices. For the heater an Agilent E3641a power supply was used. The electrical voltage across the

heater, the current through the heater, as well as the Seebeck voltage generated in the sample due to the temperature gradient, were all measured using a set of Keithley 2700 multimeters. The temperature T_0 of the copper heat sink was measured using a Pt100 electrical resistance on top of the copper heat sink, close to the sample, attached to a FLUKE 45 multimeter.

Measurement Procedure

All measurements were performed in a temperature range between 10 - 90°C with temperature steps of 10°C, starting from 10°C. When the temperature of the PT100 arrived at a stable level (temperature change smaller than 0.01 °C within 10 min) the supply voltage was sweeped three times from 10 - 40 V, in steps of 3 V. In order to prevent a potential temperature rise in the heat sink, the voltage supply to the heater was only switched on long enough (∼10 s) to measure the voltage across the heater, the electrical current through the heater and the thermal voltage across the sample. Then, before going to the next voltage step, the sample was allowed to reach thermal equilibrium, by waiting for a few seconds. It should also be noted that an additional resistance (∼ 2 kΩ) was placed in front of the heater in order to improve the measurement stability. Therefore only a fraction of the potential drop was generated across the heater.

After the three voltage sweeps, the resistance R of the sample was measured, using a four point measurement, before going to the next temperature step. Due to the assembly of the sample the resistance measured includes the resistance of the nanowires as well as the contact resistances of the gold and silver filled contact electrodes.

Data Processing and Evaluation

In order to calculate the Seebeck coefficient and the thermal conductivity, the temperature drop ΔT across the sample, that is generated by the thin film heater on top, needs to be known. When an electrical heating power N is dissipated in the heater, the temperature increase with respect to the heat sink temperature T_0 can be evaluated by the resistance change of the heater using:

$$(T - T_0) = \frac{\Delta R_H}{\beta R_H(T_0)}, \tag{5.3}$$

where R_H is the electrical resistance of the heater, ΔR_H the change in resistance when power is supplied to the heater and β the associated temperature coefficient. In order to estimate $R_H(T_0)$, first the resistance $R_H(T)$ was calculated for each supply voltage using the measured voltage across the heater and the electrical current through the heater. From a plot of R_H against the heating power N, the y-axis intercept was taken as $R_H(T_0)$. The temperature coefficient β was then calculated from the slope of $R_H(T)$ against T. The thermal gradient calculated this way is applied across the whole sample, going from the heater on top to the copper heat sink at the bottom. In case of a cross plane heat flux, the ratio of the temperature increase and the heating power represents the total thermal resistance R_T of the sample, which is given by:

$$\frac{T - T_0}{N} = R_T = R_{Sub} + R_{Int} + R_H + R_{NWA}, \tag{5.4}$$

where R_{Sub}, R_{Int}, R_H and R_{NWA} are the thermal resistance of the substrate, interfaces (Al_2O_3 insulation, Au layer and silver epoxy), heater and polymer containing nanowires, respectively. To apply the method, the thermal resistance R_{NWA} needs to be the dominating term in eq. 5.4, which will now be shortly evaluated. It should be noted that this method is not only applicable for nanowire assemblies (NWA), but also thin film samples that obey the requirements. Table 5.1 lists the dimensions and physical parameters of the sample used in order to evaluate the thermal resistances of the setup. In order to estimate the thermal resistance of the substrate, one also needs to consider the thermal spreading resistance of the substrate, which cannot be described by simple geometrical dimensions. A rough approximation of the spreading thermal resistance in case of a line shaped heater with a width b_{Heater} is given by:

$$R_{Sub} = \frac{b_{Heater}}{\lambda_{Sub}}, \tag{5.5}$$

where λ_{Sub} is the thermal conductivity of the substrate. For a more precise determination of the substrate and heat sink thermal resistance simulations are required, which can be found in [111].

Table 5.1: Dimensions and physical parameters of the sample layers used for the evaluate of the thermal resistances of the setup.

Material	**Length** l **[mm]**	**Width** b **[mm]**	**Thickness** d **[μm]**	**Therm. Cond.** λ **[W/mK]**	**Therm. Res.** R **[K/W]**
$Bi_{0.9}Sb_{0.1}$ Heater	6	1	0.1	4	0.0021
Al_2O_3 Insulation	6	1	0.1	30	0.0006
Au Contact	6	1	1	100	0.0017
Nanowire Assembly	6	1	30	0.5	10
Ag-filled Epoxy	10	1	10	3.5	0.2857
Si Substrate	20	20	300	150	0.005
Cu Heat Sink	20	20	2000	400	0.125

Using the values given in table 5.1, the thermal resistance of the nanowire assembly amounts to ~96% of the total thermal resistance, clearly dominating the thermal resistance in the system. The second biggest contribution with ~2.7 % is given by the silver epoxy. For the calculation of the Seebeck coefficient and the thermal conductivity it will therefore be assume that the temperature gradient along the nanowire assembly is 2.7 % lower than the measured temperature gradient. Therefore, in order to calculate the thermal conductivity of the nanowire assembly eq. 5.4 can be written as:

$$\frac{\Delta T_D}{N} = R_{NWA} = \frac{d_{NWA}}{\lambda_{NWA} b l}, \tag{5.6}$$

where $\Delta T_D = \Delta T_{NWA} + \Delta T_{Epoxy}$, N is the heating power, d_{NWA} is the thickness of the nanowire assembly

and b and l are the width and length, respectively. The Seebeck coefficient is calculated by:

$$S = \frac{U_{Th}}{\Delta T_{NWA}}, \tag{5.7}$$

with U_Th being the measured voltage when the temperature difference is applied. Since gold has a Seebeck coefficient of ∼0.4 $\mu V K^{-1}$ and silver of ∼0.2 $\mu V K^{-1}$, the additional contributions of the gold thin film and leads, as well as of the silver epoxy is neglected. Considering the measurement accuracy, the most crucial parameter is the temperature gradient ΔT_D, whose uncertainty was evaluated to be about 15 %, whereas the uncertainty of the electrical quantities U_{Th}, R_H, N and R are detected with an uncertainty of smaller than 1 %. The error of the geometrical sample dimensions is smaller than 4% by using an optical microscope.

5.4 Results

Figure 5.11 shows exemplary the dependence of the measured thermo voltage on the generated temperature gradient for different ambient temperatures for a Sb nanowire array with 10^8 wires/cm^2 and a wire diameter of ∼120 nm. As assumed from eq. 4.1, there is a linear relationship between the generated voltage and the temperature gradient, with the slope being the Seebeck coefficient. Figure 5.12 shows the calculated Seebeck values for the same Sb nanowires array as well as for a 30 μm thick Sb network, prepared in a template irradiated with $4 \times 1 \cdot 10^9$ i/cm^2 and a pore diameter of ∼150 nm, in dependence of the temperature. It should be noted that the electrical insulation between the sample and the heater in case of the nanowire network was done using a layer of photoresist instead of the Al_2O_3 ALD coating.

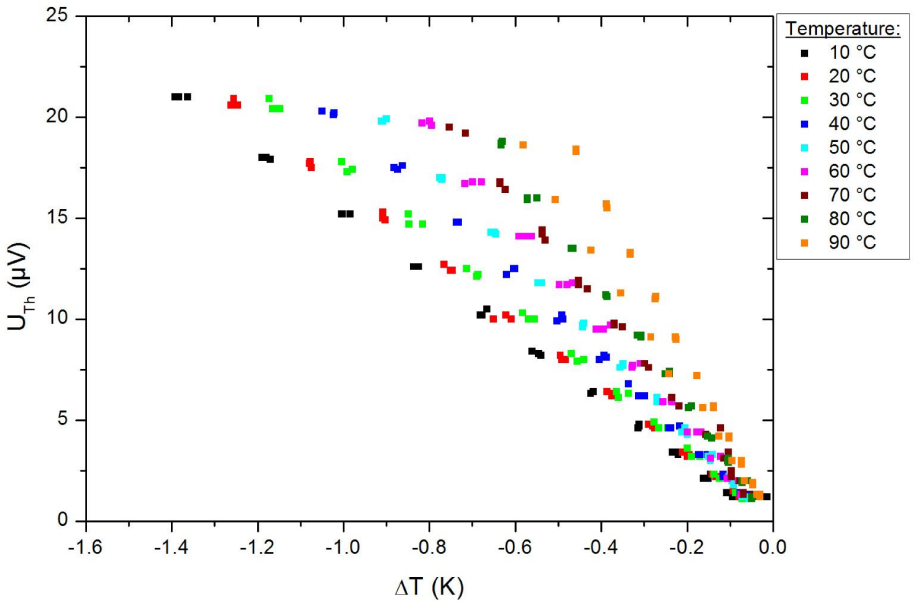

Figure 5.11: Measured thermo voltage in dependence of the temperature gradient at different ambient temperatures for a Sb nanowire array with 10^8 i/cm^2 and a wire diameter of ∼120 nm.

Both samples show a linear increase of the Seebeck coefficient with increasing temperature, which is similar to the measurements shown before using another setup for lower temperatures. Also the values obtained at 300 K fit well with the previous measurements, proving that the calculated temperature gradient should be correct. Figure 5.13 shows the relative electrical resistance of the Sb nanowire array (black) and the Sb network (red). Again, the exact amount of connected wires of the sample is unknown, thus only the relative resistance values will be shown. Both samples show a linear increase of the resistance with increasing temperature (metallic behavior), as was also observed with the measurement setup used before.

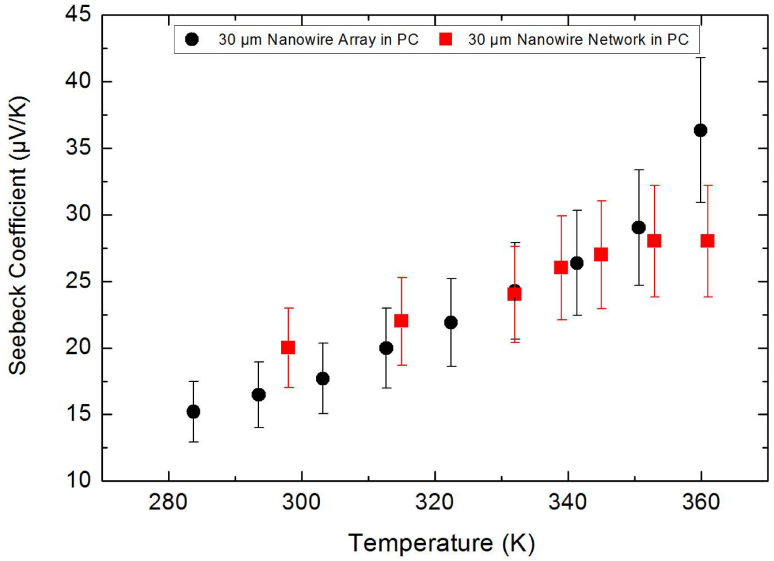

Figure 5.12: Seebeck coefficient as a function of temperature of a 30 μm thick array of 10^8 i/cm^2 Sb nanowires with a diameter of ∼120 nm (black) and a 30 μm thick Sb network, grown in a template irradiated with $4 \times 1 \cdot 10^9$ i/cm^2 with a pore diameter of ∼150 nm (red).

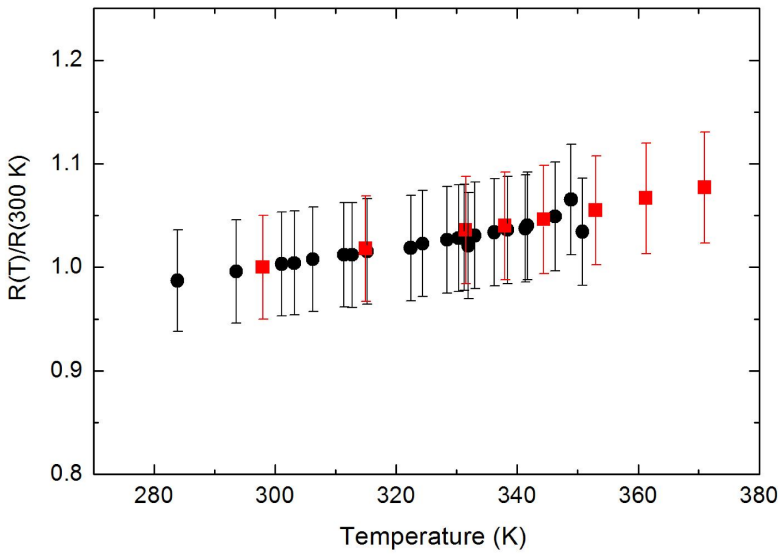

Figure 5.13: Relative electrical resistance as a function of temperature of a 30 μm thick array of 10^8 i/cm^2 Sb nanowires with a diameter of 120 nm (black) and a 30 μm thick Sb network, prepared in a template irradiated with $4 \times 1 \cdot 10^9\ i/cm^2$ with a pore diameter of ∼150 nm (red).

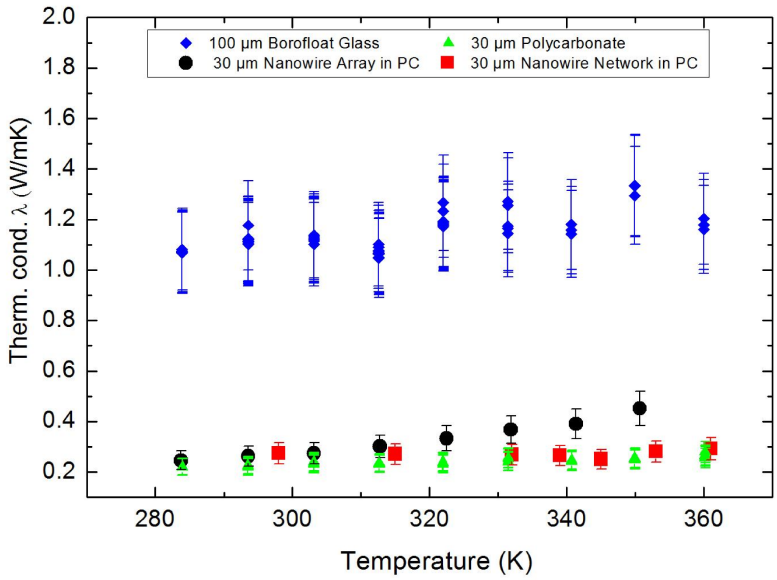

Figure 5.14: Measured thermal conductivities of a 100 μm thick borofloat glass (blue), a 30 μm thick polycarbonate foil (green), a 30 μm thick array of 10^8 i/cm^2 Sb nanowires with a diameter of 120 nm (black) and a 30 μm thick Sb network, grown in a template irradiated with $4 \times 1 \cdot 10^9$ i/cm^2 with a pore diameter of ∼150 nm (red).

Figure 5.14 shows the measured thermal conductivities of a 100 μm thick borofloat glass (blue), a 30 μm thick polycarbonate foil (green), a 30 μm thick Sb nanowire array with 10^8 wires/cm^2 with a diameter of 120 nm (black) and a 30 μm thick Sb network, grown in a template irradiated with $4 \times 1 \cdot 10^9$ i/cm^2 and pore diameters of ∼150 nm (red). The thermal conductivities of the borofloat glas as well as of the pristine polycarbonate were measured in order to test the setup. Since both samples are non-conductive no insulating layer was applied between the samples and the heater. Both materials show thermal conductivities that are expected from literature, namely ∼0.21 W/mK for polycarbonate [69] and ∼1.15 W/mK for borofloat glass [208]. The thermal conductivity of the nanowire network is constant within the measurement error and has a value of ∼0.27 W/mK which is only slightly larger than the value of the pristine polycarbonate. Also the nanowire array shows a low thermal conductivity starting at ∼0.24 W/mK at 283 K but rising to ∼0.45 W/mK at 350 K. This might indicate that the nanowire network compared to arrays is in fact able to stronger suppress the thermal conductivity, as predicted [15]. However more measurements are required to support this claim.

Due to the unknown values of the contact resistances of the sample, the figure of merit for the two nanowire assemblies is not calculated, as this value would suffer from a large uncertainty.

5.5 Summary

This chapter describes the measurements of the cross plane Seebeck coefficient and electrical resistance of the nanowire arrays and nanowire networks of Sb and Bi, presented in chapter 2.3. Both the electrical resistance and the Seebeck coefficient were measured between room temperature and 40 K using the setup shown in figure 5.1.

Sb nanostructures exhibited a positive Seebeck coefficient between 18 - 25 μV/K at room temperature,

that linearly decreased as a function of the temperature to 3 - 4 μV/K at 60 K. The Seebeck coefficient at 300 K of bulk Sb is reported to be in the order of 40 μV/K for the trigonal direction ([00.1]) and 10 μV/K for the binary direction ([10.0]). Considering that the presented nanowires show a texture in [01.2] direction, the measured Seebeck coefficients are comparable to the bulk material. The results showed no influence of wire diameter and/or wire density on the Seebeck coefficient.

Relative resistance R(T)/R(300 K) vs. temperature measurements evidenced in all cases a metal-like behavior. For arrays the relative resistance did not vary much with the wire diameter. For Sb nanowire networks however, smaller wire diameters showed a smaller decrease of the electrical resistance with decreasing temperature, what is attributed to a higher carrier scattering at the wire surface.

The Seebeck coefficient of Bi nanowire assemblies showed a non-monotonous dependence on the temperature. At 300 K the Seebeck coefficient of Bi nanowire arrays was in the range of -48 - -20 μV/K. The Bi nanowire networks had Seebeck coefficients in the range between -44 - -22 μV/K at 300 K. For wire diameters smaller than 140 nm the Seebeck coefficient at 300 K decreases with decreasing wire diameter, which can be attributed to the contribution of surface states on the charge carrier transport. At about 250-200 K for nanowire arrays or ∼170 K for nanowire networks, the Seebeck coefficient becomes positive before reverting back to zero. There is a clear trend that the higher the transition temperature to a positive Seebeck coefficient, the larger the maximum positive Seebeck coefficient. Also the larger the diameter of the wires, the lower is the transition temperature. The arrays prepared with surfactant tend to show larger positive values of the Seebeck, which might be related to the lower texture of the samples. The network samples in general show the lowest positive Seebeck when compared with arrays of the same diameter, which is probably due to different scattering processes and/or due to a different crystal structure. In general the observed behavior fits well to the theory of mean free path limited transport.

Also the relative electrical resistance shows a non-monotonous behavior in dependence on the temperature. The maximum resistance shifts to larger temperatures with smaller wire diameters. In the case of diameters between 60 - 40 nm this can lead to an almost linear dependence on the temperature. The observed behavior is usually attributed to finite- and quantum size effects reported in literature.

A steady state method for the complete thermoelectric characterization (Seebeck coefficient, thermal conductivity, electrical resistance) of nanowire assemblies in polymer and thin films was developed. Test measurements in a temperature range between 280 - 360 K of the thermal conductivity of borofloat glass and polycarbonate confirmed the functionality of the approach. The use of a $Bi_{0.9}Sb_{0.1}$ heater in combination with a ALD deposited layer of Al_2O_3 as electrical insulation allowed to measure the Seebeck coefficient, thermal conductivity, electrical resistance, in cross plane direction, of embedded Sb nanowire arrays and Sb nanowire networks. The observed Seebeck coefficient and electrical resistance behavior fit well with the values measured using the other setup. The thermal conductivity of the Sb nanowire assemblies was in the order of 0.2 W/mK, i.e. as low as the pristine polycarbonate and much lower than the bulk value of ∼ 24 W/mK [200].

6 Fabrication of Nanowire-Based Thermocouples

"The eye sees only what the mind is prepared to comprehend.
- Robertson Davies

Thin film thermoelectric devices are already commonly used for a variety of sensor and cooling applications [209, 210, 129]. Since the sensing thermoelectric films spread over a certain area on the surface of the device, the number of thermocouples that can be placed on a device is limited by the required area of the films on the surface. Therefore, a vertical alignment of thermocouples could lead to an improved usage of space. With respect to this, vertical aligned nanowires would allow to increase the number of elements per surface area, which could be used to increase the resolution or the power output of a device.

This chapter presents the preparation of arrays of vertically aligned, nanowire-based thermocouples. For a more detailed description of thermocouples and the benefits of nanowires in thermoelectric application, see chapter 4.4. The individual thermocouples consist of a leg of antimony and a leg of bismuth, each leg being composed of bunches of individual, vertically aligned, parallel nanowires. At first a description of the state of the art will be presented. Afterward the concept of the chosen fabrication route is introduced, before discussing the experimental details and challenges encountered during the yet implemented steps of the process.

6.1 State of the Art

Several works have already been published that evaluate the use of vertically aligned nanowire arrays as thermocouples. Nevertheless commercial implementation is challenging, partly due to the high complexity of the assembly process.

For example Kim et al. prepared two prototype devices based on nanowires arrays [211]. One made of electrodeposited Bi_2Te_3 nanowires in anodic aluminum oxide (AAO) templates, with wire diameters of 200 nm and wire lengths of 60 μm. The other one made of Si nanowires grown via a vapour liquid solid (VLS) method, with wire diameters between 100-200 nm and wire lengths of 20 μm, that have been subsequently embedded in parylene. Estimations of the efficiency of the Si nanowire device, based on measurements of the electrical and thermal transport properties, showed that it is comparable to a device made from bulk Si, making it not suitable for application [113]. However, due to the large abundance of silicon and the strong decrease in thermal conductivity in thinner wires, further efforts seem promising [30].

Keyani et al. [144] have prepared hybrid nanowire-bulk devices as a mean to characterize nanowires. The devices consist of $Bi_{0.3}Sb_{0.7}$ nanowires in AAO as the n-type leg and a $Bi_{0.4}Sb_{1.6}Te_3$ bulk element as the p-type leg. The wires were prepared by potentiostatic electrodeposition and showed a very homogeneous growth in length and areal density. The homogeneity was achieved due to a low growth speed during deposition. The grown wires had a diameter of ~100 nm and a length of 50 μm, but did not completely fill the entire length of the pores. This was done intentionally, so that after wire growth, nickel could be deposited on top of the wires until it filled the remaining volume of the pores, which served as protection of the wires and as a mechanical robust contact layer. To assemble the device, all components were connected to copper pads by using a low temperature solder. Electrical measurements showed that the

nanowires had a higher electrical resistivity than the comparable bulk material, which was attributed to the contact resistances and an unfavorable microstructure of the nanowires. Used as a Peltier device, a maximum temperature difference of $7°C$ was achieved. The temperature difference was limited by the high thermal conductivity of the anodic alumina membrane. Lastly, also the efficiency of the device was measured, using the Harman technique. The figure of merit ZT was found to be 0.12, which is almost equal to the efficiency of a device that had been made from bulk material.

While the devices mentioned above consisted of a nanowire leg and a bulk leg, Okamura [212] published a patent suggesting the assembly of a thermoelectric device, with the p- and n-type leg consist of single nanowires. The idea is to use a template, preferably AAO, onto which an electrode structure is crafted. This first electrode pattern defines the areas where the wires should grow and also serves as a protection for the later grown nanowires. On top of this electrode a second electrode pattern is structured, using photolithography. This second electrode pattern allows the sequential electrodeposition of a n- and a p-type material into the appropriate pores. As an alternative, the use of a photoresist in order to isolate the areas where wires should not grow is mentioned. The pores themselves should have a preferred diameter of 5 nm to 100 nm and a length of 1 μm to 500 μm. Following the wire deposition, an electrode pattern is prepared on top, which connects the p- and n-type wires. Lastly the second electrode layer is removed and replaced with a final electrode on the bottom, that is patterned using photolithography.

In [213] Völklein et al. described the preparation of a thermal sensor, using nanowire arrays as thermocouples on top of a silicon wafer, which works as a heat sink for the final device. Figure 6.1 presents a summary of the preparation process. The required electrode structure is patterned on top of the silicon wafer after an electrically insulating layer of SiO_2 or Si_3N_4 is applied to it. The electrode pattern also allows to later connect the individual thermocouples. An ion track-etched membrane is then placed on top of the electrode structure. Alternatively, a PMMA or SU8 negative resist can be applied on top of the electrode structure, irradiated and track-etched. Using the electrodes on the bottom side, p- and n-type material is electrodeposited in a sequential process inside the pores of the template. After wire growth, as in the case of Okamura, a metal layer is structured in order to connect the two thermocouple legs. On top of these connections, a radiation absorbing layer with large absorption in the infrared, is deposited. As a final step, the template material is removed in a suitable organic solvent in order to improve the sensitivity and detectivity of the device. A similar theoretical process route can also be found in the work of Koukharenko et. al. [214].

Lindeberg et al. [130] used ion track-etched polyimide templates to prepare thermocouples of nickel and antimony nanowire arrays. One side of the template was completely covered with a copper seed layer and reinforced with a lithographically patterned nickel layer, which later worked as the interconnect of the thermocouple legs. In order to select the growth areas, a layer of photoresist was patterned on top of the membrane. Then antimony was deposited into the pores that were not covered by photoresist. Afterwards the photoresist layer was replaced with a new layer of patterned photoresist, this time covering the antimony nanowires and allowing the deposition of nickel in pores next to the areas containing antimony. In the following step, both materials were connected to each other via a lithographically patterned gold layer on top of the membrane. At this point all thermocouples are still connected to each other by the copper seed layer. In order to separate the thermocouples, the surplus copper is etched away, while the nickel layer on top served as an etch mask. This results in a structure where all the thermocouples are connected in series to each other. Finally, an absorption layer was applied onto the top layer (gold) of the thermocouples. The electrical properties as well as the IR-response of the final device were measured. The electrical resistance of a thermocouple was higher than the calculated values. The authors propose that this is either due to a non-homogeneous filling of the pores or due to the fact that the nanowires exhibit a different electrical conductivity when compared to bulk material. With regard to the use as thermal detector it was found that such a device exhibits white noise and the highest voltage response to a

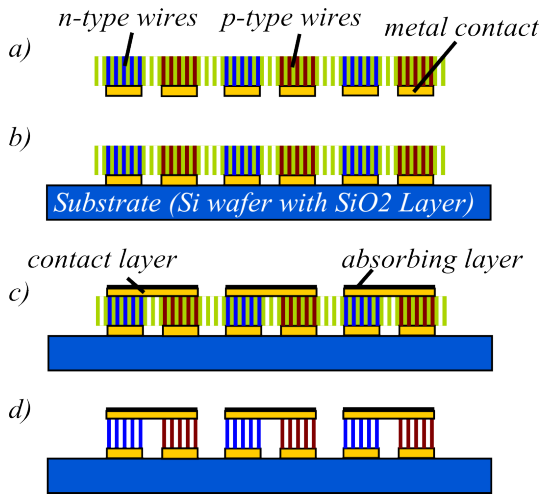

Figure 6.1: Preparation of a nanowire-based sensor: a) Sequential electrodeposition of p- and n-type nanowire arrays via structured contact pads in the pores of an ion track-etched template. b) Transfer of the prepared structure on a silicon heat sink. c) Deposition/patterning of a metal contact layer and an absorbing layer. d) Dissolution of the template foil.

pulsed light source was found to be 1.9 mV, when 126 thermocouples had been connected in series and an absorption layer had been applied onto the thermocouples. In order to measure the absolute temperature with such a device, a reference temperature is needed. Based on the previous design of Lindeberg [130], Mao et al. [28] prepared a new device, crafting a nickel thermoresistor onto the bottom of the device. Using such a device, it was found that in the temperature range between 20 - 70 °C, a simple linear relation can be used to correlate the temperature of a measured object, with the signals generated by the device. Additionally, due to the reduced thickness of the device, response times of 100 ms were found.

In this work we try to prepare vertically aligned, nanowire-based thermocouples by sequential electrodeposition of Bi and Sb in the pores of ion track-etched polycarbonate templates. In order to select the areas where a material is deposited, a lithographically structured backelectrode is prepared on one side of the template. The following section presents the process route that was theoretically developed prior to the experimental work.

6.2 Theoretical Fabrication Process

The schematics in figure 6.2 and 6.3 show the theoretical process route for the preparation of arrays of individual nanowire thermocouples using ion track etched polycarbonate templates. For each step a side view as well as a top view of the sample is shown. The sides of the templates are distinguished by a (T) for the top- and (B) for bottom-side.

The process starts with the preparation of a lithographically structured metallic contact layer on the bottom side of an etched ion-track template (Step 1-3), which will serve as the working electrode during the electrochemical deposition of the nanowires in step (5) and (6). In chapter 2.1 a detailed description on the preparation of ion track-etched membranes is given.

Step (1) consists of the preparation of a metallic layer on the bottom side of the template. This layer is subsequently structured via contact lithography, using a "positive" photoresist, that is spin coated onto the

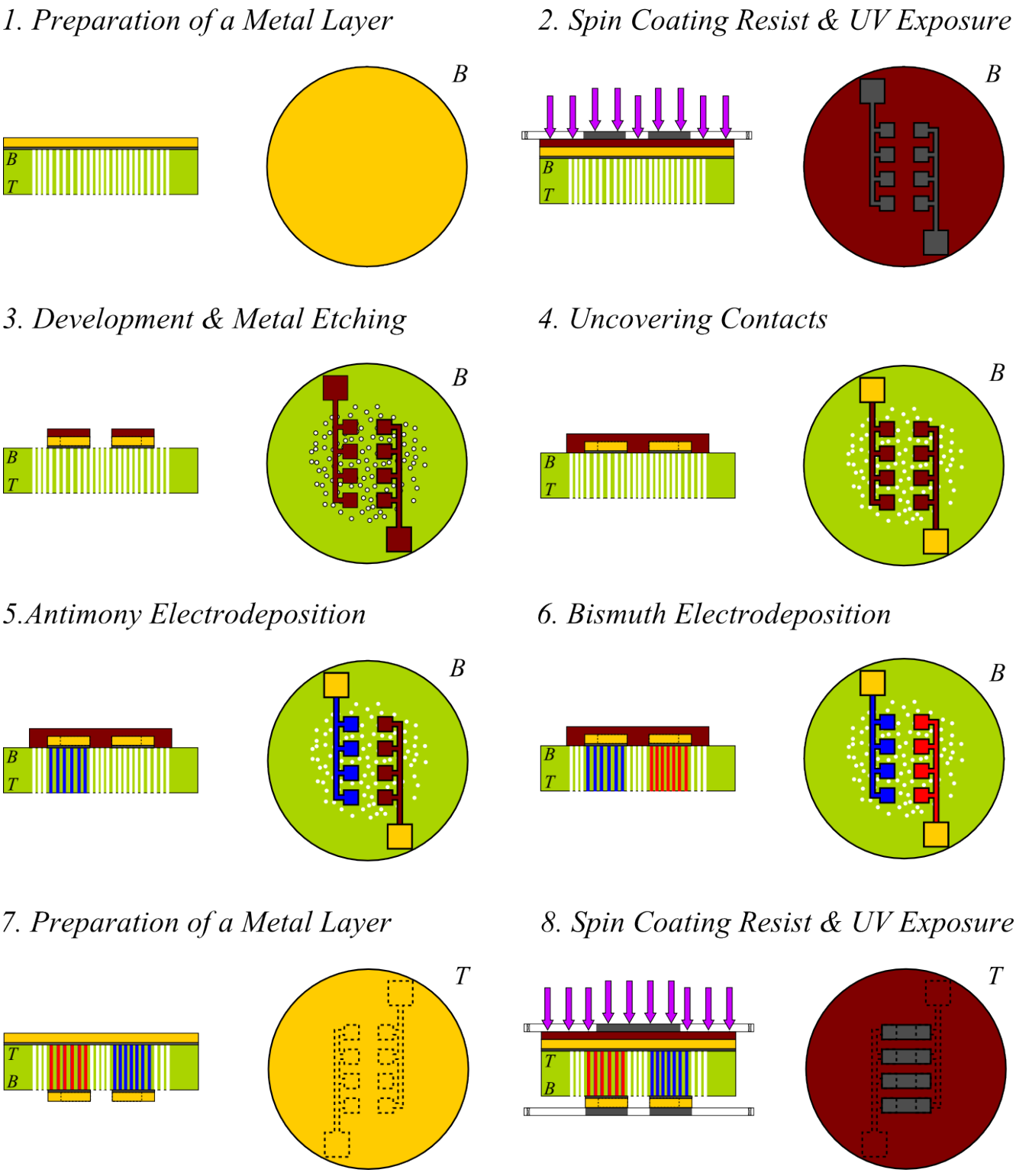

Figure 6.2: Side and top view of a template during the fabrication of nanowire-based thermocouples part I. The legend can be found in part II (figure 6.3). 1-3) Preparation of electrical contacts for electrodeposition, 4-6) Sequential deposition of Sb and Bi inside the pores of the template. 7-9) Preparation of electrical connections between the separate legs of the nanowire thermocouples on the top side of the template. The marks B and T identify the bottom and top side of the sample, respectively.

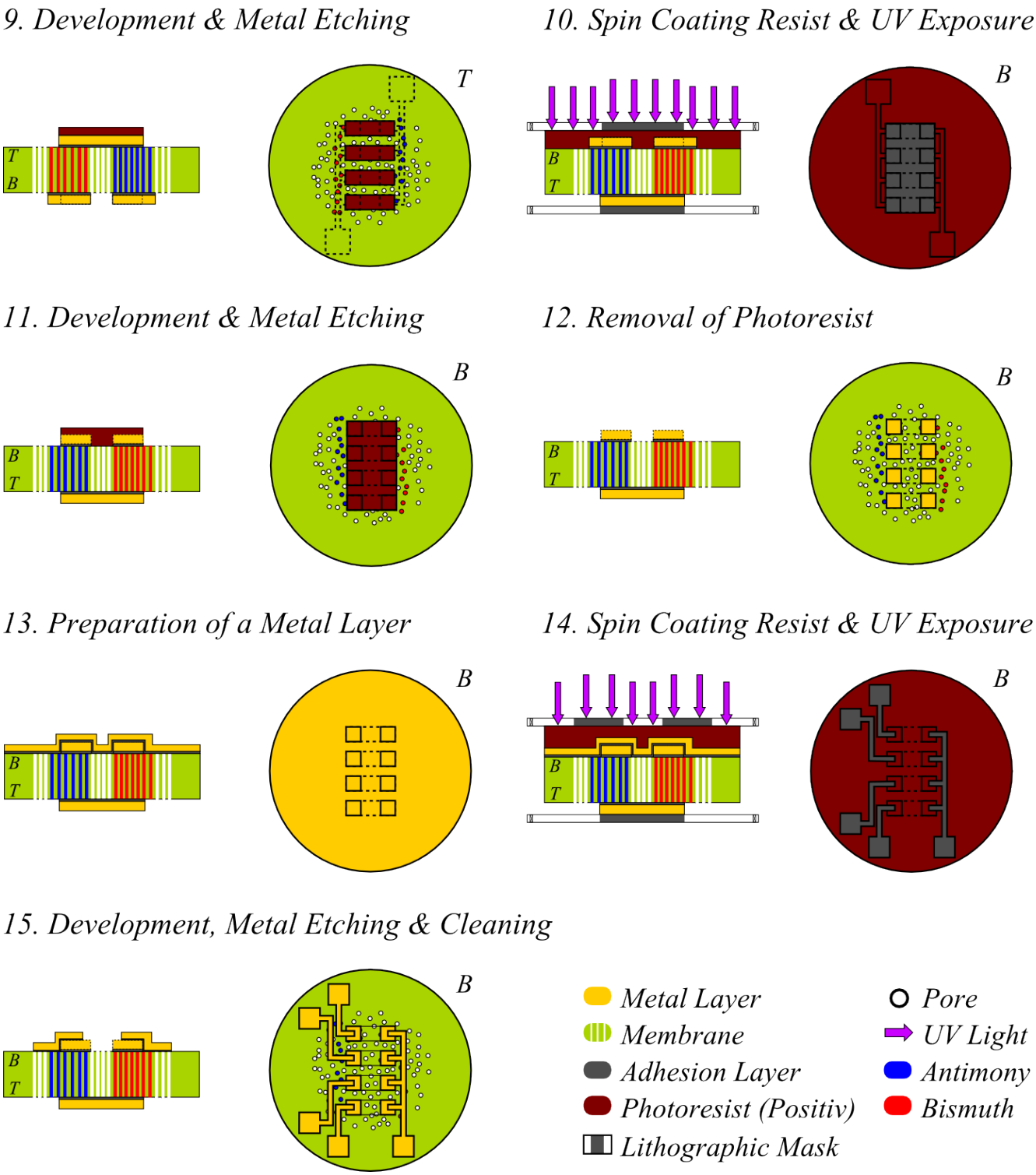

Figure 6.3: Side and top view of a template during the fabrication of nanowire-based thermocouples part II. 9-12) Removal of the initial contact lines that were used for electrodeposition. 13-15) Preparation of electrical contacts on the bottom side of the template, which allow the individual connection of each nanowire thermocouple. The marks B and T identify the bottom and top side of the sample, respectively.

sample, step (2) and (3). For a "positive" photoresist, areas that are exposed to UV-light becomes more soluble in a photoresist developer, therefore after development of the photoresist the pattern of the mask is transferred to the photoresist. Application of an appropriate etching solution will now remove only the metal in areas that are not covered by photoresist, transferring the pattern from the lithographic mask to the metal.

The schematic of the lithographic mask used in step (2) is depicted in figure 6.4. It is divided into 16 lines with a line width of 10 μm that end into larger contact pads (2 mm x 2 mm), placed at opposite sides on the bottom side of the template. Attached to each line are 120 small metal pads with a size of 50 x 50 μm, which define the growth area of the thermocouple legs. One small pad being an individual leg, two adjacent pads of different materials will later form the individual thermocouples. This leads to 960 individual thermocouples throughout the whole structure.

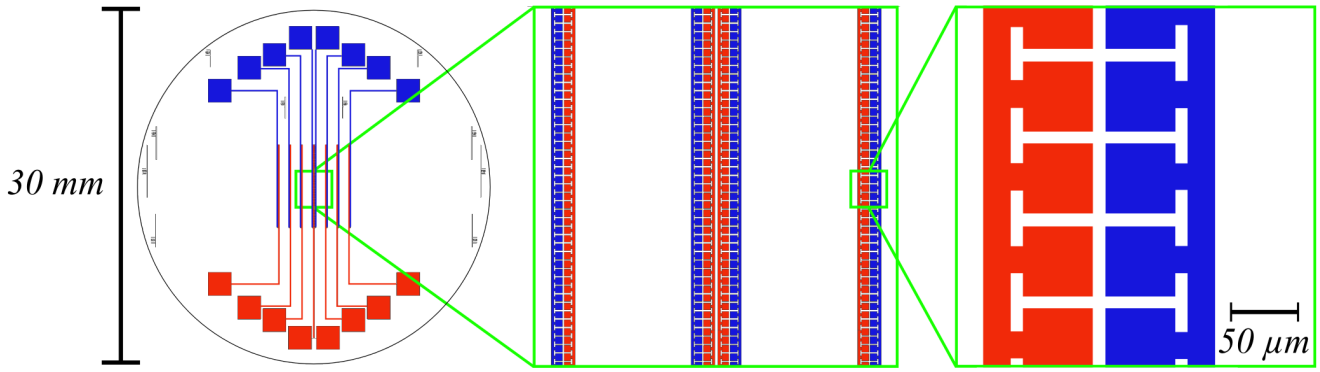

Figure 6.4: Schematic of the lithographic mask for the electrodes used for the sequential deposition of Sb and Bi inside the pores. The left side shows the whole structure that is transferred to the template. The right side shows a closeup of the central area of the mask where the individual thermocouple legs are generated. The colors indicate whether the small pads are connected to one of the large red or blue contacts.

It would also be possible to generate the structured metal layer by a so called "Lift-off" process, where a "negative" photoresist is lithographically structured to generate a negative image of the desired structure. In case of a "negative" resist the parts exposed to UV-light become insoluble to a photoresist developer. After development the resist therefore shows the negative pattern of the lithographic mask. After metallization the photoresist can be removed with a suitable etchant, so that the metal is "lift-off" the samples. The metal layer only stays attached to the sample in areas where the resist had been developed prior to metallization, leading to the same structure as the process with the "positive" resist. However, the "Lift-off" process was not considered, as the solvent inside the photoresist (PGMEA) can damage the template and especially destroy the pores [215].

In order to guarantee good electrical contact to the large contact pads for the following electrodeposition of material, the photoresist is removed from the larger outer contact pads (step 4). This is done by hand using cotton swabs and isopropanol.

For electrodeposition the template with the structured backelectrode is placed between two Teflon cells, similar to figure 2.18b). For electrical contacting one Teflon compartment, shown in figure 6.5, is equipped with two separate stainless steel contacts, that are pressed onto the sample using springs. This allows the individual electrical connection of the different areas of the structured backelectrode (blue and red areas in figure 6.4.

Figure 6.5: Photograph of Teflon compartment with two stainless steel contacts used for the sequential electrodeposition of material inside the pores of an ion track-etched membrane with structured contacts. The two separate contacts allow the individual electrical connection of the different areas of the structured backelectrode (blue and red), shown in figure 6.4.

At first antimony is deposited in one of the two areas, by electrical contacting to one of the metal contacts (step 5). After electrodeposition the used Sb electrolyte is removed and the Teflon compartment rinsed with DI-water several times, in order to remove all Sb electrolyte leftovers, before the Bi electrolyte is filled in. Then bismuth is electrodeposited in the other area, by electrical contacting to the other metal contact (step 6). When the deposition is finished the Bi electrolyte is removed and the Teflon compartment rinsed with DI-water several times and the sample is dried with nitrogen.

Please note that the sequence of electrodeposition (first Sb, then Bi) is important. Preliminary experiments showed, that in a reverse order no electrically contact could be made to the Bi nanowires, possibly due to oxidation of the bismuth during the antimony deposition.

Steps (7-9) in figure 6.2 and 6.3, show the process to electrically connect the Sb and Bi filled areas on the top-side of the template, in order to form individual thermocouples. A metallic layer is prepared on the top side of the template (step 7) and structured via contact lithigraphy (step 8-9). In order to correctly align the top and bottom side of the sample, the masks for the galvanic contacts and for the connection of the thermocouples are aligned to each other, using a double-side mask aligner. Then the sample is aligned to the mask for the galvanic contacts. A two mask alignment like this is used whenever a structure on the top side needs to be aligned with the structure on the bottom side and this step will not be specifically mentioned further on. At the end of these steps, the two individual thermocouple legs, made from Sb and Bi, which are located adjacent each other, are connected to one another.

At this point of the process all the thermocouples are connected to each other via the contacts for electrodeposition on the bottom side of the sample. To generate an array of individual thermocouples, these electrical connections must be removed without removing the metal pads of the thermocouple legs. For this, the pads at the bottom are covered with a layer of photoresist, that is subsequently structured via contact lithography, so that it only covers the pads of the thermocouple legs (step 10). The contact lines can now be removed using a suitable etch solution (step 11). In order to allow the preparation of the final contact structure, the photoresist covering the gold pads from the previous step is removed (step 12) and a new metal layer is prepared on top of the pads (step 13) and lithographically structured by using the lithographic mask shown in figure 6.6 (step 14) . After development of the resist, removal of the uncovered metal layers and final removal of leftover photoresist the device is finished (step 15).

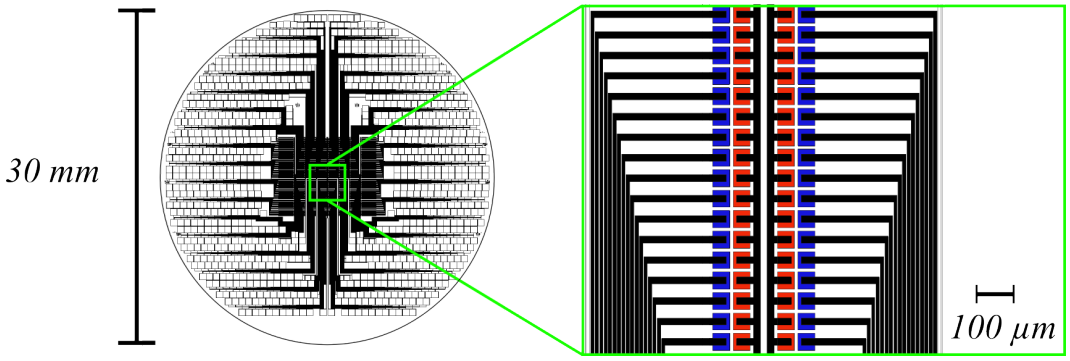

Figure 6.6: Schematic of the lithographic mask for the electrical contacts of the individual nanowire thermocouples. The left side shows the whole structure that is transferred to the template. Surrounding the central area are the contact pads for wire bonding. The right side shows a closeup of the central area containing the thermocouples. Blue and red indicate the thermocouple legs of different materials and black indicates the contact lines.

Each individual thermocouple can now be contacted by the 0.6 mm x 0.6 mm contact pads on the outer rim of the device. To improve the performance, the polymer membrane could be removed in a next step, in order to prevent the parasitic heat transport through the polymer matrix.

6.3 Experimental Details and Challenges

The following sections present the experimental preparation of the structured electrodes for electrodeposition as well as the sequential deposition of antimony and bismuth in the pores of an ion track-etched membrane, using said electrodes. Due to various challenges, only the steps 1-6 of the theoretically presented process could be implemented experimentally yet. Additionally, experiments on the removal of the polycarbonate matrix via reactive ion etching (RIE) are presented.

6.3.1 Preparation of Structured Metal Contacts on Polycarbonate

It is crucial for the metal contacts to stick to the polymer and completely cover the template pores, in order to protect the polymer from the photoresist and to obtain good results during the electrodeposition process.

Various approaches were tested to prepare the metal layer, with the most promising results being achieved by sputtering a ∼200 nm thin layer of gold on top of the smooth side of the polycarbonate membrane, using an Edwards S150B sputter coater at a chamber pressure of $\sim 10^{-1}$ torr with 1.5 kV and a current of ∼18 mA. Subsequently this layer was reinforced by electrodeposition of gold, using a commercial electrolyte (Gold-SF by METAKEM). The electrodeposition was done at room temperature, at a potential of -0.7 V vs. a gold spiral anode in a two electrode setup. In order to improve the adhesion of the fabricated layers to the template surface, gold was then deposited inside the pores, by using the prepared gold layer as a working electrode. The idea behind was, that the thereby grown Au nanowires anchor the Au layer to the template surface. For deposition the same setup and electrolyte kind was used as for the Au layer. This time however the deposition was done for 15 minutes, at a potential of -0.6 V vs. a gold spiral anode.

To improve the handling of the samples for the following lithography process the template was attached to a silicon wafer using Kapton tape. Then a layer of AZ 5214E photoresist (MicroChemicals) was applied on top by spin coating. For this purpose 1 ml of photoresist was dropped on top of the gold layer. The sample was then spun at 1000 rpm for 2 sec, so that the resist could spread over the surface and subsequently spun at 3500 rpm for 30 sec, so that the surplus photoresist was removed from the surface.

The sample was then placed on top of a hotplate with a temperature of 110 °C for 5 minutes for a soft bake of the resist and then set aside for another 5 minutes so the resist could rehydrate. Afterward, the mask for lithography was placed on top and the complete assembly was placed inside a double sided mask aligner. The resist was exposed to UV-light for 7.5 s with an intensity of ∼26 mW/cm^2 leading to a total dose of ∼195 mJ/cm^2.

Following this, the photoresist was developed at room temperature, using a AZ 726MIF developer (MicroChemicals). The development usually needed ∼30 s in order to completely remove the irradiated resist. Afterward the sample was rinsed with DI-water for 2 min in order to remove any residual developer. Although the developer contains NaOH, no increase of the pore size was observed after the process. After drying the sample using nitrogen gas, the uncovered gold was removed by Lugols iodine at room temperature. Usually a 500 nm thick gold layer was removed in ∼1 min. After a final rinsing of the sample, in order to remove residuals of the etching solution, the sample was kept in DI-water overnight, to make sure etchant residues left inside the pores will be completely dissoluted.

Figure 6.7 shows a) a light microscope image, as well as b) a SEM image of the electrode pattern after the lithography process. The gold layer shows no open porosity and appears to stick well to the template surface. Figure 6.7c) shows the ∼2.5 μm long gold nanowires grown inside the template in order to improve the adhesion of the gold layer. Even though not many samples were prepared this way, the initial results with this kind of electrodes look promising for further experimentation.

Other tests with gold layers without the anchoring nanowires were usually not successful, as these gold layers showed unreliable adhesion to the template surface. Additional experiments were conducted where the surface roughness of the template was increased by reactive ion etching (RIE) for 2 min, before sputtering the gold on top. As seen in chapter 2.3, the reactive ion etching does not completely remove all the polymer, but leaves polymer residuals that might allow the gold to adhere better to the surface. However, the adhesion did not improve satisfactorily and since the pores were also enlarged during the RIE process, the gold layer did not completely close the pores, leading to deposition on the backside of the electrodes, as shown in figure 6.8.

In addition to the processes mentioned above, also gold layers with an additional chromium layer in between gold and polycarbonate have been tested, but were not as reliable as the pure gold layers. For the first experiments with this layer structure ∼10 nm Cr and successive ∼500 nm Au were sputtered onto the rough side of the template, using a Balzers BA 500 sputter coater. This sputtering machine is equipped with two separate DC magnetron targets, which allows the preparation of the layers without breaking the vacuum. The chromium layer was prepared by using known standard parameters (440 V, 140 mA, 3·10^{-}3mbar) resulting in a growth rate of ∼2 Å/s, whereas for the gold layer the sputter voltage was adjusted, so that a growth rate of 10 Å/s was achieved (∼360 V, ∼170 mA). The growth rate was measured in situ using an oscillating quartz crystal. The rough side was chosen at first, since the sputtered metal layers adhere better to this side. The following lithography process for the Cr/Au layers was done in the same way as the one mentioned above, with the addition that the chromium layer was etched using Orange etch at room temperature, after the gold was removed. Usually it took ∼15 sec in order to remove the ∼10 nm Cr thin layer. After the lithographic process, severe underetching of the metal layers was observed, most likely due to the high surface roughness of the rough side of the template. This

even went so far, that the contact lines, that should connect the areas of growth with the outer contact pads, were disconnected. Therefore, it was decided to prepare the contacts on the smooth side of the templates, which is in contrast to the generation of the nanowire assemblies previously mentioned in this work (chapter 2.2.3).

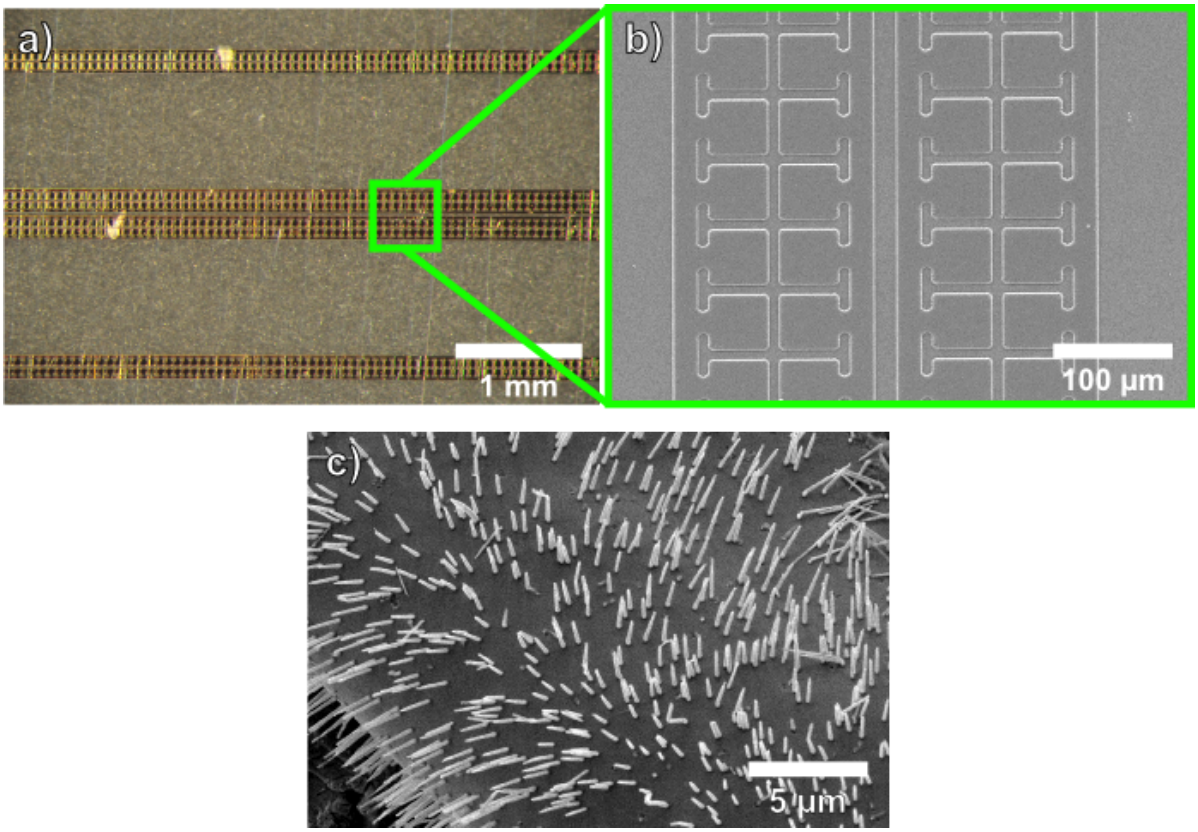

Figure 6.7: Light microscope image a) and SEM image b) of a structured electrode pattern after successful lithographical structuring. c) SEM image of a patterned electrode, side facing the template, with ∼2.5 μm long gold nanowires, grown for improved adhesion.

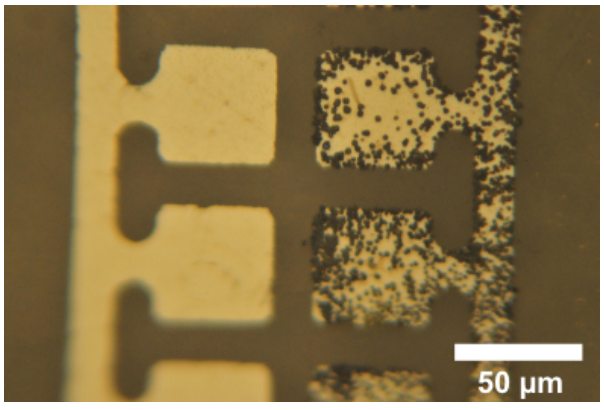

Figure 6.8: Light microscope image of an electrode pattern made from pure gold on top of a template that was treated with a RIE process to increase the surface roughness. Due to the reactive ion etching also the pores were enlarged and the sputtered gold layer did not completely close the pores anymore, leading to the formation of antimony caps on the backside of the gold electrodes after electrodeposition.

The Cr/Au layers prepared on the smooth side seemed to stick well to the template surface after the lithography process and electrodeposition in the selected areas was possible in some cases. However most of the times, after the sample was kept in DI-water overnight, or during the electrodeposition step, the contacts would peel of from the chromium layer, which in the later case lead to inhomogeneous depositions. Figure 6.9 shows a light microscopy image of an area where the gold layer detached from the chromium adhesion layer. The distribution of the holes in the chromium layer resembles the pattern of ion tracks, although the pores should have a smaller diameter. This observation can be explained by the fact that the Orange etch had access to the open pores on the top side of the membrane. Thereby it was possible for the etching solution to enter the pores and remove the chrome from underneath the gold. It was noticed that the adhesion of the metal layers on membranes with larger pores was worse as compared to smaller pores which can be explained by the fact that the etching solution should be able to pass easier through larger pores. A finally indication that the chrome was underetched through the pores was a color change from gray to golden, when observing the contact pads through the template, before and after the application of Orange etch.

In order to protect the chromium layer from the Orange etch, one could also grow gold nanowires inside the template, prior to the lithography process. With this one would possibly have the anchoring effects already seen in the first mentioned pure gold contact structures, as well as an improved adhesion of the contacts on the surface of the template.

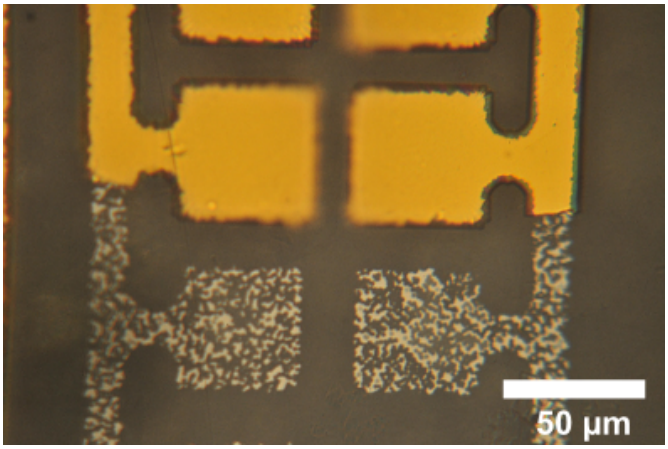

Figure 6.9: Light microscopy image of an area where the gold layer detached from the chrom adhesion layer. The holes visible in the chrom layer remind of pores, however they have a bigger diameter than the etched pores, which indicates an underetching of the chrom layer.

6.3.2 Sequential Growth of Sb and Bi Nanowires on Preselected Areas

As mentioned in the proposed preparation route (section 6.2), Sb and Bi are successively deposited inside the pores of a template by using the structured electrodes prepared on the bottom side of the template (figure 6.7 a) and b)). To test the quality of the electroplating process and the structured contacts, first only Sb or Bi is deposited in the selected areas on the sample, i.e. by contacting all electrodes at once. The electrodeposition process is equal to the process described for nanowire arrays/networks in chapter 2.2.3. In order to obtain a fast indication on the homogeneity of the electroplating, the deposition was allowed to continue for an additional hour, after cap growth started. In most of the presented cases, the electrodes were prepared from chromium/gold layers without additional gold nanowires deposited inside the pores. Therefore, effects due to a bad contact can not be completely excluded in the experiments.

Antimony Deposition

In the case of Sb different pulsed potentials were tested, ranging from -230 mV to -260 mV vs. SCE for the on-potential (reduction) and -120 mV to -150 mV vs. SCE for the off-potential. The on-/off-times of the voltage pulses were 20 ms and 100 ms, respectively. The optimum Sb growth seemed to have been obtained when the deposition was performed at on-/off-potentials of -250 mV/-130 mV vs. SCE. If the adhesion of the contacts was good, the caps formed a homogeneous layer, that ran along the whole contact on the top side of the sample (figure 6.10 a) and c)). The grown cap layer easily breaks of and in order to remove it, it is sufficient to dip the sample into a running ultrasound bath for a few seconds. Examination of the wires underneath these caps shows, that the wires grow in a homogeneous way in most of the pores, as can be seen in figure 6.10 b) and d). In order to obtain the image in figure 6.10 b), a Au layer was prepared on top of the grown Sb caps by sputtering and electrodeposition, using the same parameters as in chapter 2.2.3. This was done in order to generate a stable substrate for the grown Sb caps, as in the next step the polymer was removed using DCM. In principle figure 6.10 b) should show a top view of the structured electrode. However, during the dissolution of the polycarbonate the contacts broke lose from the grown nanowires, leaving only the nanowires behind. The wires, held together by the caps, nicely replicate the structure of the contact pads, again showing the homogeneous growth in the selected areas.

Bismuth Deposition

For bismuth electrodeposition, on-potentials between -250 mV and -210 mV vs. SCE and off-potential between -150 mV and -120 mV vs. SCE were tested, using on-/off-times of 20 ms and 100 ms, respectively. Best results were obtained with an on-/off-potential of -220 mV/-140 mV vs. SCE. However, these parameters are not yet optimal, as it can be seen in figure 6.11 a), the caps usually did not form a closed layer, but formed in spots. Figure 6.11 b) shows the grown Bi nanowires still embedded inside the template, after a 2 min RIE etching was performed, in order to access the wires below the surface. As already suspected by the cap growth, the wires did not homogeneously fill the pores, but grew in patches in the areas of the electrodes, marked by yellow lines. It should be stressed that effects from a bad adhesion of the back electrode can not be completely excluded and more experiments need to be performed to finally conclude on the matter.

Antimony → Bismuth Depositions

For the sequential deposition of Sb and Bi, the optimal potentials mentioned in the previous sections were applied for growth. However, in preliminary experiments it was observed that Sb nanowire arrays, that were immersed in the Bi electrolyte at 40°C, showed that the wires were dissolved in it. However, in experiments at room temperature, the Sb nanowire arrays seemed to be more stable. Therefore, the sequential depositions of Sb and Bi were conducted at room temperature. Additionally, Sb caps were allowed to grow for an additional hour after cap growth started. The cap layer on top of the Sb nanowires should then further prevent any dissolution of the Sb nanowires. It might not be necessary to completely suppress the dissolution of antimony during the bismuth deposition, as the growth of $Bi_{1-x}Sb_x$ alloy nanowires might actually be beneficial due to the higher expected Seebeck coefficient of the alloy. Therefore, as long as the Sb wires do not get dissolved, and nanowires are formed during the deposition of the second material, the process should be fine. Figure 6.12 shows a light microscope image of the prepared sample. In this case, a contact layer with gold nanowires grown into the pores was used. Sb forms a dense cap layer on

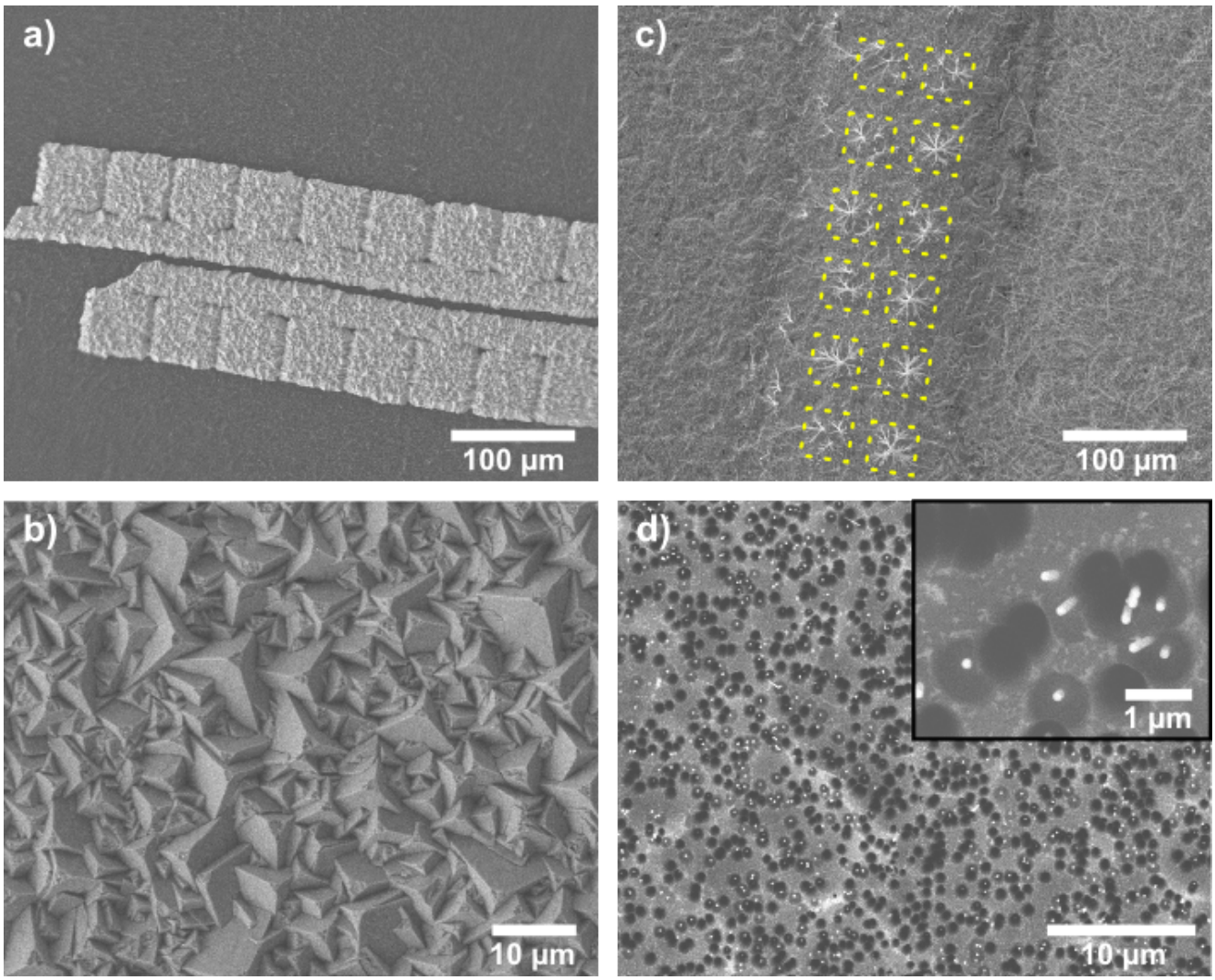

Figure 6.10: SEM images of Sb deposited in a template, using structured Cr/Au contacts. The template had pores of ∼100 nm in diameter and a pore density of 10^8 i/cm^2. Electrodeposition was done at 40°C, at an on-/off-potential of -250 mV/-130 mV vs. SCE with on-/off times of 20 ms/100 ms, respectively. a) Sb cap layer on the top side after deposition. b) Closeup of the cap layer. c) Arrangement of Sb nanowires after removal of caps and dissolution of polycarbonate in DCM. The yellow squares mark the position of the growth areas for thermocouple legs. d) Sb nanowires still embedded in the polymer, after cap removal and a RIE etching (2 min) of the polymer surface, in order to access the wires below the surface.

top of the sample, whereas the growth of Bi caps is not as dense. This fits well with the results from the previous sections, although the depositions here were done at room temperature instead of at 40°C. It should also be noted, that Bi seemed to grow more homogeneously at room temperature, which might in fact have been caused by the improved contact structure with the ingrown gold nanowires. In general this sample looked very promising, so in order to look at the deposited nanowires with the SEM, a layer of gold was deposited on the cap side and the polymer was dissolved, as shown in figure 6.13. The growth areas could be well distinguished from the surrounding gold, due to the cap structures of Sb and Bi. It seems that all grown nanowires broke off during the template removal. Since there were no wires to be tested by EDX, we investigated the material composition of the caps instead. The caps showed either pure antimony or pure bismuth peaks, with the addition of gold from the substrate (figure 6.14). Therefore it is assumed that the wires were also phase pure.

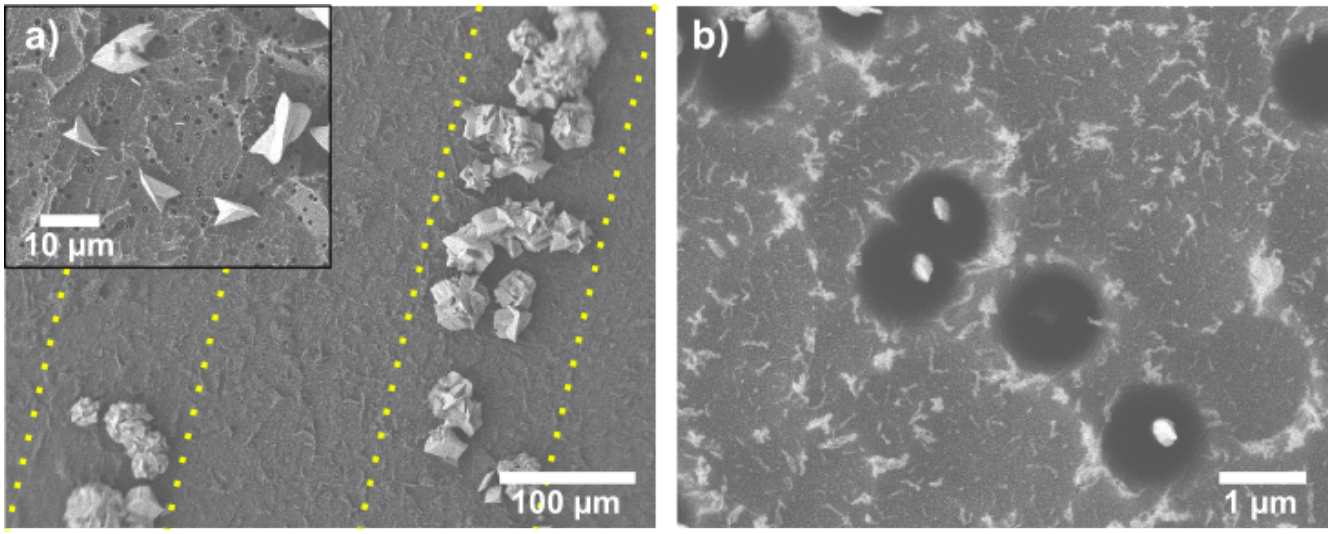

Figure 6.11: SEM images of bismuth grown inside a template with a pore density of $10^7 i/cm^2$ and a pore diameter of ∼200 nm. Electrodeposition was done at 40 $^\circ C$, using structured Cr/Au electrodes, at an on-/off-potential of -220 mV/-140 mV vs. SCE, applied for 20 ms and 100 ms, respectively. a) Bi caps formed on top of the template. The yellow lines are estimates where the structured contacts on the bottom side of the template might be. b) Bi wires reaching the surface. Polymer was removed from the surface using a RIE process, in order to access the wires below the surface.

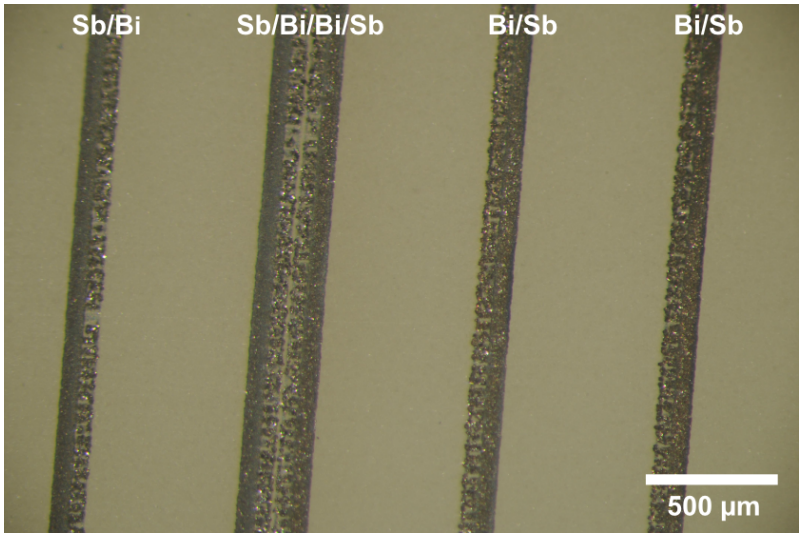

Figure 6.12: Light microscopy image of the cap layers of Bi and Sb, formed on the top side of the template. The used template had a pore density of ∼ 10^7 i/cm^2 and a pore diameter of ∼200 nm.

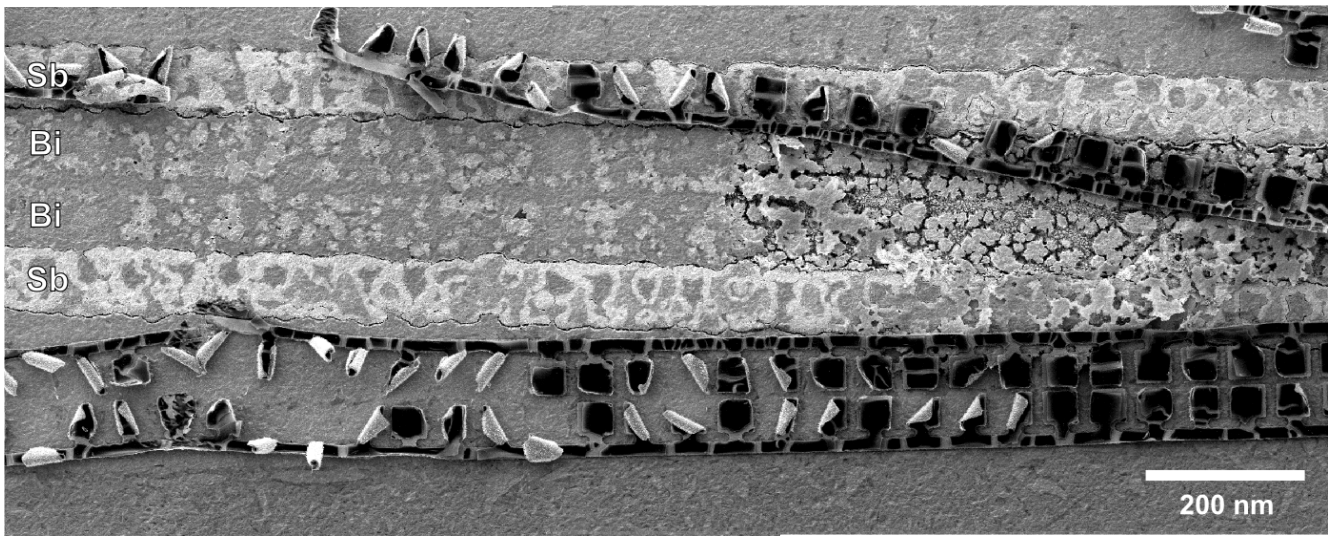

Figure 6.13: SEM image of the bottom side of the grown Sb and Bi caps after template removal. The structured contact lines broke off and lie next to the deposition area. It was not possible to locate Sb or Bi nanowires on this sample, since all of them appear to have broken off. The template used for growth had a pore density of $\sim 10^7$ i/cm^2 and a pore diameter of ∼200 nm.

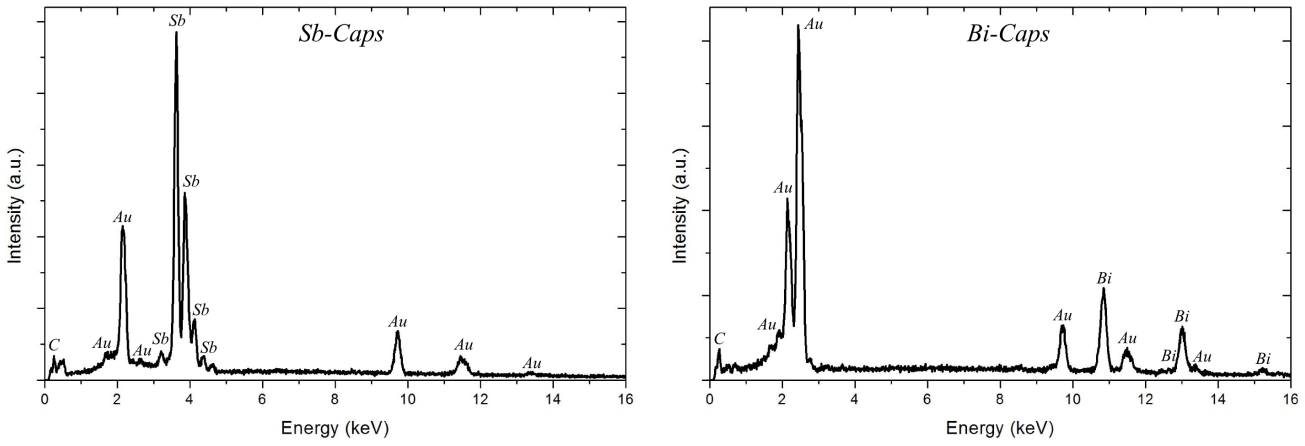

Figure 6.14: EDX patterns of the Sb and Bi caps of the sample shown in figure 6.13

6.3.3 Removal of Polycarbonate Matrix via Reactive Ion Etching

The parasitic heat exchange through the polymer matrix can severely reduce the efficiency of nanowire-based thermoelectric devices. In the worst case, if the thermal conductivity of the matrix material is too high, the advantages gained by the use of nanowires may even be lost completely [68]. Therefore, it would be best to remove the polycarbonate matrix. When wet chemical methods are used for its removal, the polycarbonate usually undergoes swelling. This can lead to breaking of nanowires or rip off of the contact electrodes from the top and/or the bottom of the nanowire-based device as presented here. Therefore, the complete removal of the polycarbonate matrix by dry etching methods, i.e. reactive ion etching (see chapter 2.3) was investigated.

For this investigation, parallel arrays of Sb nanowires were prepared ($\sim 10^8$ wires/cm^2, diameter ~160 nm, length of 30 μm). Afterward, ~1.5 μm of the polycarbonate surface was removed by reactive ion etching (2 x 1.5 min, 30 sccm O_2 flow, 250 W, 60 mbar chamber pressure). This should enable the access to a larger number of nanowires, as was shown in chapter 2.3 [111]. Then, on top of this surface, contact pads of Cr/Au were prepared using the same sputter and lithography process as described in section 6.3.1 above.

Figure 6.15 a) shows a SEM image of the top view of one of the contact pads, after the polymer had been removed in a multi-step RIE process (30 sccm O_2 flow, 250 W, 60 mbar chamber pressure). Here every 5 minutes the etching process was interrupted for ~5 minutes and the sample was rotated by 180°, in order to improve the homogeneity of the etching process. The small hillocks seen on top of the contact are formed by the gold layer covering the pores of the template, that were enlarged by the RIE process prior to the preparation of the Cr/Au layer. When the sample is tilted by 45°, it is possible to observe the wires below the contact pad (figure 6.15 b)). The wires underneath the pad all appear undamaged after the etching process and the wire diameters fall into the range expected for the elecrodeposited nanowires, which further indicates that no severe damage occurred to the wires during the etching process. In fact, even the wires in areas not covered by the metal contact seem undamaged, as seen in figure 6.15 c) and d). This shows, that it is possible to remove the polycarbonate without severely damaging the nanowires. However it should be noted that the use of an oxygen plasma might oxidize the surface or even the whole nanowire. To what extend this oxidation process took place was not clarified and needs to be investigated. There are also still polymer residues found between the wires, showing that a total removal of the polymer is difficult and might require the use of a wet chemical process.

The effects on a sample, when the RIE process is carried on without break, is shown in figure 6.16. Here the polycarbonate was removed by etching the samples for 2 x 30 minutes, using the same process parameters as in the process above. After the first 30 minutes the sample was rotated by 180°. In the areas not covered by a contact pad no intact wires were found. In fact, most of them seemed to have decomposed into smaller pieces, as can be seen in figure 6.16 c). The situation is a bit different underneath the contact pads, figure 6.16 a) and b). Also here most of the wires seemed to have decomposed, but further below the pad the wires seemed to still be intact, probably because they were still covered by polymer. The most probable explanation for this observation is, that the plasma process generated to much heat, which then made the nanowires become unstable and decompose.

Although the polymer can be almost completely removed from the areas that are not covered by a metal pad, the question still remains how large the under-etching at the contact pads is. Therefore, the area underneath the metal pads was uncovered by removing the material with Lugols iodine and Orange etch. A SEM image of the resulting structure is shown in figure 6.17. There are still some residues of the metal contact visible, however the edges of the pads were completely uncovered and it was possible to

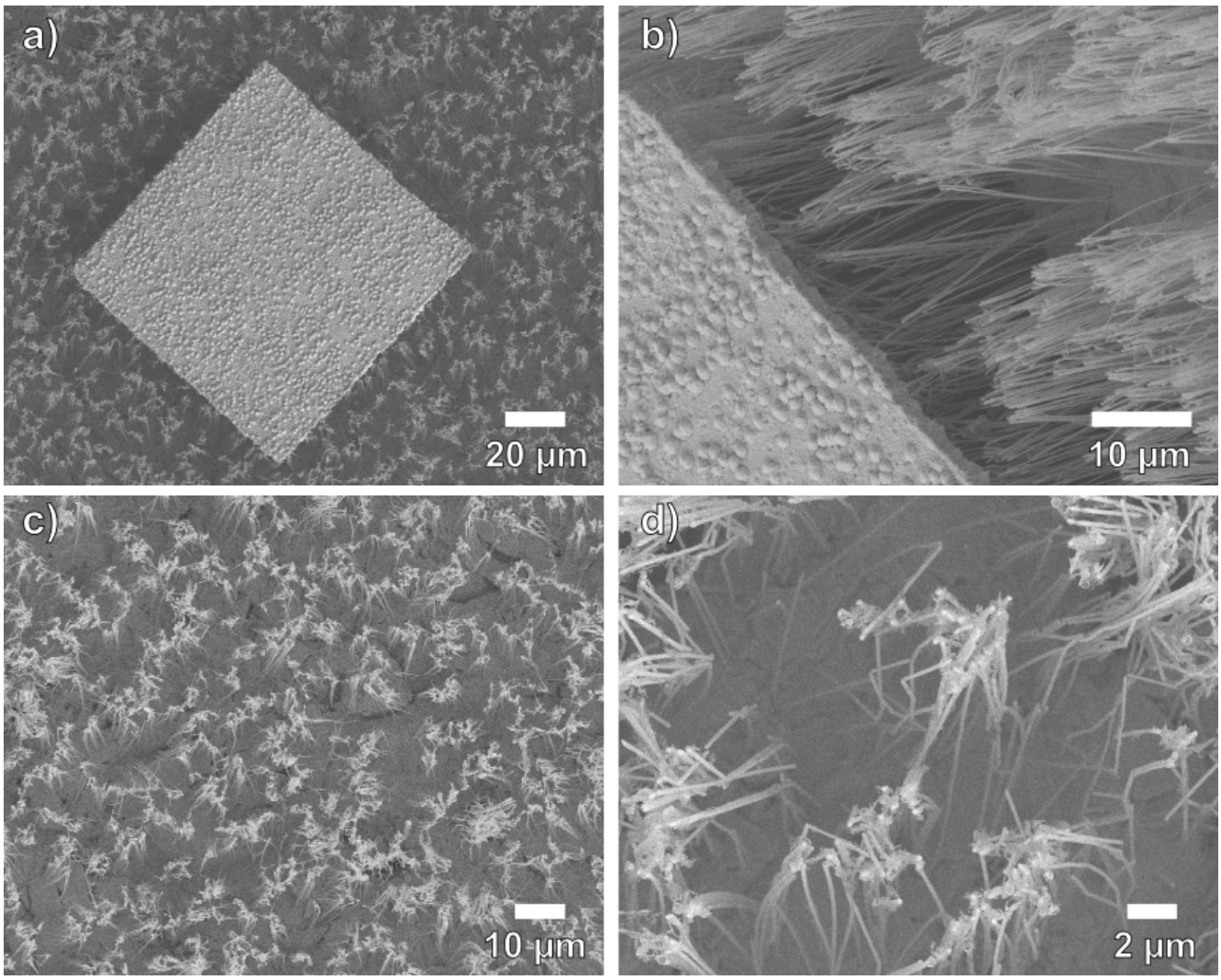

Figure 6.15: SEM image of a sample, after the complete polycarbonate had been removed in a multi-step RIE process. a) Top view of a Cr/Au contact pad. The small hillocks on top of the pad form on top of the pores in order to close them. b) Sb nanowires below the contact pad, when the sample was tilted by 45°. c) and d) Area not covered with a metal layer. Although the wires appear to be bend and entangled by polymer residues, all of them still appear to be intact.

observe nanowires still embedded in polymer. By measuring of the edge lengths of the residual polymer, an etch rate of $\sim$0.1 μm/min, of the polymer below the contact, was derived. Taking into account that the oxygen plasma might oxidize the wires, that it still leaves polymer residues behind and that it is not able to completely remove the polymer below the contact pads, a change of gas composition inside the plasma, or a combined approach with wet chemical methods, should be considered in order to improve the process.

6.4 Summary and Outlook

This chapter described a multi step process, developed to fabricate Sb- and Bi-nanowire-based thermocouples. First optical lithography was used to structure a metal electrode on top of a polycarbonate ion

track-etched template. This contact allowed to sequentially electrodeposit Sb and Bi in independent areas on the template. When only depositing one material, best growth conditions for Sb were found at 40°C at a pulsed potential of -250 mV/-130 mV vs. SCE and on-/off-times of 20 ms/100 ms, respectively. For Bi best results at 40°C have been obtained at a pulse potential of -220 mV/-140 mV vs. SCE, when using the same on-/off times as in the case of Sb.

When depositing both materials sequentially in the same template the temperature had to be decreased to room temperature, in order to prevent the dissolution of Sb in the Bi electrolyte. Although the same potentials as mentioned above were used for the materials, the results regarding the homogeneity of the deposition were similar. EDX measurement of the grown caps showed that indeed pure materials were deposited at room temperature, proving that Sb was not dissolved into the Bi electrolyte.

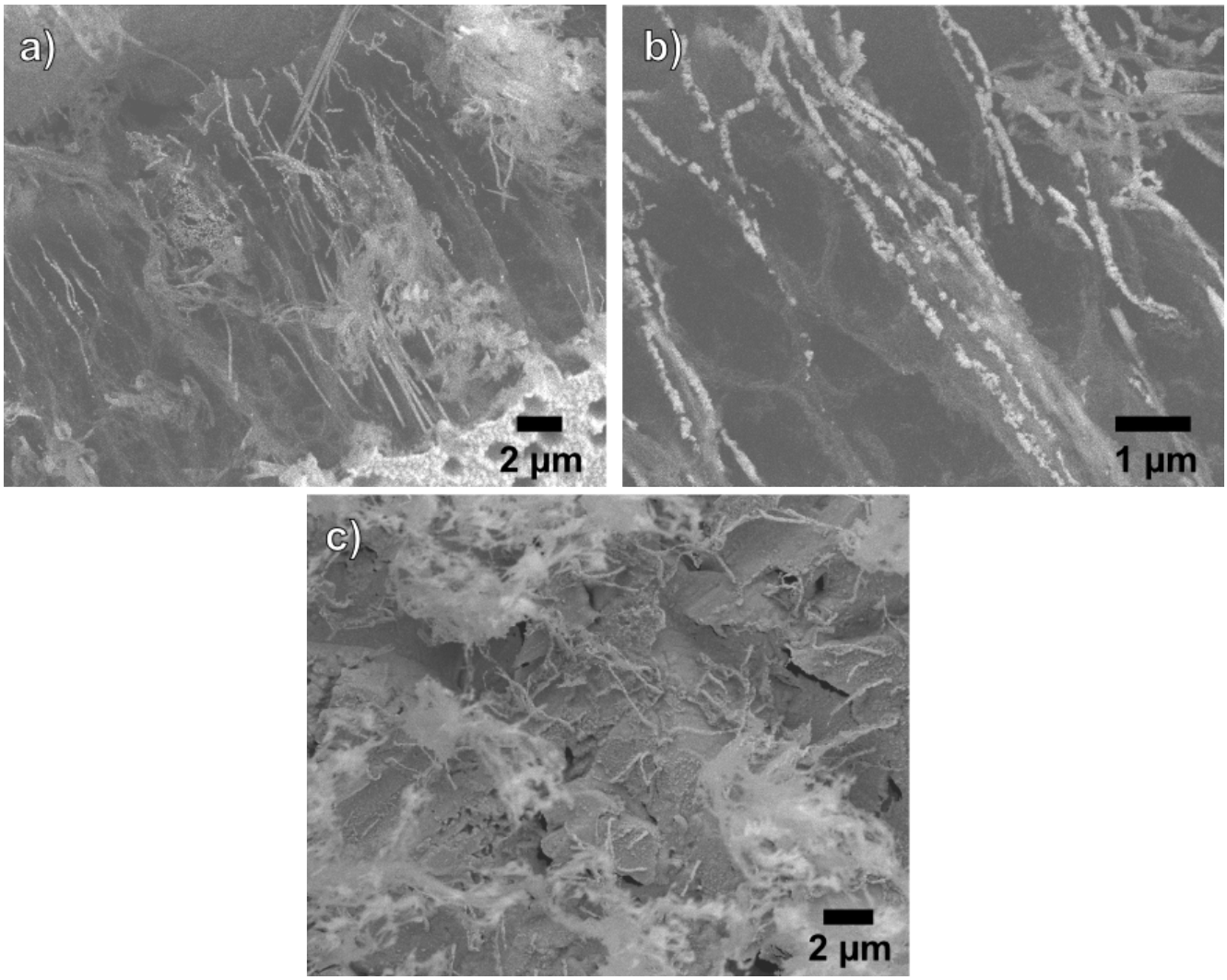

Figure 6.16: SEM images of Sb nanowires after the polycarbonate had been completely removed, using a two step RIE process. a) and b) damaged Sb nanowires below the contact pad, when the sample was tilted by 45°. Most of the wires have decayed into smaller parts, hold in place by polymer residues. c) Area not covered by a contact pad. Here even stronger decayed nanowires were found between clouds of residual polymer.

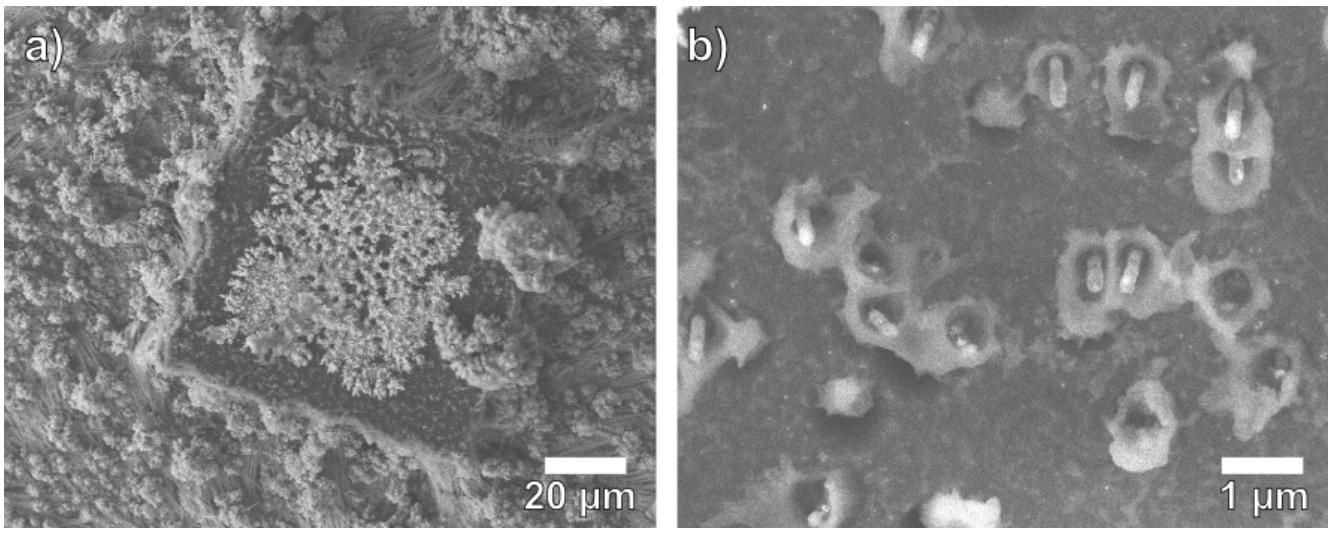

Figure 6.17: Area of a contact pad, after the complete polymer had been removed in a multi-step RIE process and the contact on top had been removed by chemical etching. There are still residues of contact, however, the edges of the former contact pad were uncovered and wires that were still embedded in the polymer could be found.

Additional experiments were conducted to remove the polycarbonate matrix by reactive ion etching, in order to eliminate the parasitic heat exchange through the polymer. Using a oxygen plasma the procedure proved to be suitable, but requires careful control of the process conditions in order to not damage the wires.

7 Summary and Outlook

In this thesis, arrays of parallel and interconnected $Bi_{1-x}Sb_x$ nanowires with wire diameters ranging between 30 and 400 nm were fabricated by pulsed potential electrochemical deposition in ion-track membranes. This process allows to control wire diameter, wire density, their alignment as well as composition and crystal structure systematically and independently, making these samples ideal model systems to study their intriguing transport properties.

By adding a surfactant (Dowfax 2a1) to the electrolyte uniform nanowire growth on $\sim cm^2$ areas were achieved, with filling ratios as large as 100% in 30 nm diameter pores. A detailed systematic investigation of the electrodeposition parameters resulted in the following parameter set for the most homogeneous growth:

Table 7.1: Most homogeneous electrodeposition conditions for growth at 40°C for Sb, Bi and $Bi_{0.85}Sb_{0.15}$ nanowire networks, when using a pulse potential with on-/off-times of 20 ms and 100 ms, respectively.

Material	On-potential [mV vs. SCE]	Off-potential [mV vs. SCE]	Temperature [°C]
Sb	-260	-130	40
Bi	-200	-170	20
$Bi_{0.85}Sb_{0.15}$	-220	-170	40

All synthesized nanowire arrays and nanowire networks were analyzed by various methods, including SEM, TEM and XRD. The arrays of Sb and Bi grown without surfactant developed a strong {01.2} and {11.0} texture, respectively, that decreased slightly when the surfactant was added to the used electrolyte. Surface morphology and crystal size were not affected by the presence of the surfactant. Sb wires and networks exhibited a very smooth surface whereas Bi nanowires and networks showed some roughness. For both materials several μm long single crystalline sections were observed in the representative case of $\sim$80 nm diameter wires.

Experiments using tilted nanowire arrays suggest that the crystal orientation parallel to the wire axis is independent on the pore tilt. However, TEM measurements on nanowire networks showed that single crystal growth can continue across a junction without disturbance, leading to a tilt of growth direction along the pore axis between the connected wires.

While the deposition conditions for Sb nanowire networks are optimal, work continues on the growth processes of Bi networks in order to further improve the growth uniformity and surface roughness. If the surface roughness is controlled well, this could be used to further decrease the thermal conductivity of the nanowire assemblies by increasing the phonon scattering on the surface.

As previously reported for parallel $Bi_{1-x}Sb_x$ nanowire arrays, the composition of $Bi_{1-x}Sb_x$ can successfully be adjusted by the electrolyte composition and electrodeposition conditions. Since the best thermoelectric properties are expected for wires oriented along the <00.1> direction, efforts should be made to grow $Bi_{1-x}Sb_x$ nanowires and nanowire networks with this crystal orientation.

The Seebeck coefficient of Bi and Sb nanowire assemblies prepared with and without surfactant were measured systematically between 300 and 40 K while embedded in the polymer template. Sb showed

a linear decrease of the positive Seebeck coefficient as a function of decreasing temperature and no dependence on the wire diameter. The absolute electrical resistance of Sb decreased with decreasing temperature as expected for semimetals. For thinner wires the relative decrease of the resistance is smaller, which is attributed to the influence of finite size effects. Since the Seebeck coefficient on one hand does not depend on the wire diameter and the thermal conductivity by the phonons is severely suppressed in small diameter wires due to scattering, an enhanced thermoelectric efficiency (zT) is expected for the thinner Sb nanowires when compared to the bulk material.

In the case of Bi a non-monotonous dependence of the Seebeck coefficient as a function of temperature is recorded. When decreasing the temperature from room temperature down to 40 K, the Seebeck coefficient displays a sign change from positive to negative, which is attributed to the limitation of the mean free path of the charge carriers. The temperature at which the Seebeck coefficient changes sign decreases with increasing wire diameter. Also for wire diameters smaller than 140 nm a decrease in the Seebeck coefficient is observed with decreasing wire diameter, that might be assigned to the contribution of surface states to the transport properties. The electrical resistivity showed a non-monotonic dependence on temperature which is attributed to finite and quantum size effects. As the Seebeck coefficient of Bi can be positive and negative depending on the temperature and wire diameter, this may allow to produce pure Bi thermocouples using nanowires with different diameters instead of different materials.

A method was developed to characterize the complete set of cross plane thermoelectric properties (Seebeck coefficient, electrical- and thermal conductivity) of thin films and nanowire assemblies embedded in a template. The sample is glued to a silicon wafer that is covered with a Si_3N_4 insulating film, using a silver-filled epoxy. The sample is covered by a Al_2O_3 layer, to electrical insulate the sample electrically from the $Bi_{0.9}Sb_{0.1}$ heater, that is applied afterward and used to generate a temperature gradient.

Measurements on Sb nanowire assemblies using this method showed similar results for the Seebeck coefficient and behavior of the electrical conductivity as reported above. The thermal conductivity was in the order of 0.27 W/mK, which is in the order of the polycarbonate template, i.e. much lower than the bulk value of Sb.

In order to improve the measurement accuracy the temperature measurement on the bottom of the sample needs to be improved. This could be done by etching a window into the Si_3N_4 insulating film, in order to connect the silver epoxy with the pure silicon substrate just beneath the sample. This way the silver epoxy and silicon would form a thermocouple which can be used to measure the temperature on the bottom side of the sample.

In the future, Hall measurements as well as magneto resistance measurements should be conducted in order to determine charge carrier mobilities and the contribution of topological surface states to the transport. Also angle resolved photo electron spectroscopy might be considered in order to characterize the electronic bandstructure of these materials.

Alternatively to polycarbonate, polyethylene terephthalate PET can also be used as template material to fabricate wires with rough surfaces, which might lead to an additional decrease in thermal conductivity by enhanced phonon scattering.

Currently the pores of ion track-etched templates can have an aspect ratio in the order of 1000. In order to produce long wires with smaller diameters, atomic layer deposition could be used to conformal coat the pores. This would then allow to study nanowires with diameter where surface states clearly dominate the transport or interact with another.

In the future, the nanowire assemblies of the binary compound $Bi_{1-x}Sb_x$ should also be characterized regarding the Seebeck coefficient. It is worth to mention that all properties have been measured on as-grown nanowires and that further treatments, such as annealing or doping (e.g. $(Bi_{1-x}Sb_x)_2Te_3$) should be investigated and is regarded as a promising strategy to increase the thermoelectric performance of nanowire assemblies.

In the last part of this thesis the preparation of a lithographically structured Au layer on top of a polycarbonate template has been successfully developed and tested. This structured electrode was subsequently used to sequentially electrodeposit Sb and Bi in individual and separate areas of the ion track-etched membrane. Efforts should be made to contact the Sb and Bi areas with one another, to form thermocouples made of nanowire arrays. If this is successful it would be possible to prepare small and thin thermoelectric devices, especially infrared sensors.

As the template route for preparation is quite versatile, several designs of the device could be realized. Simulations predict e.g. that the use of pyramidal shaped legs, or with regards to this conical nanowires, would improve the generated temperature difference between top and bottom of the device [216]. The use of a conical geometry would also increase the mechanical stability of the individual pillars significantly.

Additionally nanowire networks are very promising for implementation in thermoelectric devices, as they present a self-supported, mechanically stable and electrically reliable nanowire-based macrostructure [29].

8 Supplementary Information

8.1 Cyclic Voltammograms of Electrolytes

Figures 8.1 to 8.3 shows the cyclic voltammograms of the used electrolytes at 40°C, using a sputtered gold layer with a diameter of 8 mm as the working electrode and a platinum wire as a counter electrode. The measurement was started at 0 V vs. SCE, then going to negative voltages using a scanrate of 10 mV/s.

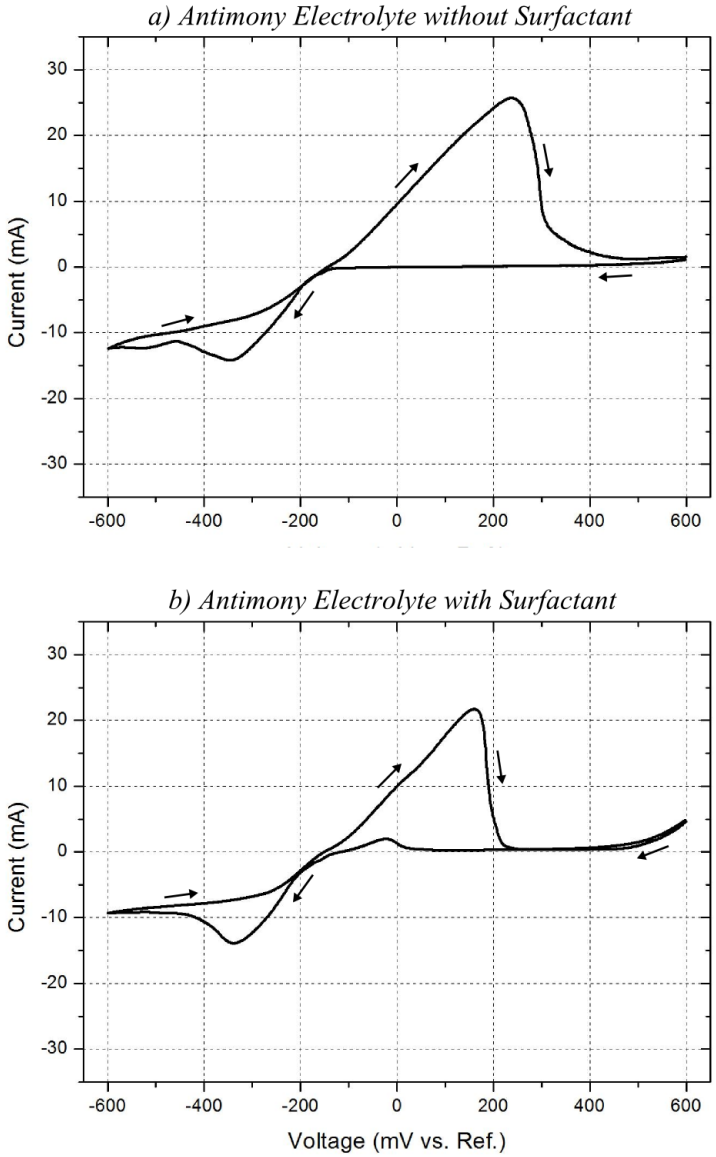

Figure 8.1: a) Second cycle of the cyclic voltammogram of the Sb electrolyte without added surfactant. b) Second cycle of the cyclic voltammogram of the Sb electrolyte with added surfactant.

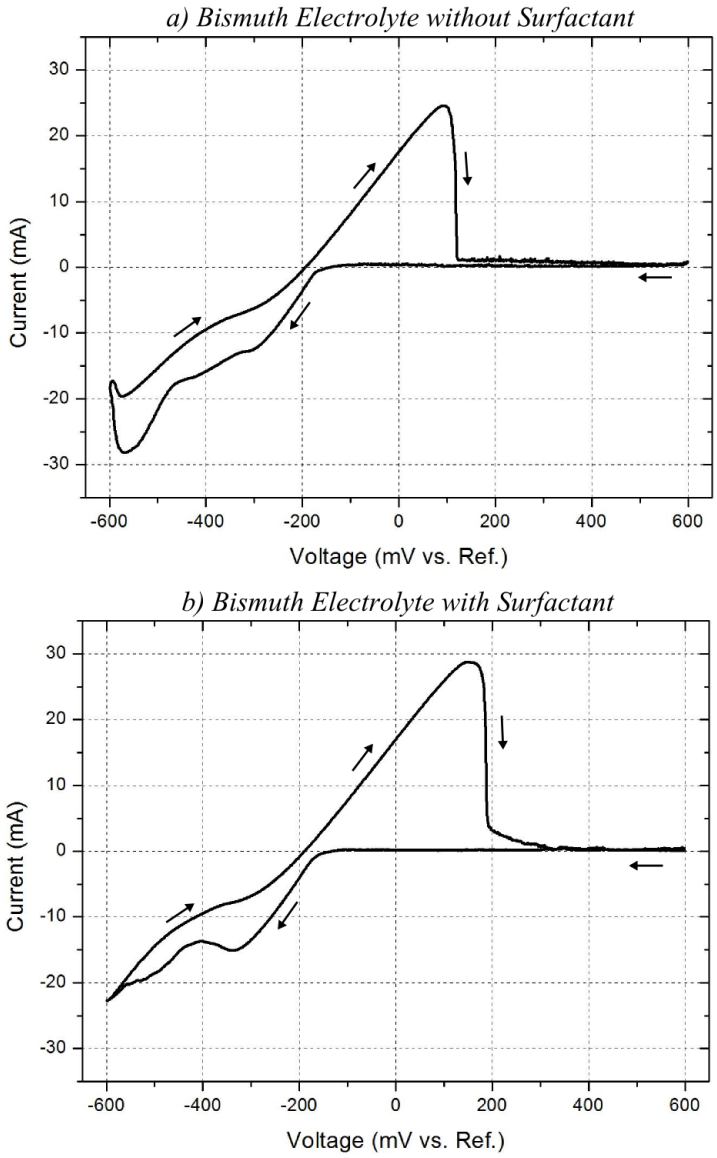

Figure 8.2: a) Second cycle of the cyclic voltammogram of the Bi electrolyte without added surfactant. b) Second cycle of the cyclic voltammogram of the Bi electrolyte with added surfactant.

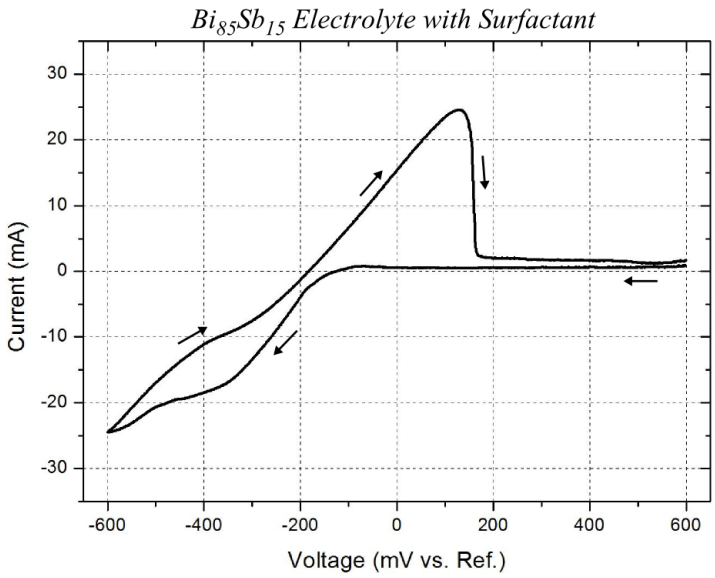

Figure 8.3: Second cycle of the cyclic voltammogram of the $Bi_{0.85}Sb_{0.15}$ electrolyte with added surfactant.

8.2 Morphology of Bi Networks Grown in Templates Irradiated from Three Directions

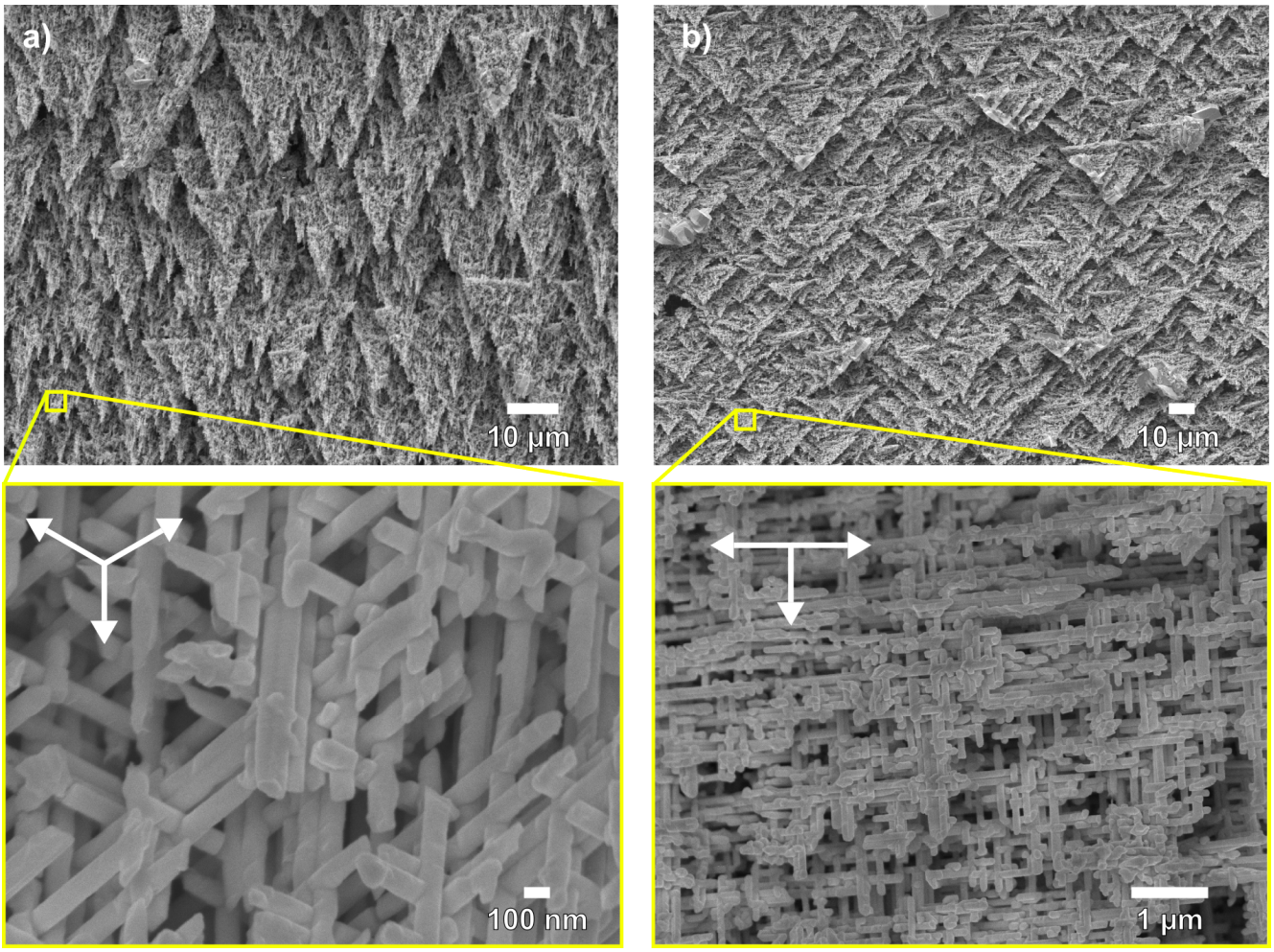

Figure 8.4: Morphology of Bi networks grown in templates irradiated with $1 \cdot 10^9$ i/cm^2 from three directions, having a pore diameter of ∼100 nm. The irradiation directions are shown as white arrows inside the close ups of the networks.

8.3 Temperature Measurement of Diodes & Seebeck of Phosphorbronze

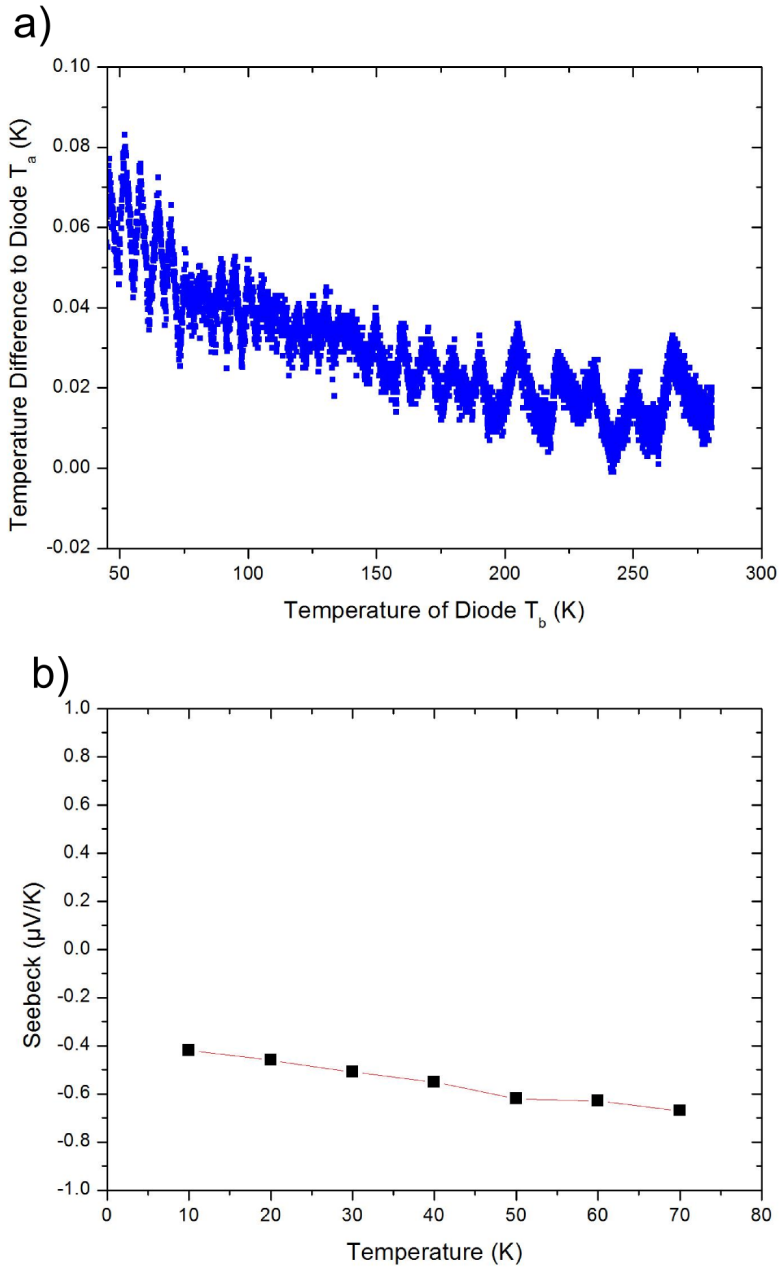

Figure 8.5: a) Measured temperature difference between used diodes in the setup shown in figure 5.1, when both diodes are mounted close to one another on the same substrate in the sample chamber. Although the diodes should show the same temperature an offset between the diodes can be observed which leads to errors in the calculated Seebeck coefficients. b) Seebeck of used phosphor bronze wires, measured at the RheinMain University of Applied Sciences by Fatima Boui.

8.4 Seebeck Measurements without Thermal Conducting Paste

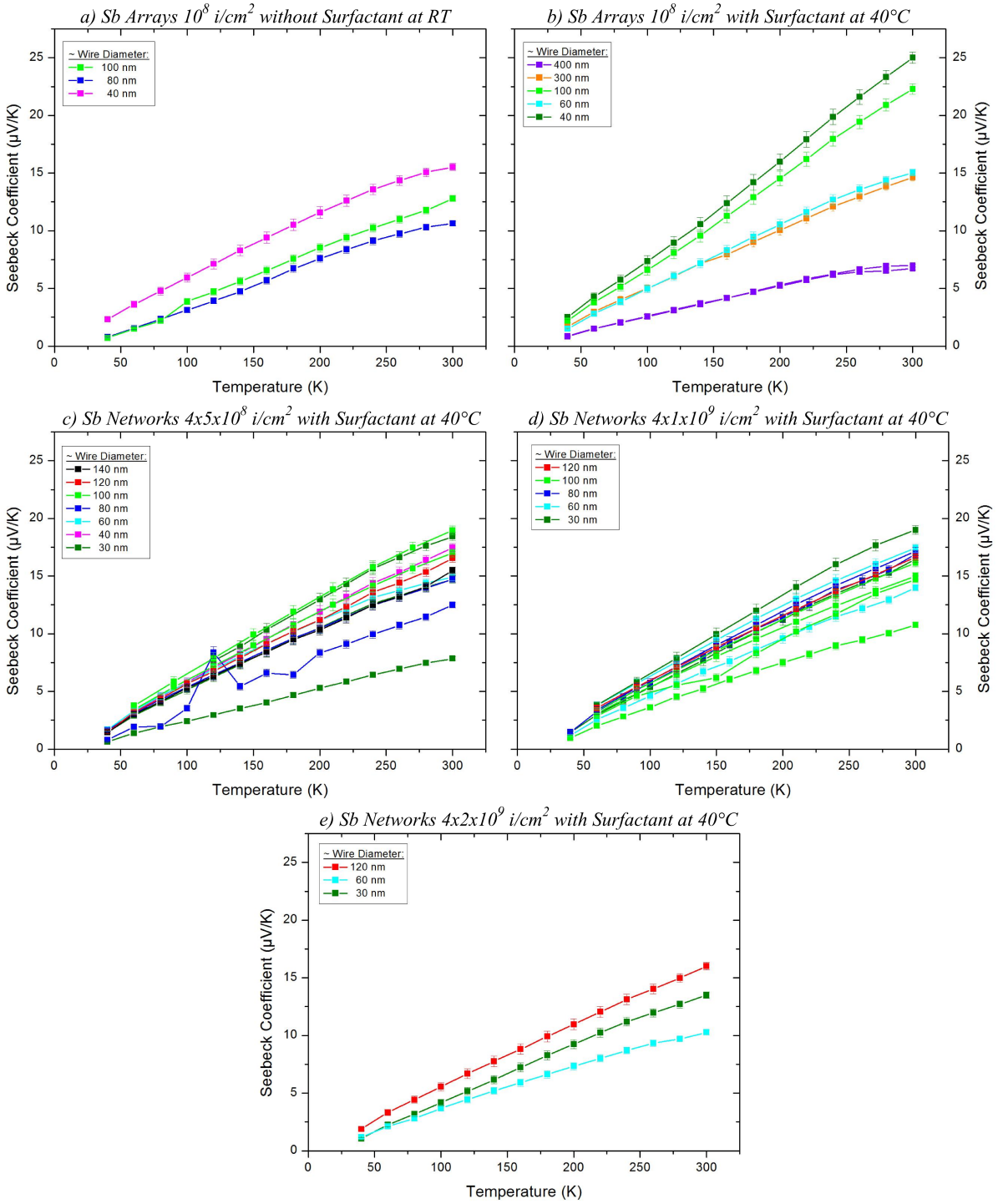

Figure 8.6: Seebeck coefficients of Sb nanowire assemblies as a function of temperature, without thermal paste in between the sample and the copper blocks.

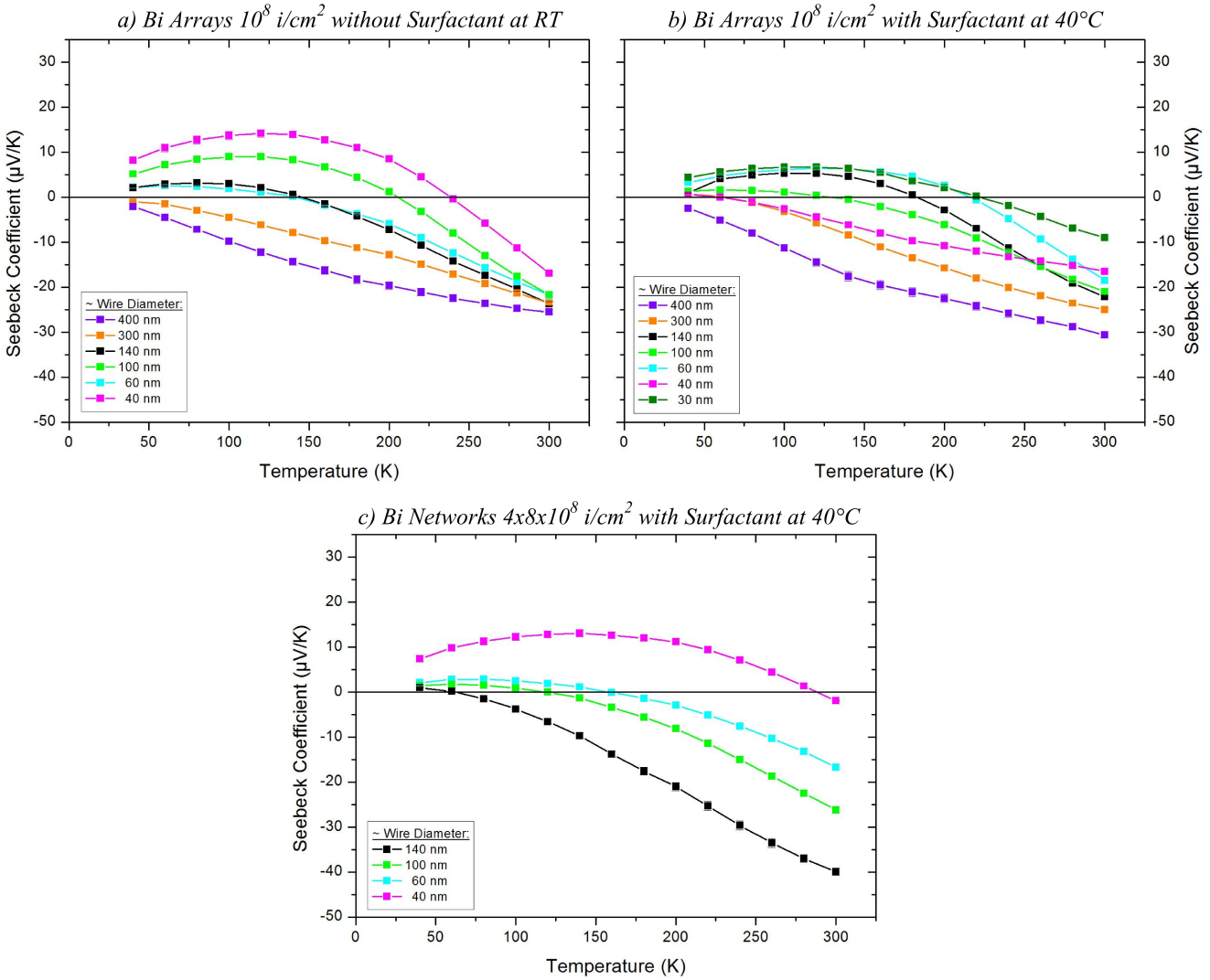

Figure 8.7: Seebeck coefficients of Bi nanowire assemblies as a function of temperature, without thermal paste in between the sample and the copper blocks.

8.5 Etching Solutions

Chromium etchant ("Orange Etch")[217]:

Perchloric acid ($HClO_4$).....164 g
Ceric ammonium nitrate ($Ce(NH_4)_2(NO_3)_6$.....42 ml
DI-Water (H_2O).....1000 ml

Gold etchant ("Tri-iodide" or "Lugols Iodine")[217]:

Potassium iodide (KI).....400 g
Iodine (I_2).....200 g
DI-Water (H_2O).....1000 ml

Acknowledgement

"You've got to be around people who encourage you,
advice you and want to see you go even higher and higher,
than they themselves have attained!"
-Israelmore Ayivor, Shaping the dream

A doctoral thesis is never just the work of a single person alone. A lot of people are involved all around it, be it by giving advice, helping in the lab or just by sharing a pep talk over coffee. But as little as some of these contributions might seem, they are essential for a successful and fulfilling work. Here now, I want to show my gratitude to those who helped making this possible, be it by words or deeds.

First of all I want to thank Prof. Christina Trautmann and Prof. Friedemann Völklein for their supervision of the postgraduate work as well as them welcoming me in their respective research groups at the GSI Helmholtz Center for Heavy Ion Research and the RheinMain University of Applied Sciences, respectively. They always had an open door whenever a question arose and I am thankful for the amount of fruitful discussions, which greatly enhanced my knowledge in their respective fields.

I also would like to express my gratitude to my supervisors as well as Prof. Wolfgang Ensinger and Prof. Robert Stark for there readiness to be part of my examination committee and especially Prof. Trautmann and Prof. Ensinger for acting as referee for this thesis.

I thank Dr. Maria Eugenia Toimil-Molares for her guidance of the work throughout the years. I am grateful for all the advices she gave me and the shared knowledge about the whole processes to prepare nanowires, not to mention the numerous encouraging words and proof reading of the thesis.

A special thanks goes to Dr. Sven Müller for teaching me the basics of sample preparation and for his almost foreseeing ideas, although not around anymore when I started the thesis, he had a large impact on all the processes within this work.

I thank Dr. Marco Cassinelli and Prof. Wouter Maijenburg, the best office mates one could wish for, for all the fruitful discussions and fun on the side. Especially our table football games are something I dearly miss.

I would also like to acknowledge my colleagues on the same quest as me: Fatima Boui, Giuseppa Distefano, Dr. Janina Krieg, Dr. Katharina Kupka, Dr. Liana Movsesyan, Dr. Jana Schmitt, Dr. Anne Spende, Dr. Loïk "Loki" Burr, Dr. Christian Huber, Dr. Peter Katrik, Jacob Lee, Simon Pascal, Alexey Prosvetov, Dr. Anton Romanenko and Nils Ulrich. Thank you for sharing this crazy time with me. See you all next beamtime ;)

Another thanks goes to Andreas Maier and Dr. Kay-Obbe Voss. Whenever there was a problem with the different setups they were there to help and give advice. I especially want to thank Andreas for all the discussion we had. Although scary at first, I always came out of them with a bit of enlightenment.

I want to express my gratitude to Dr. W. Sigle from the Max Planck Institute for Solid State Research in Stuttgart for HRTEM measurements as well as Dr. J. Brötz from the Technische Universität Darmstadt for XRD measurements. I also want to thank Dr. M. A. Carrillo Solano and Dr. Florent Yang for their help to obtain some last minute SEM images.

Another huge "Thank You" goes to Roland Rohloff, Patrick Kuhn, David Koch, Sarina Paulus and Leonard Edens, who supported me as interns or Bachelor students. Their work greatly contributed to this one and I am very grateful for there help. Without them this thesis would not be the same and I wish them the very best for their future.

Many thanks also go to Elko Schubert, Arne Siegmund and the GSI workshop for their help building the electrochemical cells and other equipment, as well as Christina Kunz for introducing me to the world of lithography.

Altogether I am thankful to all my colleagues at the IMtech and the Materials Research group for providing a great working atmosphere, stimulating discussions and numerous cakes.

I also want to thank the DFG for the funding of this work within the Priority Program SPP 1386, "Nanostructured Thermoelectric Materials:Theory, Model Systems and Controlled Synthesis", as well as the Rhein-Main University of Applied Sciences and the Helmholtz Graduate School for Hadron and Ion Research "HGS-HIRe for FAIR" for additional funding.

Finally I want to express my deepest gratitude to my family, Karin and Paul Wagner as well as Tanja and Till Neunhoeffer. I thank them for the constant support and encouragement they gave me throughout my life. Thanks for having my back even in the darkest of times.

Curriculum Vitae

Michael Florian Peter Wagner

Date of Birth: 29th of November 1984
Birthplace: Königstein im Taunus
Nationality: German

Professional Experience

01/2017 - present	Research associate at the GSI Helmholtz Centre for Heavy Ion Research GmbH Department of Materials Research, head Prof. Dr. C. Trautmann
05/2013 - 12/2016	Research associate at the RheinMain University of Applied Sciences, Institute of Microtechnologies, head Prof. Dr. F. Völklein Project: "Nanostructured Thermoelectric Materials: Theory, Model Systems and Controlled Synthesis"
05/2012 - 12/2012	Diploma thesis at the GSI Helmholtz Centre for Heavy Ion Research GmbH, Department of Materials Research, head Prof. Dr. C. Trautmann Titel of thesis: "Fabrication of Antimony 3D Nanowire Networks for Thermoelectric Applications"
11/2011 - 02/2012	Student assistant at the Technical University Darmstadt, Department of Nonmetallic-Inorganic Materials, head Prof. Dr. J. Rödel
07/2011 - 09/2011	Internship at the GSI Helmholtz Centre for Heavy Ion Research GmbH, Department of Materials Research, head Prof. Dr. C. Trautmann
07/2008 - 03/2011	Student research assistant at the Technical University Darmstadt, Department of Nonmetallic-Inorganic Materials, head Prof. Dr. J. Rödel

Education

05/2013 - present	PhD Thesis at the Technical University Darmstadt, Department of Ion-Beam-Modified Materials, head Prof. Dr. C. Trautmann Titel: "Nanowire Assemblies for Thermoelectric Applications"
10/2006 - 03/2013	Technical University Darmstadt, study of Materials Science Finished with degree: Diplom Ingenieur
10/2004 - 03/2006	Julius-Maximilians University Würzburg, study of Nanostructure Technology
08/1995 - 06/2004	Privatgymnasium Dr. Richter, Kelkheim im Taunus
06/1991 - 07/1995	Primary school In den Sindlinger Wiesen, Kelkheim im Taunus

Scientific Contributions

Papers:

"Fabrication and thermoelectrical characterization of three-dimensional nanowire networks"
M. F. P. Wagner, F. Völklein, H. Reith, C. Trautmann, and M. E. Toimil-Molares,
Phys. Status Solidi A 213, No.3, 610-619, DOI 10.1002/pssa.201532616

Posters:

Seebeck coefficient of Bi and Sb nanowire assemblies produced by electrodeposition
M.F.P. Wagner, S. Paulus, P. Kuhn, J. Brötz, C. Trautmann, K.-O. Voss, M.E. Toimil-Molares
International Workshop on "Thermoelectric Nanomaterials", 2018, Berlin (Germany)

Template-based Synthesis of Nanowire-Arrays and Nanowire-Networks for thermoelectric Applications"
M. Wagner, M. Cassinelli, C. Trautmann, M.E. Toimil-Molares, F. Völklein
WE-Heraeus-Seminar, 2018, Bad Honnef (Germany)

Characterisation and Electrodeposition $Bi_{1-x}Sb_x$ Nanowire-Networks in Etched Ion-Track Membranes for Thermoelectric Applications
M.F.P. Wagner, S. Müller, C. Trautmann, F. Völklein, M.E. Toimil-Molares
International Workshop on Thermoelectrics: A voyage from fundamentals to applications 2016 Hurtigruten Cruise Ship (Norway)

"Characterisation and Electrodeposition of $Bi_{1-x}Sb_x$ Nanowire- Networks in Etched Ion-Track Membranes for thermoelectric Applications"
M. Wagner, S. Müller, H. Reith, C. Trautmann, F. Völklein, M.E. Toimil-Molares
International Workshop on Electrodeposited Nanostructures, 2015, in Balatonfüred, (Hungary)

"Characterisation and Electrodeposition of $Bi_{1-x}Sb_x$ Nanowire- Networks in Etched Ion-Track Membranes for thermoelectric Applications"
M. Wagner, S. Müller, H. Reith, C. Trautmann, F. Völklein, M.E. Toimil-Molares
International Symposium of swift heavy ions in matter, 2015, Darmstadt (Germany)

"Electrodeposition of Sb Nanowire-Networks in Etched Ion-Track Membranes and their Characterization"
M. Wagner, S. Müller, H. Reith, C. Trautmann, F. Völklein, M.E. Toimil-Molares
International Workshop on Electrodeposited Nanostructures, 2014, in Oberwesel (Rhine Valley) (Germany)

Talks:

Ion-track technologie for the fabrication of $Bi_{1-x}Sb_x$ nanowire networks for thermoelectric applications
M.F.P. Wagner, S. Paulus, P. Kuhn, J. Brötz, C. Trautmann, K.-O. Voss, M.E. Toimil-Molares
SHIM-ICACS, 2018, Caen (France)

"Electrodeposition of $Bi_{1-x}Sb_x$ nanowire networks and the determination of their Seebeck coefficient"
M. Wagner, S. Paulus, P. Kuhn, J. Brötz, C. Trautmann, K.-O. Voss, M.E. Toimil-Molares
International Workshop on Electrodeposited Nanostructures, 2017, Sofia (Bulgaria)

"Template-based Synthesis of Nanowire-Arrays and Nanowire-Networks for thermoelectric Applications"

M. Wagner, M. Cassinelli, C. Trautmann, M.E. Toimil-Molares, F. Völklein
WE-Heraeus-Seminar: Electrons and Phonons: Inferfaces and Interactions, 2015, Bad Honnef (Germany)

"Thermoelectric properties of individual bismuth compound nanowires and nanowire arrays, and their reliability: towards nanowire-based microstructured thermoelectric devices"
M. Wagner, M. Cassinelli, Prof. F. Völklein, Dr. M.E. Toimil-Molares
DFG-Schwerpunktprogramm SPP 1386 Statusmeeting, 2015, Bad Aussee (Austria)

"Development and template-based synthesis of nanowire-arrays and nanowire-networks based on bismuth and antimony for thermoelectric applications"
M. Wagner, M.E. Toimil-Molares, C. Trautmann, F. Völklein
Annual international conference on thermoelectrics & european conference on thermoelectrics, 2015, Dresden (Germany)

"Development and template-based synthesis of nanowire-arrays and nanowire-networks based on bismuth and antimony for thermoelectric applications"
M. Wagner, M.E. Toimil-Molares, C. Trautmann, F. Völklein
European Materials Research Society Meeting, 2015, Lille (France)

Awards:

Giersch Excellence Award 2017
Giersch Excellence Award 2016
Best Poster Award - International Workshop on Electrodeposited Nanostructures, 2014

Bibliography

[1] Chacos, B. *IBMs crazy-thin 7nm chip will hold 20 billion transistors*. PCWorld. 2015.

[2] Vu, C. *Research alliance builds new transistor for 5nm technology*. phys.org/news/2017-06-alliance-transistor-5nm-technology.html. 2017.

[3] *A Look Inside Nanotechnology*. AMPITIAC Newsletter. 6. 2002.

[4] Ramsden, J. *Applied Nanotechnologie*. Elsevier, 2009.

[5] Prorok, B. *MEMS and Nanotechnology, Volume 5: Proceedings of the 2015 Annual Conference on Experimental and Applied Mechanics*. Ed. by Starman, L. 1st ed. Conference Proceedings of the Society for Experimental Mechanics Series. Springer International Publishing, 2016.

[6] Tan, S. and Jalil, M. *Introduction to the physics of nanoelectronics*. Woodhead Publishing, 2012.

[7] Bonca, J. and Kruchinin, S., eds. *Electron Transport in Nanosystems*. Proceedings of the NATO Advanced Research Workshop on Electron Transport in Nanosystems. Springer, 2007.

[8] Volz, S., ed. *Microscale and Nanoscale Heat Transfer*. Springer, 2007.

[9] Iadonisi, G., Cantele, G., and Chiofalo, M., eds. *Introduction to Solid State Physics and Crystalline Nanostructures*. Springer, 2014.

[10] Bhushan, B., ed. *Springer Handbook of Nanotechnology*. 3rd. Springer, 2010, pp. 119–167.

[11] Toimil-Molares, M. "Characterization and properties of micro- and nanowires of controlled size, composition, and geometry fabricated by electrodeposition and ion-track technology". In: *Beilstein Journal of Nanotechnology* 3 (2012), pp. 860–883. ISSN: 2190-4286. DOI: 10.3762/bjnano.3.97.

[12] Picht, O. et al. "Tuning the Geometrical and Crystallographic Characteristics of Bi_2Te_3 Nanowires by Electrodeposition in Ion-Track Membranes". In: *The Journal of Physical Chemistry C* 116 (2012), pp. 5367–5375. DOI: 10.1021/jp210491g.

[13] Hicks, L. and Dresselhaus, M. "Effect of quantum-well structures on the thermoelectric figure of merit". In: *Physical Review B* 47 (1993), p. 12727.

[14] Hicks, L. and Dresselhaus, M. "Thermoelectric figure of merit of a one-dimensional conductor". In: *Physical Review B* 47 (1993), p. 16631.

[15] Roslyak, O. and Piryatinski, A. "Thermoelectric properties of semiconductor nanowire networks". In: *Journal of Applied Physics* 119 (2016), p. 125107. DOI: 10.1063/1.4944715.

[16] Fleurial, J.-P. et al. *Thermoelectrics: From space power systems to terrestrial waste heat recovery applications*. Thermoelectrics Applications Workshop. 2011.

[17] Bell, L. "Cooling, Heating, Generating Power, and Recovering Waste Heat with Thermoelectric Systems". In: *Science* 321.5895 (2008), pp. 1457–1461. ISSN: 0036-8075. DOI: 10.1126/science.1158899. eprint: http://science.sciencemag.org/content/321/5895/1457.full.pdf.

[18] Teo, J., Fu, L., and Kane, C. "Surface States of the Topological Insulator $Bi_{1x}Sb_x$". In: *Physical Review B* 78 (2008), pp. 1–15. DOI: 10.1103/PhysRevB.78.045426.

[19] Gooth, J. et al. "Thermoelectric performance of classical topological insulator nanowires". In: *Semiconductor Science and Technology* 30 (2014), p. 015015. DOI: 10.1088/0268-1242/30/1/015015.

[20] Cassinelli, M. “Thermoelectric Properties of $Bi_{1-x}Sb_x$ Nanowires Electrodeposited in Etched Ion-Track Membranes”. PhD thesis. Technische Universität Darmstadt, 2016.

[21] Krieg, J. “Characterization of individual Bi_2Te_3 nanowires electrodeposited in etched ion-track membranes for nano-ARPES and electrical transport studies”. PhD thesis. Technische Universität Darmstadt, 2017.

[22] Rabin, O., Lin, Y.-M., and Dresselhaus, M. “Anomalously high thermoelectric figure of merit in $Bi_{1-x}Sb_x$ nanowires by carrier pocket alignment”. In: *Applied Physics Letters* 79.1 (2001), pp. 81–83. DOI: 10.1063/1.1379365.

[23] Tang, S. and Dresselhaus, M. “Electronic phases, band gaps, and band overlaps of bismuth antimony nanowires”. In: *Physical Review B* 89 (2014), p. 045424. DOI: 10.1103/PhysRevB.89.045424.

[24] Lenoir, B. et al. Proceedings of the fifthteenth international conference on thermoelectrics. 1-13. 1996.

[25] Völklein, F. et al. “Microchip for the Measurement of Seebeck Coefficients of Single Nanowires”. In: *Journal of Electronic Materials* 38 (2009), pp. 1109–1115.

[26] Rojo, M. et al. “Review on measurement techniques of transport properties of nanowires”. In: *Nanoscale* 5 (2013), p. 11526. DOI: 10.1039/c3nr03242f.

[27] *Special Issue: Nanostructured Thermoelectrics*. Physica Status Solidi A: Applications and Materials Science. 213. 2016.

[28] Mao, F. et al. “A polymer foil non-contact IR temperature sensor with a thermoresistor integrated on the back of a vertically configured thermopile”. In: *Sensors and Actuators A* 179 (2012), pp. 56–61. ISSN: 0924-4247. DOI: 10.1016/j.sna.2012.03.022.

[29] Pennelli, G. et al. “Seebeck Coefficient of Nanowires Interconnected into Large Area Networks”. In: *Nano Letters* 13 (2013), 2592–2597. DOI: 10.1021/nl400705b.

[30] Pennelli, G. “Review of nanostructured devices for thermoelectric applications”. In: *Beilstein Journal of Nanotechnology* 5 (2014), pp. 1268–1284. ISSN: 2190-4286. DOI: 10.3762/bjnano.5.141.

[31] Kim, J., Shim, W., and Lee, W. “Bismuth nanowire thermoelectrics”. In: *Journal of Materials Chemistry C* 3 (46 2015), pp. 11999–12013. DOI: 10.1039/C5TC02886H.

[32] Tang, S. and Dresselhaus, M. “Electronic properties of nano-structured bismuth-antimony materials”. In: *Journal of Materials Chemistry C* 2 (2014), pp. 1–17. DOI: 10.1039/c4tc00146j.

[33] Cucka, P. and Barrett, C. “The Crystal Structure of Bi and of Solid Solutions of Pb, Sn, Sb and Te in Bi”. In: *Acta Crystallographica* 15 (1962), pp. 865–872.

[34] Dismukes, J. et al. “Lattice parameter and density in bismuth-antimony alloys”. In: *Journal of Chemical and Engineering Data* 13 (1968), pp. 317–320.

[35] Lenoir, B. et al. “Tranport properties of Bi-rich Bi-Sb alloys”. In: *Journal of Physics and Chemistry of Solids* 57 (1995), p. 89.

[36] Vegard, L. “Die Konstitution der Mischkristalle und die Raumfüllung der Atome”. In: *Zeitschrift für Physik* 5 (1924), pp. 17–26. DOI: 10.1007/BF01349680.

[37] Dasgupta, N. et al. “25th Anniversary Article: Semiconductor Nanowires - Synthesis, Characterization, and Applications”. In: *Advanced Materials* 26.14 (2014), pp. 2137–2184. ISSN: 1521-4095. DOI: 10.1002/adma.201305929.

[38] Banerjee, S., Dan, A., and Chakravorty, D. “Synthesis of conducting nanowires”. In: *Journal of Materials Science* 37.20 (2002), pp. 4261–4271. ISSN: 1573-4803. DOI: 10.1023/A:1020663731437.

[39] Rawtani, D. et al. “Emerging strategies for synthesis and manipulation of nanowires: a review”. In: *Reviews on Advanced Materials Science* 40.2 (2015), pp. 177–187.

[40] Spende, A. et al. “TiO_2, SiO_2, and Al_2O_3 coated nanopores and nanotubes produced by ALD in etched ion-track membranes for transport measurements”. In: *Nanotechnology* 26 (2015), p. 335301.

[41] Movsesyan, L. et al. “Influence of electrodeposition parameters on the structure and morphology of ZnO nanowire arrays and networks synthesized in etched ion-track membranes”. In: *Semiconductor Science and Technology* 31 (2015), p. 14006.

[42] Burr, L. et al. “Surface Enrichment in Au–Ag Alloy Nanowires and Investigation of the Dealloying Process”. In: *The Journal of Physical Chemistry C* 119 (2015), p. 20949.

[43] Hu, H. et al. “Solvothermal synthesis of antimony nanowire bundles, tube-groove-like nanostructures and dendrites”. In: *Journal of Crystal Growth* 261 (2004), pp. 485–489.

[44] Wang, D. et al. “Formation of antimony nanotubes via a hydrothermal reduction process”. In: *Nanotechnology* 14 (2003), pp. 748–751.

[45] Tang, C. et al. “Thermal Expansion Behaviors of Bismuth Nanowires”. In: *Journal of Physical Chemistry C* 113 (2009), pp. 5422–5427.

[46] Wang, Y. et al. “Antimony Nanowires Self-Assembled from Sb Nanoparticles”. In: *J. Phys. Chem. B* 1008 (2004), pp. 16723–16726.

[47] Wang, X.-S. et al. “Self-assembly of antimony nanowires on graphite”. In: *Applied Physics Letters* 88 (2006), p. 233105. DOI: 10.1063/1.2208374.

[48] Schoendorfer, C. et al. “Focused ion beam induced synthesis of a porous antimony nanowire network”. In: *JOURNAL OF APPLIED PHYSICS* 102 (2007), p. 044308. DOI: 10.1063/1.2771044.

[49] Glocker, D. and Skove, M. “Field effect magnetoresistance in small bismuth wires”. In: *Physical Review B* 15 (1977), pp. 608–616.

[50] Chiu, P. and Shih, I. “A study of the size effect on the temperature-dependent resistivity of bismuth nanowires with rectangular cross-sections”. In: *Nanotechnology* 15 (2004), pp. 1489–1492. DOI: 10.1088/0957-4484/15/11/020.

[51] Stanley, S. et al. “An investigation of the growth of bismuth whiskers and nanowires during physical vapour deposition”. In: *Journal of Physics D: Applied Physics* 45 (2012), p. 435304. DOI: 10.1088/0022-3727/45/43/435304.

[52] Reppert, J. et al. “Laser-assisted synthesis and optical properties of bismuth nanorods”. In: *Chemical Physics Letters* 442 (2007), pp. 334–338. DOI: 10.1016/j.cplett.2007.05.076.

[53] Bhimarasetti, G. and Sunkara, M. “Synthesis of Sub-20-nm-Sized Bismuth 1-D Structures Using Gallium-Bismuth Systems”. In: *Journal of Physical Chemistry B* 109 (2005), pp. 16219–16222.

[54] Cheng, Y.-T. et al. “Stress-induced growth of bismuth nanowires”. In: *Applied Physics Letters* 81.17 (2002), pp. 3248–3250. DOI: 10.1063/1.1515885.

[55] Matkasymova, A., Omurzak, E., and Sulaimankulova, S. “Nanorods of Metallic Bismuth and Antimony by the Impulse Plasma in Liquid”. In: *Journal of Cluster Science* 20 (2009), pp. 153–158. DOI: 10.1007/s10876-008-0230-5.

[56] Zhou, B., Li, X.-H., and Zhu, J.-J. “Controllable Synthesis of One-Dimensional Chinelike Superstructures of Homogeneous $Bi_{100-x}Sb_x$ Alloys via a Template-Free Electrodeposition”. In: *Crystal Growth and Design* 7.11 (2007), pp. 2276–2278.

[57] Heremans, J. et al. “Bismuth nanowire arrays: Synthesis and galvanomagnetic properties”. In: *Physical Review B* 61.4 (2000), pp. 2921–2930.

[58] Müller, S. et al. “Electrochemical Synthesis of $Bi_{1-x}Sb_x$ Nanowires with Simultaneous Control on Size, Composition, and Surface Roughness”. In: *American Chemical Society* 12 (2012), pp. 615–621. DOI: 10.1021/cg200685c.

[59] Cassinelli, M. et al. “Structural and compositional characterization of $Bi_{1-x}Sb_x$ nanowire arrays grown by pulsed deposition to improve growth uniformity”. In: *Nuclear Instruments and Methods in Physics Research B* 365 (2015), pp. 668–674. ISSN: 0168-583X. DOI: 10.1016/j.nimb.2015.07.107.

[60] Martin, J. et al. “Ordered three-dimensional interconnected nanoarchitectures in anodic porous alumina”. In: *Nature Communications* 5 (Oct. 2014), p. 5130. DOI: 10.1038/ncomms6130.

[61] Sergelius, P. et al. “Electrochemical synthesis of highly ordered nanowires with a rectangular cross section using an in-plane nanochannel array”. In: *Nanotechnology* 25 (2014), p. 504002. DOI: 10.1088/0957-4484/25/50/504002.

[62] Spende, A. “Surface Modification of Etched Ion-Track Polymer Membranes by Atomic Layer Deposition”. PhD thesis. Technische Universität Darmstadt, 2016.

[63] Zhang, Z., Ying, J., and Dresselhaus, M. “Bismuth quantum-wire arrays fabricated by a vacuum melting and pressure injection process”. In: *Journal of Materials Research* 13.7 (1998), pp. 1745–1748. DOI: 10.1557/JMR.1998.0243.

[64] Zhang, Z. et al. “Processing and Characterization of Single-Crystalline Ultrafine Bismuth Nanowires”. In: *Chemistry of Materials* 11.7 (1999), pp. 1659–1665. DOI: 10.1021/cm9811545. eprint: http://dx.doi.org/10.1021/cm9811545.

[65] Lin, Y.-M. et al. “Transport properties of $Bi_{1-x}Sb_x$ alloy nanowires synthesized by pressure injection”. In: *Applied Physics Letters* 79.5 (2001), pp. 677–679. DOI: 10.1063/1.1385800. eprint: http://dx.doi.org/10.1063/1.1385800.

[66] Trautmann, C. “Observation and chemical treatment of heavy-ion tracks in polymers”. In: *Nuclear Instruments and Methods in Physics Research Section B: Beam Interactions with Materials and Atoms* 105 (1995), pp. 81–85. ISSN: 0168-583X. DOI: 10.1016/0168-583X(95)00555-2.

[67] Fischer, B. and Spohr, R. “Production and use of nuclear tracks: imprinting structure on solids”. In: *Reviews of Modern Physics* 55 (4 1983), pp. 907–948. DOI: 10.1103/RevModPhys.55.907.

[68] Hillhouse, H. and Tuominen, T. “Modeling the thermoelectric transport properties of nanowires embedded in oriented microporous and mesoporous films”. In: *Microporous and Mesoporous Materials* 47.1 (2001), pp. 39–50. ISSN: 1387-1811. DOI: 10.1016/S1387-1811(01)00289-X.

[69] Eibel, O. et al. *Thermoelectric Bi_2Te_3 Nanomaterials*. Wiley-VCH, 2015.

[70] *Makrofol, Elektroisolierfolien aus Polycarbonat*. Bayer.

[71] Spohr, R. *Ion Tracks and Microtechnology, Principles and Applications*. Ed. by Bethge, K. 1st ed. Vieweg, 1990.

[72] Hellborg, R., Whitlow, H., and Zhang, Y. *Ion Beams in Nanoscience and Technology*. Springer Berlin Heidelberg. 2010.

[73] Sigmund, P. *Particle Penetration and Radiation Effects Volume 2*. Springer International Publishing, 2006.

[74] Sertova, N. et al. “Investigation of initial stage of chemical etching of ion tracks in polycarbonate”. In: *Nuclear Instruments and Methods in Physics Research Section B: Beam Interactions with Materials and Atoms* 267.6 (2009), pp. 1039–1044. ISSN: 0168-583X. DOI: 10.1016/j.nimb.2009.02.045.

[75] Bethe, H. “Zur Theorie des Durchgangs schneller Korpuskularstrahlen durch Materie”. In: *Annalen der Physik* 397.3 (1930), pp. 325–400. ISSN: 1521-3889. DOI: 10.1002/andp.19303970303.

[76] Bloch, F. “Zur Bremsung rasch bewegter Teilchen beim Durchgang durch Materie”. In: *Annalen der Physik* 408.3 (1933), pp. 285–320. ISSN: 1521-3889. DOI: 10.1002/andp.19334080303.

[77] Fleischer, R., Price, P., and Walker, R. “Ion Explosion Spike Mechanism for Formation of Charged Particle Tracks in Solids”. In: *Journal of Applied Physics* 36.11 (1965), pp. 3645–3652. DOI: 10.1063/1.1703059.

[78] Wang, Z. et al. “The S e sensitivity of metals under swift-heavy-ion irradiation: a transient thermal process”. In: *Journal of Physics: Condensed Matter* 6.34 (1994), pp. 6733–6750.

[79] Ziegler, J. “SRIM-2003”. In: *Nuclear Instruments and Methods in Physics Research Section B: Beam Interactions with Materials and Atoms* 219 (2004), p. 1027.

[80] Ferain, E. and Legras, R. “Heavy ion tracks in polycarbonate. Comparison with a heavy ion irradiated model compound (diphenyl carbonate)”. In: *Nuclear Instruments and Methods in Physics Research Section B: Beam Interactions with Materials and Atoms* 82.4 (1993), pp. 539–548. ISSN: 0168-583X. DOI: 10.1016/0168-583X(93)96008-Z.

[81] Cornelius, T. et al. “Investigation of nanopore evolution in ion track-etched polycarbonate membranes”. In: *Nuclear Instruments and Methods in Physics Research Section B: Beam Interactions with Materials and Atoms* 265.2 (2007), pp. 553–557. ISSN: 0168-583X. DOI: 10.1016/j.nimb.2007.10.004.

[82] Schwerionenforschung GmbH, G. H. für. *Universal Linear Accelerator of GSI*. https://www.gsi.de/en/researcl 2018.

[83] DeSorbo, W. “Ultraviolet effects and aging effects on etching characteristics of fission tracks in polycarbonate film”. In: *Nuclear Tracks* 3.1 (1979), pp. 13–32. ISSN: 0191-278X. DOI: 10.1016/0191-278X(79)90026-X.

[84] Cornelius, T. et al. “Nanopores in track-etched polymer membranes characterized by small-angle x-ray scattering”. In: *Nanotechnology* 21 (2010), p. 155702. DOI: 10.1088/0957-4484/21/15/155702.

[85] Pépy, G. et al. “Cylindrical nanochannels in ion-track polycarbonate membranes studied by small-angle X-ray scattering”. In: *Journal of Applied Crystallography* 40.s1 (2007), s388–s392. DOI: 10.1107/S0021889807000088.

[86] Apel, P. et al. “Structure of polycarbonate track-etch membranes: Origin of the "paradoxical" pore shape”. In: *Journal of Membrane Science* 282 (2006), pp. 393–400. ISSN: 0376-7388. DOI: 10.1016/j.memsci.2006.05.045.

[87] Apel, P. et al. “Track size and track structure in polymer irradiated by heavy ions”. In: *Nuclear Instruments and Methods in Physics Research B* 146 (1998), pp. 468–474.

[88] Apel, P. et al. “Morphology of latent and etched heavy ion tracks in radiation resistant polymers polyimide and poly(ethylene naphthalate)”. In: *Nuclear Instruments and Methods in Physics Research B* 185 (2001), pp. 216–221.

[89] Apel, P. et al. “Etching of nanopores in polycarbonate irradiated with swift heavy ions at 15 K”. In: *Nuclear Instruments and Methods in Physics Research B* 245 (2006), pp. 284–287. DOI: 10.1016/j.nimb.2005.11.164.

[90] Li, L. et al. “Pulsed Electrodeposition of Large-Area, Ordered $Bi_{1-x}Sb_x$ Nanowire Arrays from Aqueous Solutions”. In: *Journal of Physical Chemistry B* 108.50 (2004), p. 19381.

[91] Schlesinger, M. and Paunovic, M. *Modern Electroplating*. 5th ed. John Wiley and Sons, 2010.

[92] Bard, A. and Faulkner, L. *Electrochemical Methods, Fundamentals and Applications*. Ed. by Harris, D. 2nd ed. John Wiley and Sons, 2001.

[93] Roy, S. and Hansal, W. *Pulse Plating*. Eugen G. Leuze Verlag KG, 2012.

[94] Paunovic, M. and Schlesinger, M. *Fundamentals of Electrochemical Deposition*. second. Wiley and Sons, 2006.

[95] Schuchert, I. "Elektroschemische Untersuchungen zur Abscheidung und zum Korrosionsverhalten von Kupfermikrostrukturen". PhD thesis. Technische Universität Darmstadt, 2000.

[96] Bond, A. et al. "A comparison of the chronoamperometric response at inlaid and recessed disc microelectrodes". In: *Journal of Electroanalytical Chemistry* 249 (1988), pp. 1–14.

[97] Chen, Y. et al. "Orientation-controllable growth of Sb nanowire arrays by pulsed electrodeposition". In: *Materials Chemistry and Physics* 126.1 (2011), pp. 386 –390. ISSN: 0254-0584. DOI: 10.1016/j.matchemphys.2010.11.005.

[98] Bousso, R. et al. "Eternal inflation predicts that time will end". In: *Physical Review D* 83 (2 2011), p. 023525. DOI: 10.1103/PhysRevD.83.023525.

[99] Li, l. et al. "Pulsed electrodeposition and unique properties of one-dimensional Bi-based nanostructures in porous alumina membranes". In: *Pure and Applied Chemistry* 82 (2017), pp. 2075–2095. DOI: 10.1351/PAC-CON-09-11-08.

[100] Chandrasekar, M. and Pushpavanam, M. "Pulse and pulse reverse plating -Conceptual, advantages and applications". In: *Electrochimica Acta* 53.8 (2008), pp. 3313–3322. ISSN: 0013-4686. DOI: 10.1016/j.electacta.2007.11.054.

[101] Roy, S. and Landolt, D. "Determination of the practical range of parameters during reverse-pulse current plating". In: *Journal of Applied Electrochemistry* 27 (1997), pp. 299–307.

[102] Picht, O. "Growth and Characterization of Bismuth Telluride Nanowires". PhD thesis. Ruperto-Carola University of Heidelberg, 2010.

[103] Vereecken, P. et al. "Electrodeposition of $Bi_{1-x}Sb_x$ Thin Films". In: *Journal of the Electrochemical Socienty* 150 (2003), pp. 131–139.

[104] Wagner, M. "Fabrication of Antimony 3D Nanowire Networks for Thermoelectric Applications". MA thesis. Technische Universität Darmstadt, 2012.

[105] Williams, D. and Carter, C. *Transmission Electron Microscopy*. Ed. by David, B. Springer, 2009.

[106] Spieß, L. et al. *Modern Röntgenbeugung*. Ed. by Spieß, L. Vieweg+Teubner, 2009.

[107] Schmidt, P. *Praxis der Rasterelectronenmikroskopie und Mikrobereichsanalyse*. Ed. by Schmidt, P. Expert Verlag, 1994.

[108] Reimer, L. *Scanning Electron Microscopy: physics of image formation and microanalysis*. Ed. by Schawlow, A., Siegman, A., and Tamir, T. Springer series in optical sciences, 1998.

[109] Harris, G. "Quantitative measurement of preferred orientation in rolled uranium bars". In: *Philosophical Magazine Series* 7 (1952), p. 113. DOI: 10.1080/14786440108520972.

[110] Burr, L. "Ion-Track Technology Based Synthesis and Characterization of Gold and Gold Alloys Nanowires and Nanocones". PhD thesis. Technische Universität Darmstadt, 2016.

[111] Wagner, M. et al. "Fabrication and thermoelectrical characterization of three-dimensional nanowire networks". In: *Phys. Status Solidi A* 213 (2016), pp. 610–619.

[112] Yu, S. et al. "Nano Wheat Fields Prepared by Plasma-Etching Gold Nanowire-Containing Membranes". In: *Nano Letters* 3 (2003), pp. 815–818.

[113] Abramson, A. et al. "Fabrication and Characterization of a Nanowire/Polymer-Based Nanocomposite for a Prototype Thermoelectric Device". In: *Journal of Microelectromechanical Systems* 13.3 (2004), pp. 505–513.

[114] Palumbo, F. et al. “SuperHydrophobic and SuperHydrophilic Polycarbonate by Tailoring Chemistry and Nano-texture with Plasma Processing”. In: *Plasma Processes and Polymers* 8 (2011), pp. 118–126.

[115] Maurer, F. et al. “Preferred growth orientation of metallic fcc nanowires under direct and alternating electrodeposition conditions”. In: *Nanotechnology* 18 (2007), p. 135709. DOI: 10.1088/0957-4484/18/13/135709.

[116] Cornelius, T. et al. “Controlled fabrication of poly- and single-crystalline bismuth nanowires”. In: *Nanotechnology* 16 (2005), S246–S249. DOI: 10.1088/0957-4484/16/5/020.

[117] Rowe, D., ed. *Thermoelectrics Handbook*. CRC Press, 2006.

[118] Goldsmid, H. *Introduction to Thermoelectricity*. Ed. by Hull, R. et al. Springer, 2010.

[119] Nolas, G., Sharp, J., and Goldsmid, H. *Thermoelectrics Basic Principles and New Materials Developments*. Ed. by Zunger, A. et al. Springer, 2001.

[120] Seebeck, T. “Ueber die magnetische Polarisation der Metalle und Erze durch Temperatur-Differenz”. In: *Annalen der Physik* 82.2 (1826), pp. 133–160. ISSN: 1521-3889. DOI: 10.1002/andp.18260820202.

[121] Cusack, N. and Kendall, P. “The Absolute Scale of Thermoelectric Power at High Temperature”. In: *Proceedings of the Physical Society* 72.5 (1958), pp. 898–901.

[122] Peltier, J. “Nouvelles expériences sur la caloricité des courants électrique”. In: *Annales de Chimie et de Physique* 56 (1834), pp. 371–386.

[123] Thomson, W. “On the Dynamical Theory of Heat”. In: *Phyilosophical Transaction of the Royal Society* 3 (1851), pp. 91–98.

[124] Riffat, S. and Ma, X. “Thermoelectrics: a review of present and potential applications”. In: *Applied Thermal Engineering* 23.8 (2003), pp. 913–935. ISSN: 1359-4311. DOI: 10.1016/S1359-4311(03)00012-7.

[125] Mayer, H. and Krechetnikov, R. “Walking with coffee: Why does it spill?” In: *Physical Review E* 85 (2012), p. 046117.

[126] Zebarjadi, M. “Electronic cooling using thermoelectric devices”. In: *Applied Physics Letters* 106.20 (2015), p. 203506. DOI: 10.1063/1.4921457.

[127] Zhao, D. and Tan, G. “A review of thermoelectric cooling: Materials, modeling and applications”. In: *Applied Thermal Engineering* 66.1 (2014), pp. 15–24. ISSN: 1359-4311. DOI: 10.1016/j.applthermaleng.2014.01.074.

[128] Elarusi, A., Attar, A., and Lee, H. “Optimal Design of a Thermoelectric Cooling/Heating System for Car Seat Climate Control (CSCC)”. In: *Journal of Electronic Materials* 46.4 (2017), pp. 1984–1995. ISSN: 1543-186X. DOI: 10.1007/s11664-016-5043-y.

[129] Bali, A., Chetty, R., and Mallik, R. *Thin Film Structures in Energy Applications*. Ed. by Moorthy, S. B. K. Springer International Publishing, 2015.

[130] Lindeberg, M. et al. “A PCB-like process for vertically configured thermopiles”. In: *Journal of Micromechanics and Microengineering* 18.6 (2008), p. 065021. DOI: 10.1088/0960-1317/18/6/065021.

[131] Su, S. et al. “Performance optimization analyses and parametric design criteria of a dye-sensitized solar cell thermoelectric hybrid device”. In: *Applied Energy* 120 (2014), pp. 16–22. ISSN: 0306-2619. DOI: 10.1016/j.apenergy.2014.01.048.

[132] Fisac, M., Villasevil, F., and López, A. “High-efficiency photovoltaic technology including thermoelectric generation”. In: *Journal of Power Sources* 252 (2014), pp. 264–269. ISSN: 0378-7753. DOI: 10.1016/j.jpowsour.2013.11.121.

[133] OBrien, R. et al. “Safe radioisotope thermoelectric generators and heat sources for space applications”. In: *Journal of Nuclear Materials* 377.3 (2008), pp. 506–521. ISSN: 0022-3115. DOI: 10.1016/j.jnucmat.2008.04.009.

[134] Bennett, G. et al. “Mission of Daring: The General-Purpose Heat Source Radioisotope Thermoelectric Generator”. In: *International Energy Conversion Engineering Conference (IECEC)*. American Institute of Aeronautics and Astronautics, 2006. DOI: 10.2514/6.2006-4096.

[135] Liang, X. et al. “A review and selection of engine waste heat recovery technologies using analytic hierarchy process and grey relational analysis”. In: *International Journal of Energy Research* 39.4 (2015), pp. 453–471. DOI: 10.1002/er.3242.

[136] Leonov, V. and Vullers, R. “Wearable electronics self-powered by using human body heat: The state of the art and the perspective”. In: *Journal of Renewable and Sustainable Energy* 1.6 (2009), p. 062701. DOI: 10.1063/1.3255465. eprint: http://dx.doi.org/10.1063/1.3255465.

[137] Baumann, S. et al. *Bedeutung der Mikroelektronik für Industrie 4.0*. Positionspapier aus der AG Silicon Germany. 2014.

[138] Kim, J. et al. “Thermoelectricity in semiconductor nanowires”. In: *Physica Status Solidi RRL* 7.10 (2013), pp. 1–14. DOI: /10.1002/pssr.201307239.

[139] Altenkirch, E. “Über den Nutzeffekt der Thermosäule”. In: *Physikalische Zeitschrift* 10 (1909), pp. 560–568.

[140] Altenkirch, E. “Elektrothermische Kälteerzeugung und reversible elektrische Heizung”. In: *Physikalische Zeitschrift* 7 (1911), pp. 920–924.

[141] Birkholz, U., Fettig, R., and Rosenzweig, J. “Fast Semiconductor Thermoelectric Devices”. In: *Sensors and Actuators* 12.2 (1987), pp. 179–184. ISSN: 0250-6874. DOI: 10.1016/0250-6874(87)85015-1.

[142] Twaha, S. et al. “A comprehensive review of thermoelectric technology: Materials, applications, modelling and performance improvement”. In: *Renewable and Sustainable Energy Reviews* 65 (2016), pp. 698–726. ISSN: 1364-0321. DOI: 10.1016/j.rser.2016.07.034.

[143] Qi, Y. et al. “Thermoelectric devices based on one-dimensional nanostructures”. In: *Journal of Materials Chemistry A* 1 (20 2013), pp. 6110–6124. DOI: 10.1039/C3TA01594G.

[144] Keyani, J., Stacy, A., and Sharp, J. “Assembly and measurement of a hybrid nanowire-bulk thermoelectric device.” In: *Applied Physics Letters* 89 (2006), p. 233106. DOI: 10.1063/1.2400199.

[145] DiSalvo, F. “Thermoelectric Cooling and Power Generation”. In: *Science* 285 (1999), p. 703. DOI: 10.1126/science.285.5428.703.

[146] Casati, G., Mej`a-Monasterio, C., and Prosen, T. “Increasing Thermoelectric Efficiency: A Dynamical Systems Approach”. In: *Physical Review Letters* 101 (2008), p. 016601. DOI: 10.1103/PhysRevLett.101.016601.

[147] Heremans, J. “Low-dimensional Thermoelectricity”. In: *Acta Physica Polonica A* 108 (2005), p. 609.

[148] Heremans, J. et al. “Enhancement of Thermoelectric Efficiency in PbTe by Distortion of the Electronic Density of States”. In: *Science* 321 (2008), p. 554. DOI: 10.1126/science.1159725.

[149] Szczech, J., Higgins, J., and Jin, S. “Enhancement of the thermoelectric properties in nanoscale and nanostructured materials”. In: *Journal of Materials Chemistry* 21 (2010), pp. 4037–4055. DOI: 10.1039/c0jm02755c.

[150] Jeffrey, G., Snyder, S., and Toberer, E. “Complex thermoelectric materials”. In: *Nature* 7 (2008), pp. 105–114.

[151] Völklein, F. et al. “The experimental investigation of thermal conductivity and the Wiedemann–Franz law for single metallic nanowires”. In: *Nanotechnology* 20 (2009), p. 325706. DOI: 10.1088/0957-4484/20/32/325706.

[152] Mul̈ler, S. “Morphological, Structural, and Composition Characterization of Electrodeposited $Bi_{1-x}Sb_xNanowires$”. PhD thesis. Ruprecht-Karls-Universitaẗ in Heidelberg, 2012.

[153] Carruthers, P. “Theory of Thermal Conductivity of Solids at Low Temperature”. In: *Reviews of Modern Physics* 33.1 (1961), pp. 92–138.

[154] Dismukes, J. et al. “Thermal and Electrical Properties of Heavily Doped GeSi Alloys up to 1300°K”. In: *Journal of Applied Physics* 35 (1964), pp. 2899–2907. DOI: 10.1063/1.1713126.

[155] Xiao, Z. et al. “Nanoscale $BixTe_3/Sb_2Te_3$ multilayer thin film materials for reduced thermal conductivity”. In: *Nuclear Instruments and Methods in Physics Research B* 242 (2006), pp. 201–204.

[156] Wang, Y. et al. “Thermoelectrics in misfit-layered oxides $[(Ca,Ln)_2CoO_3]_{0.62}[CoO_2]$: From bulk to nano”. In: *Nano Energy* 1 (2012), pp. 456–465.

[157] Martin, J., Wang, H., and Nolas, G. “Optimization of the thermoelectric properties of $Ba_8Ga_{16}Ge_{30}$”. In: *Applied Physics Letters* 92 (2008), p. 222110. DOI: 10.1063/1.2939438.

[158] Brown, S. et al. “$Yb_{14}MnSb_{11}$: New High Efficiency Thermoelectric Material for Power Generation”. In: *Chemistry of Materials* 18 (2006), pp. 1873–1877.

[159] Kishimoto, K., Tsukamoto, M., and Koyanagi, T. “Temperature dependence of the Seebeck coefficient and the potential barrier scattering of n-type PbTe films prepared on heated glass substrates by rf sputtering”. In: *Journal of Applied Physics* 92 (2002), pp. 5331–5339. DOI: 10.1063/1.1512964.

[160] Vashaee, D. and Shakouri, A. “Improved Thermoelectric Power Factor in Metal-Based Superlattices”. In: *Physical Review Letters* 92 (2004), p. 106103.

[161] Berland, K. et al. “Enhancement of thermoelectric properties by energy filtering: Theoretical potential and experimental reality in nanostructured ZnSb”. In: *Journal of Applied Physics* 119 (2016), p. 125103. DOI: 10.1063/1.4944716.

[162] Cornett, J. and Rabin, O. “Thermoelectric figure of merit calculations for semiconducting nanowires”. In: *Applied Physics Letters* 98 (2011), p. 182104. DOI: 10.1063/1.3585659.

[163] Hochbaum, A. et al. “Enhanced thermoelectric performance of rough silicon nanowires”. In: *Nature Letters* 451 (2008), pp. 163–168. DOI: 10.1038/nature06381.

[164] Li, J.-F. et al. “High-performance nanostructured thermoelectric materials”. In: *NPG Asia Materials* 2 (2010), pp. 152–158. DOI: 10.1038/asiamat.2010.138.

[165] Li, D. et al. “Thermal conductivity of individual silicon nanowires”. In: *Applied Physics Letters* 83 (2003), pp. 2934–2936. DOI: 10.1063/1.1616981.

[166] Kazan, M. et al. “Thermal conductivity of silicon bulk and nanowires: Effects of isotopic composition, phonon confinement, and surface roughness”. In: *Journal of Applied Physics* 107 (2010), p. 083503. DOI: 10.1063/1.3340973.

[167] Rojo, M. et al. “Thermal conductivity of Bi_2Te_3 nanowires: How size affects phonon scattering”. In: *Nanoscale* 20 (2017), pp. 6741–6747. DOI: 10.1039/C7NR02173A.

[168] Harrison, P. *Quantum wells, wires and dots*. John Wiley and Sons, London, 2005.

[169] Dresselhaus, M. et al. *Springer Handbook of Nanotechnology*. Ed. by Bhushan, B. 3rd. Springer, 2010, pp. 119–167.

[170] Fuchs, K. “The conductivity of thin metallic films according to the electron theory of metals”. In: *Mathematical Proceedings of the Cambridge Philosophical Society* 34 (1938), pp. 100–108. DOI: 10.1017/S0305004100019952.

[171] Mayadas, A. and Shatzkes, M. “Electrical-Resistivity Model for Polycrystalline Films: the Case of Arbitrary Reflection at External Surfaces”. In: *Physical Review B* 1 (1970), p. 1382.

[172] Fuchs, K. “The conductivity of thin metallic films according to the electron theory of metals”. In: *Mathematical Proceedings of the Cambridge Philosophical Society* 34 (1936), pp. 100–108.

[173] Dingle, R. “The Electrical Conductivity of Thin Wires”. In: *Proceedings of the Royal Society* 201 (1950), p. 545. DOI: 10.1098/rspa.1950.0077.

[174] Sondheimer, E. “The mean free path of electrons in metals”. In: *Advances in Physics* 50 (2001), pp. 499–537. DOI: 10.1080/00018735200101151.

[175] Hansen, M. “Colloquium: Topological insulators”. In: *Reviews of Modern Physics* 82 (2010), p. 3045. DOI: 10.1103/RevModPhys.82.3045.

[176] Pankratov, O., Pakhomov, S., and Volkov, B. “Supersymmetry in heterojunctions: band-inverting contact on the basis of $Pb_{1-x}Sn_xTe$ and $Hg_{1-x}Cd_xTe$”. In: *Solid State Communications* 61 (1987), pp. 93–96.

[177] Hamdou, B. et al. “Surface state dominated transport in topological insulator Bi_2Te_3 nanowires”. In: *Applied Physics Letters* 103 (2013), p. 193107. DOI: 10.1063/1.4829748.

[178] Shin, H. et al. “The surface-to-volume ratio: a key parameter in the thermoelectric transport of topological insulator Bi_2Se_3 nanowires”. In: *Nanoscale* 28 (2016), pp. 1–6. DOI: 10.1039/C6NR01716A.

[179] Cassinelli, M. et al. “Influence of surface states and size effects on the Seebeck coefficient and electrical resistance of $Bi_{1x}Sb_x$ nanowire arrays”. In: *Nanoscale* 9 (2017), pp. 3169–3179. DOI: 10.1039/C6NR09624G.

[180] Toimil-Molares, M. et al. “Fragmentation of nanowires driven by Rayleigh instability”. In: *Applied Physics Letters* 85 (2004), p. 5337. DOI: 10.1063/1.1826237.

[181] Cassinelli, M. et al. “Low temperature annealing effects on the stability of Bi nanowires”. In: *Physica Status Solidi A: Applications and Materials Science* 213 (2016), pp. 603–609. DOI: 10.1002/pssa.201532613.

[182] Silva, R. et al. “Short versus long silver nanowires: a comparison of in vivo pulmonary effects post instillation”. In: *Particle and Fibre Toxicology* 11 (2014), pp. 1–20. DOI: 10.1186/s12989-014-0052-6.

[183] Zimmerman, J. et al. “Cellular uptake and dynamics of unlabeled freestanding silicon nanowires”. In: *Science Advances* 2 (2016), p. 1601039.

[184] Lenoir, B. et al. “Effect of antimony content on the thermoelectric figure of merit of $Bi_{1-x}Sb_x$”. In: *Journal Physics Chemistry Solids* 59 (1998), pp. 129–134.

[185] Issi, J.-P. “Low Temperature Transport Properties of the Group V Semimetals”. In: *Australian Journal of Physics* 32 (1979), p. 585.

[186] Heremans, J. and Trush, C. “Thermoelectric power of bismuth nanowires”. In: *Physical Review B* 59 (1999), p. 12579.

[187] Dresselhaus, M. et al. “Low-dimensional thermoelectric materials”. In: *Physics of the Solid State* 41 (1999), p. 679.

[188] Zhang, Y. et al. “Electrical transport properties of single-crystal antimony nanowire arrays”. In: *Physical Review B* 73 (2006), p. 2006. DOI: 10.1103/PhysRevB.73.113403.

[189] Cornelius, T. and Toimil-Molares, M. “Nanowires”. In: ed. by Prete, P. INTECH, 2010. Chap. Finite- and Quantum-size Effects of Bismuth Nanowires, p. 414.

[190] Heremans, J. et al. “Transport properties of antimony nanowires”. In: *Physical Review B* 63 (2001), p. 085406.

[191] Zhang, Y., Li, L., and Li, G. “Fabrication and anomalous transport properties of an Sb/Bi segment nanowire nanojunction array”. In: *Nanotechnology* 16 (2005), pp. 2096–2099. DOI: 10.1088/0957-4484/16/10/020.

[192] Lin, Y.-M. et al. “Thermoelectric properties of $Bi_{1-x}Sb_x$ nanowire arrays”. In: *Material Research Society Symposium Proceedings* 691 (2002), G10.6.

[193] Moore, A. et al. “Thermal conductivity suppression in bismuth nanowires”. In: *Journal of Applied Physics* 106 (2009), p. 034310. DOI: 10.1063/1.3191657.

[194] Roh, J. et al. “Observation of Anisotropy in Thermal Conductivity of Individual Single-Crystalline Bismuth Nanowires”. In: *American Chemical Society Nano* 5 (2011), p. 3954. DOI: 10.1021/nn200474d.

[195] Xu, N., Xu, Y., and Zhu, J. “Topological insulators for thermoelectrics”. In: *Quantum Materials* 2 (2017), pp. 1–9. DOI: 10.1038/s41535-017-0054-3.

[196] Mun, E. et al. “Experimental Setup for the Measurement of the Thermoelectric Power in Zero and Applied Magnetic Field”. In: *arXiv:1003.0921 [physics.ins-det]* 1 (2010), pp. 1–18.

[197] Lowhorn, N. et al. “Round-Robin Studies of Two Potential Seebeck Coefficient Standard Reference Materials”. In: *Thermoelectrics* 26th International Conference on Thermoelectrics (2008), p. 361. DOI: 10.1109/ICT.2007.4569495.

[198] Murata, M. et al. “Theoretical modeling of electrical resistivity and Seebeck coefficient of bismuth nanowires by considering carrier mean free path limitation”. In: *Journal of Applied Physics* 121 (2017), p. 014303. DOI: 10.1063/1.4973191.

[199] Krieg, J. et al. “Exploring the electronic structure and chemical homogeneity of individual Bi_2Te_3 nanowires by nano-angle-resolved photoemission spectroscopy”. In: *Nano Letters* 16 (2016), p. 4001.

[200] Völklein, F. and Kessler, E. “Thermal Conductivity and Thermoelectric Figure of Merit of Antimony Thin Films”. In: *Physica Status Solidi B* 158 (1990), p. 521. DOI: 10.1002/pssb.2221580213.

[201] Harris, L. and Corrigan, F. “The mean free path for the carrier in antimony”. In: *Journal of Physics and Chemistry of Solids* 26 (1965), pp. 307–310.

[202] Lin, Y.-M. et al. “Transport properties of Bi nanowire arrays”. In: *Applied Physics Letters* 76 (2000), p. 3944. DOI: 10.1063/1.126829.

[203] Murata, M. et al. “Mean free path limitation of thermoelectric properties of bismuth nanowire”. In: *Journal of Applied Physics* 105 (2009), p. 113706. DOI: 10.1063/1.3131842.

[204] Nikolaeva, A. et al. “Diameter-dependent thermopower of bismuth nanowires”. In: *Physical Review B* 77 (2008), p. 035422. DOI: 10.1103/PhysRevB.77.035422.

[205] Zhang, Z. et al. “Electronic transport properties of single-crystal bismuth nanowire arrays”. In: *Physical Review B* 61 (2000), p. 4850. DOI: 10.1103/PhysRevB.61.4850.

[206] Cronin, S. et al. “Making electrical ccontact to nanowires with thick oxide coating”. In: *Nanotechnology* 13 (2002), pp. 653 –658.

[207] Reith, H. “Untersuchung von Size-Effekten thermischer TransportkoefTransport von Nanodrähten”. PhD thesis. Johann Wolfgang Goethe- Universität in Frankfurth am Main, 2012.

[208] Völklein, F. and Zetterer, T. *Einführung in die Mikrosystemtechnik*. Springer Vieweg, 2000, p. 22.

[209] Boyer, A. and Cissè, E. “Properties of thin film thermoelectric materials: application to sensors using the Seebeck effect”. In: *Materials Science and Engineering B* 13 (1992), pp. 103–111. DOI: 10.1016/0921-5107(92)90149-4.

[210] Lashkevich, I., Fragoso, O., and Gurevich, Y. “Thin-film thermoelectric cooling”. In: *Technical Physics* 54 (2009), pp. 289–297.

[211] Kim, W. et al. “Nanowire Arrays for Thermoelectric Devices”. In: *Proceeding Heat Transfer Summer Conference* 1 (2003), pp. 101–104. DOI: 10.1115/HT2003-47320.

[212] Okamura, Y., Kohler, T., and Miyawaki, M. *Fabrication of nanoscale thermoelectric devices*. US Patent App. 10/666,787. 2005.

[213] Huzel, D. et al. “Characterization and Application of Thermoelectric Nanowires”. In: *Nanowires - Implementations and Applications*. Ed. by Hashim, A. Rijeka: InTech, 2011. Chap. 14. DOI: 10.5772/19656.

[214] Koukharenko, E. et al. “Towards a nanostructured thermoelectric generator using ion-track lithography”. In: *Journal of Micromechanics and Microengineering* 18.10 (2008), p. 104015.

[215] Abbas, A. S., Yavuz, M., and Cui, B. “Polycarbonate electron beam resist using solvent developer”. In: *Microelectronic Engineering* 113 (2014), pp. 140–142. ISSN: 0167-9317. DOI: 10.1016/j.mee.2013.08.006.

[216] Fabián-Mijangos, A., Min, G., and Alvarez-Quintana, J. “Enhanced performance thermoelectric module having asymmetrical legs”. In: *Energy Conversion and Management* 148 (2017), pp. 1372–1381. DOI: 10.1016/j.enconman.2017.06.087.

[217] Walker, P. and Tarn, W. *Handbook of Metal Etchants*. Ed. by Walker, P. and Tarn, W. CRC Press LLC, 1991.

9 Declaration of Academic Integrity

Thesis Statement pursuant to § 22 paragraph 7 of APB TU Darmstadt
I hereby formally declare that I, Michael Florian Peter Wagner, have written the submitted thesis independently. I did not use any additional support except for the quoted literature and other sources mentioned in this thesis. I clearly marked and separately listed all of the literature and all of the other sources which I employed when producing this academic work, either literally or in content. This thesis has not been handed in or published before in the same or similar form.
In the submitted thesis the written copies and the electronic version are identical in content.

Erklärung zur Abschlussarbeit gemäß § 22 Abs. 7 APB der TU Darmstadt
Hiermit versichere ich, Michael Florian Peter Wagner, die vorliegende Dissertation ohne Hilfe Dritter und nur mit den angegebenen Quellen und Hilfsmitteln angefertigt zu haben. Alle Stellen, die Quellen entnommen wurden, sind als solche kenntlich gemacht worden. Diese Arbeit hat in gleicher oder ähnlicher Form noch keiner Prüfungsbehörde vorgelegen.
In der abgegebenen Thesis stimmen die schriftliche und elektronische Fassung überein.

Date:October 7, 2018 Signature: